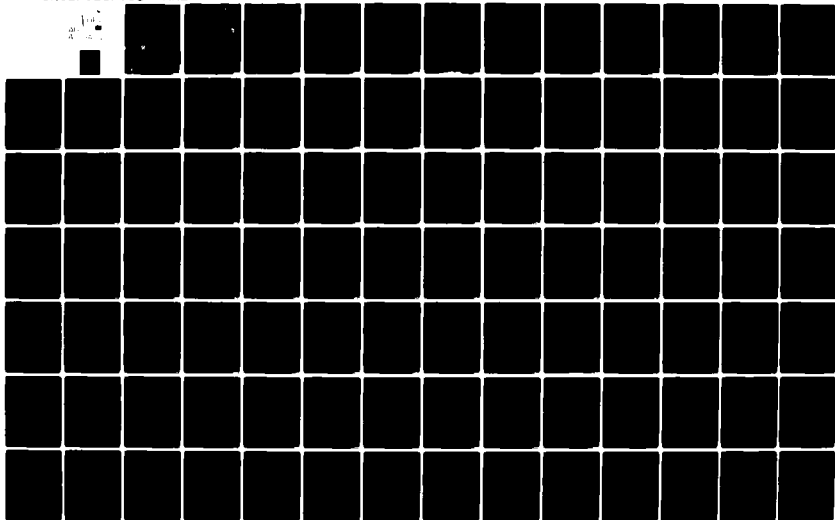
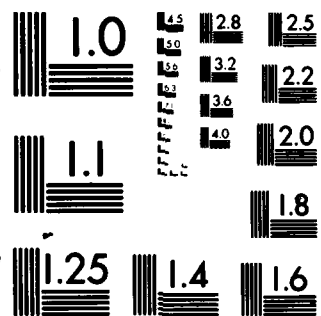


AD-A091 852 PRINCETON UNIV NJ DEPT OF MECHANICAL AND AEROSPACE --ETC F/G 19/1  
CONVECTIVE IGNITION OF PROPELLANT CYLINDERS IN A DEVELOPING CRO--ETC(U)  
SEP 80 A BIRK, L H CAVENY DAA629-79-C-0140  
UNCLASSIFIED MAE-1486 ARO-13108.1-E NL





MICROCOPY RESOLUTION TEST CHART  
NATIONAL BUREAU OF STANDARDS-1963-A

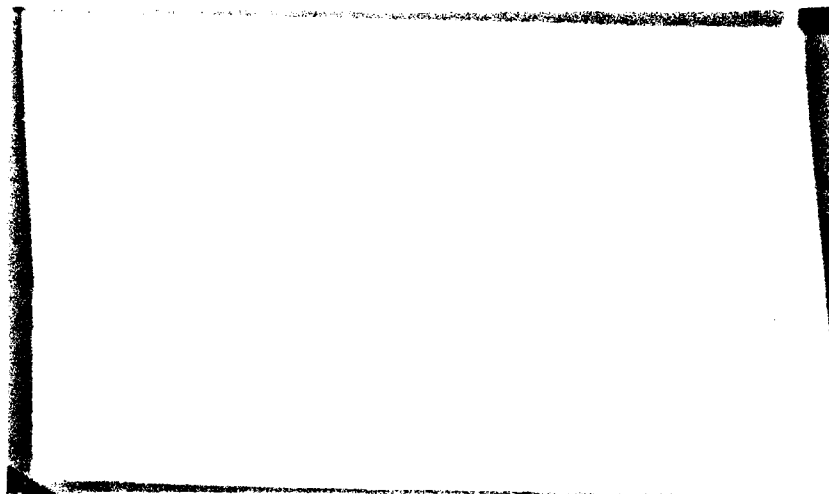
AD A091852

LEVEL

ARD 13108.1-E; 14200.1-EX  
15994.2-E

4

Princeton University



SPIC  
NOV 5 1980  
C

Department of  
Mechanical and  
Aerospace Engineering

DISTRIBUTION STATEMENT A  
Approved for public release;  
Distribution Unlimited

ENC. FILE COPY

8C11 03 065

(4)  
(9) Final rept. Oct 75-Aug 80;

(18) ARS, AIO

(19) 13108.1-1,  
14200.1-1

(6) **CONVECTIVE IGNITION  
OF PROPELLANT CYLINDERS  
IN A DEVELOPING CROSS-FLOW FIELD.**

**FINAL REPORT TO THE  
ARMY RESEARCH OFFICE**

Submitted By

(10) Aviezer Birk and Leonard H. Caveny

DTIC  
ECTE  
NOV 5 1980  
D  
C

Performed under U. S. Army Research Office

GRANT DAAG29-78-G-0153

CONTRACT DAAG29-79-C-0140

(15) DAAG-29-78-G-0153

(11) September 1980

MAE Report No. 1486

(12) 194  
(14) MAE-1486-2A  
ARE-15974.2-E

1. Approved for public release; distribution unlimited.
2. Reproduction in whole or in part is permitted for any purpose of the United States Government.

Department of Mechanical and Aerospace Engineering  
PRINCETON UNIVERSITY  
Princeton, New Jersey 08544

4110732

503

UNCLASSIFIED

SECURITY CLASSIFICATION OF THIS PAGE (When Data Entered)

REPORT DOCUMENTATION PAGE		READ INSTRUCTIONS BEFORE COMPLETING FORM
1. REPORT NUMBER	2. GOVT ACCESSION NO. <b>AD-AC 91 852</b>	3. RECIPIENT'S CATALOG NUMBER
4. TITLE (and Subtitle) CONVECTIVE IGNITION OF PROPELLANT CYLINDERS IN A DEVELOPING CROSS FLOW FIELD		5. TYPE OF REPORT & PERIOD COVERED FINAL <b>OCT 75-</b> <del>June 1978</del> -Aug. 1980
7. AUTHOR(s) Aviezer Birk Leonard H. Caveny		6. PERFORMING ORG. REPORT NUMBER MAE-1486
9. PERFORMING ORGANIZATION NAME AND ADDRESS Princeton University Princeton, NJ 08544		8. CONTRACT OR GRANT NUMBER(s) <b>76 G 0044; 76 G 0270</b> DAAG29-78-G-0153 DAAG29-79-C-0140
11. CONTROLLING OFFICE NAME AND ADDRESS U. S. Army Research Office Durham, NC		10. PROGRAM ELEMENT, PROJECT, TASK AREA & WORK UNIT NUMBERS
14. MONITORING AGENCY NAME & ADDRESS (if different from Controlling Office)		12. REPORT DATE September 1980
		13. NUMBER OF PAGES 175
		15. SECURITY CLASS. (of this report) UNCLASSIFIED
		15a. DECLASSIFICATION/DOWNGRADING SCHEDULE
16. DISTRIBUTION STATEMENT (of this Report)  Approved for public release; distribution unlimited.		
17. DISTRIBUTION STATEMENT (of the abstract entered in Block 20, if different from Report)		
18. SUPPLEMENTARY NOTES  THE VIEW, OPINIONS, AND/OR FINDINGS CONTAINED IN THIS REPORT ARE THOSE OF THE AUTHOR(S) AND SHOULD NOT BE CONSTRUED AS AN OFFICIAL DEPARTMENT OF THE ARMY POSITION, POLICY, OR DE- CISION, UNLESS SO DESIGNATED BY OTHER DOCUMENTATION.		
19. KEY WORDS (Continue on reverse side if necessary and identify by block number)  solid propellants                      flame spreading gun propellants                        shock tunnel convective ignition                    heat flux measurement		
20. ABSTRACT (Continue on reverse side if necessary and identify by block number)  → The sensitivities of ignition delay time and site to the ambient conditions (i.e., flow velocity, pressure, temperature and gas composition) were inves- tigated under high heat flux conditions (e.g., 100 cal/cm <sup>2</sup> -s). A shock tunnel was used to provide up to 20 ms of flowing heated gas at: 1 to 22 MPa, 1800 to 2300 K, 5 to 300 m/s. Test gases were 100%N <sub>2</sub> , 10%O <sub>2</sub> /90%N <sub>2</sub> and 50%O <sub>2</sub> /50%N <sub>2</sub> . Instrumentation included radiation detectors, high-speed shadowgraph sequences, pressure probes and heat flux gauges. Most of the tests were conducted with		

DD FORM 1 JAN 73 1473 EDITION OF 1 NOV 65 IS OBSOLETE

UNCLASSIFIED

SECURITY CLASSIFICATION OF THIS PAGE (When Data Entered)

UNCLASSIFIED

- 11 -

SECURITY CLASSIFICATION OF THIS PAGE(When Data Entered)

nitrocellulose-based propellants. The effect of high heating rates accompanying the initial flow transients and boundary layer development were very prominent in producing sub-millisecond ignition delays for oxygen-containing flows. Indeed, during their brief period (on the order of 0.2 ms) the heat fluxes are 4 to 5 times higher than the corresponding well developed flow values. Flame blow-off occurred for high Reynolds numbers (e.g., 16,000), low free stream oxygen content flows. Depending on the flow conditions first ignition occurred distinctly at the leading edge, trailing edge or at the flow separation region. Compared to triple-based propellant, single-based and double-based propellants ignited more rapidly in oxygen-containing flows. The experimental results indicate clearly that for the range of ambient conditions tested, the ignition is a gas phase process. The ignition processes in nonsteady reactive boundary layer flows were analyzed for the front stagnation flow region. The solution includes the boundary layer development and the transition to quasi-steady burning. A phenomenological analysis of ignition likelihood along the cylinder circumference is given based on local Damkohler numbers.

UNCLASSIFIED

SECURITY CLASSIFICATION OF THIS PAGE(When Data Entered)

# PREFACE

Thanks are extended to Mr. Chris R. Felsheim who carried out skillfully the propellant processing and component fabrication, and to Mr. Louis M. Pokrocos for his ingenious design and fabrication of electronic devices which were important to the calibration and data acquisition. Mr. Samuel O. Morris contributed during the initial phases of the apparatus development.

The authors thank Prof. William A. Sirignano, particularly for his guidance during the formulation of the analytical model. Also appreciated is the careful review of the experimental results by Prof. Irvin Glassman. Stimulating discussions with Dr. Moshe BenReuven were very important to the development of the numerical algorithm in this work.

This research was supported by the Army Research Office in Durham, North Carolina. The program manager was Mr. James J. Murray. The research benefited from technical interactions with the Ballistic Research Laboratories, in particular the discussions with Dr. Kevin White and Mr. Carl W. Nelson.

This report is also the Ph.D. dissertation of Aviezer Birk and carries number 1486-T in the records of the Department of Mechanical and Aerospace Engineering.

Accession For		<input checked="checked" type="checkbox"/>
RTIS GRA&I		<input type="checkbox"/>
DTIC TAB		<input type="checkbox"/>
Unannounced		
Justification		
By _____		
Distribution/		
Availability Codes		
Avail and/or		
Special		
Diet	<input checked="checked" type="checkbox"/>	

TABLE OF CONTENTS

	<u>PAGE</u>
FORM 1473 . . . . .	i
PREFACE . . . . .	iii
TABLE OF CONTENTS . . . . .	iv
LIST OF TABLES . . . . .	vii
LIST OF FIGURES . . . . .	viii
NOMENCLATURE . . . . .	xiii
 SECTION I <u>INTRODUCTION</u> . . . . .	 1
 SECTION II <u>PREVIOUS IGNITION STUDIES, PARTICULARLY REGARDING</u> <u>BALLISTIC PROPELLANTS</u> . . . . .	 3
A. The General Scope of Propellant Ignition . . . . .	3
(i) Experimental Techniques . . . . .	3
(ii) Ignition Models . . . . .	4
B. Convective Ignition Studies . . . . .	5
(i) Ignition of Flat Plate Configurations . . . . .	6
(ii) Ignition of Cylindrical Configurations . . . . .	7
C. Ignition Dynamics . . . . .	8
D. The Combustion Characteristics of Nitrocellulose- Based Propellants . . . . .	9
 SECTION III <u>THEORETICAL ANALYSIS OF CONVECTIVE IGNITION OF A</u> <u>CYLINDRICAL PROPELLANT UNDER CROSS FLOW CONDITIONS</u> . . . . .	 11
A. Introduction . . . . .	11
B. Basic Physical Considerations of Gas Phase Convective Ignition of a Circular Cylindrical Propellant . . . . .	12
C. Studies of Flow Past Circular Cylinders . . . . .	13
D. Studies of Ignition in a Reactive Boundary Layer . . . . .	16
E. Basic Equations of Unsteady Reactive Boundary Layer Coupled to Solid Phase . . . . .	17
(i) Gas Phase Equations . . . . .	18
(ii) Solid Phase Equations . . . . .	21
F. Front Stagnation Point Solution . . . . .	23
(i) Formulation . . . . .	23
(ii) Discussion of the Stagnation Flow Ignition . . . . .	27
(iii) Time Scales of the Problem . . . . .	28
G. Ignition Criteria . . . . .	30
H. Numerical Predictions of the Ignition Model for the Front Stagnation Region . . . . .	32
(i) The Effects of Various Thermal, Chemical and Flow Properties . . . . .	34
(ii) The Effect of the Flow Transient Conditions on the Ignition Process . . . . .	36
I. Ignition Mechanisms in Regions Beyond the Front Stagnation Region . . . . .	40
(i) Front Surface Ignition . . . . .	40

(ii) Rear Surface Ignition (Regions 2 and 3 - Fig. 7)	41
J. Summary	44
SECTION IV <u>EXPERIMENTAL APPARATUS</u>	46
A. Introduction	46
B. General Features of Shock Tunnel Operation	47
C. Description of the Experimental Shock Tunnel and its Accessories	49
(i) Test Section (Fig. 29)	50
(ii) Test Specimen	50
(iii) Optical System for High Speed Photography	51
D. Ignition Detection	51
E. Instrumented Cylinder	53
F. Data Acquisition and Instrumentation	54
G. Evaluation of the Performance of the Shock Tunnel	55
(i) Pressure Data and Test Time	55
(ii) Starting Process of the Flow in the Test Section	56
(iii) Remarks Concerning the Calculation of Steady State Flow Conditions (Appendix III)	58
SECTION V <u>EXPERIMENTAL RESULTS</u>	60
A. Introduction	60
B. Discussion of the Heat Transfer Data Obtained from the Instrumented Cylinder	61
C. Ignition Detection	64
(i) Ignition Data from the Photodetectors	64
(ii) Ignition Data from the Line Scan Reticon Camera	65
(iii) Ignition Data from High Speed Photography	66
D. Ignition Trends for the Various Propellants	66
E. The Sensitivity to Free Stream Oxidizer ( $O_2$ )	69
(i) Propellant Ignition	69
(ii) Polymer Ignition	72
F. Flame Spreading and Blow-off Phenomena	72
G. Ignition and Flame Spreading in Tandem Configurations	76
H. Microscopic Study of the Specimen Surface	78
I. Photographic Study of Specimen Burning Under Various Flow Conditions	79
SECTION VI <u>CONCLUSIONS</u>	81
LIST OF REFERENCES	83
TABLES	93
FIGURES	96

	<u>PAGE</u>
APPENDIX I <u>DERIVATION OF NON-STEADY REACTIVE BOUNDARY LAYER</u> <u>EQUATIONS FOR UNSTEADY FLOW CONDITIONS</u>	161
APPENDIX II <u>THE NUMERICAL SCHEME FOR THE FRONT STAGNATION</u> <u>IGNITION EQUATIONS</u>	163
APPENDIX III <u>CALCULATIONS OF THE PHYSICAL CONDITIONS IN THE TEST</u> <u>SECTION</u>	168
APPENDIX IV <u>CONSTRUCTION AND OPERATION OF THIN FILM GAUGES</u>	171
APPENDIX V <u>MOUNTING CONFIGURATION AND PERFORMANCE OF THE</u> <u>MINIATURIZED PRESSURE TRANSDUCER IN THE INSTRUMENTED</u> <u>CYLINDER</u>	174

LIST OF TABLES

	<u>PAGE</u>
Table 1 : Propellant Formulation	93
Table 2 : Main Test Conditions	94
Table 3 : Values of Physical Properties Used in Calculations	95

LIST OF FIGURES

<u>FIGURE</u>	<u>CAPTION</u>	<u>PAGE</u>
1	Reaction scheme of combustion processes of double-based propellants.	96
2	Evolution of the local surface temperature of a convectively heated propellant cylinder.	97
3	Physical model of the interaction of solid phase-gas phase processes, leading to gas phase ignition.	97
4	Examples of flow and reaction processes that occur when a propellant cylinder is ignited by convection.	98
5	Flow conditions around a cylinder for subcritical and critical Reynolds numbers. (from Ref. 52)	99
6	Illustration of flow patterns around two cylinders showing effect of separation condition. (from Ref. 62)	99
7	Flow field around a cylinder in cross flow showing three zones where ignition criterion are being examined.	100
8	The predicted evolution of the ignition process at the stagnation zone exhibits dramatic dependence of free stream oxidizer content.	101
9	Predicted boundary layer profiles of fully developed flame for two magnitudes of gas phase heat release.	102
10	The evolution of the boundary layer profiles from ignition (A) to fully developed flame (D).	103
11	Demonstration of the role of free stream oxidizer as ignition promoter for two cases of fuel rich and fuel balanced propellants. a) $Y_{OX} = 0.5$ - Fuel rich propellant ignites faster. b) $Y_{OX} = 0$ - Both propellants ignite in about the same time.	104
12	Boundary layer profiles corresponding to Fig. 11 cases.	105
13	The effects of gas phase activation energy on the ignition process.	106
14	The effects of gas phase heat release on the ignition process.	106
15	The effects of free stream oxidizer for a case of higher convective flow velocity.	107

<u>FIGURE</u>	<u>CAPTION</u>	<u>PAGE</u>
16	The role of the thermal properties ratio $\epsilon$ is very prominent in convective ignition process.	107
17	Boundary layer profiles corresponding to Fig. 15.	108
18	The magnitude of the pressure has a tremendous effect on the ignition process.	109
19	The effects of varying free stream temperature on the ignition process.	109
20	Boundary layer profiles for lower gas phase activation energy.	110
21	Boundary layer profiles for higher pressure.	110
22	Boundary layer profiles for higher free stream temperature.	110
23	The variation of predicted ignition delay time versus Reynolds number exhibits strong dependence on the amount of free stream oxidizer.	111
24	Surface temperatures at the ignition time of Fig. 23 are very dependent on both the Reynolds number and the free stream oxidizer.	112
25	The dependence of the ignition process on the amount of subsurface heat release is very weak.	113
26	The ignition process for a case of a large initial surface temperature jump is very sensitive to free stream oxidizer.	113
27	The very large instantaneous heat fluxes associated with strong pressure pulse decrease ignition delay time appreciably.	114
28	Wave diagram showing pressure and temperature profiles for shock tunnel operation.	115
29	Schematic diagram of the shock tunnel and detail of the test section.	116
30	Schlieren and shadowgraph optical systems. (from Ref. 19)	117
31	Spectral response of detection system and its individual elements. (from Ref. 19)	117
32	Calibration of photo-detectors by means of a rotating miniature light bulb.	118
33	Calibration of output from photo-detectors.	119

<u>FIGURE</u>	<u>CAPTION</u>	<u>PAGE</u>
34	Overall view of the test section and paraphernalia.	120
35	Inert cylinder instrumented for heat flux and pressure measurements.	121
36	Mounting platform, specimens and accessories.	122
37	Instrumentation for the convective ignition experiment.	123
38	Overall view of the control consoles of gas and electronic systems for the convective ignition experiment.	124
39	Experimentally determined Mach number values of the incident shock wave at the entrance to the test section are lower than the theoretical values.	125
40	Typical pressure data a) test section static pressure - top b) pressure indication for incident shock wave speed - bottom.	126
41	Comparison of test section pressure data taken at two locations: a) instrumented cylinder - (6). b) bottom wall - (5).	126
42	Pressure distribution measured around the cylinder perimenter (compilation of three tests) indicates high reproducibility of test conditions. a) Test time pressure distribution is very uniform. b) The pressure distribution during the flow settling period.	127
43	Wave structure of the starting process of the flow.	128
44	The structure and magnitude of the surface temperature and heat flux distribution around the cylinder perimenter during the settling period of the flow indicate very strong initial flow transients.	129
45	Temperature transients on pyrex cylinders.	130
46	Heat fluxes corresponding to Fig. 45 conditions.	131
47	Increasing the ambient pressure results in increased heating rates and more rapid surface temperature rise.	132
48	Time to achieve a prescribed temperature rise is very dependent upon $Re_D$ and pressure.	133

FIGURE	CAPTION	PAGE
49	Average heat flux during the steady period of the flow is the highest at the front stagnation point for the entire $Re_D$ range of tests.	134
50	Typical photo-detector output signals. a) M30 propellant under low oxygen content flow (90%N <sub>2</sub> &10%O <sub>2</sub> , U = 6.3 m/s). b) M26 propellant under high oxygen content flow (50%N <sub>2</sub> &50%O <sub>2</sub> , U = 23.4 m/s).	135
51	Transient ignition phenomena are distinguished in the case of M30 propellant under high velocity and oxygen content flow (U = 60.8 m/s, 50%N <sub>2</sub> &50%O <sub>2</sub> ).	136
52	Ignition and flame spreading detection by means of the Reticon line scan camera. a) Calibration of the output signal from the scan camera. b) Test time output signal from the scan camera marks distinctly the arrival of the shock wave and the onset of ignition.	137
52a	Detailed look at the scan camera output during the onset of ignition and subsequent flame spreading. The periodic output signal prior to ignition. Ignition occurs at the flow separation region. Flame spreads on the entire specimen surface.	138
53	Photographs showing convective ignition events (M26 propellant, 1.63 MPa, 1740 K, 140 m/s, 50%N <sub>2</sub> &50%O <sub>2</sub> , $Re_D$ = 55,000).	139
54	Ignition data showing decreasing ignition times with increasing velocity, oxygen and pressure (for triple-based M30 propellant).	140
55	Ignition data obtained under high temperature and constant pressure conditions (M30 propellant).	141
56	Ignition data showing decreasing ignition times with increasing velocity, oxygen and pressure (for double-based M26 propellant).	142
57	Statistical diagram of flame spreading tendencies as a function of oxygen concentration and Reynolds number (M30 propellant).	143
58	Ignition trends as demonstrated by a series of partially inert cylindrical specimens.	144
59	Propellant ignition trends as a function of oxygen content and Reynolds number.	145

FIGURE	CAPTION	PAGE
60	Ignition trends for several special situations.	146
61	Time-wise and space-wise flame spreading as a function of flow velocity (M30 propellant, 90%N <sub>2</sub> &10%O <sub>2</sub> ).	147
62	Comparison between flame spreading as a function of velocity in inert and reactive flows (100%N <sub>2</sub> , 90%N <sub>2</sub> &10%O <sub>2</sub> , M30 propellant).	148
63	Flame spreading as a function of pressure in inert and reactive flows (100%N <sub>2</sub> , 90%N <sub>2</sub> &10%O <sub>2</sub> , M30 propellant).	149
64	Flame spreading as a function of velocity for M26 propellant containing graphite (100%N <sub>2</sub> ).	150
65	Flame spreading for various tandem configurations in inert and reactive flows (100%N <sub>2</sub> , 90%N <sub>2</sub> &10%O <sub>2</sub> , M30 propellant).	151
66	Photographs showing flame spreading for the specimen configurations of Fig. 65 .	152
67	Photomicrographs of M30 specimen surface before and after exposure to test conditions.	153
68	Photomicrographs of M26 specimen surface before and after exposure to test conditions.	154
69	Photomicrographs of burnt surfaces of M30 specimen taken from the front stagnation flow region and from the flow separation region.	155
70	Photomicrographs of burnt surfaces of NC/TMETN and HMX/PU specimens.	156
71	Photographs showing kaleidoscope of burning phenomena under cross flow conditions (Plexiglas specimen, 50%N <sub>2</sub> &50%O <sub>2</sub> , U < 15 m/s).	157
72	Sequence of photographs showing front surface boundary layer fluctuations (M30 propellant, 90%N <sub>2</sub> &10%O <sub>2</sub> , U = 5.6 m/s, 5000 frames/s).	158
73	Photographs showing flame appearance for a range of flow velocities (M26 propellant, 50%N <sub>2</sub> &50%O <sub>2</sub> , U = 6.5 m/s, U = 17.2 m/s, U = 71.5 m/s).	159
74	Photographs depicting flame luminosity in special situations. a) Flame extinction for cases A&B of Fig. 73 . (pictures A,B respectively) b) The flame of M26 propellant is much more luminous than the flame of M30 propellant.	160

NOMENCLATURE

- $a_t$  - ( $=a, t_f$ ), see Eq. (40c)
- $A$  - Area, Appendix III,  $\text{cm}^2$
- $A_P$  - Pre-exponent factor of pyrolysis rate expression,  $\text{cm}/\text{sec}$
- $A_R$  - Pre-exponent factor of gas phase reaction rate expression,  $\text{cm}^3/\text{g-sec}$
- $A_S$  - Pre-exponent factor of solid phase reaction rate expression,  $1/\text{sec}$
- $\hat{C}$  - Speed of sound, Appendices III,V,  $\text{m}/\text{sec}$
- $C_p$  - Specific heat capacity,  $\text{cal}/\text{g-K}$
- $D$  - Cylinder diameter,  $\text{cm}$
- $D_{12}$  - Diffusion coefficient,  $\text{cm}^2/\text{sec}$
- $D_A$  - Damkohler number (general), ratio of flow residence time to a reaction time
- $D_G$  - Gas phase Damkohler number, defined by Eq. (22a)
- $D_S$  - Surface Damkohler number, defined by Eq. (22a)
- $D_{SO}$  - Solid phase Damkohler number, defined by Eq. (22a)
- $E_P$  - Pyrolysis activation energy,  $\text{cal}/\text{mole}$
- $E_R$  - Gas phase activation energy,  $\text{cal}/\text{mole}$
- $E_S$  - Solid phase activation energy,  $\text{cal}/\text{mole}$
- $F$  - Velocity function, defined by Eq. (7)
- $g$  - Defined by Eq. (22b)
- $G$  - Defined by Eq. (23)
- $\hat{h}$  - Enthalpy,  $\text{cal}/\text{g}$
- $h'$  - Heat transfer coefficient,  $\text{cal}/\text{cm}^2\text{-sec-K}$
- $h$  - Defined by Eq. (22b)
- $\hat{H}$  - Enthalpy of flow in shock tunnel, Appendix III,  $\text{cal}/\text{g}$
- $h_s$  - Defined by Eq. (22b)
- $H$  - Defined by Eq. (23)

- HF - Surface heat flux on gas side, defined by Eq. (38),  $\text{cal/cm}^2\text{-sec}$
- $\hat{I}$  - Light emission intensity
- I - Total energy,  $\text{cal/g}$
- K - Thermal conductivity,  $\text{cal/cm-sec-K}$
- $l_{\text{ssr}}$  - Subsurface reaction thickness, Eq. (36),  $\text{cm}$
- $l_{\text{th}}$  - Thermal wave thickness, Eq. (36),  $\text{cm}$
- Le - Lewis number
- $L_v$  - Latent heat of evaporation,  $\text{cal/g}$
- M - Mach number
- $\hat{M}$  - Molecular weight
- n - Stoichiometric ratio
- Nu - Nusselt number
- P - Pressure, MPa
- Pr - Prandtl number
- q - Surface heat flux, Appendix IV,  $\text{cal/cm}^2\text{-sec}$
- $Q_R$  - Gas phase heat of reaction,  $\text{cal/g}$
- $Q_S$  - Solid phase heat of reaction,  $\text{cal/g}$
- R - Radius of cylinder,  $\text{cm}$
- Re - Reynolds number
- $\mathcal{R}$  - Universal gas constant,  $\text{cal/mole-K}$
- $\tilde{\mathcal{R}}$  - Gas constant,  $\text{cal/g-K}$
- RR - Reaction rate, defined in Fig. 9
- s - Defined by Eq. (6)
- Sc - Schmidt number
- t - time,  $\text{sec}$
- $t_f$  - Flow residence time, defined by Eqs. (9),(20),  $\text{sec}$
- $t_g$  - Gas phase time scale, Eq. (34),  $\text{sec}$
- $t_{\text{ref}}$  - Time of application of transient free stream conditions, see Eq. (40),  $\text{sec}$

- $t_{so}$  - Solid phase time scale, Eq. (34), sec
- $t_{WK}$  - Residence time of flow at the wake, sec
- $T$  - Temperature, K
- $\hat{T}$  - Cycle time of vortex shedding in the wake, sec
- $u$  - Velocity component tangential to the wall, m/sec
- $U$  - Velocity (general), m/sec
- $v$  - Velocity component normal to the wall, m/sec
- $V_{REG}$  - Regression velocity of solid surface, Eq. (15), cm/sec
- $\dot{w}$  - Volumetric rate of production of a species, g/cm<sup>3</sup>-sec
- $\dot{w}_s$  - Rate of solid molecules decomposition, 1/sec
- $W$  - Shock wave speed, Appendix III, m/sec
- $x$  - Coordinate tangential to the wall, cm
- $y$  - Coordinate normal to the wall, cm
- $Y$  - Mass fraction of a species
- $Z$  - Defined by Eq. (23)
- $\phi$  - Angle from front stagnation point, degrees
- $\alpha$  - Fractional mass of fuel constituent of propellant
- $\hat{\alpha}$  - Thermal diffusivity, cm<sup>2</sup>/sec
- $\hat{\gamma}$  - Specific heat ratio
- $\delta$  - Defined by Eq. (22b)
- $\epsilon$  - Defined by Eq. (22b)
- $\eta$  - Defined by Eqs. (6),(21)
- $\eta_s$  - Defined by Eq. (16)
- $\hat{\theta}$  - Generalized-implicit parameter, Appendix II
- $\theta$  - Dimensionless gas temperature, defined by Eq. (10)
- $\theta_{so}$  - Dimensionless solid phase temperature, defined by Eq. (16)
- $\theta_p$  - Defined by Eq. (22c)
- $\theta_R$  - Defined by Eq. (22c)

- $\theta_S$  - Defined by Eq. (22c)  
 $\mu$  - Viscosity, g/cm-sec  
 $\rho$  - Density, g/cm<sup>3</sup>  
 $\tau$  - Dimensionless time, defined by Eqs. (9),(21)

Subscripts and Superscripts

- BL - Boundary layer  
D - Based on cylinder diameter  
DP - Decomposition products  
e - At the boundary layer edge  
ef - Maximum value obtained at some time at the boundary layer edge  
exp - Experimental  
E - At the front stagnation boundary layer edge  
E1 - See Eq. (40)  
Ef - See Eq. (40)  
F - Fuel  
i - Of species i  
ign - At ignition time  
j - Time level in finite difference algorithm, Appendix II  
I - Inert  
K - Of equation K, Appendix II  
n - Space mesh number in finite difference algorithm, Appendix II  
OX - Oxygen  
p - Predicted, Appendix II  
P - Product  
S - Solid phase  
SP - At flow separation zone

ST - Starting values of numerical solution, Appendix II  
W - Wall (surface)  
WK - At the wake  
o - Initial value  
 $\infty$  - At infinity

Abbreviations

NC - Nitrocellulose  
NG - Nitroglycerin  
NGU - Nitroguanidine

## SECTION I

### INTRODUCTION

Ignition of a solid propellant is the complex physico-chemical process of the initiation of its combustion by means of external heat supply, i.e., by an igniter. Clearly, ignition is a time-dependent process. In that respect there are two time scales to be considered: the ignition delay time and the transition time to a self sustained flame. The ignition delay time, a difficult parameter to define, is the elapsed time from the activation of the igniter to the initial attainment of net exothermic chemical run-away reactions. The controlling reaction may occur below, above, or at the propellant surface; hence, the terms of solid phase, gas phase, or heterogeneous ignition are used. The transition time to fully developed flame may be on the scale or much faster than the ignition delay time. Both the ignition time scales and the ignition location depend on the rate of energy transfer, its mode, the ambient conditions, and the particular propellant involved.

Solid propellants are used primarily in rocket motors and in ballistic applications (i.e., gun charges). Many igniters are solid propellant charges which are initiated very rapidly as compared to the main charge. The igniter ejects hot gaseous and/or condensed combustion products which heat the main propellant charge. In the case of a rocket motor propellant, the charge is usually a single long cylindrical propellant. In the case of guns, the charge is composed of many cylindrical or spherical propellant grains (typically, diameters range from 0.1 to 1 cm). The dominant heat transfer mode is convective, though conductive heat transfer from the impinging particles and radiation from the cloud of the particles and from the flame may be important factors, especially in rocket propellant ignition.

While in the case of a rocket motor the effective geometrical configuration associated with the convective flow is that of a flat plate flow, the situation in gun charges is that of a bank of cylinders (or spheres) in cross flow. Thus the flow structure is more complex, being composed of stagnation flow, flat plate flow and wake flow. Typical ignition delay times in the latter case are in the millisecond range. Under such conditions ignition is a gas phase phenomenon and the transition time to fully developed flame is on the order of magnitude of the ignition delay.

Convective heating occurs under very rapidly developing pressure and velocity fields. It is further complicated by shock waves and a high rate of mass addition from the grains; thus, the heat transfer is not amenable to clean-cut theoretical or empirical analyses.

The thermo-chemical response of the propellants to the heating conditions is equally complex. Typically, for rocket motor applications, the propellant is a composite consisting of an oxidizer in granular form imbedded in a polymeric fuel binder for mechanical integrity. It also includes solid additives (like aluminum) and various catalysts and plasticizing agents. Ballistic propellants are usually homogeneous propellants which consist primarily of nitrocellulose and some explosive material (usually nitroglycerin). They are sub-divided into single-based, double-based and triple-based propellants depending on the number of their

main components. Some additional materials are added to serve as burning-rate modifiers or stabilizers.

During decades of research, a great deal of knowledge has been accumulated regarding ignition situations which resemble solid rocket motor applications [1]. As such, most of the geometries used were of the flat plate type and ignition delays were in the range of tens and hundreds of milliseconds. Only under shock tube heating conditions or by using practical igniters were milli-second ignition delay times obtained. The main parameter sought was the ignition delay time and little attention was paid to the dynamics of the transition to full flame development and spreading. Most experimental and theoretical work employed steady heating conditions (i.e., constant pressure and velocity in the case of convective ignition) and they were aimed mainly at determining the location of the first run-away chemical reaction occurrence (solid phase, gas phase and at the surface). In contrast, the ignition site (i.e., location along the specimen) was not of much consideration since for most test conditions and geometries, ignition was almost always obtained if the igniter source was applied for a sufficient period of time.

The present work addresses itself to the situation of gun propellant ignition. It is aimed at elucidating ignition and flame spreading phenomena in the cases of propellant grains under transient cross flow conditions particularly in situations where the chemical reaction time is on the order of the flow residence time around the propellant grain. This research is a step in filling the gap that exists between ignition studies of idealized situations and practical ballistic ignition ones.

The present work investigates the ignition of cylindrical propellants (mostly nitrocellulose-based) under shock tunnel induced cross flow conditions. Understanding the ignition phenomena on individual cylinders is considered a prerequisite to understanding the ignition processes in beds of cylinders. In addition to comparative studies of the ignition delays of the various propellants per se, a special emphasis is placed on distinguishing the ignition sites and the flame spreading (and blow off) tendencies as functions of the external flow velocity pressure and oxidizer content. Also investigated is the role of the initial flow transients in obtaining ultra-rapid ignition processes (sub-millisecond times). Numerical solutions are carried out for front stagnation region ignition. The solutions include the effects of the initial flow transients as well as general flow non-steadiness. They cover the transition process to quasi-steady burning. The likelihood of ignition at other sites, rather than the front stagnation region (e.g., at the wake), is inferred from those solutions. In particular, situations where ignition is never realized despite high heating rate, are identified.

## SECTION II

### PREVIOUS IGNITION STUDIES, PARTICULARLY REGARDING BALLISTIC PROPELLANTS

#### II -A. The General Scope of Propellant Ignition

Extensive studies have been conducted during the past 25 years in the field of propellant ignition, mainly with respect to rocket propulsion. The present discussion is not intended to be a comprehensive review of the ignition work, since recent reviews of the main experimental and theoretical results already exist [2-5]. Only the salient features of ignition expressed in these efforts will be discussed here with the emphasis on those which are more relevant to the present work.

Most ignition research has emphasized the question of how long it takes for the run-away chemical reactions (which lead to ignition) to build up, rather than the dynamics of the approach to steady state.

In order to devise a tractable mathematical model to describe the ignition process, theoreticians tend to ascribe the ignition process to a single dominant one-step chemical reaction. Since the location of that reaction is not obvious, there have arisen three main models of propellant ignition associated with the postulated location of that reaction, i.e., solid phase ignition, gas phase ignition, and heterogeneous ignition (gas-solid interface). The providing of experimental evidence to that effect is still a very important goal of any experimental endeavor.

#### (i) Experimental Techniques

In order to simplify the interpretation of ignition results, the more important experimental work employed a single mode of heat transfer in a precisely controlled manner: conductive heat transfer by means of either hot wire [6,7] or end wall shock tube hot gas [8,9]; radiative heat transfer from an arc image [10-12] or laser [13]; or convective heat transfer from hot gas generators [14-16] or shock tunnel flow [17,18]. Besides the intrinsic differences in the heating modes (for example in radiation studies the opacity of the surface is a factor), the experiments differed greatly in the heat transfer rates applied (1-100 cal/cm<sup>2</sup>-sec). While for the lower heat transfer rates (ignition delay in the seconds range) solid phase processes are dominant, for the higher heat transfer rates (ignition delay in the millisecond range), the chemical run-away reaction location shifts to the gas phase as the solid thermal wave is very thin and the regression rate is fast. Therefore one should exercise caution in drawing general conclusions from any particular experimental work.

Most experimental efforts also differ in the ambient conditions of pressure and gas composition. In a reactive environment, gas phase or heterogeneous ignition is favored if the heat transfer rates and pressure are sufficiently high.

Experimental ignition results may be susceptible to some extent to the ignition criteria used, e.g., surface temperature rise, luminosity from the developing flame, pressure rise. Each of these corresponds to a different stage of the ignition process.

(ii) Ignition Models

Keeping in mind the variety of the experimental conditions employed, it is not surprising that there has been experimental evidence in support of any of the three ignition models mentioned before being dominant or controlling. A very comprehensive review of this subject can be found in Ref. 19. In the following discussion the fundamentals of these models will be examined as well as the nature of their results.

Historically, the first model suggested was the solid phase model. In this model, the ignition phenomenon is explained by a run-away chemical reaction distributed inside the bulk of the solid phase; therefore, the ignition delay time is dependent directly on the externally applied heat flux, but not on the ambient conditions. Theoretical analysis of this model was first put forth by Hicks [20]. Various other theoretical developments are summarized in Ref. 4. In most of them, a zeroth reaction order was assumed and reactant depletion was neglected. Most commonly, constant heat flux cases have been treated. The numerical solution of Bradley [22] was rather insensitive to reactant depletion and reaction order chosen. Similar trends were obtained from a solution based on an asymptotic method [21]. With respect to the solid phase model, ignition delay times are correlated directly to the heat flux applied and it is meaningful to talk about ignition surface temperature. Plots of ignition delay versus heat flux on logarithmic coordinates, as predicted from various solid phase theories, are given in Ref. 24 for certain selected values of reaction activation energy and heat release. Notably, the curves form straight lines whose slopes are almost identical. Thus, the theories differ only in their predicted magnitudes of the ignition delay times, but not in their functional dependence on the heat flux (i.e., simple power law). The rather simple functional dependence of the ignition delay on the heat flux enables the reduction of solid phase reaction parameters from well controlled low heat flux experiments [16] (up to  $10 \text{ cal/cm}^2\text{-sec}$ ). As already alluded, the various theories will yield different values. In general, corroboration of the solid phase ignition model is found in experiments where the inert heat up period constitutes most of the ignition delay time, since that period depends solely on the magnitude of the external heat flux applied.

As other experiments which employed higher heat flux [10] showed strong dependence of the ignition delay time on the ambient gas pressure and oxidizer concentration, there arose the need for a different ignition model based on gas phase processes. Both the gas phase and the heterogeneous ignition models incorporate the gas phase processes and as such explain the ignition delay sensitivity to ambient conditions.

The gas phase model was proposed first by McAlevy [8]. Basically it states that the vaporized decomposition products of the propellant react in the gas phase adjacent to the propellant surface. The thermal boot-strapping process of ignition proceeds thru the heat feed-back from the gas phase to the propellant surface. The gas phase theory was advanced further by Hermance et al. [25] and by Hermance and Kumar [26]. The latter solved a set of partial differential equations describing the ignition of a double-base homogeneous propellant suddenly exposed to a hot stagnant oxidizer containing gas (end wall shock tube conditions). Unlike earlier work they included the full coupling between the gas phase and the solid phase, and permitted the surface temperature to rise. They indicated that

the dependence of the ignition behavior upon the external oxidizer is strongly influenced by the choice of ignition criterion and therefore developed a light emission criterion for ignition [27].

In contrast to the solid phase model, the ignition delay time in the case of the gas phase model is not a simple power law function of the heat flux and the surface temperature at the ignition time is mostly dependent on the surface pyrolysis parameters of the propellant (which determine the gasification temperature) and on the ambient conditions.

Most of the experimental results which are explained by the gas phase ignition model could have been explained by the heterogeneous model of ignition as well. In the latter model the exothermic run-away reaction occurs at the propellant surface between the gaseous oxidizer and the solid fuel. That model was developed first by Anderson et al. [28] and advanced by Williams [29] and Waldman and Summerfield [30]. This theory evolved because it can explain the hypergolic ignition situation when the propellant surface reacts exothermically with surrounding cold, strong oxidizer-containing gas [31].

In both the gas phase and the heterogeneous ignition models no heat is assumed to be liberated in the solid phase. Both models can explain the dependence of the ignition delay on the ambient gas conditions for high heat flux stagnant environment experiments (i.e., conductive and radiative heat transfer modes). In order to distinguish between the two models, Kashiwagi [19] conducted theoretical and experimental work with the ignition of flat plate polymeric fuels under oxygen-containing shock tunnel flow. He found that only the gas phase model could properly describe the behavior of the first ignition position with varying free stream conditions, such as the fact that with high oxygen level, the first ignition position was on the forward section and with low free stream oxygen level or increased flow velocity, the first ignition position shifted downstream. If the controlling reactions occur at the surface, the ignition position should be at the forward section in any case, since the surface temperature rises there the fastest. Thus, gas phase ignition is more pronounced in convective ignition situations where the ignition delay time depends also on the flow velocity and structure.

To summarize, none of the ignition theories is likely to describe completely the ignition mechanism under any conditions. The last two theories incorporate a large number of adjustable parameters which may fit almost any particular test. The experimental evidence indicates that under low heat flux conditions (less than  $10 \text{ cal/cm}^2\text{-sec}$ ) the solid phase reaction control the ignition process. For higher heat flux conditions the gas phase reactions are the important ones. Recently, an attempt was made by Bradley [32] to combine the three models to one unified theory. However owing to the large number of parameters that appear in his theory it is virtually impossible to test his theory.

## II-B. Convective Ignition Studies

Convective ignition is the technique applied in most practical situations. Experimentally it is more difficult to provide than conductive or radiative ignition since it requires a source of continuous high temperature gas flow. One way of obtaining it is by using a pyrogen igniter [33]. However in this case the pressure, velocity, and heat flux vary with

time and the gas composition is complex and not known accurately. The important convective ignition experiments were conducted either under high temperature, pressure, and velocity conditions (shock tunnels) or under moderate temperature, atmospheric pressure, and low velocity conditions of heated gas generators. As already discussed, gas phase ignition is favored in the first case (high rates of heat transfer) and solid phase ignition is favored in the second case.

#### (i) Ignition of Flat Plate Configurations

Typically, shock tunnel ignition experiments were conducted with composite propellants of flat plate configurations. When oxygen was present in the free stream, a significant reduction in ignition delay time was observed in most work [17-19], a fact which is an indication of gas phase ignition. However, Keller et al. [33] concluded that the ignition characteristics of ammonium perchlorate composites, in the entire range of their shock tunnel test conditions, were in agreement with those predicted by the thermal ignition theory (i.e., solid phase ignition). They found that for a given heat flux level, for propellants with smooth surfaces, ignition delays were not altered by the velocity of the convective gas. The higher gas temperature effect, at a given heat flux level, was to reduce ignition delay only for propellants with rough surfaces. Similarly, the presence of oxygen in the test gas affected only the ignition of propellants with rough surfaces. Though, seemingly, Keller's results are in support of the solid phase ignition mechanism, there is a basic flaw in the presentation of his results. Most of his ignition delay results are plotted versus calculated heat flux values which were deduced from thin film gauge measurement assuming that the propellant behaved as an inert and that the heat transfer coefficient was the same. Such assumptions are incorrect under shock tunnel operation due to the vaporization process of the propellant prior to ignition (ignition was detected by radiation from the flame in Keller's tests). Also, for the wide range of Keller's test conditions, the heat flux could not have been uniform during the test period since the tailored conditions of operation could not have been satisfied for the entire range (see Section IV). Thus it was not meaningful to express ignition delays versus some average deduced heat flux levels. As already discussed in the previous paragraph, it is possible to fit experimental data to thermal ignition theory provided that the inert heat up period of the propellant constitutes most of the ignition delay time. Moreover, the test sample used in Keller's experiments was very short and the space-wise observation of the ignition behavior was not done. Under high velocity convective flow, when testing short samples (low residence time), the gas phase reactions are not completed in the vicinity of the propellant surface (low Damkohler number) and the propellant decomposition products are swept and diluted downstream of the sample. Thus the ignition behavior approaches that which is predicted by the solid phase theory.

The foregoing discussion emphasized some of the features which must be considered when interpreting convective ignition results: surface roughness (possible local hot spots); heat flux uniformity; and, most uniquely to convective ignition, the sample length in direction of the flow. The latter feature was emphasized in the Kashiwagi et al. work [19]. They were the only ones to measure the space-wise ignition delay, from which they deduced that in their tests ignition was clearly a gas phase process.

Bastress and Niessen [34] used exhaust gas from a methane/oxygen gas

rocket motor in their convective ignition tests. When they replaced the inert approach material (up stream of the sample) with propellant, thus effectively lengthening its size, the ignition delay time was reduced significantly, indicating a gas phase ignition process.

Theoretical treatment of gas phase convective ignition of flat plate configurated propellants incorporates reactive boundary layer equations (which are coupled to the solid phase thru the solid-gas interface). Works in this field are discussed in Section III.

## (ii) Ignition of Cylindrical Configurations

All reported convective ignition tests with cylindrical propellants were conducted with ballistic homogeneous ones in tranverse flow under low heat flux atmospheric conditions in which ignition delay times were measured in seconds. Typical Reynolds numbers based on cylinder diameter were in the range of few hundreds. As such, ignition occurred always at the front stagnation region where the heating rates were the most intense and ignition was mostly a solid phase process.

The most comprehensive work in this subject was conducted by Churchill et al. [35]. Their investigation encompassed gas temperatures from 578 to 1070 K, velocities corresponding to Reynold numbers from 156 to 624 (3 mm diameter grains), and a complete range of oxygen-nitrogen mixtures as well as a few oxygen-carbon dioxide mixtures. Single-base and double-base propellants were tested. They conducted over 2500 tests for more than 250 different experimental conditions and obtained ignition delays from half a second to eight seconds. On a heuristic basis they correlated the ignition delay time,  $t_{ign}$  with the experimental conditions as follows:

$$t_{ign} = [A \cdot \exp(-E/RT_{gas}) \cdot Re^n]^{-1}$$

Where  $n$  is a dimensionless constant, whereas  $A$  and  $E$  are functions of gas composition and propellant composition. Due to the large number of tests conducted, the constants  $n$ ,  $A$  and  $E$  were evaluated with small statistical error by repetitive curve fitting. The above expression contains the important parameters occurring in convective ignition situations; the  $Re$  number to some power (representation of the heat flux) and the chemical reaction. Surprisingly, the results correlated well with the chemical reaction term based on the gas phase temperature ( $t_{ign}$ ). This is in contrast to anticipated dependence on the surface temperature only, as might be expected by assuming a dominating solid phase ignition. For all propellants (particularly in higher temperature cases), they found a decrease in ignition time with increasing oxygen content over the entire range of gas compositions, temperatures, and flow rates. This suggests that gas phase oxidation reactions are very important in nitrocellulose-based propellants. None of the propellants ignited consistently in pure nitrogen or carbon dioxide. Under high flow rate-low temperature conditions, the propellants frequently decomposed completely without visible ignition. For some conditions, the flame first appeared at the fringe of the gas stream and flashed back to the grain. The last phenomenon was not considered to be normal ignition and was not included in the correlation. Considering the small size of propellant diameter, the aforementioned phenomena can be explained on the basis of the gas phase ignition model (small Damkohler number).

Churchill's [35] work included situations in which a transition from solid phase controlled ignition process to gas phase ignition was obtained. This work was conducted (1956) before the suggestion of the first gas phase ignition model (1960) and ignition at other positions rather than the front stagnation region was considered a "spurious" case. In many respects the present work is an extrapolation of Churchill's work to the purely gas phase controlling ignition regime of nitrocellulose-based propellants, since these are the conditions encountered in practice.

Other work with cylindrical propellants by Lisitskii [36] and Grigorev [37] was more limited in scope. They ignited pyroxylin (nitrocellulose) cylinders by very slow convective heating (1-2 m/sec, 600-900 K, ignition delay: 10-40 sec). Under these conditions ignition was certainly a solid phase process. The goal of those tests was to determine the effective kinetic parameters of the high temperature condensed phase decomposition. Ignition delays were correlated with the heat flux coefficient and a chemical reaction temperature (in essence similar to Ref. 35). Existing empirical heat transfer correlations were employed for that purpose. Since some of the ignition delays were so long, the thermal wave at the time of ignition in those cases approached the center the cylinder; the cylinder could not have been treated as a semi-infinite body in the condensed phase energy equation. Numerical investigations to that effect were conducted by Lisitskii [38]. Those conditions are far from being realistic in practical ignition situations.

Simple representation of the heat transfer in the form-  $q = h \cdot (T_{\text{gas}} - T_{\text{surface}})$  avoids the necessity of considering the flow structure (the heat transfer coefficient  $h$  is considered to be known). That heat transfer expression was used in the earlier work of the thermal ignition theory for convective ignition situations [4]. Niioka and Williams [21] put forth a theory of the ignition of a reactive solid in a hot stagnation flow, a situation pertaining to solid phase ignition of cylinders under cross flow. In their theory the gas phase flow is explicitly described by a proper boundary layer flow equation. A rigorous ignition formula was derived by asymptotic analysis. The practical use of that formula was demonstrated by Niioka et al. [16] in their hot stagnation flow experiments. They used it to derive from the experiments the overall solid phase activation energy of a double-base propellant. They used air and helium as the test gases (568-727 K, 4-32 m/sec, 0.5-3.5 cal/cm<sup>2</sup>-sec,  $t_{\text{ign}} = 2-50$  sec) and hemispheric configured propellants. They concluded that for their test conditions the ignition was a pure solid phase phenomenon and suggested that the region of transition from solid phase to gas phase ignition be studied.

### II-C. Ignition Dynamics

All the previously discussed ignition work considered only the ignition delay period and not the transient period of transition from ignition to combustion. Also, they dealt only with quasi-steady heat transfer situations. In case of convective ignition, the starting period of the flow, or the boundary layer relaxation period, were of small importance in most work since they constituted only a very small fraction of the ignition delay period. Only in shock tunnel experiments [19] were the initial flow transients, associated with the starting of the flow, of importance.

Transient ignition situations are inherent to the practical use of ballistic propellants in gun charges where the entire combustion process is

transient. The situation there is of a packed bed of small propellant grains in a closed chamber, being ignited at one end (or along the axis) by the gaseous products from an igniter; the gas generation from the propellants upstream adds to the igniter gas to ignite the propellants down-stream in rapidly increasing pressure, temperature, and velocity fields [39,40]. The entire process of ignition and burning is completed in a few milliseconds during which the pressure rises to hundreds of MPa. Thus, the burning rate after the attainment of ignition cannot be regarded as quasi-steady, obeying a simple power law dependence on pressure.

Only a few models considered the transition from the ignition phase to steady state burning [41-43]. They all applied steady state-type expressions for heat flux versus surface regression to that period. The imposition of the steady state regression rate as an upper limit during ignition transition to sustained burning is certainly an oversimplification, particularly for a gas phase ignition situation. The most sophisticated of these models, by Baer and Ryan [42], did not consider any particular ignition process. They solved the solid phase energy equation with a moving boundary considering the effect of all reactions to be approximated as a surface heat flux and employing a simplified description of the steady state regression rate for the transition period to sustained deflagration. Their model predicted the effect of pressure on the ignition time at a given external heat flux level (even if solid phase ignition is postulated), since the regression rate is pressure dependent. They found that the net heat of gasification of the propellant, the steady state burning parameter, and the manner in which the igniter heat flux is terminated have critical effects on the transition to steady deflagration. The assumptions of their model certainly do not apply to practical gun application where the ignition process culminates in highly transient burning situations.

The effects of the external heat flux dynamics on the ignition delay was studied experimentally [44] and theoretically [45] by Rosenband et al. However, their analysis was applied only to the solid phase ignition process. They found that the ignition delay depended differently on the kinetic and thermo-physical parameters in different heat flux dynamics situations. For an increasing flux, the effect of these parameters on ignition delay is much less than for a constant or diminishing flux. For rapidly increasing flux the ignition delay may be determined solely by the dynamics of the external heat source. Thus, they concluded that the optimal conditions to determine kinetic parameters from ignition experiments are when the external heat flow diminishes with time. There is no similar work reported for the gas phase ignition process.

A rather comprehensive discussion of the various simplified ignition versus heat flux correlations as applied to ignition transient calculations in gun situations is found in Ref. 46. It was found that the calculated flame spreading rate in granular beds is sensitive to the assumed ignition criteria.

#### II-D. The Combustion Characteristics of Nitrocellulose-Based Propellants

Since a successful ignition event culminates in self-sustained burning, it is expected that steady state burning characteristics of the propellant have implications on the dynamics of the transition from ignition to steady deflagration. In that respect it is worth reviewing briefly some of the work dealing with the burning phenomena of double-based (nitrocellulose

based) propellants.

An extensive review of the literature on that subject can be found in the introduction of Ref. 47. The region in which the double-base propellant combustion occurs can be divided into four separate and independent zones: subsurface reaction zone, fizz zone, dark zone, and flame zone. A schematic diagram of the four zones and their reaction paths are shown in Fig. 1. The overall subsurface degradation is exothermic. In the fizz zone, it is believed that a second order gas phase exothermic reaction occurs. The exact details of the reaction mechanism there are still unknown. Little heat is liberated in the dark zone. It is believed that in this zone the species concentrations build up to some critical values prior to the onset of the flame zone reactions (induction period). Little is known about the physical and chemical processes which take place there. The final exothermic reactions occur at the flame zone (which is luminous). Typically, about one-half of the total heat produced from the entire reaction process is liberated in the flame zone. The combustion scheme just described is obtained under inert quiescent ambient conditions. How it differs in reactive convective flow is not known. The separate reaction zone structure certainly has implications for the dynamics of gas phase ignition process.

The importance of the steady state regression rate dependence on the pressure in the transition process from ignition to steady deflagration was discussed in the previous paragraph in connection with the work of Refs. 41-43. Non-catalyzed double-base propellants exhibit identical dependence of regression rate on pressure for the entire practical pressure range in the form:  $r = a \cdot p^n$  (i.e., the pressure index  $n$  remains constant). Typical values for  $n$  are in the range 0.6-0.9; thus the burning rate of double-base propellant is very sensitive to pressure. For some practical applications (e.g., propulsion) it is desired to obtain zones of reduced sensitivity of the burning rate to pressure. This is done by adding additives (catalysts) to the propellant; most commonly, lead and copper compounds. This results in increased burning rate at low pressure ( $n = 0.8-2$ ), followed by a plateau burning region ( $n = 0-0.2$ ), by a mesa burning region ( $n < 0$ ), and finally, as the pressure is increased further, the regular pressure dependence of non-catalyzed propellant is re-established ( $n = 0.6-0.9$ ). The physical and chemical mechanisms responsible for that phenomenon are still not well understood. A number of recent studies deal with this subject [48-50]. The ignition of catalyzed double base propellants was investigated in detail only in radiative ignition experiments conducted by DeLuca et al. [13]. They found that for double-base propellants, in general, a brief flux-dependent period of transient flame development occurred after the beginning of gasification. Before self-sustained burning was reached, this interval was followed by a relative long flux dependent period of steady state, radiation-assisted burning. In cases of catalyzed propellant ignition under low pressure conditions (1 - 1.5 MPa), the radiation assisted period of burning could be reduced significantly without extinction at the termination of the radiation. It has been established that the catalysts affect the gas phase processes and not the condensed phase. As such they are likely to affect gas phase ignition dynamics in convective flow situations. There is no published work in this area.

### SECTION III

#### THEORETICAL ANALYSIS OF CONVECTIVE IGNITION OF A CYLINDRICAL PROPELLANT UNDER CROSS FLOW CONDITIONS

##### III-A. Introduction

High speed flow around a cylinder is indeed a kaleidoscope of fluid phenomena. No simple analytical or phenomenological treatment can describe the entire flow field structure. Though the upstream front half of the cylinder is tractable to strict analytical treatment, the wake region structure is so complex as to exclude any analytical treatment but a phenomenological one. Thus, one realizes that a convective ignition process, which by definition is flow dependent, is of formidable complexity. If it were only a solid phase phenomena it could have been treated relatively easily using semi-empirical heat flux data of flow around cylinders.

However in the case where the convective ignition is mostly a gas phase phenomenon, as it is in the present research, the complexity of the problem is evident, since the gas phase reaction kinetics is coupled to the fluid flow dynamics. Therefore, the ignition trends will be examined separately in three different zones: front stagnation point zone, flow separation point zone, and the wake zone. A special emphasis will be put on the effect of transient flow conditions on the ignition performance. Such conditions are especially prominent during the starting stages of the flow and are encountered in practice as well as in the present test apparatus. To this effect, the ignition equations will be studied in their complete unsteady form, rather than assuming quasi-steadiness.

The transition dynamics from ignition to fully developed burning is also of great interest, since, in the present case of very short ignition delay times, it may constitute most of the time duration from flow initiation to steady state burning. In practice, a very vigorous ignition may trigger strong undesired pressure pulses which, in turn, interact with the burning dynamics, leading to a possible uncontrolled explosive burning. Thus, the analytical solution will proceed to the stage of steady state conditions.

The propellant, of homogeneous type, will be treated as a double-based propellant which decomposes to premixed fuel and oxidizer species. The effect of free stream oxidizer will be investigated. No attempt will be made to distinguish between the free stream oxidizer and the oxidizing species from the propellant surface. Though not too realistic, it should be emphasized, that despite years of research, the gas phase reaction kinetics of a typical double-based propellant is poorly understood. Thus, not much information is gained by a more detailed study which would distinguish between the various oxidizer components. In general, the nature of the problem is such that many physical parameters enter the picture, some of which are poorly known and are only an estimate. Therefore the purpose of the present analytical investigation is to find the general trends of the ignition performance and their dependence on the main physical parameters. Thus attention is not given to precise correlations of experimental data in terms of calculated results. However, major experimental trends will be

explained based on the theoretical analysis.

### III-B. Basic Physical Considerations of Gas Phase Convective Ignition of a Circular Cylindrical Propellant

The basic mechanism of convective ignition is depicted in Fig. 2. As the hot gas flow impinges on a propellant cylinder, thermal and viscous boundary layers develop adjacent to the cylinder surface in a time on the order of the flow time around the cylinder ( $D/U_\infty$ , typically a fraction of a millisecond). During this brief transient, the heat flux is abnormally large so that  $T_w$  rises rapidly. There may be other flow transients during the initiation period of the flow which may have a longer duration and raise the surface temperature even further. The transient flow conditions associated with the starting process of the flow in the test apparatus are discussed in Section IV. During that period the flow separates to form a wake region behind the propellant cylinder. The nature of the flow around the cylinder will be discussed in the next paragraph. Once the flow around the cylinder is established, the cylinder enters a relatively prolonged period of heat up during which the cylinder behaves as an inert one, since its temperature is too low for either significant gasification and/or the inducement of significant chemical reactions in the solid or gas phase. The temperature along the perimeter of the cylinder is clearly nonuniform and subsequent development of flame will reflect it. The first departure from this purely inert heating phase will occur at the point where surface temperature rises most rapidly. For typical nitrocellulose-based propellants, rapid decomposition ensues where the temperature increases above 500 K.

The general interaction of gas phase-condensed phase physichemical processes which lead to gas phase ignition is depicted on Fig. 3. The gas phase may be quiescent or in a state of developing or a fully developed boundary layer flow. The gas adjacent to the surface is at a much higher temperature than the surface and may contain oxidizer species. During the inert stage of the surface heat up period, the propellant surface temperature is solely determined by the transient heat feedback from the gas phase and the only properties of relevance are the gas and condensed phase thermal properties. As the gasification temperature is reached, the propellant starts to vaporize and decompose to reactive fuel and oxidizer species. The gasification and decomposition are endothermic interface processes which are strongly temperature dependent, thus a larger and larger percentage of the heat feedback from the gas phase will be consumed by the gasification process. The reactants which emerge from the surface, penetrate the adjacent gas by means of convective and diffusive mechanisms. At some distance from the surface where the temperature is sufficiently high, exothermic reactions commence. The oxidizer species which are initially present in the gas phase, diffuse to the reaction zone to participate in the reactions. The heat liberated in the reaction zone is partially fed back to the surface by a diffusion mechanism. The surface temperature increases and so does the vaporization rate. After some time the reactant species concentration and the gas phase temperature at the reaction zone is sufficiently high for a run-away chemical reaction to occur. Thus a state of ignition is approached. A transition to a steady state flame may occur according to the dashed routes shown on Fig. 2. The steady state burning occurs when, finally, a balance in heat generation and consumption is obtained. A complete analytical treatment of the aforementioned process will be given in III-D.

In general, the chemical processes that follow the condensed phase decomposition do not occur automatically and in negligible time: they are, in fact, complexly intertwined with the gas flow around the cylinder. The gaseous products emerging initially from the front of the cylinder enter the boundary layer with its higher temperature. The fate of the reactants depends on the local temperature, concentration, velocity, etc. These effects can be summarized in the form of a dimensionless parameter, a Damkohler number:

$$D_A = (t_{\text{FLOW}} / t_{\text{REACTION}})$$

For  $D_A \gg 1$ , the reaction is faster than the flow (see Fig. 4a), so that the reactants emerging from the stagnation region are consumed while still in that neighborhood. If this is the case, the heat release accompanying these reactions is partially fed back to the propellant, supplementing the convective heat transfer and yielding a bootstrapping process that can greatly accelerate ignition at the cylinder front. Ignition at the cylinder front creates hot combustion products that pour into the boundary layer and the wake, thus accelerating the ignition process elsewhere: thus, the flame spreads quickly. If  $D_A \ll 1$ , the reactants tend to be dispersed downstream before reacting (see Fig. 4b) and the vigorous bootstrapping process at the front is lost. Since reaction rate increases remarkably with pressure and temperature, increases in either of them strongly affect the value of  $D_A$ , favoring leading edge ignition.

Failure of stagnation point ignition does not mean total ignition failure. The wake behind the cylinder is an effective reactant accumulator. The residence time of a reactant molecule there is longer than the residence time of flow around the cylinder. Therefore, the reactions have ample time to go to completion there. This yields a bootstrapping process coupled to the propellant at the rear of the cylinder and ignition in the wake. The above discussion suggests that the ignition of a cylinder to a full steady state burning can be expressed as,  $t_{\text{ign}} = t_{\text{thermal}} + t_{\text{chemical}}$ . Where  $t_{\text{thermal}}$  is the time to heat up the surface to first gasification. This time can be shortened significantly if the initial transient conditions are very prominent. The second part of the delay,  $t_{\text{chemical}}$ , is dependent on the Damkohler number and it is the time which is most difficult to predict. Only closer consideration of the competing processes of reaction, diffusion and flow around the cylinder may yield a qualitatively correct description of the behavior of  $t_{\text{chemical}}$  when  $D_A$  approaches unity. Close attention should be given to the influence of Reynolds number on the nature of the boundary layer and the wake since these strongly affect the competition expressed in the Damkohler number. The dependence of the flow around circular cylinders on the Reynolds number will be discussed in the next paragraph.

### III-C. Studies of Flow Past Circular Cylinders

As was discussed above, the convective ignition phenomena of cylinders is complexly intertwined with the flow field. The structure of the flow around cylinders is most dependent on the Reynolds number of the flow. A typical range of Reynolds number for convective ignition applications is 1000 to 200,000, which is about the range covered in the present experimental program. The flow velocity is low subsonic, i.e., less than Mach 0.1. Thus, most of the following review and discussion will be limited to the aforementioned range of Re number and flow regime. The transfer of heat and mass to a circular cylinder in cross flow has long attracted much

attention. In addition to being of direct practical importance, the circular cylinder has been a convenient model for many fundamental studies on heat and mass transfer by forced convection. The distribution of local pressure and skin friction around circular cylinders has also attracted much attention because of similar reasons. There is a large volume of literature available on these subjects and only the main points most relevant to the present case will be reviewed here.

A comprehensive review of the structural aspects of the flow around circular cylinders is given by Ref. 51. There exist definite regimes of flow across the Reynolds number range, which are identifiable by virtue of their unique features. The regime of flow which extends over the range of Re number 1000 to 150,000 is called the "subcritical" regime and it is the regime which is encountered in most chemical engineering applications as well as in convective ignition applications. The next regime of flow is called the "critical" regime and it extends over the range of Re number 150,000 to 3,000,000. Some convective ignition cases may fall into this regime. Typically for the subcritical regime, the heat transfer coefficient is maximum at the front stagnation point or at the rear stagnation point. The main features are as follows: a) laminar boundary layer separation at about 80 degrees from the leading edge, b) nearly constant frequency of vortex shedding from the wake, c) forward progression of turbulence in the wake with increase in Re number, and d) moderate sensitivity to free stream turbulence and surface roughness. As a Re number of about 150,000 is approached the features of the flow change dramatically and the critical regime starts.

The main features are as follows: a) rapid narrowing of the wake corresponding to the reattachment of the separated laminar boundary layer to form a laminar bubble preceded by a turbulent boundary layer which separates at around 120 degrees, b) loss of a dominant periodicity of vortex shedding, c) progressive loss of laminar bubble with increase in Re number, and d) much stronger sensitivity to free stream turbulence and surface roughness.

A typical distribution of pressure and heat transfer coefficients around a cylinder in subcritical and critical flow regimes is given by Ref. 52 and shown on Fig. 5. Maximum heat transfer does not necessarily occur at the leading edge. When the Re number is sufficiently large, heat transfer is more enhanced in the wake region. The effect of surface roughness on the heat transfer was investigated by Ref. 53. It was found that with the increase of surface roughness, the boundary layer undergoes transition from laminar to turbulent flow at decreasing Re numbers. The flow will become "critical" at a lower Re number and the heat transfer will be affected accordingly.

The Prandtl number (Pr) of convective ignition flows is around unity; therefore, the heat transfer behavior can be inferred from the general flow structure. Information concerning effects of Pr number other than unity, may be found in Refs. 54 and 55. Effects of blockage ratio on the flow are discussed and analyzed in Ref. 55. This subject will be discussed in Section IV.

The variation in pressure distribution around cylinders is on the order of  $\rho \cdot U^2$  or  $P \cdot M^2$ , which for a low subsonic flow is only a few percent of the free stream pressure. Thus, it has only a minor effect on the gas phase

kinetics. Therefore pressure distribution studies of flow around cylinders are of secondary importance. The mechanism of heat transfer to the front surface of the cylinder is well understood (through studies of laminar boundary layer phenomenon). However, the mechanism of heat transfer to the rear surface is much less understood and there are few hypothesis to explain it. The ideas developed can be exploited to explain convective ignition in the wake and, therefore, a short summary of the main hypothesis will be given here.

Basically all the approaches are phenomenological in nature and generally fail to yield local heat transfer values but a global one for the entire rear surface. In all cases the coefficient of heat transfer is related to Re number according to the relationship  $Nu = C \cdot Re^n$ .

Richardson [56] correlated heat transfer data from the literature to find a value of  $n = 2/3$ . The correlation of  $n$  was quite good but there were considerable deviations in the value of  $C$ . He attributed it to differences in experimental conditions especially with regard to wind tunnel blockage, free stream turbulence, and compressibility effects, as well as effects due to variable surface temperatures, since some of the experiments were performed under uniform surface temperature, while others were performed under uniform heat flux conditions. It should be pointed out here that in convective ignition experiments nothing is kept uniform and therefore heat flux correlation taken from the literature to estimate  $t_{\text{thermal}}$  are dubious.

There are two basic approaches. The first one is the "intermittent penetration theory" developed by Sano and Nishikawa [57]. They assumed that the fluid which is in contact with the surface of the cylinder is periodically renewed through the process of vortex shedding. From the solution of the unsteady state heat transfer equation with a frequency of surface renewal equal to that of vortex shedding, they estimated the time average overall heat transfer rate. The agreement with experimental data was rather poor, since the dependence on Re number was to the power of  $1/2$  which is at variance with experimental evidence. A variation of this penetration model was given by Virk [58]. The second theory is the boundary layer theory proposed by Mitchell [59]. His analytical model combines the surface renewal model with conventional boundary layer theory. A new boundary layer forms on the rear surface of a bluff body each time a vortex is formed. It builds up until the vortex is shed, and then it sheds with the vortex. Here a free stream velocity for the boundary layer over the rear surface should be assumed. The total heat transfer is obtained adding a short term solution and a long term solution. The short time solution is the solution of the unsteady boundary layer neglecting the convection term. The long time solution is the conventional steady state laminar boundary layer solution. The short term solution was found to account only for about 10% of the total period; thus, the heat transfer rate is little affected by the frequency of vortex shedding. Again, the dependence on Re number was found to be to the power of  $1/2$ . However, if a turbulent boundary layer is assumed to exist on the rear surface, the Re number power dependence is 0.8. Again the comparison with experimental data was only fair though better than for the pure penetration model. Experiments conducted by Matsui et al. [60] tend to support the second theory, though his experimental results yielded a dependence of heat transfer on Re number to the power of 0.63. Using a flow visualization technique and measuring flow velocity at the wake, he found that the fluid flow behind the cylinder reverses from the rear stagnation point to the separation point with the periodical fluctuation of the vortex

shedding from the wake. The reverse flow was found to be remarkably intense.

To summarize: both theories fail to explain the experimentally found dependency of the heat transfer in the wake on Re number to the power of about  $2/3$ . The second theory (boundary layer) is much more realistic and can explain the decrease of the local heat transfer coefficient, when moving from the rear stagnation point toward the separation point, by assuming thickening of the boundary layer.

Effects of free stream turbulence on heat and mass transfer from cylinders are best reviewed by Ref. 61 and will be discussed in more detail in Section V. As mentioned before, in the subcritical regime the effects are moderate and are toward the increase in heat transfer. The effect is more pronounced on the front surface than on the rear surface.

The situation where there are two cylinders in a row in cross flow is naturally more complex, and the flow fields around the second cylinder and between the two, depend on the ratio of the distance between them ( $L$ ) to the diameter of the first cylinder ( $D$ ). This type of situation was investigated by Ref. 62. Two different flow patterns around the cylinders are shown on Fig. 5. Of importance are: a) The flow field around the second cylinder resembles the pattern of critical flow. The boundary layer separates at around 120 degrees and, consequently the static pressure and heat transfer change very dramatically in the wake of the second cylinder. b) If the distance between the two cylinders is too small, a closed vortex is formed between the two cylinders; consequently, in the case of convective ignition, reactions have ample time to proceed, and ignition and flame stabilization are certain.

The foregoing discussion suggests the existence of three distinct flow zones around cylinders: front surface, wake (and rear surface), and separation point region. Thus the convective ignition process will be investigated separately in these zones. The experimental work which will be discussed in Section V indeed revealed three distinct regions for ignition which will be referred to as: (1) Front stagnation region ignition, (2) Separation region ignition, and (3) Rear body ignition. See illustration in Fig. 7. The occurrence of the first event (1) is independent of the flow in regions (2) and (3), but events (2) and (3) are interrelated and depend on the flow in region (1).

As already mentioned, only the front surface zone is tractable to a strict analytical treatment since the flow there is of the boundary layer type. Thus, a complete theoretical model will be developed for ignition in a boundary layer flow situation.

#### III-D. Studies of Ignition in a Reactive Boundary Layer

The general concept of reactive boundary layers is extensively reviewed by Williams [63] and Chung [64]. The work in ignition of reactive boundary layers falls into two categories: work with premixed flames and work with diffusion flames. The present situation is unique in the sense that when free stream oxidizers are present, it exhibits a hybrid behavior. Ignition under fully inert conditions, however, is of the premixed flame type. Marble and Adamson [65] first studied the problem of ignition under conditions of laminar mixing between two gaseous streams of a premixed fuel

and a hot combustion product (Marble-Adamson problem). Dooley [66] and Tsuji [67] extended the problem to flat plate flame stabilization. Cheng and Kovitz [68] extended the Marble-Adamson problem to the wake of a flat plate. Sharma and Sirignano studied ignition of cold premixed combustibles by a hot body in stagnation point flow [69] and in flat plate flow [70]. They also treated the ignition in the wake of a hot projectile as a Marble Adamson problem. Unlike the earlier analyses, the nonsimilar boundary layer equations were directly integrated by a numerical method.

All the above mentioned work was with premixed flows. Work with diffusion flame in boundary layers generally assumed the Burke-Schumann flame sheet model [71]. Emmons [72] considered the mass burning rate of a flat plate of fuel without the flame sheet approximation. He used the Shvab-Zeldovich method [73] assuming the oxygen concentration at the fuel surface to be zero. Waldman [74] studied diffusion flame over wedge-shaped bodies which evaporate or sublime in equilibrium according to Clausius-Clapeyron law. The analysis of a non-similar boundary layer was carried out with the method of matched asymptotic expansions. Krishnamurthy, Williams and Seshadri [75] studied the extinction of diffusion flame in stagnation point boundary layer flow about a vaporizing fuel body by means of asymptotic theory. Their theory extensively used the Damkohler number concept. Effects of Damkohler numbers on combustion in boundary layers were investigated by means of aerothermochemical analysis by Tsuji and Matsui [76] in connection with the combustion of carbon in stagnation flow. The model included surface reaction, and two types of Damkohler numbers were defined: gas phase Damkohler number and surface Damkohler number.

Neither of the aforementioned studies included the coupling of the gas phase with the unsteady solid state even in the ignition situation. Kashiwagi and Summerfield studied experimentally [77] and analytically [78] ignition and flame spreading on solid fuels in a hot oxidizing gas. The non-similar boundary layer equations were numerically solved coupled with the unsteady solid phase. However, the gas phase equations, as in all of the other work, were assumed to be quasi-steady, thus omitting the time derivatives. That simplified the solution to a great extent and in most cases only ordinary differential equations had to be dealt with. The assumption of quasi-steadiness of the gas phase in the ignition situation is justified when the characteristic time of the gas flow is much shorter than the ignition process. Such an assumption fails in the case of very short ignition delay times and processes. The present work addresses itself to cases of complete unsteadiness of the gas phase, including even the effect of unsteady free stream velocity, pressure, and temperature. The solid phase is fully coupled to the gas phase and chemical reaction is allowed to occur in the solid phase as well as in the gas phase. Thus, the transient nature of the ignition is fully explored.

### III-E Basic Equations of Unsteady Reactive Boundary Layer Coupled to Solid Phase

The basic physical situation shown in Fig. 3 was already discussed in paragraph III-B. At  $t = 0$  a hot oxidizer flow starts to develop over the front surface of the cylinder. The transition from a quiescent condition to a fully developed boundary layer may proceed in an arbitrary manner of flow acceleration, pressure, and temperature growth. The cylinder is composed of a homogeneous solid propellant which decomposes into fuel and oxidizer

species upon being heated. The gas phase-solid phase interaction process discussed in III-B leads eventually to a run-away chemical reaction at some location in the boundary layer.

The characteristic time of the boundary layer development over the propellant specimen under the present test conditions varied in the range of 50 to 300  $\mu$ sec. Many of the ignition delay times were in the submillisecond range; thus, neither the thermal induction period nor the chemical induction period of the ignition process can be treated in a quasisteady manner.

Since the Re number of interest here is in the range of 1000 to 150000, the boundary layer approximation is assumed to be valid for the present ignition problem. This approximation breaks down after ignition, except at the stagnation point region. The reason is that the conduction term in the direction of the flow, neglected in the boundary layer approximation, is not negligible after ignition. However, the approximation is valid during most of the induction period until intense flame is developed. The boundary layer over the front surface is considered to be laminar. This assumption is reasonable considering the Reynolds number range of the flow and it is also supported by heat flux measurements taken with an instrumented cylinder as will be discussed in Section V.

#### (i) Gas Phase Equations

The governing reactive boundary layer equations are as follows:

Continuity:

$$\rho \left( \frac{\partial \rho}{\partial t} + u \frac{\partial \rho}{\partial x} + v \frac{\partial \rho}{\partial y} \right) = 0 \quad (1)$$

Momentum:

$$\rho \left( \frac{\partial u}{\partial t} + u \frac{\partial u}{\partial x} + v \frac{\partial u}{\partial y} \right) = -\frac{\partial p}{\partial x} + \frac{\partial}{\partial y} \left( \mu \frac{\partial u}{\partial y} \right) \quad (2)$$

Energy:

$$\rho \left( \frac{\partial T}{\partial t} + u \frac{\partial T}{\partial x} + v \frac{\partial T}{\partial y} \right) = \frac{\partial}{\partial y} \left[ \frac{\mu}{Pr} \frac{\partial T}{\partial y} + \mu \left( 1 - \frac{1}{Pr} \right) \frac{1}{2} \frac{\partial u^2}{\partial y} \right] - \frac{\partial}{\partial y} \left[ \left( \frac{1}{Le} - 1 \right) \rho D_{12} \sum_i \hat{h}_i \frac{\partial Y_i}{\partial y} \right] + \frac{\partial \dot{q}}{\partial t} \quad (3)$$

Conservation of i-th species:

$$\rho \left( \frac{\partial Y_i}{\partial t} + u \frac{\partial Y_i}{\partial x} + v \frac{\partial Y_i}{\partial y} \right) = \frac{\partial}{\partial y} \left( \rho D_{12} \frac{\partial Y_i}{\partial y} \right) + \dot{w}_i \quad (4)$$

Equation of State:

$$p = p_0 = \left( \sum_i \frac{Y_i}{M_i} \right) \rho R T \quad (5)$$

where  $Y_i = \frac{\rho_i}{\rho}$  is the mass fraction of species i

and  $\hat{h}_i = \int_0^T c_{p,i} dT + \hat{h}_i^0$  is the enthalpy of species i,

so that  $\hat{h} = \sum_i Y_i \cdot \hat{h}_i$  is the total enthalpy

and  $I = \hat{h} + \frac{u^2}{2}$  is the total energy.

$Pr \triangleq \frac{c_p \mu}{k}$  is the Prandtl number.

$Le \triangleq \frac{c_p \rho D_{12}}{k}$  is the Lewis number.

The assumptions that were made:

- (1) Fick's law of diffusion holds, assuming equal diffusion coefficient.
- (2) The mixture of gases behaves as perfect gas.

A new coordinate system is defined, using the Levy [79] and Howarth-Dorodnitsyn [80] transformations:

$$S = \int_0^x \rho_e \mu_e u_e dx \quad \eta = \frac{u_e}{(2s)^{1/2}} \int_0^y s dy \quad (6)$$

A velocity function, F, is defined such that:

$$F = F(\eta, S, \tau) \quad u(s, \eta, \tau) = u_e(s, \tau) \cdot \frac{\partial F}{\partial \eta} \quad (7)$$

Thus the new independent variables are:

$$S = S(x, t) \quad \eta = \eta(x, y, t) \quad \tau = \tau(x, t) \quad (8)$$

A residence time,  $t_f$ , is defined such that:

$$\frac{1}{t_f} \triangleq \frac{\partial \tau}{\partial t} \triangleq \frac{\rho_e \mu_e u_e^2}{2s} \quad (9)$$

Using the newly defined coordinate system and functions, the boundary layer equations (1)-(4) are transformed to a non-similar form, retaining the nonsteadiness of the velocity, pressure, and temperature. The new form of equations is not standard and, therefore, the key steps in deriving the equations are given in Appendix I. The set of equations obtained is in the most general form and will be simplified further by the following assumptions:

- 1) The specific heat is the same for all the gaseous species and is constant.
- 2) The molecular weights of all species are equal and the diffusion coefficients of all species are equal.
- 3) The Prandtl, Schmidt and Lewis numbers are equal to unity.
- 4)  $\frac{s \cdot \mu}{s_e \cdot \mu_e} = 1$  everywhere in the flow field.

The above assumptions are commonly found elsewhere in the combustion literature. They simplify the equations to a great extent, and yet the basic features of the exact solution are retained. Considering the lack of knowledge of the exact chemical kinetics process, the above simplifications are justified. Dealing with low subsonic flow,  $M^2 \ll 1$ ,  $u_e^2 \ll h$ , the kinetic energy is neglected in the energy equation.

Defining:

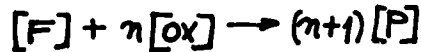
$$\Theta \triangleq \frac{T}{T_{ef}} \quad (10)$$

$T_{ef}$  is the maximum temperature obtained in the free stream after some time  $t$ .

Then:

$$I = c_p T_{ef} \left( \Theta + \frac{\sum Y_i \hat{h}_i}{c_p T_{ef}} \right)$$

Gas phase reaction: Assuming one-step irreversible chemical reaction subjected to second-order Arrhenius kinetics, of the form:



So that:

$$\dot{W}_F = -s^2 \cdot A_R \cdot Y_F \cdot Y_{OX} \cdot e^{-E_R/RT}$$

Thus the boundary layer equations (App. I, equations (I-5) to (I-7)), assume the form:

$$\begin{aligned} -\frac{\partial^2 F}{\partial \eta^2 \partial \tau} + \frac{\partial^2 F}{\partial \eta^2} + F \cdot \frac{\partial^2 F}{\partial \eta^2} &= \frac{2S}{u_e} \cdot \frac{\partial u_e}{\partial S} \cdot \left[ \left( \frac{\partial F}{\partial \eta} \right)^2 - \Theta \cdot \frac{T_{ef}}{T_e} \right] + \\ &+ 2S \cdot \left( \frac{\partial F}{\partial \eta} \cdot \frac{\partial^2 F}{\partial \eta \partial S} - \frac{\partial F}{\partial S} \cdot \frac{\partial^2 F}{\partial \eta^2} \right) + u_e \cdot t_f \cdot \frac{\partial T}{\partial x} \left( \frac{\partial F}{\partial \eta} \cdot \frac{\partial^2 F}{\partial \eta \partial \tau} - \frac{\partial F}{\partial \tau} \cdot \frac{\partial^2 F}{\partial \eta^2} \right) + \\ &+ \frac{1}{u_e} \cdot \frac{\partial u_e}{\partial \tau} \cdot t_f \cdot \left( \frac{\partial F}{\partial \eta} - \Theta \cdot \frac{T_{ef}}{T_e} \right) + \frac{\partial S}{\partial \tau} \cdot t_f \cdot \frac{\partial^2 F}{\partial \eta \partial S} - \\ &- \frac{\partial F}{\partial x} \cdot t_f \cdot \frac{\partial u_e}{\partial \tau} \cdot \left[ \left( \frac{\partial F}{\partial \eta} \right)^2 + \Theta \cdot \frac{T_{ef}}{T_e} \right] - \left( \frac{\partial S}{\partial \tau} \cdot \frac{t_f}{2S} - \frac{\partial u_e}{\partial \tau} \cdot \frac{t_f}{u_e} \right) \cdot \eta \cdot \frac{\partial^2 F}{\partial \eta^2} \end{aligned} \quad (11)$$

$$\begin{aligned}
 -\frac{\partial Y_i}{\partial t} + \frac{\partial^2 Y_i}{\partial \eta^2} + F \cdot \frac{\partial Y_i}{\partial \eta} = & t_f \cdot p_e \cdot \frac{T_e}{T_{e,f}} \cdot A_n \cdot \frac{Y_F \cdot Y_{O_2}}{\theta} \cdot e^{-\theta_n/\theta} + \\
 & + 2S \cdot \left( \frac{\partial F}{\partial \eta} \cdot \frac{\partial Y_i}{\partial s} - \frac{\partial F}{\partial s} \cdot \frac{\partial Y_i}{\partial \eta} \right) + u_e \cdot t_f \cdot \frac{\partial F}{\partial x} \cdot \left( \frac{\partial F}{\partial \eta} \cdot \frac{\partial Y_i}{\partial t} - \frac{\partial F}{\partial t} \cdot \frac{\partial Y_i}{\partial \eta} \right) + \\
 & + \frac{\partial S}{\partial t} \cdot t_f \cdot \frac{\partial Y_i}{\partial s} - \left( \frac{\partial S}{\partial t} \cdot \frac{t_f}{2S} - \frac{\partial u_e}{\partial t} \cdot \frac{t_f}{u_e} \right) \cdot \eta \cdot \frac{\partial Y_i}{\partial \eta}
 \end{aligned} \quad (12)$$

$$\begin{aligned}
 -\frac{\partial \theta}{\partial t} + \frac{\partial^2 \theta}{\partial \eta^2} + F \cdot \frac{\partial \theta}{\partial \eta} = & -t_f \cdot p_e \cdot \frac{T_e}{T_{e,f}} \cdot \frac{Q_p}{C_p} \cdot A_n \cdot \frac{Y_F \cdot Y_{O_2}}{\theta} \cdot e^{-\theta_n/\theta} + \\
 & + 2S \cdot \left( \frac{\partial F}{\partial \eta} \cdot \frac{\partial \theta}{\partial s} - \frac{\partial F}{\partial s} \cdot \frac{\partial \theta}{\partial \eta} \right) + u_e \cdot t_f \cdot \frac{\partial F}{\partial x} \cdot \left( \frac{\partial F}{\partial \eta} \cdot \frac{\partial \theta}{\partial t} - \frac{\partial F}{\partial t} \cdot \frac{\partial \theta}{\partial \eta} \right) + \\
 & + \frac{\partial S}{\partial t} \cdot t_f \cdot \frac{\partial \theta}{\partial s} - \left( \frac{\partial S}{\partial t} \cdot \frac{t_f}{2S} - \frac{\partial u_e}{\partial t} \cdot \frac{t_f}{u_e} \right) \cdot \eta \cdot \frac{\partial \theta}{\partial \eta}
 \end{aligned} \quad (13)$$

In the above equations, the free stream velocity, pressure and temperature are arbitrary functions of time. The residence time  $t_f$  is therefore also a function of time and the response of the equations to any perturbation depends on the instantaneous value of  $t_f$ . The equations are two-dimensional in space ( $s, \eta$ ) and may be applied to any arbitrary surface shape as, for example, the front surface of a cylinder.

The coupling of the above equations with the solid phase is through the boundary conditions. This subject will be discussed next.

#### (ii) Solid Phase Equations

Assumptions:

1) The temperature gradients along the surface are much smaller than those perpendicular to it. Thus, the solid phase energy equation assumes a one dimensional form. This assumption is completely valid at the stagnation point region and during most of the ignition induction period elsewhere.

2) A subsurface chemical reaction of the zeroth order is assumed [50], whose control mechanism is solid phase decomposition.

$$\dot{w}_s = -A_s \cdot e^{-E_s/R \cdot T_s}$$

Neglecting species diffusion, the following equations are obtained:

Energy:

$$C_{p,s} \cdot p_s \cdot \left( \frac{\partial T_s}{\partial t} + V_{reg} \cdot \frac{\partial T_s}{\partial y_s} \right) = k_s \cdot \frac{\partial^2 T_s}{\partial y_s^2} + Q_s \cdot p_s \cdot \dot{w}_s \quad (14)$$

Specie:

$$\frac{\partial Y_s}{\partial t} + V_{reg} \cdot \frac{\partial Y_s}{\partial y_s} = -\dot{w}_s \quad (14a)$$

$V_{REG}$  is the regression velocity. It will be expressed by an Arrhenius

pyrolysis law. Thus, it depends only on the surface temperature.

$$V_{REG} = A_p \cdot e^{E_p / RT_w} \quad (15)$$

Defining:

$$\eta_s \triangleq \frac{1}{(\alpha_s \cdot t_f)^{1/2}} \cdot y_s \quad \Theta_{so} \triangleq \frac{T_s}{T_{sf}} \quad (16)$$

and also:

$$\hat{\alpha}_s \triangleq \frac{K_s}{\rho_s C_{ps}}$$

The solid phase equations in their transformed form are:

$$\begin{aligned} \frac{\partial \Theta_{so}}{\partial \tau} + \frac{\partial s}{\partial t} \cdot t_f \cdot \frac{\partial \Theta_{so}}{\partial s} + \left( \frac{V_{REG} \cdot t_f^{1/2}}{\hat{\alpha}_s^{1/2}} - \frac{1}{2} \cdot \frac{\partial t_f}{\partial t} \cdot \eta_s \right) \cdot \frac{\partial \Theta_{so}}{\partial \eta_s} = \\ = \frac{\partial^2 \Theta_{so}}{\partial \eta_s^2} + \frac{Q_s \cdot t_f}{C_{ps} \cdot T_{sf}} \cdot \dot{w}_s \end{aligned} \quad (17)$$

$$\begin{aligned} \frac{\partial y_s}{\partial \tau} + \frac{\partial s}{\partial t} \cdot t_f \cdot \frac{\partial y_s}{\partial s} + \left( \frac{V_{REG} \cdot t_f^{1/2}}{\hat{\alpha}_s^{1/2}} - \frac{1}{2} \cdot \frac{\partial t_f}{\partial t} \cdot \eta_s \right) \frac{\partial y_s}{\partial \eta_s} = \\ = -t_f \cdot \dot{w}_s \end{aligned} \quad (17a)$$

$s, \eta, t_f$  are the same variables defined before for equations (11)-(13).

The initial conditions and boundary conditions which couple the boundary layer equations (11)-(13) to the solid phase equations (16)-(17) are given here in their basic initial form:

$$\begin{array}{lll} t=0 & u_e=0 & V_{REG}=0 \\ y \geq 0 & P_e = P_0 & \\ (y_s \geq 0) & T_e = T_0 & \\ & Y_{Ox} = Y_{Oxe} & \\ & Y_F = 0 & \\ & T_s = T_0 & \\ & Y_s = 1 & \end{array} \quad (18a)$$

$$\begin{array}{lll} t=0^+ & u_e = u_1 & \\ y > 0 & P_e = P_0 & \\ (y_s > 0) & T_e = T_0 & \\ & Y_{Ox} = Y_{Ox1} & \\ & Y_F = 0 & \\ & T_s = T_s(y_s) & \end{array} \quad (18b)$$

$$\begin{aligned}
 t > 0^+ & \quad u = 0 \\
 y = 0 & \quad v = v_w = \frac{\rho_s}{\rho_w} \cdot V_{\infty} = \frac{\rho_s}{\rho_w} \cdot A_p \cdot e^{-\frac{E_p}{R T_w}} \\
 (y_s = 0) & \quad -k_w \left( \frac{\partial T}{\partial y} \right)_w = k_s \left( \frac{\partial T_s}{\partial y_s} \right)_w - \rho_s \cdot V_{\infty} \cdot L_v \\
 & \quad T = T_w \\
 & \quad -\rho_w \cdot D_w \left( \frac{\partial Y_{O_2}}{\partial y} \right)_w + \rho_w \cdot v_w \cdot Y_{O_2 w} = \rho_s \cdot V_{\infty} \cdot (1 - \alpha) \\
 & \quad -\rho_w \cdot D_w \left( \frac{\partial Y_F}{\partial y} \right)_w + \rho_w \cdot v_w \cdot Y_{F w} = \rho_s \cdot V_{\infty} \cdot \alpha
 \end{aligned} \tag{18c}$$

$$\begin{aligned}
 t > 0^+ & \quad u_e = u_e(t) \\
 y = \infty & \quad P_e = P_e(t) \\
 (y_s = \infty) & \quad T_e = T_e(t) \\
 & \quad Y_{O_2} = Y_{O_2 e} \\
 & \quad Y_F = 0 \\
 & \quad T_s = T_0 \\
 & \quad Y_s = 1
 \end{aligned} \tag{18d}$$

The boundary conditions reflect the non-slip conditions, the blowing at the surface, the energy matching, the conservation of mass at the surface, and conditions at the gas phase boundary layer edge and solid phase thermal wave edge. It is assumed that the solid phase pyrolyzes at the surface to fuel and oxidizer, with fractional mass ratios of  $\alpha$  and  $1 - \alpha$  respectively.

The initial conditions are: quiescence at time  $t = 0$  and some given step function of free stream conditions at time  $t = 0^+$ . Thereafter the free stream conditions vary with time in a given manner.

The boundary layer and solid phase equations constitute a set of parabolic partial differential equations which can be solved numerically for the given boundary and initial conditions (Eq. (18)). However, the complexity of the problem is immense and solving it in two spacial dimensions is beyond the scope of the present work. Thus, the solution for the entire front surface of a cylinder will not be investigated numerically but phenomenologically. Since one of the goals of the present work is to investigate convective ignition under general unsteady conditions, the equations above will be applied to the front stagnation point region; thus, the problem will be transformed to one-dimensional in space but the non-steadiness will be retained.

### III-F. Front Stagnation Point Solution

#### (i) Formulation

The free stream velocity at the front stagnation point region is assumed to correspond to a potential flow around the cylinder even in the unsteady case (see for example Ref. 81). Thus, for a cylinder of radius  $R$ , the boundary layer edge velocity is:

$$u_e(x,t) = \frac{2 \cdot u_{\infty}(t)}{R} \cdot x \quad (19)$$

$u_{\infty}(t)$  is an arbitrary time variant.

As already assumed,  $\rho \cdot \mu$  is a function of pressure only; therefore:

$$\begin{aligned} \rho_e \cdot \mu_e &= C_1 \cdot P_e & C_1 &= \frac{\rho_{ef} \cdot \mu_{ef}}{P_{ef}} & P_e &\approx P_{\infty}(t) \\ & & & & T_e &\approx T_{\infty}(t) \end{aligned} \quad (19a)$$

Noting also that  $\frac{1}{P_e} \cdot \frac{\partial P_e}{\partial x} \ll \frac{1}{R}$ , while  $\frac{1}{u_e} \cdot \frac{\partial u_e}{\partial x} \sim O(1/R)$ ,

the residence time is

$$t_f = \frac{R}{2 \cdot u_{\infty}(t)} \quad (20)$$

Also,  $\frac{2S}{u_e} \cdot \frac{\partial u_e}{\partial S} = 1$  and  $\frac{\partial}{\partial S} = 0$  inside the boundary layer so that:

$$\tau = \tau(t) \quad F = F(\eta, t)$$

The independent variables thus obtained are:

$$\eta = \frac{1}{(t_f \cdot \rho_e \mu_e)^{1/4}} \cdot \int_0^y s dy \quad \eta_s = \frac{1}{(\alpha_s \cdot t_f)^{1/2}} \cdot y_s \quad \tau = \int_0^t t_f' dt \quad (21)$$

The following parametric groups are defined:

Damkohler numbers:

$$D_e \triangleq t_f \cdot \rho_e \cdot \frac{T_e}{T_{ef}} \cdot A_n \quad - \text{Gas phase Damkohler number}$$

$$D_s \triangleq t_f \cdot \frac{\rho_s^2}{\rho_e \mu_e} \cdot A_p^2 \quad - \text{Surface Damkohler number} \quad (22a)$$

$$D_{so} \triangleq t_f \cdot A_s \quad - \text{Solid phase Damkohler number}$$

Thermal and physical properties:

$$\gamma \triangleq \frac{C_{p2}}{C_p} \quad - \text{Heat capacity ratio}$$

$$\varepsilon \triangleq \frac{\rho_s \cdot k_s \cdot C_{p2}}{\rho_e \cdot k_e \cdot C_p} \quad - \text{Thermal properties ratio}$$

$$g \triangleq \frac{L_v}{C_p \cdot T_{ef}} \quad - \text{Ratio of heat of evaporation of propellant to static enthalpy of the flow.}$$

(22b)

$$h \triangleq \frac{Q_R}{C_P \cdot T_{ef}}$$

- Ratio of heat of gas phase reaction  
to static enthalpy of the flow

$$h_s \triangleq \frac{Q_s}{C_{ps} \cdot T_{ef}}$$

- Ratio of heat of solid phase reaction  
to static enthalpy of the flow

Chemical kinetics values:

$$\theta_R \triangleq \frac{E_R}{R \cdot T_{ef}}$$

- Nondimensional activation energy  
of gas phase reaction

(22c)

$$\theta_s \triangleq \frac{E_s}{R \cdot T_{ef}}$$

- Nondimensional activation energy  
of solid phase reaction

$$\theta_P \triangleq \frac{E_P}{R \cdot T_{ef}}$$

- Non dimensional pyrolysis activation energy

New dependent variables are defined:

$$G \triangleq \frac{\partial F}{\partial \eta}$$

$$Z \triangleq Y_{ox} - \eta \cdot Y_F$$

$$H \triangleq \theta + \frac{h}{\eta} \cdot Y_{ox}$$

(23)

The last two definitions of (23) will render the boundary layer equations into a Schvab-Zeldovich [51] form, thus reducing the number of nonlinear terms on the right hand side of the equations. With the above definitions the boundary layer equations (11)-(13) written for the stagnation flow assume the final form:

$$G = \frac{\partial F}{\partial \eta}$$

$$-\frac{\partial G}{\partial \tau} + \frac{\partial^2 G}{\partial \eta^2} + F \cdot \frac{\partial G}{\partial \eta} = G^2 - \Theta \cdot \frac{\gamma_2}{\gamma_1} + \frac{t_2}{2} \cdot \frac{1}{\gamma_1} \cdot \frac{d\gamma_1}{dt} \cdot (G - \Theta \cdot \frac{\gamma_2}{\gamma_1}) + \frac{t_2}{2} \cdot (\frac{1}{\gamma_1} \frac{d\gamma_1}{dt} - \frac{1}{\gamma_2} \frac{d\gamma_2}{dt}) \cdot \eta \cdot \frac{\partial G}{\partial \eta} \quad (24)$$

$$-\frac{\partial H}{\partial \tau} + \frac{\partial^2 H}{\partial \eta^2} + F \cdot \frac{\partial H}{\partial \eta} = \frac{t_2}{2} \cdot (\frac{1}{\gamma_1} \frac{d\gamma_1}{dt} - \frac{1}{\gamma_2} \frac{d\gamma_2}{dt}) \cdot \eta \cdot \frac{\partial H}{\partial \eta} \quad (25)$$

$$-\frac{\partial H}{\partial \tau} + \frac{\partial^2 H}{\partial \eta^2} + F \cdot \frac{\partial H}{\partial \eta} = \frac{t_2}{2} \cdot (\frac{1}{\gamma_1} \frac{d\gamma_1}{dt} - \frac{1}{\gamma_2} \frac{d\gamma_2}{dt}) \cdot \eta \cdot \frac{\partial H}{\partial \eta} - \frac{t_2}{C \cdot \gamma_2 \cdot \gamma_1} \cdot \frac{d\gamma_2}{dt} \cdot \Theta \quad (26)$$

$$-\frac{\partial \Theta}{\partial \tau} + \frac{\partial^2 \Theta}{\partial \eta^2} + F \cdot \frac{\partial \Theta}{\partial \eta} = -[(H - \Theta) \cdot \eta + Z] \cdot \frac{(H - \Theta)}{\Theta} \cdot D_0 \cdot e^{-\Theta/\Theta_0} + \frac{t_2}{2} \cdot (\frac{1}{\gamma_1} \frac{d\gamma_1}{dt} - \frac{1}{\gamma_2} \frac{d\gamma_2}{dt}) \cdot \eta \cdot \frac{\partial \Theta}{\partial \eta} - \frac{t_2}{C \cdot \gamma_2 \cdot \gamma_1} \cdot \frac{d\gamma_2}{dt} \cdot \Theta \quad (27)$$

The solid phase equations are:

$$-\frac{\partial \Theta_{s1}}{\partial \tau} + \frac{\partial^2 \Theta_{s1}}{\partial \eta_s^2} + \left[ \left( \frac{D_2}{\epsilon} \right)^{1/2} \cdot \eta \cdot e^{-\Theta_s/\Theta_0} - \frac{t_2}{2} \cdot \frac{1}{\gamma_1} \cdot \frac{d\gamma_1}{dt} \cdot \eta_s \right] \cdot \frac{\partial \Theta_{s1}}{\partial \eta_s} = -h_s \cdot D_{s0} \cdot e^{-\Theta_s/\Theta_0} \quad (28)$$

$$-\frac{\partial \gamma_s}{\partial \tau} + \left[ \left( \frac{D_2}{\epsilon} \right)^{1/2} \cdot \eta \cdot e^{-\Theta_s/\Theta_0} - \frac{t_2}{2} \cdot \frac{1}{\gamma_1} \cdot \frac{d\gamma_1}{dt} \cdot \eta_s \right] \cdot \frac{\partial \gamma_s}{\partial \eta_s} = D_{s0} \cdot e^{-\Theta_s/\Theta_0} \quad (29)$$

The boundary conditions for the above equations are as follows:

$$\begin{aligned} \tau &= 0 \\ \eta &\geq 0 \\ (\eta_s &\geq 0) \end{aligned}$$

$$\begin{aligned} G &= 1 \\ \Theta &= \frac{T_0}{T_{0s}} \\ Z &= Y_{0s} \\ H &= \frac{T_0}{T_{0s}} + \frac{A}{\eta} \cdot Y_{0s} \\ \Theta_{s0} &= \frac{T_0}{T_{0s}} \\ \gamma_s &= 1 \end{aligned}$$

(30a)

$$\begin{aligned}
 \tau > 0^+ \\
 \eta > 0 \\
 (\eta_s > 0)
 \end{aligned}
 \quad
 \begin{aligned}
 G &= 1 \\
 \Theta &= \frac{T_{s1}}{T_{s2}} \\
 Z &= Y_{Ox} e \\
 H &= \frac{T_{s1}}{T_{s2}} + \frac{A}{\eta} \cdot Y_{Ox} e \\
 \Theta_{s0} &= \frac{T_s(\eta_s)}{T_{s2}}
 \end{aligned}
 \quad (30b)$$

$$\begin{aligned}
 \tau > 0^+ \\
 \eta = 0 \\
 (\eta_s = 0)
 \end{aligned}
 \quad
 \begin{aligned}
 G_w &= 0 \\
 F_w &= -(D_s)^{1/2} \cdot e^{-\Theta_r/\Theta_w} \\
 \Theta &= \Theta_w \\
 \left(\frac{\partial Z}{\partial \eta}\right)_w + F_w \cdot Z_w &= [1 - \alpha \cdot (1 + \eta)] \cdot F_w \\
 \left(\frac{\partial H}{\partial \eta}\right)_w + F_w \cdot H_w &= \left(\frac{\partial \Theta}{\partial \eta}\right)_w + [\Theta_w + (1 - \alpha) \cdot \frac{A}{\eta}] \cdot F_w \\
 -\left(\frac{\partial \Theta}{\partial \eta}\right)_w - \varepsilon^{1/2} \cdot \left(\frac{\partial \Theta_{s0}}{\partial \eta_s}\right)_w &= g \cdot F_w
 \end{aligned}
 \quad (30c)$$

$$\begin{aligned}
 \tau > 0^+ \\
 \eta = \infty \\
 (\eta_s = \infty)
 \end{aligned}
 \quad
 \begin{aligned}
 G_{\infty} &= 1 \\
 \Theta_{\infty} &= \frac{T_{s1}}{T_{s2}} \\
 Z &= Y_{Ox} e \\
 H &= \frac{T_{s1}}{T_{s2}} + \frac{A}{\eta} \cdot Y_{Ox} e \\
 \Theta_{s0} &= \frac{T_s}{T_{s2}} \\
 Y_s &= 1
 \end{aligned}
 \quad (30d)$$

## (ii) Discussion of the Stagnation Flow Ignition

As evidenced from Eqs. (24)-(29), there is no dependence on  $x$  for the temperature and species concentration profiles, and the boundary layer thickness is constant along the surface. Thus, there is no preference for ignition to occur at any specific point along the surface. Furthermore, the surface temperature is constant with  $x$  and the accumulated amount of fuel evaporated along  $x$  is balanced exactly by dilution from the external flow so that reaction rate is the same everywhere. Ignition, if it occurs, should occur simultaneously over the entire region.

The front stagnation blow region is the region where Eq. (19) holds. Typically, the external flow around the front half of a cylinder, up to about 60 degrees along the perimeter, satisfies:

$$U_e = 2 \cdot U_{\infty} \sin \frac{x}{R} \quad (31)$$

Eq. (19) is a good approximation to Eq. (31) up to about 30 degrees from the front stagnation point. Thus, the front stagnation flow region subtends about 60 degrees of the front perimeter.

Despite the one-dimensional appearance of Eqs. (24)-(29), the physical processes typical to convective ignition are well entrenched in the

equations in the form of the various Damkohler numbers.

The role of the gas Damkohler number  $D_G$  was already discussed in III-B. It has a major role in determining ignition site, as well as delay time. If it is too small, ignition may occur at other portions of the cylinder rather than at the stagnation region. The surface Damkohler number  $D_S$  is a ratio of flow residence time to fuel loading time. Its main effect is on ignition delay time which is shorter for a larger  $D_S$ . The solid phase Damkohler number  $D_{SO}$  determines the relative contribution of subsurface heat release to the increase in surface temperature, as compared to heat transfer from the gas phase.

The parameter  $h$  is important in providing sufficient energy as a stimulus for the fast reaction rate necessary for ignition.

The thermal property  $\epsilon$  (Eq. (22b)) is of major importance. It is a measure of the thermal response of the solid phase to changes in the gas phase. From the classic theory of heat conduction, it can be shown [82] that when two semi-infinite bodies of different temperatures,  $T_g$  and  $T_o$ , are brought into contact, the contact surface assumes instantly a value given by:

$$T_w = \frac{T_g - T_o}{1 + \epsilon^{1/2}} + T_o \quad (32)$$

Such is the case of conductive ignition. When the propellant surface is suddenly exposed to hot gas, the surface temperature jumps instantly to a value compatible with Eq. (32). Such conditions occur, for example, in shock tube tests [8]. In convective ignition a similar surface temperature jump occurs at time  $t = 0^+$ , but unlike the conductive case, the surface temperature will rise thereafter at a rate compatible with the convective heat transfer mechanism (i.e., boundary layer flow). A smaller  $\epsilon$  results in a larger initial surface temperature jump and, therefore, in a substantial reduction in ignition delay time. The time for the surface temperature to reach some value under specified heating conditions is also proportional to  $\epsilon$ .

### (iii) Time Scales of the Problem

As already discussed in III, the ignition delay time can be expressed as  $t_{\text{thermal}} + t_{\text{chemical}}$ . This is, however, a simplified phenomenological interpretation. During  $t_{\text{thermal}}$ , all the terms in Eqs. (24)-(25) which contain the various Damkohler numbers are negligible in magnitude as compared to the other terms. For a given  $\epsilon$  and steady free stream conditions, the surface temperature is merely a function of  $\tau$ . Therefore, the time it takes for the surface temperature to rise from its initial value to a given value is a linear function of the free stream velocity.

In the case of steady free stream conditions, the time scale of non-steadiness in the gas phase is about  $\tau \sim 1$ . During this period the boundary layer develops to its steady state thickness. This can be shown from Eq. (24) (realizing that  $G$  is bounded between 0 and 1).

Thus:

$$t_{BL} \approx t_f$$

After that period, in the absence of unsteadiness in the free stream flow, the gas phase may be treated as quasi-steady until ignition occurs. The solid phase, however, is unsteady during the entire ignition process. By analyzing the solid phase equation (28) and the energy transfer boundary condition (Eq. (30c)), it can be shown that the time scale for a significant change in solid phase temperature is  $\epsilon$  times larger than the time scale for a similar gas phase temperature change.

Thus after  $t \sim t_f$ , a new time scale can be defined:  $\tau_i = \epsilon \cdot \tau$ .  
In the present problem  $\epsilon \sim 400$ .

The quasi-steadiness conditions in the gas phase prevail unless there is a significant variation in the magnitude of any dependent variable on a time scale equal or less than  $t_f$ . Such is the case when strong non-steadiness in the free stream flow occurs or when a rapid transition to ignition takes place.

It is obvious from Eqs. (24)-(27) that it is the magnitude of the fractional change in free stream conditions that affects the quasi-steadiness.

In particular:

$$\frac{1}{u_e} \cdot \frac{du_e}{dt} > \frac{1}{t_f} \quad \frac{1}{P_e} \cdot \frac{dP_e}{dt} > \frac{1}{t_f} \quad (33)$$

As significant gasification starts (which is evidenced by the regression of the solid phase surface), more time scales enter the problem. The respective time scales for the solid phase and gas phase associated with the gasification phenomenon are [83]:

$$t_{so} = \frac{\hat{a}_s}{V_{RFs}} \quad t_g = \frac{\hat{a}_g}{V_w^2} \quad (34)$$

Using the physical values from Table 3 (which are typical for the test conditions) the magnitudes of the time scales (34) are:

For  $T_w = 340$  C (close to steady state burning condition):

$$t_{so} \sim 7 \text{ msec} \quad t_g \sim 0.03 \text{ msec}$$

For  $T_w = 280$  C (typical ignition conditions):

$$t_{so} \sim 121 \text{ msec} \quad t_g \sim 0.52 \text{ msec}$$

Since typically  $t_{so} \gg t_{ign}$ , the solid phase is highly unsteady during the ignition process. The ratio of the above times depends only on the physical parameters. From mass continuity at the surface:

$$\frac{t_g}{t_{so}} = \frac{K \cdot C_{ps} \cdot J}{K_s \cdot C_p \cdot J_s} \quad (35)$$

For the values calculated, the above ratio is 233; thus, the gas phase may be assumed quasi-steady in relation to the solid phase. In comparison, a typical residence time is  $t_r = 0.1$  msec, which is in the range of  $t_g$ . These times are incorporated in the surface Damkohler number  $D_s$ .

After the occurrence of ignition a transition to steady state takes place and a thermal wave length associated with  $t_{so}$  is distinguished. Also, the subsurface reaction becomes appreciable. The length scales associated with the thermal wave and subsurface reaction are:

$$l_{th} = \frac{\hat{\alpha}_s}{V_{reg}} \quad l_{ssr} = l_{th} \cdot \frac{R \cdot T_w}{E_s} \quad (36)$$

For  $T_w = 340$  C the values are:  $l_{th} = 14 \mu m$ , and  $l_{ssr} = 0.4 \mu m$ . These values are much smaller than the cylinder radius, which is 3.5 mm, and therefore the one-dimensional treatment of the solid phase is justified. In addition,  $l_{ssr}$  is very thin as compared to  $l_{th}$  and can be assumed quasi-steady compared to the solid phase thermal process (Eq. (28)), but not compared to the gas phase.

From the above discussion it is clear that several time scales of various processes coexist during the convective ignition process. They are quite distinguishable in magnitude during  $t_{thermal}$  and when steady state burning is obtained, but their relative magnitudes are quite ambiguous during the onset of the ignition itself and special care should be taken when dealing with the convective ignition equations (24)-(30) for that process. However, the period of that process is not well defined and therefore, though the equations may be simplified for definite durations of the total ignition period, they are solved here numerically in their complete form for the entire period.

### III-G Ignition Criteria

The exact state of ignition is an ill-defined quantity and therefore any ignition criterion selected is somewhat arbitrary. In general, the theoretical ignition criterion is not directly related to an experimental one.

Discussion of ignition criteria in gas phase ignition models may be found in Ref. 25. In all cases ignition was attributed to some state of gas phase distribution during the ignition period. One criterion was based on the assumption that ignition occurs whenever heat generation at any point in the gas phase exceeds heat losses at this point. This is mathematically equivalent to stating that  $\partial T / \partial t = 0$  at ignition, or that some temperature peak is developed. Ref. 25 argued that this criterion need not necessarily lead to incipient ignition and thus offered another criterion which stated that ignition occurs when the maximum gas temperature at any station in the gas phase exceeds the free stream gas phase temperature  $T_e$  by a specified amount. Thus, at ignition  $T = \alpha \cdot T_e$  where  $\alpha > 1$ . Another ignition criterion often employed is the integrated heat balance. Ignition occurs when the heat generation due to chemical reactions integrated over the entire gas phase at a given time is equal to and increasing more rapidly than the heat conducted out of the boundary layer at the solid-gas interface. Thus:

$$A_R \cdot Q_R \cdot \int_0^{\delta} \rho^2 \cdot Y_F \cdot Y_{Ox} \cdot e^{-E_R/RT} \cdot dy + (k \cdot \frac{\partial T}{\partial y})_w \geq 0 \quad (37)$$

All the above criteria appear to be physically reasonable and they constitute the mathematical approximation basis for the theoretical ignition studies.

Since generally the experimental ignition criterion is based on light emission detection, the theoretical criteria discussed are seemingly not directly related to the experimental ones.

Kashiwagi [19] based his ignition criterion on the chemical reaction rate. He integrated the chemical reaction rate across the boundary layer and checked the derivative with respect to time to determine when run-away conditions take place. Thus:

$$\frac{d}{dt} \left[ \int RR \cdot dy \right] > A^* \quad ; \quad RR \sim Y_{Ox} \cdot Y_F \cdot e^{-E/RT}$$

$A^*$  is some arbitrary value. He also related the RR to the light emission from the boundary layer, as follows:

Considering the emission of light to be a quasi-equilibrium process.

$$\hat{I} \sim \int Y_{emittance, specie} \cdot e^{-\frac{h\nu}{kT}} \cdot dy \sim \int RR \cdot e^{-\frac{h\nu}{kT}} \cdot dy$$

$$I \sim \int RR' \cdot dy$$

where  $h$  and  $k$  are Planck's and Boltzmann's constants, and  $\nu$  is the frequency of the emitted light.

$$RR' \sim Y_{Ox} \cdot Y_F \cdot e^{-\left(\frac{EA + RT\nu}{RT}\right)}$$

is a reaction rate having a new activation energy. Thus his ignition criterion resembles the experimental one. He however used  $RR$  instead of  $RR'$  in his criterion taking activation energies of about 18 kcal/mole. Considering light emission in the near ultra-violet (3500Å), the corresponding activation energy of  $RR'$  is over 50 kcal/mole. Thus,  $RR'$  is far more sensitive to an increase in gas temperature (which indicates imminent ignition) than  $RR$ .

Kumar and Hermance [27] applied the light emission criterion more directly. They assumed that the concentration of the emitting species is proportional to the concentration of the product species and therefore expressed the light emission intensity as:

$$\hat{I} \sim \int Y_p \cdot e^{-\frac{h\nu}{kT}} \cdot dy$$

They defined the ignition delay as the time  $t^*$  required for  $\hat{I}$  to reach some value  $\hat{I}^*$ . They considered an emitting species in the near ultra violet, e.g., CN or OH which undergo thermal excitation.

In both aforementioned criteria there is some degree of arbitrariness in the chosen values of  $A^*$  or  $\hat{I}^*$ . Though the last criterion is the most related one to the experimental criterion, it is nevertheless deficient. In the lack of knowledge of the exact light emission process it is very difficult to establish the value of  $\hat{I}^*$ . Also, relating directly the emitted species concentration to that of the product is arbitrary. The emitted species if they are radicals like CN or OH are more likely to be found between the main reaction zone and the surface, unlike the products.

All of the above criteria are related to some state of gas phase distribution. Only the heat balance criterion (Eq. (37)) includes an interface process, i.e., heat flux from the gas to the solid phase.

In light of the inherent arbitrariness of most of the pure gas phase related ignition criteria, a new criterion is suggested here. It is based on the runaway conditions of heat flux at the interface, i.e., the propellant surface. Ignition is assumed to occur when:

$$\frac{d(HF)}{dt} = 0 \quad ; \quad \frac{d^2(HF)}{dt^2} > 0 \quad (38)$$

$$HF \triangleq (K \frac{\partial T}{\partial y})_w$$

It is also assumed that HF due to free stream conditions is either steady or decreasing. The rationale for the above criterion is as follows: In the absence of any heat generation in the gas phase, the heat flux to the solid surface decreases with time or stabilizes on some steady state value. During  $t_{\text{thermal}}$  the surface temperature  $T_w$  rises steadily. The heat transfer to the surface decreases, since it is proportional to the temperature difference  $T_e - T_0$ .  $T_w$  growth may cease when significant gasification ensues, a process which is enthohermic and exponentially dependent on  $T_w$ . The heat transfer is reduced further because of the blowing effect. Thus an accelerated heat transfer at the surface against an increasing blowing effect is a strong indication of run-away fuel vapor consuming exothermic reaction in the gas phase, i.e., ignition. Note that the heat transfer to the surface finally stabilizes on a value compatible with steady state burning. This criterion reveals the onset of ignition in its earliest stage and it is quite different from the heat balance criterion Eq. (37)). Physically, it is more sensible than the criterion of Ref. 37, since it reflects the run-away of the energy transfer at the solid-gas interface which must precede sustained burning.

### III-H Numerical Predictions of the Ignition Model for the Front Stagnation Flow Region

The calculations for the ignition model for the front stagnation flow region (Eqs. (24)-(30)) were carried out numerically on an HP 21-MXE computer. The numerical method used in this work is a generalized implicit scheme. A variable time step is used to account for the various time scales of the problem. The nonlinear terms in the equations are linearized around predicted values and for each time step; the solution is reiterated until the calculated values are sufficiently close to the predicted ones. The surface boundary conditions are strongly non-linear due to the exponential term of  $V_{\text{REG}}$ , in which the surface temperature  $T_w$  appears in the exponent. Therefore an estimated  $T_w$  is used as a boundary condition rather than the heat flux, thus rendering the boundary condition linear. The finite difference elements form a tridiagonal matrix which is solved using a computer routine developed by Ref. 120. The heat flux boundary condition which couples the solid phase to the gas phase is then checked and if not satisfied a new  $T_w$  is estimated. The solution is reiterated until that boundary condition is satisfied. Complete details of the numerical solution are given in Appendix II. The solution includes the boundary layer development and the transition from ignition to steady state burning. Solution accuracy was checked by varying the size of the time steps. Results of the pure gasification problem solution agreed very well with those found in the literature. The physical constants and the nominal free

stream conditions used are those specified in Table 3. The physical constants are typical to a double-based propellant like M26. The results of the calculations are summarized in Figs. 8-27.

Most commonly in the ignition literature, theoretical ignition data is merely given in terms of ignition delay time versus any variable parameter. It is one of the goals of the present theoretical work to predict the entire evolution of the convective ignition process from the onset of the flow until the establishment of a fully developed flame. Accordingly, one form of presentation of the calculated results (e.g., Fig. 8) shows the evolution of surface temperature and heat flux versus the non-dimensional time  $\tau$ . The presentation of surface temperature ( $T_w$ ) evolution with time is similar to the depiction given in Fig. 2. The choice of  $\tau$  instead of  $t$  is to emphasize the dependence of  $t_{\text{chemical}}$  on  $t_f$  (through the various Damkohler numbers) and also to render the figures more general. The logarithmic scale chosen for  $\tau$  compresses the long-time scale of the steady inert heating and yet enables a detailed look at the initial transient process of boundary layer development.

In all of the calculated cases, the initial temperature of the propellant was 27 C. The initial surface temperature jump is given by Eq. (32). During the boundary layer development time ( $\tau \sim 1$ ),  $T_w$  increases further only slightly as compared to that jump. The validity of Eq. (32) was checked by solving the equations of flow numerically: once with starting conditions for  $T_w$  and solid and gas phase temperature distribution which are based on Eq. (32), (see Appendix II), and once with  $T_w = T_s$ . In the last case, by using very fine time increments ( $\Delta\tau \sim 10^{-5}$ ),  $T_w$  and the corresponding temperature distributions approached the starting conditions of the first solution in about three time steps. Indeed, during the initial period of the boundary layer development the main mode of heat transfer is conduction. The role of that jump in shortening the ignition delay is apparent from the figures.

The presentation of the surface heat flux (HF) is given in order to demonstrate and justify the ignition criterion given by Eq. (38). In all cases investigated, the fulfillment of the ignition criterion indeed resulted in transition to a fully developed flame. When that transition period is characterized by large  $dHF/dt$ , the ignition process is considered to be "intense". Such an intense process may result in overshoots of  $T_w$  and HF as seen, for example, in Fig. 8. In practical applications such overshoots may be an important link in a transition to explosive burning.

Some of the time scales of the problem are manifested by the HF curves. The period of boundary layer development,  $\tau \sim 1$ , is characterized by high values of HF.  $t_{\text{thermal}}$  is the time when the HF curves start to diverge. The state of fully developed flame is obtained when  $T_w$  and HF reach some very slowly varying values. Typically, it is around  $\tau = 100$ . The solid phase at that time is still far from reaching its steady state values and full steady state conditions are obtained much later. However, the final values of  $T_w$ , HF, and the boundary layer profiles do not change appreciably from the values at  $\tau \sim 100$ .

The boundary layer profiles constitute the other form of results presentation (e.g., Fig. 9). The distribution of velocity, temperature, species concentration, and reaction rate (RR) in the boundary layer are given for  $\tau \sim 100$  which corresponds in most cases to the attainment of the

aforementioned quasi-steady conditions of  $T_w$  and HF. The RR defined in Fig. 9 is the original reaction rate term that would have appeared in the species equations for  $Y_{OX}$  and  $Y_F$ . Its magnitude reveals a great deal about the flame structure.

The product species concentration distribution  $Y_p$  is shown in order to give some indication about possible light emission intensity from the flame. If indeed the emitting species concentration is related to  $Y_p$  (as suggested by [62]), then the light emission is most intense if  $Y_p$  assumes large values at the higher temperature regions of the boundary layer.

$Y_p$  is given by:  $Y_p = 1 - Y_I - Y_F - Y_{OX}$ . Thus the inert species concentration,  $Y_I$ , has to be calculated. The equation for  $Y_I$  is similar to Eq. (25). i.e.:

$$-\frac{\partial Y_I}{\partial \tau} + \frac{\partial^2 Y_I}{\partial \eta^2} + F \cdot \frac{\partial Y_I}{\partial \eta} = \frac{t_z}{2} \cdot \left( \frac{1}{U_w} \cdot \frac{dU_w}{dt} - \frac{1}{A} \cdot \frac{dA}{dt} \right) \cdot \eta \cdot \frac{\partial Y_I}{\partial \eta} \quad (39)$$

The boundary conditions are:

$$\left. \begin{array}{l} \tau=0 \quad \eta>0 \\ \tau>0 \quad \eta=0 \end{array} \right\} Y_I = 1 - Y_{OXe} \quad (39a)$$

$$\tau>0 \quad \eta=0 \left\} \left( \frac{\partial Y_I}{\partial \eta} \right)_w + F_w Y_{Iw} = 0$$

Note that Eq. (39) is not coupled directly to Eqs. (24)-(29).

The value of  $Y_p$  also gives an indication about the validity of the numerical solution. If  $Y_p < 0$ , the solution is certainly erroneous.

Note that the dimensional coordinate  $y$  is used rather than  $n$ . This way a better physical interpretation is obtained from the boundary layer structure and its swelled thickness due to heat release is demonstrated.

#### (i) The Effects of Various Thermal, Chemical and Flow Properties

The following subsections discuss and interpret the calculated results which are depicted in Figs. 8-27. Whenever not specified the nominal values of Table 3 apply.

Free stream oxidizer effects are best demonstrated in Fig. 8. Ignition delay is greatly shortened when a large amount of free stream oxidizer is present. The intensity of the ignition process (i.e.,  $dHF/d\tau$ ) is also dependent on the value of  $Y_F$  at the time of ignition ( $Y_{F,ign}$ ). In the case of  $Y_{OXe} = 0$ ,  $Y_{F,ign}$  is certainly the largest and consequently the ignition process is rather intense. Note the overshoots in HF for  $Y_{OXe} = 0.5$  and in  $T_w$  for  $Y_{OXe} = 0$ . They are both associated with the intensity of the ignition.

The amount of gas phase heat release  $Q_R$  is of paramount importance for the ignition process and the final flame structure. Note that the  $Q_R$  used is the heat of combustion, and not the heat of explosion, since it is the heat of combustion which is used in the equations. Typically, the propellants used are fuel rich and their oxygen balance is around -30%.

Consequently, their heat of explosion is lower by about 500 cal/gm<sub>propellant</sub> than  $Q_R$ .

Fig. 14 demonstrates dramatically how the ignition process is dependent on  $Q_R$ . Note that no ignition is obtained for  $Q_R = 1500$  cal/gm, and the ignition intensity for  $Q_R = 1750$  cal/gm is rather weak as compared to  $Q_R = 2000$  cal/gm (the nominal conditions). The flame structure for the last two cases is investigated in Fig. 9. Note the existence of two distinct flame zones. The stronger one is the closer to the surface and it is a premixed flame which is nourished by the propellant premixed vapors. The second zone is further away from the surface and it is a diffusion flame type. It exists only for a case of fuel rich propellant when free stream oxidizer is present. Note the higher temperature and the more intense premixed flame zone for the larger  $Q_R$ . Note also the larger boundary layer thickness and the longer distance of the diffusion flame zone for the larger  $Q_R$ . An important observation is that the temperature profile on the free stream side of the premixed flame zone of the larger  $Q_R$  is rather flat. Thus the second flame has little role in sustaining the steady state burning, and heat transfer to the surface is clearly dependent only on the premixed flame adjacent to the surface.

The attainment of ignition and its intensity are, however, clearly dependent on  $Y_{O_{2E}}$ . It serves as a pilot to the flame. In Fig. 10, four stages in the period between the onset of ignition (A) and the establishment of steady state flame (D) are depicted in terms of boundary layer profile distributions. Note the thickening of the boundary layer and the gradual formation of the two separate flame zones.

Since the order of reaction is taken as  $n = 2$ , a fuel balanced propellant corresponds to  $\alpha = 0.334$ , the nominal value of  $\alpha = 0.5$  corresponds to a fuel rich propellant. The ignition trends of these two cases are depicted in Fig. 11. In the case  $Y_{O_{2E}} = 0.5$ , the fuel rich propellant ignites first. In the case  $Y_{O_{2E}} = 0$ , the ignition time of both propellants is about the same; however, ignition intensity is stronger for the fuel balanced propellant. Due to the more complete combustion at the premixed flame zone, the burning of the fuel balanced propellant occurs at elevated  $T_w$ . The corresponding boundary layer profiles for Fig. 11 cases are given in Fig. 12. Note the absence of the secondary flame zone in sub-figures A, C, D.

The effect of gas phase activation energy  $E_R$  is shown in Fig. 13. The ignition process is very strongly dependent on  $E_R$ . It is shorter, more intense, and stabilizes on higher  $T_w$  for a smaller  $E_R$ . The boundary layer profiles reflect that trend. Compare Fig. 20 with Fig. 12-A (which is for the nominal  $E_R = 14$  kcal/mole).

The higher velocity situation, i.e.,  $U_E = 50$  m/s, is investigated in Fig. 15 and Fig. 17. In this case, the Damkohler numbers are 5 times smaller than the nominal ones (i.e.,  $U_E = 10$  m/s). Ignition is even more sensitive to the presence of  $Y_{O_{2E}}$ . Note the higher convective heat flux associated with the higher velocity. The boundary layer is much thinner (Fig. 17). In subfigures 17-A-B the flame (at  $\tau \sim 100$ ) is not fully developed. Even for the fully developed flame of 17-C the two flame zones are less distinguishable, as compared to the lower  $U_E$  case.

The role of  $\epsilon$  is investigated in Fig. 16. The solid line represents

the nominal value.  $\epsilon^{1/2}$  is used instead of  $\epsilon$  because it is the term  $\epsilon^{1/2}$  that appears in the equations. The first effect is on the magnitude of the initial surface temperature jump (Eq. (32)). In addition, the solid phase temperature rises slower for larger  $\epsilon$  (see discussion in III-F); consequently, the effect on the ignition delay is immense.

The effects of varying the free stream conditions of pressure ( $P_E$ ) and temperature ( $T_E$ ) are investigated in figures 18,19,21,22. In the case of an increased  $P_E$  (while keeping  $T_E$  the same), the density is increased and accordingly the value of  $\epsilon$  is decreased. The effects are similar to those described before (Fig. 16). In addition, increased density means larger Damkohler numbers and, therefore, shorter ignition delays. Thus, the effects are both thermal and chemical. Note that the  $T_w$  stabilizes on higher values as  $P_E$  is increased, a fact well known from experimental work. Increasing  $T_E$  (while keeping  $P_E$  the same) does not change the value of  $\epsilon$ , (since  $P_E \cdot \mu_E \propto f(T_E)$ ). However, the initial surface temperature jump is increased (Eq. (32)). Due to the higher temperature the heat transfer and the reaction rate are increased and the ignition delay is substantially shortened. However, when flame is established the heat transfer to the surface is, as already discussed, much less affected by the free stream value of  $T_E$ , and therefore unlike the case of elevated  $P_E$ , the elevated  $T_E$  does not result in noticeable elevated steady state  $T_w$ .

The competition between the thermal and chemical processes is most evident when the free stream velocity  $U_E$  is increased. On one hand the heat transfer rate is increased, but on the other hand the Damkohler numbers  $D_G$  and  $D_S$  are decreased. A compilation of ignition delays for a wide range of  $U_E$  is given in Fig. 23, versus the Reynolds number of the flow. The ignition delay does not change appreciably after  $Re = 10,000$  and in the case of  $Y_{O_{XE}} = 0$  it starts to increase at that point. The declining of  $D_G$  with  $Re$  is a key factor in that behavior.

Note that for the conditions of Fig. 23, the  $Re$  can be expressed as:  $Re = C/D_G$ , where  $C$  is some constant.

Note also that for low  $Re$  the curve of  $Y_{O_{XE}} = 0.1$  is close to the curve of  $Y_{O_{XE}} = 0.5$ , however for higher  $Re$  it starts to approach the  $Y_{O_{XE}} = 0$  curve. This phenomenon is more enhanced in Fig. 24 where  $T_w$  at the time of ignition is plotted versus  $Re$ . Fig. 24 demonstrates the fact that for gas phase ignition there is not one unique ignition surface temperature. As  $D_G$  and  $D_S$  decline with  $Re$ , larger  $Y_{O_{XE}}$  is required to affect ignition appreciably.

The curves in Figs. 23 and 24 are slightly wiggled due to the fact that the ignition criterion used (Eq. (38)) does not define the ignition time very sharply when the ignition intensity is weak.

#### (ii) The Effect of Flow Transient Conditions on the Ignition Process

Two types of transient conditions were investigated. The first one deals with a case when an abnormal initial surface temperature jump occurs, more than what would have been expected from Eq. (32). Such conditions are typical to the experimental apparatus used in the present research. The conditions are discussed in detail in Sections IV and V. The second type of transient conditions deals with non-steadiness of free stream pressure, temperature, and velocity. The abnormal surface temperature jump is

discussed first.

In some cases of the starting process, the flow is very agitated. A rapid succession of wave motions reverberating precedes the establishment of a forward flow about the cylinder (the experimental case). During that period  $T_w$  rises abnormally high and some temperature distribution in the solid phase is established. As the wave motion relaxes the flow develops normally as in the common case. For the numerical solution, a large initial surface temperature jump was assumed which is compatible with the present experimental values. Unlike the experimental results, the time is counted from the time of the initial transient relaxation. An initial solid phase temperature distribution compatible with the length of the initial transient period ( $\tau_p$ ) is assumed. Though oversimplified, the initial conditions are devised to simulate the present experimental conditions.

The starting conditions are in accordance with Eq. (II-4), (Appendix II):

$$\left. \begin{array}{l} \tau=0 \\ \tau_s \geq 0 \end{array} \right\} \tau_{ef} \cdot \theta_{so} = \left[ (T_w - T_0) \cdot \left( \frac{\sqrt{\tau_s}}{2 \cdot \sqrt{\tau_p}} + 1 \right) \right] \cdot e^{-\sqrt{\tau_s} \cdot \frac{1}{\sqrt{\tau_p}} \cdot \tau_s} + T_0$$

$$T_w = 600 K, \tau_p = 3$$

The parameters used are the nominal ones expressed in Table 3.

The effects of varying subsurface heat release,  $Q_s$ , are examined in Fig. 25. Since the initial solid phase temperature is sufficiently high, an appreciable subsurface heat release ensues and  $T_w$  rises further. Since  $\tau_p$  is very short, the thermal wave associated with it is very narrow and dissipates rapidly into the solid phase depth. As the boundary layer develops, the heat flux to the surface declines very fast and is unable to sustain the high  $T_w$ . Thus rapid cooling of the solid phase proceeds. Due to the very high activation energy of the subsurface chemical reaction, the reaction stops as  $T_w$  declines. At some time  $T_w$  will start rising again, due to the steady convective heat transfer, finally leading to a state of ignition. As  $T_w$  gets sufficiently high, an appreciable sub-surface heat release ensues again. Since the sub-surface reaction zone is very thin (Eq. (36)), the residence time of a solid particle there is very small and consequently only a small temperature change occurs across the reaction zone ( $\sim \tau \cdot T_w / E_s$ ). Thus, for the conditions calculated, the amount of  $Q_s$  is of minor importance for the ignition process, as it is evident from Fig. 25. It affects, though, the final  $T_w$  obtained for the steady state conditions. Relatively, it has a more pronounced role when  $P_E$  is lower, since then the heat transfer from the gas phase is greatly reduced.

The effects of the amount of  $Y_{O_{2E}}$  on the ignition process for the conditions discussed are investigated in Fig. 26. The effects are very dramatic. Indeed, in the case of  $Y_{O_{2E}} = 0.5$ , ignition occurs very early in the stage of boundary layer development. As  $T_w$  drops and the boundary layer develops, HF drops also but to a level only slightly lower than the steady state burning value. The case of  $Y_{O_{2E}} = 0.1$  exhibits a very short period of early ignition, followed by extinction, and then reignition much later. The overall conclusion is that for the special case of very strong initial transients which result in an abnormal initial  $T_w$  jump, the amount of  $Y_{O_{2E}}$  is of critical importance for the ignition process. If it is sufficiently high, ignition delay may be shortened by an order of magnitude.

The second type of transient conditions that deals with  $P_E$ ,  $T_E$  and  $U_E$  unsteadiness was discussed briefly in III-E - Eq. (33). The investigation is aimed at determining how  $t_{\text{thermal}}$  is affected when  $P_E$ ,  $U_E$ , and  $T_E$  do not assume their full values instantly at  $t = 0^+$ , but rather rise at a finite rate to their final values. The question is under what conditions the instantaneous heat transfer,  $HF$ , is different from its corresponding quasi-steady values. When  $HF$  behaves quasi-steadily, the effect on  $t_{\text{thermal}}$  is rather obvious. Before continuing it is worthwhile to mention some work in this field.

The first two efforts are theoretical and considered free stream velocity unsteadiness only. Yang and Huang [84] analyzed the compressible laminar boundary layer over an insulated or isothermal flat plate moving with an arbitrary time-variant velocity. They recognized that a deviation from quasi-steady conditions occurs when  $u/du/dt \ll 1$ . They found different trends depending on whether the flow had constant acceleration or positive acceleration. Tokuda and Yang [81] analyzed the unsteady, incompressible laminar forced convection around the front stagnation point of a cylinder in arbitrary, time-variant velocity. They found that positive acceleration results in higher wall shear stress, a lower heat transfer rate for a specified wall temperature, and higher wall temperature for a specified wall heat flux, than the corresponding quasi-steady values. Their results were quite similar in trends to Ref. 84.

Other experimental and theoretical efforts consider mainly pressure unsteadiness. Nikanjam and Greif [85], studied the unsteady heat transfer from a nonreacting gas to the end wall of a channel during a piston compression of a single stroke. Besides their experimental work they carried out a simple solution of the boundary layer adjacent to the wall, assuming that the gas outside the boundary layer is compressed isentropically. Thus, they used the isentropic relations between pressure and temperature for the boundary layer edge. Goluba and Borman [86] studied the heat fluxes at the end-wall of a tube in which shock-fronted, longitudinal pressure waves were generated. Their theoretical aspect of the work dealt with boundary layer equations identical to Ref. 85. They found a very large instantaneous heat flux which increased with increasing the pressure ratio across the waves. It was proportional to the square root of the product of the wave frequency and the time-averaged pressure of the oscillations. They found also that the compression of the boundary layer by the shock front caused the gas temperature to have a maximum value within the boundary layer.

The unsteady conditions that were applied to the numerical solution are in a way a compilation of the conditions studied in the aforementioned works. Both the pressure and the velocity unsteadinesses were considered in a way which combined positive and negative acceleration. The free stream temperature was considered to be dependent isentropically on the pressure. The conditions investigated are basically approximations to step functions of pressure and velocity with varying steepnesses. They are as follows:

$$\begin{array}{ll} & P_E = P_0 \\ t=0 & T_E = T_0 \\ & U_E = U_0 \end{array} \quad (40a)$$

$$\begin{aligned} 0^+ \leq t < t_{\text{ref}} \quad & P_E = P_{E1} \\ & T_E = T_{E1} = T_{Ef} \cdot (P_{E1}/P_{Ef})^{\frac{\gamma-1}{\gamma}} \\ & U_E = U_{E1} \end{aligned} \quad (40b)$$

$$\begin{aligned} t_{\text{ref}} \leq t < \infty \quad & P_E = (P_{E1} - P_{Ef}) \cdot [a_1 \cdot (t - t_{\text{ref}}) + 1] \cdot e^{-a_1 \cdot (t - t_{\text{ref}})} + P_{Ef} \\ & T_E = T_{E1} \cdot (P_{E1}/P_{Ef})^{\frac{\gamma-1}{\gamma}} \\ & U_E = (U_{E1} - U_{Ef}) \cdot [a_1 \cdot (t - t_{\text{ref}}) + 1] \cdot e^{-a_1 \cdot (t - t_{\text{ref}})} + U_{Ef} \end{aligned} \quad (40c)$$

$$\begin{aligned} t \rightarrow \infty \quad & P_E = P_{Ef} \\ & T_E = T_{Ef} \\ & U_E = U_{Ef} \end{aligned} \quad (40d)$$

In the equations above the steepness of the applied  $P_E$  and  $U_E$  profiles is controlled by the parameter  $a_1$ .

In Fig. 27 only the pressure,  $P_E$  (and accordingly  $T_E$ ), is varied. Also:  $u_{E1} = u_{Ef} = 10$  m/s,  $t_{\text{ref}}/t_{ff} = 1$ , where  $t_{ff}$  is  $t_f$  which corresponds to  $u_{Ef}$ . The parameter  $a_t$  is defined as:  $a_t = a_1 \cdot t_f$ . As evident from Fig. 27, the pressure steps were applied at the final stage of the boundary layer development period ( $\tau \sim 1$ ), and for durations less than that period. This is in accordance with Eq. (33). It is apparent that the instantaneous heat flux associated with the strong impulses ( $a_t = 5$ ,  $a_t = 50$ ), exceed by a significant amount the corresponding quasi-steady values. Indeed for  $a_t = 50$  the jump in  $T_w$  approached a value which corresponds to Eq. (32) (if it were used). Thus, the maximum obtainable surface temperature growth corresponds to applying the maximum ambient flow conditions at the time  $t = 0^+$ .

The boundary layer recovers from the onset of the ambient pressure in a time on the order of  $t_f$ .

It is also evident from Fig. 27 that when  $P_E$  is applied on a time scale which is greater than  $t_f$ , the enormous shortening in  $t_{\text{thermal}}$  (due to the temperature jump) is lost.

Velocity impulses were also applied in a manner similar to the pressure impulses. The effects were found to be small compared with the pressure impulse effects, and therefore they are not shown in a figure.

The effects are as follows: a) for strong impulses ( $a_t > 10$ ), heat fluxes lower than the corresponding quasi-steady values occur; this trend is in accordance with Ref. 81, and b) for weak impulses, the heat flux corresponds to the quasi-steady values; and since the instantaneous  $t_f$  rises slower,  $t_{\text{thermal}}$  is increased.

When both  $P_E$  and  $U_E$  were changed simultaneously in the range:  $P_{E1} - P_{Ef} = 0.86 - 1.72$  MPa, and  $U_{E1} - U_{Ef} = 5 - 10$  m/s, the results were very similar to Fig. 27.

Indeed in the boundary layer equations (24)-(30), the terms corresponding to positive  $U_E$  growth have opposite signs to the time derivative terms. Thus, accelerating velocity may have cooling effects. The corresponding pressure terms have the same signs as the time derivative terms. In addition, most of the pressure and velocity non-steady terms are multiplied by  $\eta \cdot \frac{\partial}{\partial \eta}$  terms. Such terms assume the value zero, at both the wall and the edge of the boundary layer, and thus do not have a strong effect on heat transfer; however, the middle section of the boundary layer profiles are distorted during the onset of ambient conditions impulses. Indeed, local temperature peaks were found to occur in the boundary layer during the onset of steep pressure rise. This is in accordance with Ref. 86. A large non-steady pressure term which is not multiplied by  $\eta \cdot \frac{\partial}{\partial \eta}$  appears in the energy related equations (26),(27). That term is the one most responsible for the high instantaneous heat flux during a steep pressure rise.

The numerical scheme used is capable of handling the effects of non-steadiness during  $t_{\text{chemical}}$  as well, however the author found it to be beyond the scope of the present work. Not all of the parameters appearing in equations (24)-(30) were investigated numerically. The author chose to investigate those parameters whose effects are more difficult to predict.

### III-I Ignition Mechanism in Regions Beyond the Front Stagnation Region

#### (i) Front Surface Ignition

As the flow leaves the front stagnation region, the rate of external flow velocity acceleration  $\partial u_e / \partial x$  decreases, and the boundary layer thickens until separation of flow occurs at around 90 degrees where  $(\partial u / \partial y)_w = 0$ . The flow in the boundary layer is described by equations (11)-(13) which are three-dimensional in  $s, \eta$  and  $\tau$ , and therefore are an order of magnitude more difficult to solve than the front stagnation region equations. Such solutions are beyond the scope of the present work. Nevertheless, the likelihood of any portion of the front surface of the cylinder to ignite before the stagnation region seems to be remote. Indeed, the experimental results given in Section V support this hypothesis. It can also be reasoned from Eqs. (11)-(13) and from the empirical knowledge of the surface temperature ( $T_w$ ) distribution around cylinders under cross flow conditions.

The trend (see discussion in III-C, and experimental results - Section V) is for  $T_w$  to fall quite sharply from its value at the front stagnation zone to a value much lower at the separation zone (90 degrees). Since the dependence of the propellant evaporation on  $T_w$  is strongly exponential (Eq. (15)), little evaporation occurs beyond the stagnation zone. Indeed, the fuel vapors originated at the stagnation zone are much diluted by external mass flux into the thickening boundary layer. Therefore, the chemical reaction rate there is too slow to result in ignition and serves only to further dilute the mixture. The main reaction zone is shifted away from the surface and less of the heat generated is fed to the surface.

From previous discussion and from Eq. (30), the value of  $F_w$  increases sharply with  $s$  and consequently the terms  $F/s$  in equations (11)-(13) are positive. Also:  $\partial F / \partial \eta > 0$ ,  $\partial Y_1 / \partial s < 0$ ,  $\partial \theta / \partial s < 0$ ,  $\partial \theta / \partial \eta > 0$ . The distance coordinate,  $s$ , appears explicitly in the right-hand side terms of equations (11)-(13). The equations which contain the chemical reaction

rate terms (RR) are (12) and (13). Regarding steady free stream conditions, the right-hand side terms which are left are:  $t_f \cdot RR$ , and  $2 \cdot s \cdot (\dots)$ . In gas phase ignition situation, if  $2 \cdot s$  is sufficiently large, the second term may lead to ignition if it has the same sign as  $\partial \theta / \partial x$ . Such is the situation in flat plate ignition [78]. Indeed, in Eq. (13) that term supports ignition. However, the main ignition supporting term,  $t_f \cdot RR$ , is very rapidly decreasing with  $s$ , since  $RR$  is strongly dependent on  $\theta$  and  $Y_i$  and both are decreasing with  $s$ . The residence time  $t_f$  given by Eq. (9) and calculated for the external velocity given by Eq. (31) is increased by a factor of 2 when moving from the front stagnation point to the 90 degree point. That increase is far from compensating for the decrease in  $RR$ .

Though a complete numerical solution is required to find the ignition trends over the entire front surface of a cylinder, it may be concluded from the foregoing discussion, that in the front surface region, ignition is more likely to occur first at the front stagnation zone. The entire front surface is ignited by means of flame spreading from the stagnation zone.

#### (ii) Rear Surface Ignition (Regions 2 and 3 - Fig. 7)

Under steady conditions, the fluid in the wake flows from the rear stagnation point to the separation points with periodic fluctuation. The frequency of the fluctuation is equal that of the vortex shedding in the wake, i.e.,  $0.2 \cdot U_\infty / D = 0.05 / t_f$ . The circulation velocity  $U_{wk}$  depends on the  $Re$  number and it is in the range  $0.5 \cdot U_\infty$  [60]. Since the Navier Stokes equations of flow cannot be simplified for regions (2) and (3), any attempt to predict ignition in these regions will be phenomenological in essence, taking into account the general features of flow there (which are observed experimentally).

#### Rear body ignition - region (3)

The basic principles of the heat transfer mechanism to the rear surface were discussed in III-C, (particularly, the work of Refs. 58 and 59). The same rationale may be extended to the treatment of the ignition mechanism of propellant in this region.

The basic mechanism is that of renewed wake vortex flow in a frequency  $f = 0.05 / t_f$  (the vortex shedding frequency). Every time a new vortex is established, the rear portion of the cylinder is suddenly exposed to a flow of velocity  $U_{wk}$ , temperature  $T$ , and oxidizer content  $Y_{Ox, wk}$ . The surface temperature of the propellant  $T_w$  rises with time as every cycle contributes heat flux to the surface. Though that mechanism is oversimplified, it nevertheless explains the observed trends and magnitudes of heat transfer to cylinders under established steady flow conditions. Experiments with shock-induced flow around cylinders [87] revealed that the vortex shedding phenomenon starts from the very early stages of the flow, though it does not become regular before  $t \sim 30 t_f$ . A similar situation is encountered also in the present research. Thus, short ignition delays occur within the development period of the regular wake flow. Therefore, the phenomenon of cyclic renewal of flow in the wake is of considerable importance even for cases of short ignition delays ( $t_{ign} < 30 t_f$ ).

During each cycle the flow around the rear stagnation point can be described similarly to the front stagnation point equation starting every time from a new higher solid phase temperature. The significance of the

transient time of the boundary layer development on the rear surface depends on the ratio of the wake flow residence time  $t_{WK} = R/2U_{WK}$  to the cycle time:  $T \sim 10 \cdot R/U_{\infty}$ . If  $t_{WK}/T \sim U/20U_{WK} > 0.5$ , the flow is mainly transient. Heat flux during the transient time is higher than during the steady state. Since the above ratio is normally around 0.1, the transient features of ignition must not be overlooked and the rear stagnation boundary layer equations should not be considered quasi-steady, even in a case of ignition times much longer than  $t_{WK}$ .

Note that similar to the Damkohler numbers  $D_G$  and  $D_S$ , wake Damkohler numbers  $D_{G,WK}$  and  $D_{S,WK}$  may be defined for the rear surface, such that:

$D_{G,WK} = D_G \cdot t_{WK}/t_f$        $D_{S,WK} = D_S \cdot t_{WK}/t_f$   
Since  $t_{WK} > t_f$  ignition may be preferred at the rear stagnation point, provided that the surface temperature there is sufficiently high. The rear stagnation surface temperature generally lags only slightly behind the front stagnation surface temperature. Such is the case for the present experimental flow range. Though the surface decomposition rate is very sensitive even to small temperature differences, the sudden proximity of the gas phase reaction zone to the surface at the outset of any new cycle and the considerably larger rear surface Damkohler numbers are very important factors in rendering the rear stagnation point likelihood for first ignition.

The possibility of favoured ignition sites on the rear surface between the rear stagnation zone and the separation point is ruled out because of similar reasons as the front surface situation discussed before.

All of the aforementioned is valid for the assumption that the rear surface boundary layer is laminar in nature. The results of the current work and other works discussed in III-C conform to that assumption. The flow in the far wake is, however, turbulent. Some degree of turbulence is probably inherent even to near wake flow, i.e., close to the rear surface. It may promote ignition by momentarily pushing the reaction zone closer to the surface.

Another factor in promoting ignition at the rear surface is that the wake behind the cylinder is an effective reactant accumulator. As a first approximation, the wake can be viewed as a well-stirred reactor into which the solid phase decomposition products (from the cylinder front and rear) pour. That refers mostly to the turbulent far wake. Realizing that the wake is not a sharply defined region, one can still write a conceptually useful species balance for the accumulation of these products in the wake:

$$\rho_{WK} \cdot Vol_{WK} \cdot \frac{dY_{DP,WK}}{dt} = M_{BL} \cdot Y_{DP,BL} - M_{WK} \cdot Y_{DP,WK} - \rho_{WK}^2 \cdot Y_{DP,WK} \cdot A_R \cdot e^{-E_R/R \cdot T_{WK}}$$

This states that the rate of increase of the mass fraction of the decomposition products in the wake is equal to their flow rate through the boundary layer, minus their rate of outflow with the gas leaving the wake, and minus their rate of consumption.

Referring to Fig. 1, it should be emphasized that the important reactions for ignition leading to self-sustained burning are the fizz zone reactions, which occur inside the boundary layer in close proximity to the surface. If they do not runaway, ignition will not occur. The flame zone reactions in the case of the wake also may be important since they release a

large amount of energy and may raise the average wake temperature above  $T$ , thus, promoting ignition due to higher average boundary layer temperature profile.

The trouble with the above species balance in the wake is that it is very difficult even to approximate the magnitudes of the terms appearing there. Resorting again to the rough approximation of cyclic renewal of flow in the wake, it is assumed that reactant accumulation occurs only during a cycle period and starts over with each new cycle. From the front stagnation flow calculation it was found that on the average only 50% of the decomposition products are consumed while in the boundary layer. Assuming that all the boundary layer unburnt reactants pour into the wake, and that they originate from the front stagnation zone subtending roughly  $1/3$  of the cylinder perimeter, the inflow of reactants into the wake is:

$$M_{BL} \sim \frac{1}{2} \cdot S_S \cdot V_{REG} \cdot \frac{D\pi}{3} \sim \frac{D \cdot S_S \cdot V_{REG}}{2}$$

Assuming that the wake size is  $Vol_{WK} \sim D^2$  and the accumulation period is  $\hat{T} \sim 5 \cdot D/U_\infty$ , during most of the which the chemical reaction rate is negligible, then:

$$Y_{DP,WK} \sim \frac{D \cdot S_S \cdot V_{REG} \cdot \hat{T}}{2 \cdot D^2 \cdot S_{WK}} \sim \frac{2.5 \cdot S_S \cdot V_{REG}}{S_{WK} \cdot U_\infty}$$

In the expression above  $V_{REG}$  corresponds to the front stagnation zone surface temperature. From the numerical solution in that region the value of  $V_{REG}$  at the time of ignition is in the range 0.1 - 0.3 cm/s. Assuming  $S_{WK} \sim S_e$ , and substituting the nominal values of Table 3 in the above expression, a value of about 0.01 is obtained for  $Y_{F,WK}$ . This value is too low to result in a bulk ignition situation in the wake. However, it can promote ignition in the rear surface boundary layer, where it is superimposed on the local decomposition products concentration, and the heat liberated is directly fed to the surface.

Assuming that  $V_{REG}$  is proportional at most to  $U_\infty^{1/2}$  (which is proportional to the heating rate), the expression above predicts inverse dependence of  $Y_{F,WK}$  on  $U_\infty^{1/2}$ ; thus, as the free stream velocity increases the role of reactants accumulation in the wake is diminished. The above expression is an upper approximation for a stirred reactor situation. In reality, reactants originating from the front boundary layer may enter the wake region in a more concentrated manner on loop stream lines similar to the ones shown in Fig. 7 and the local  $Y_{F,WK}$  may be appreciably larger.

The foregoing discussion predicts and explains situations and mechanisms for which ignition may occur at the wake, preferably at the rear stagnation point region, even if it does not occur at all on the front surface. The situation is too complex to predict ignition delay magnitudes in the wake and, therefore, the flow conditions for which ignition occurs first at the wake are a matter for experimentation.

#### Separation region ignition - region (2)

Though it is difficult to assign any length scales to this region, it will be referred to as the region confined between the separation line and the propellant wall in close proximity to the separation point which is around 90 degrees (see Fig. 7). It is assumed that the residence time of any fluid particle in this region is much longer than  $t_f$  or  $t_{WK}$ . Since the

gas temperature on the separation line is that of the bottom portion of the separated boundary layer (which is close to  $T_{W,SP}$ ), it is assumed that the gas temperature in this region is about  $T_{W,SP}$ . Species concentrations in this region are accumulated by diffusion and convection to values which are close to the highest corresponding values on the boundaries. Thus,  $Y_{F,SP}$  = the highest of  $Y_{F,BL}$  or  $Y_{F,WK}$  (generally  $Y_{F,BL}$ ). The same applies to  $Y_{OX,SP}$ . Experimentally, it has been found that  $T_{W,SP}$  is the slowest growing surface temperature. Ignition may occur when the rate of temperature growth in the gaseous phase due to chemical reaction between the fuel and oxidizer is much larger than the rate of temperature growth of the propellant surface. It is very difficult to approximate the values of  $Y_{F,SP}$  and  $Y_{OX,SP}$  because the flow around the separation zone is not well defined. The lowest approximation to those values are  $Y_{OX,SP}$  and  $Y_{F,SP}$  calculated for the wake as a stirred reactor. Ignition may be favored in this region because of the absence of convective flow to sweep the reacting species off the surface, or in other words, very long residence times (dead air situation). Postponement of ignition is due to the slow growth of  $T_{W,SP}$ .

As for the rear surface ignition, there is no way to predict relative ignition delay magnitude for that region except by solving the Navier Stokes equations for the entire cylinder surface, or by resorting to extensive experimentation.

### III-J Summary

The numerous studies regarding flow around circular cylinders indicate the existence of a very complex flow at their wake. Therefore, only the front surface of the cylinder is amenable to strict analytical treatment of the boundary layer type. The non-steady reactive boundary layers for the general case of free stream non-steadiness were developed in transformed coordinates and coupled by proper boundary conditions to the solid phase equations. The resultant set of 3-D partial differential equations was too complex to be treated numerically for the entire front surface. Thus the equations were modified for the front stagnation region and were reduced to 2-D (time and distance perpendicular to the surface-coordinates). Nevertheless, all major parameters of importance to convective flow, i.e., Damkohler numbers and thermal and chemical properties, were identified in the equations and free stream non-steadiness was included.

An ignition criterion was defined and the equations were solved numerically for a range of values of the key parameters in their general non-steady form.

The effect of the free stream oxidizer was investigated and found to be very prominent in promoting ignition. The effect of the oxidizer also leads to the formation of distinct pre-mixed and diffusion flame zones as the steady state burning situation is approached.

The importance of the thermal and chemical properties was demonstrated and the roles of the Damkohler numbers were interpreted. Initial flow transients as well as general free stream non-steadiness were investigated and the pressure non-steadiness was found to be the most important.

Based on known trends of cylinder surface temperature distribution, three separate zones of the cylinder perimeter were distinguished as possible candidates for first ignition sites, i.e., front stagnation zone,

rear stagnation zone, and separation point zone. Similarity was drawn between the front and the rear stagnation flows. The ignition mechanisms in the separation zone and rear stagnation zone were discussed phenomenologically.

It is concluded that failure of ignition in the front stagnation zone does not necessarily lead to a total failure of ignition. Longer residence time at the rear surface of the cylinder, and the accumulation there of reactants, initially originated from the front surface, are the major factors rendering the rear half favorable for ignition. However, one must resort to experimentation in order to determine the magnitudes and trends of ignition delays in that zone.

## SECTION IV

### EXPERIMENTAL APPARATUS

#### IV-A. Introduction

For the purpose of attaining prompt ignition of solid propellants by means of convective flow, one needs a source capable of discharging hot gases at a high rate of mass flow. In practical situations, an igniter which may be a solid propellant is used. The composition of the gaseous products of a practical igniter is very complex and it is difficult to control the flow properties of its gases (i.e., velocity, pressure, temperature). Therefore, in laboratory experiments which are being used to clarify the complex dependence of convective ignition on gas composition and flow parameters, it is not desirable to use an igniter. The ideal ignition source is one whose composition and physical quantities are known and whose flow parameters can be varied over a wide range. A shock tunnel is a laboratory apparatus meeting these requirements, provided that the ignition phenomenon can occur within the short available test time. Indeed, the objective of the present research is the elucidation of the ignition phenomenon for the conditions of high heat flux when ignition delay is measured in milliseconds. Since a shock tunnel apparatus can provide these conditions, it is used in the present research.

The onset of ignition was determined by detecting light emission from the propellant surface. The experimental ignition criterion differs somewhat from the theoretical one. The relations between the two criteria were discussed in the previous section and it was concluded that the differences in the trend of ignition phenomena should be small.

The present research deals with the ignition of cylindrical propellants under cross flow conditions. The phenomenological aspects of flow around cylinders and the intrinsic dependence of the ignition and flame spread trends on the flow structure are discussed in length in the previous section. In that respect direct visualization of the ignition events and flow structure is very desirable. Therefore, the test section is configured to enable good access for schlieren and shadowgraph high speed photography. Indeed, the extensive use of shadowgraph high-speed-motion, color photography in this research resulted in much better understanding of ignition mechanisms of granular propellants.

Measurements of heat transfer to the propellant specimen are very desirable since they reveal unsteady characteristics of the flow which can not be inferred otherwise, especially during the initial flow transients. Since it is impractical to measure directly heat transfer rates to the propellant surface, a specially instrumented cylinder was developed for that purpose. It also contained a miniaturized pressure transducer. Operating on the principle of thin film gauge, it measured surface temperature and heat flux under actual shock tunnel conditions.

Practical nitrocellulose based propellants were used in most of the test series. Thus, the data obtained are of direct practical relevance.

The effects of free stream oxidizers on ignition of composite propellants are well known [17-19]. They are less known for nitrocellulose

based propellants. Practical igniter gases always contain oxidizers. Also, unburnt oxidizer-containing propellant gases have an important role in packed bed ignition situations (toward which this research is oriented). Therefore, the test gases for this research were composed of  $O_2/N_2$  mixtures. Though most of the oxidizer species of nitrocellulose-based propellants are of the  $NO_x$  type, nevertheless the formation of  $O_2$  and  $O$  is a necessary link in all oxidation processes and they are always present in practical systems. The sensitivity of ignition trends to the presence of  $O_2$  may serve as a common basis for comparison of the ignitability of various propellants as well as pure polymers. Key steps of gas phase reactions of burning propellants may be inferred from the ignition sensitivity to the presence of  $O_2$ .

#### IV-B. General Features of Shock Tunnel Operation

The shock tunnel is a device which generates high pressure and temperature gas flow for very short periods of time. Its principal use is in the scientific research fields of gas dynamics, physics, and chemical kinetics. Though employed first at the end of the last century, the peak period of its development and extensive use extended from the late 1940's until the late 1960's. Reviews of its design, development, and performance were widely published. Therefore, the main features of its operation will be discussed here very concisely.

A basic schematic diagram of a shock tunnel construction and operation is given in Fig. 28. Basically it is a long pipe, divided by a diaphragm into two sections which contain different gases with different pressures. The higher pressure section is called the driver. The lower pressure section is called the driven section and it contains the test gas. For best performance, a low molecular weight gas is chosen for the driver, most commonly helium (due to its inert characteristics). As the diaphragm is suddenly removed, the pressure discontinuity generates a shock wave,  $S$  (Fig. 28), which propagates through the driven section (followed by its induced high pressure and temperature flow - (Region 2)). If the end wall of the driven section is closed, the facility is merely referred to as a shock tube. If the test gas is discharged through an opening at the end wall and flows through a test section, the facility is referred to as a shock tunnel. The opening area is made sufficiently small so that a strong reflected shock wave,  $SR$ , propagates back up stream and raises the pressure and temperature even further (Region 5). In the case of a shock tube the gas in Region 5 is quiescent. In shock tunnel operation, it is discharged through the test section. Ideally, if the driven section is of uniform cross section, the flows in Regions 2 and 5 are one-dimensional and are characterized by uniform pressures and temperatures. The experimental conditions in Regions 2 and 5 can be widely changed by choosing different driver and driven gas compositions, and mainly by applying different initial values of pressure and temperature across the diaphragm.

In order to achieve a long test time under uniform flow conditions, any formation of wave motion disturbances in Region 5 should be avoided. The interaction of  $SR$  with the contact surface  $C$  may just give rise to such a disturbance in the form of either an expansion wave or a shock wave traveling through Region 5 toward the test section. It is possible to avoid such a situation. For any given gas composition there is one particular value of incident shock wave ( $S$ ) Mach number for which  $SR$  will pass through  $C$  without giving rise to any disturbance. Though seemingly it dictates a

particular choice of operating conditions, in reality there is some range of Mach numbers for which the disturbances are not prominent. Fig. 28 depicts the conditions for which there are no disturbances in Region 5. These conditions are called - "tailored conditions". Refer to Refs. 88-90 for details. Ideally, when operating under tailored conditions, the flow parameters at the test section remain unaltered until the arrival of either the contact surface or the head (H) or the foot (F) of the rarefaction wave produced when the diaphragm bursts. It has been discovered, however, that non-ideal flow in long shock tunnels drastically reduces the available test time predicted from ideal models and also attenuates the ideal flow properties.

The ideal theory treats constant speed motions of the shock wave S and the contact surface C. As can be seen from Fig. 28 the distance between S and C increases linearly with the distance from the diaphragm. Therefore, ideally in order to get longer test time, a longer shock tunnel is required. Actually, a boundary layer is developed behind S and the mass loss to it causes the speed of S to decrease and the speed of C to increase until they approach some limiting separation distance [91,92]. This phenomenon imposes an upper bound for the shock tunnel test time. Therefore, experimentally it is useful to determine the shock wave (S) speed close to the end wall in order to calculate correctly the strength of the reflected shock (SR). Due to the wall boundary layer, the flow between S and C is clearly non-uniform. Generally, the flow non-uniformities are greatest for long length, small-diameter shock tubes operating under low pressures, since the boundary layer is more pronounced then. They are also greater for larger and lower S Mach numbers. All fluid properties increase in value between S and C [93]. A general treatment of these phenomena is given by Mirels [94,95].

The behavior of the reflected shock wave SR is also non-ideal. A bifurcation of the shock is developed near the wall due to its interaction with the boundary layer that was formed behind S. Under certain conditions the stagnation pressure of the boundary-layer gas is less than that of the free stream, so it fails to penetrate SR and gathers at the foot of SR as a ball of fluid. Consequently, the velocity of SR is attenuated. The velocity of the gas passing through the bifurcated part of SR (two oblique shock waves) is less reduced than that passing through the main portion of SR (normal shock). As SR is transmitted through C, the cold gas of Region 3 passing through the bifurcation attains much lower temperature than the gas in Region 5 and its velocity is much higher than that of the latter. Consequently, a stream of cold flow is formed which moves along the walls toward the test section with velocity greater than the main body of hot flow of Region 5. This phenomenon is quite insidious and difficult to detect. It may result in a considerable shortening of the effective test time. Comprehensive treatment of that phenomenon may be found in Refs. 96-98.

The contact surface itself may develop instabilities when SR is transmitted through it. It has to do with the phenomenon of Taylor instability [99]. When two fluids of different densities are accelerated in a direction perpendicular to the interface, the interface may develop an instability. Contact surface instability may result in premature arrival of cold gas to the test section, a situation similar to the bifurcation effect previously discussed. Treatment of this phenomenon may be found in Ref. 100. Experimentally it is found that the bifurcation phenomenon results in much more severe consequences.

Since the flow properties behind S are not uniform, the strength of SR changes as it travels away from the test section. In general, it is very difficult to predict analytically the non-ideal flow conditions, especially for the situation of shock tunnel operation where the flow in Region 5 is coupled to the downstream flow in the test section. Nevertheless, the deviations of the flow properties from the ideal ones are typically in the range 10-25%; therefore, the shock tunnel performance can be evaluated in advance applying the ideal equations. If any of the flow properties is known experimentally, the balance of the flow properties may be found quite accurately by applying proper corrections to the ideal equations. The tailored conditions must be found experimentally (for shock tunnel operation). A first approximation is given by the solution of the ideal equations. (See Appendix III).

Other non-ideal characteristics of the shock tunnel operation include heat loss to the walls and opening of the diaphragm. They are, however, negligible for the case of large scale shock tunnels. The change of the specific heat of the gases with the temperature should be taken into account.

A very important process for shock tunnel operation is the starting of the flow through the test section which depends greatly on the geometry of the test section and the specimen mounted there. The settling time of that process (Fig. 28) is not negligible in most shock tunnel applications. Discussion of the starting process in the particular shock tunnel used for this experimental work, is given in IV-F.

#### IV-C. Description of the Experimental Shock Tunnel and its Accessories

The shock tunnel facility used in this work is the one built and used by Kashiwagi and Summerfield [19]. The test section was modified for this research. Helium is used as the driver gas, and mixtures of oxygen and nitrogen as the driven gas. The tailored conditions are satisfied for incident shock Mach numbers, ( $M_S$ ), in the range of 3.73 - 3.79 depending on the composition of the driven gas and on the exhaust nozzle.

The shock tube dimensions are optimal in the sense that the available test time for operation under tailored conditions is very close to the upper limit dictated from the non-ideal effects of the boundary layer build up behind the shock wave S. The shock tunnel dimensions are fairly large. The length of the driver section is 9.7 m and the length of the driven section is 8.5 m - (Fig. 29). The inside diameter is 9.7 cm. The available test time is in the range 12 - 18 ms depending on the exhaust nozzle area.

The shock wave is initiated by rupturing a double diaphragm by means of lowering the pressure between the two diaphragms. A precise control on the driver and driven operating pressures is achieved using this technique. The diaphragms, made of soft aluminum, were not inscribed prior to their mounting. A set of cross-shaped knife blades, mounted in the driven transition section, cut the diaphragms as they bulge under pressure. That assures clean rupture of the soft aluminum diaphragms without the formation of aluminum debris. Though small pieces of aluminum were sometimes observed in the test section, the high speed photographs showed that the debris arrived much later after the end of the available test time. The driven section was air cleaned from aluminum debris before each test. Minute

quantities of aluminum dust, (which cannot be observed photographically), are formed as the diaphragms rupture. A special test was devised to find the time of arrival of that dust to the test section. A He-Cd laser beam was passed through the side windows across the test section. Light reflection from dust particles was detected by the optical system through the top window only after the end of the test time.

The incident shock Mach number was measured by four 603A Kistler pressure transducers located 0.108 m, 0.997 m, 3.283 m and 5.112 m from the entrance to the test section. As already discussed in IV-B, the shock wave does not travel with a constant speed. The shock Mach number at the reflecting wall was extrapolated from the measured values along the tube. It was done for all the tests. The reproducibility of the incident shock Mach number was within 1%.

#### (i) Test Section (Fig. 29)

The test section has a square cross-section of 32 mm. It enables one to observe the experimental phenomena without any optical distortion. Also, the flow around the specimen is truly two-dimensional. The flow in the test section is low subsonic and it is controlled by means of a variable area nozzle downstream of the test section. That nozzle was choked during the test time. Convective ignition at higher subsonic (and supersonic) velocities is less probable because of the small Damkohler numbers of the flow (see Section III). Quartz windows were constructed at the top and the side walls of test section to provide access for ignition detection and flow visualization. A 603A Kistler pressure transducer was mounted flush at the bottom wall of the test section to measure the static pressure. The entire bottom portion of the test section is removable. It serves as the mounting platform for the test specimens and houses the Kistler pressure transducer. All electrical leads pass through it (see also Fig. 36).

Up to four test specimens can be mounted in a tandem configuration with variable distances between them.

#### (ii) Test Specimen

Most of the experimental work was carried out with the propellants specified in Table 2, (i.e., M1, M26, M30, NC/TMETN, HMX/PU). A number of tests were conducted with Plexiglass as a pure fuel. All specimens were machined to cylindrical shapes as follows: length = 15.2 mm, OD = 7 mm, ID = 3.2 mm. The blockage ratio is therefore - 0.22. Since the flow is low subsonic, the deviations from ideal flow conditions around a cylinder are expected to be small. The mounting configuration in the test section is shown in Fig. 29. Pictures of the machined propellants mounted on cylindrical holders and their supports are shown in Fig. 36. The propellant and its holder constitute a uniform cylinder, 24.4 mm in length. The entire propellant section of this cylinder is considered to be under uniform two-dimensional flow conditions, isolated from any flow irregularities near the supports.

The propellants M1, M26 and M30 are standard practical nitrocellulose-based propellants which were originally fabricated to cylindrical shapes. They were machined to the above specified dimensions (which are quite close to the practical ones). The propellant NC/TMETN was formulated at Princeton University. It is used to investigate the effects of various additives on

the ignition and burning properties of nitrocellulose-based (NC) propellants. HMX/PU is a high-energy, experimental composite propellant which was used in this work merely for the purpose of comparing the ignitability of HMX propellants to NC propellants.

The propellant surfaces were machined smooth. All specimens were checked visually before the tests for surface irregularities. To obtain reproducibility of the experimental results, only propellants with smooth surfaces were used. A measure of the pre-test machined surface may be inferred from Figs 67,68.

### (iii) Optical System for High Speed Photography

Since convective ignition is so highly dependent on the flow structure, it was judged necessary to observe the flow and the ignition process simultaneously. It was done by means of high-speed, motion photography, taken through a schlieren and shadowgraph optical system originally constructed by Ref. 19. A schematic layout of the optical system is given in Fig. 30 (see also Fig. 34). A continuous light source, an Osram Mercury Super Pressure Lamp HBO 100 Watt, was used. The schlieren field mirrors have a 15 cm diameter and a 180 cm focal length. Both Hycam and Fastax high-speed movie cameras were used at a nominal rate of about 5000 frames/sec. The Hycam gives a higher quality picture but its effective f number is greater than the Fastax. The Hycam by virtue of its fast shutter time capability was used to get sharper pictures of the flow structure (e.g., arrival of shock wave - Fig. 53). The Fastax was used to get flame pictures under lower illumination conditions. Mostly color pictures were taken, using Kodak Ektachrome type 7241EF and VNF films. A blue color filter was placed in front of the mercury lamp, thus the shadowgraph (or schlieren) flow structure was recorded by the film in blue. As ignition and flame spread occur, the luminosity of the flame (typically in yellow to red) is superimposed on the blue background of the flow structure. That technique enabled one to distinguish the flame behavior from that of the flow by virtue of the excellent blue-red color contrast. The shadowgraph system was found sufficiently sensitive and was preferably used, since it required lower light intensity.

### IV-D. Ignition Detection

Though high speed photography could have been utilized to detect ignition, the accuracy and the sensitivity of the photographic system was determined to be unsatisfactory due to the following reasons: a) the best time resolution obtained is 0.2 ms, which is lower than required to distinguish the first ignition position, and b) the film sensitivity is too low to record the cases when the flame radiation in the yellow-red is too weak. The high speed photography is, however, very useful in showing the extent of flame spread and its distance from the burning surface.

Most of the ignition data in this research was obtained using photomultiplier tubes for ignition detection.

Six RCA IP28 photomultiplier tubes were used to distinguish the first ignition position and the direction of the flame spread. Since the photomultiplier tube is quite large compared with the test specimen, Bausch and Lomb fiber optics were used to transfer the light output from the test section to the photomultipliers. The fiber optics were trained down on the

specimen through the quartz window on the top of the test section. A Corning filter, 7-54 which has transmission of 2300-4200 Å, was used to reduce the background radiation associated with the arrival of the shock wave. The optical combination is the original one used by Kashiwagi [19]. The detectable wave length range with this combination of photomultiplier tube, filter, and fiber optics, is shown in Fig. 31. It covers the near ultra-violet range.

Due to its low wave length the spectral region chosen to look for ignition is relatively free from background noise which is mainly in the visible. The infrared background noise is very strong during the test time due to the heating of the test section walls by the shocked flow. As already mentioned, there was a very strong radiation associated with the arrival of the shock wave. For the  $N_2/O_2$  test gas mixture used, the radiation was visible in the yellow and was found to be very strongly dependent on the incident shock Mach number. Though radiation in the yellow may result from sodium contamination in the shock tube, the radiation persisted despite careful cleaning of the shock tunnel walls. That radiation in the visible lasted typically 2 ms into the test time and prevented detection of ignition during that period in the visible spectra. Using the near ultra-violet range for ignition detection solved almost completely that problem. A few tests were conducted with Argon as the test gas and the background radiation was extremely strong over the entire spectra so as to prevent ignition detection even in the ultra-violet. That problem was also encountered by Ref. 101 in connection with chemical kinetics measurements in shock tubes by chemiluminescent radiation.

It was reported in Ref. 19 that detectors with different wavelength sensitivities in the range 3000-5500 Å gave equivalent ignition delay times. The test conditions of Ref. 19 were similar to those of this work. The experimental results of this work confirm the insensitivity of ignition delay measurements on the visible spectra used for detection (see Section V). Atallah et al. [102] found that this did not apply in the region between the visible and the infrared, but their ignition delays were relatively long in the range of 60 ms and the infrared spectrum was used to detect the increase of surface temperature. The most likely species to emit radiation in the spectrum range chosen for this work are NH and NO which have strong lines at around 3750-3800 Å, and 3950 Å, respectively. Indeed, these spectra were always found in Maltsev [103] experiments with the burning of NC-based propellants.

A considerable technical difficulty was the focusing of the fiber optics on the small cylindrical surface of the propellant. In order to be able to distinguish the first ignition position and the flame spread direction, each fiber optics should be limited to transmit the light originating from the boundary layer adjacent to a small segment of the cylinder surface. The segments should subtend the 180 degrees along the cylinder perimeter from the leading edge to the trailing edge without much overlapping. Special optical units were devised for that purpose (Fig. 29). Due to spatial constraints, a couple of fiber optics are housed per unit. Each unit is mounted on a vertical slide and can also be rotated sideways. The area under observation and the sensitivity of each detector system were calibrated by rotating a specimen size cylinder equipped with a subminiature elongate light bulb mounted on its surface, in place of the propellant specimen. A picture of the calibration system is shown in Fig. 32. A rack and pinion mechanism was used for rotation of the cylinder. The

sensitivities of all detectors were adjusted to the same values. The calibration results are shown in Fig. 30. Special emphasis was laid on the proper coverage of the main anticipated ignition zones (see Section III). Note that part of the wake region beyond the point of 180 degrees is also covered. Note also that detectors number 5 and 6 overlap. It was done intentionally. Detector 5 was used without filtering. Thus, its spectral response extended from the near ultra-violet to the near infrared. It was used for comparison purposes and also to detect the arrival of the shock wave by virtue of its very strong induced radiation in the visible, thus providing the time zero for the ignition delay time counting.

A new experimental technique for ignition and flame spread detection was tried successfully in this work. The photomultipliers-fiber optics system was replaced by a Reticon model LC64P analog/digital line scan camera (see Fig. 34). A brief description of this camera is given here.

The operation of the Reticon camera is analogous to that of a photographic camera with the exception that the film plane is replaced by a row of 64 tiny photodiodes. The spectral response of these photodiodes extends from the near ultra-violet to the near infrared. The field of view (depends on working distance and the choice of lens) is imaged by the lens onto the photodiode array which is scanned electronically to produce a staircase analog output with each level having an amplitude proportional to the light intensity on the corresponding photodiode. Thus, a spatial resolution of 64 points is obtained of the image scanned, which in our case is the propellant surface. The photodiode array is scanned by an internal clock which switches from diode to diode at a preset frequency  $f$ . After sampling the last diode there is a built-in delay of five clock periods before again sampling the first diode on the next scan. Thus the line scan time is given by  $t_L = 69/f$ .  $t_L$  is adjustable from 0.2 ms to 40 ms. The longer is  $t_L$ , the higher the sensitivity, since the output is the integration of light intensity during  $t_L$ .

The camera was used in this work only for the purpose of feasibility studies. Better recording instrumentation and a better camera are required for the present work. Ignition detection tests with this system are discussed in Section V.

#### IV-E. Instrumented Cylinder

As illustrated in Fig. 32 an instrumented (inert) cylinder 7 mm in diameter (same as the propellant specimens) was devised to include three thin platinum film calorimeters and a high-frequency Kulite pressure transducer which could be rotated to measure the pressure and temperature distribution around the circumference. The thin film gauge and the pressure transducer portions of the cylinder can be counter rotated to any desired angle of attack to the flow. The thin film gauge measures the surface temperature simultaneously at three angles 90 degrees apart. Its response time is about 15  $\mu$ s.

The construction of the thin film gauge, its operation, and the procedure to deduce the heat flux values from the temperature measurements are discussed in Appendix IV. The significance of the heat flux measurements was already discussed in the introduction to this section.

It was considered desirable to measure the static pressure distribution on

the cylinder itself in order to:

- a) Determine whether there exists significant pressure variations around the cylinder circumference due to blockage effects (blockage ratio 0.22).
- b) Compare the static pressure measured on the cylinder to that measured at the bottom of the test section, especially during the settling time of the flow in the test section.
- c) Investigate the correlation between pressure disturbances and variations in heat flux. General flow nonsteadiness characteristics may be deduced from that data.

The mounting configuration of the Kulite subminiature pressure transducer and its effects on its performance are discussed in Appendix V. Its response time is better than 100  $\mu$ s.

The thin film gauge and pressure transducer components of the instrumented cylinder are shown in Fig. 35 as a part of a general layout of the major test specimens and their supports. Note the small size of the components.

#### IV-F. Data Acquisition and Instrumentation

A layout of the instrumentation for the experiments is shown in Fig. 33. Two major recording devices were used:

- (1) Biomation 1015 Waveform Recorder
  - minimum sample interval 10  $\mu$ s.
  - 4 channels capability. 1024 10-bit words per channel.
- (2) Honeywell 5600 C Analog Tape Recorder.
  - recording speed 60 in/sec.
  - 80 KC frequency response.
  - 14 channels capability.

The Biomation recording is almost noise free and therefore it was used to record test section pressure and thin film gauge data. Typically, a sample interval of 20  $\mu$ s was used for 2 channels, recording 2048 words per channel, thus, covering about 40 ms of test time (e.g., Fig. 40a). The data recorded by the Biomation were transmitted to the HP 21-MXE mini-computer for storage and analysis.

The tape recorder was used to record the photodetectors data and driven section pressure transducers data (shock wave speed). The level of noise introduced to the data as it was recorded on the tape was not considered detrimental to the analysis of those data. It was advantageous to have those data on tape, since it enabled batch processing of several tests at a time. In turn, the data recorded on the tape was recorded by the Biomation, digitized, and transmitted to the HP computer.

Another recording device was used for a special purpose: a Nicolet 1075 Digital Oscilloscope. Since it has a 1  $\mu$ s sample interval capability, it was used to record high resolution pressure data for the settling period of the flow.

#### IV-G. Evaluation of the Performance of the Shock Tunnel

As already discussed in IV-B, the flow conditions in a large scale shock tunnel are not ideal in the sense that the flow properties in Region 5 (Fig. 28) are not uniform and the test time is shorter than the expected ideal one. The importance of working under tailored conditions was stressed since it assures best uniformity of test conditions and longest available test time. The extent of the non-ideal effects on the available test time in the experimental shock tunnel facility used in this work was discussed by Ref. 19, and, therefore, it will be mentioned here only briefly. More emphasis will be laid on those features of the shock tunnel flow conditions which have direct bearing on the interpretation of the current experimental program results.

A good indication of the extent of the non-ideal features of the shock tunnel is obtained from the amount of attenuation of the incident shock wave speed as it propagates along the driven section. It was found that the initial shock speed at the diaphragm station was very close to the ideal one, however, that speed decreased by about 7% by the time the shock arrived at the entrance to the test section (plane of reflection). The range of the experimental shock wave Mach numbers for the test conditions of Table 1 is given in Fig. 39. The comparison of the theoretical values indicates attenuation of about 7% over the entire range.

##### (i) Pressure Data and Test Time

Typical pressure data taken in each test is shown in Fig. 40. The incident shock wave speed is calculated from the bottom curve. For the nominal temperature tests of Fig. 35, typical values of shock speeds at the entrance to the test section are as follows: 1307 m/sec for 100%  $N_2$ , 1300 m/sec for 10%  $O_2$  / 90%  $N_2$  and 1276 m/sec for 50%  $O_2$  / 50%  $N_2$ .

The available test time could be estimated from the test section pressure trace (Fig. 40 - top curve). The sharp drop in pressure, after about 17 ms from the initial pressure rise, indicates the arrival of the rarefaction wave (see Fig. 28) and signals the end of the test time. The calculations and data of Ref. 19 indicate that for the current work range of test section velocities, the end of test time is indeed brought upon by the rarefaction wave. As concluded by Ref. 19, premature arrival of cold flow due to the bifurcation effect (IV-B) terminates the practical test period sooner to the pressure drop in cases of higher test section velocities. It was inferred from heat flux measurements taken at the test section. A sharp fall of heat flux values indicated the arrival of cold flow. Test times measured in this work using the heat flux data from the instrumented cylinder were always in good agreement with those measured from the pressure data (Fig. 40)

The upper pressure trace of Fig. 40 is for the nominal test conditions (operation under tailored conditions, Mach 3.72 - 3.78) and is quite uniform. Nevertheless, there is a slight gradual increase in test section pressure during the test time. This is in accordance with the non-ideal phenomena discussed in IV-B. A few high temperature tests were conducted slightly off the tailored test conditions (Mach 4.08, Fig. 39) and the increase was about 20% and also gradual. In any case, the average of the pressure values for the duration of the ignition delay was used for the interpretation of the ignition data discussed in Section V. Since ignition delays were generally much shorter than the test times, the errors were not significant. Using adiabatic relations [104], it is approximated that the temperature rise due to a 10%

pressure rise is only 3%.

The period of settling of the flow in the test section is around 1 ms. As evidenced from Fig. 40, it is characterized by a strong overshoot and undershoot of the test section pressure. It will be discussed later in connection with the starting process of the flow in the test section.

The pressure trace discussed is the one measured at the bottom wall of the test section. This trace is compared to the pressure measured using the instrumented cylinder. Fig. 41 is typical of the data obtained (note that the scales are different). Though the high frequency components of the pressure are quite similar in both traces, the long time trend of the average pressure value is somewhat different. The bottom wall pressure is increasing gradually during the entire test time. The instrumented cylinder pressure drops slightly and then increases. The average test time pressure values, however, are very similar. This phenomenon may indicate longer settling time for the inner core flow.

The small pressure ripples on the pressure traces are inherent to the test section geometry for the specific operation conditions and they are remarkably reproducible. Fig. 42 is a demonstration to that effect. Note that Fig. 42 is a compilation of three separate tests. The pressure traces measured at 0, 90, 180 degrees to the flow are very similar. Only the points 0 and 180 degrees deviate slightly after 10 ms. It can be concluded that the effects of the blockage ratio (greater than zero) are negligible. Therefore, it is justified to assign one pressure value to each test for the entire cylinder surface.

A better resolution of the pressure distribution around the cylinder during the initial flow transients is shown in Fig. 42b. The pressure rise trends for the first 0.2 ms at the 0 degrees point and at the 90, 180 degrees points are different. This has to do with the starting process of the flow which is discussed next.

#### (ii) Starting Process of the Flow in the Test Section

The starting process for the flow in the shock tunnel is very important, particularly for convective ignition tests, since very high heat fluxes may be associated with it. Indeed, one of the reasons for constructing the heat flux gauge (IV-E) was to study the heat flux associated with the starting process.

The starting process for the particular test section configuration is very complex, since the cylindrical specimen, being mounted between two nozzles (the entrance to the test section and the choked nozzle downstream), participates actively in that process.

The starting process through nozzles was studied in connection with hypersonic flow produced in shock tunnels downstream of expansion nozzles. Amann [105] and Smeets [106] observed the existence of a standing shock wave which delayed the steady flow through the nozzle. Amann found that the geometry of the nozzle was important to that process. The diffraction of a shock wave by a cylinder was studied by Heilig [107] and Bryon and Gross [108]. Based on their studies and others, a simplified wave diagram (and structure) was constructed to describe the flow during most of the starting period (see Fig. 43).

Referring to Fig. 43 the starting process is as follows.

As the incident shock wave S reaches the area constriction at the entrance to the test section, it is partially reflected as SR and partially transmitted as ST. The flow at the entrance to the test section is sonic and a rarefaction wave RRF is formed to accelerate the flow to suitable values compatible with those behind ST. The diffraction process of ST on the cylinder is such that a reflected shock wave STR is formed with initial strength to stagnate the flow at the front stagnation point and a transmitted shock wave STT starts moving past the cylinder. At some distance along the cylinder perimeter, the point P lifts itself from the surface and a contact surface C is formed. The pressure behind Q decreases very significantly as the point moves toward the rear stagnation point. The velocity behind Q may be supersonic.

In the high-speed motion pictures taken only situation 4 of Detail A was observed (much higher framing rate than what was available was required to observe situations 1, 2, 3).

The reflection of STR from the test section walls, the contact surface C, and rarefaction RRF results in succession of wave motion in the test section to which the cylindrical specimen is exposed. A reflected shock wave, STTR, from the nozzle downstream adds to the unsteadiness of the flow and has a large effect on the heat transfer to the rear portion of the cylinder.

The strengths of ST and STR upon impinging of ST on the front stagnation point Q were calculated for the nominal operating pressure ratio of 2.86/0.06 MPa and incident shock Mach number  $M_S = 3.73$ . The following values were obtained:

$$\begin{array}{ll} M_S = 3.73 & M_{SR} = 2.21 \\ M_{ST} = 4.84 & M_{STR} = 2.44 \\ P_Q = 3.03 \text{ MPa} & T_Q = 2826 \text{ K} \end{array}$$

Note that  $M_{ST} > M_S$

In contrast, the steady state conditions at the test section (which are reached after the settling period) are:

$$P_Q = 1.72 \text{ MPa} \quad T_Q = 1850 \text{ K}$$

Thus, as ST impinges on the cylinder, the pressure and the temperature at the front stagnation region jump instantaneously to values which are higher than the steady state ones. Referring to Detail A of Fig. 43, it may be realized that those high values are attenuated very rapidly in a time duration on the order of the shock wave diffraction on the cylinder  $\sim 10 \mu\text{s}$ ; similar high values may exist on the rear stagnation point of the cylinder as STTR impinges upon it.

The settling period of the flow is characterized by a succession of pressure waves impinging on the cylinder surface with decreasing strengths until eventually steady state conditions are obtained. The wave motion between the nozzles and the cylinder results in a very agitated flow. In the shadowgraph high-speed motion photography taken, a situation of flow reversal was observed (which is associated with the formation of STTR). The flow direction is switched twice until the final forward motion is established. Since the flow at the wake of the cylinder is turbulent, the cylinder surface is exposed to turbulent flow as the flow reverses itself. Much higher than

laminar values of heat transfer to the cylinder surface are expected during that period.

Instrumented cylinder surface temperatures and heat flux distributions during the settling period of the flow are given in Fig. 44. The prominent heat flux peaks are the indication of the pressure wave impinging on the cylinder surface and the exceptionally high values of  $\partial P/\partial t$ ,  $\partial T/\partial t$ , and  $\partial u/\partial t$  associated with them (see discussion III-F,H). The high sustained values of heat fluxes during the entire period are most likely the result of strong turbulence associated with the flow reversal. As a result, the values of surface temperature obtained at the end of that period are about 3 times higher than the predicted ones based on laminar flow. The temperature rise during that period is much higher than that which is calculated from Eq. (32), which gives the temperature jump for sudden exposure of the cylinder to the full magnitude of the ambient conditions. As the flow is established forward, the turbulence is swept away and the high heating rates subside.

The heat flux trends in Fig. 44 are in accordance with the wave diagram of Fig. 43 discussed before. As can be seen, only the front half of the cylinder is highly heated during STT diffraction on it, since this region is then exposed to the highest pressure and temperature values. However, the rear surface of the cylinder experiences comparable heating rates during the period of flow which starts when STTR impinges upon it (the sudden heat flux peak observed at 90-180 degrees after about 0.2 ms). It is then exposed to reverse turbulent flow and the high heat flux is sustained thereafter. The 90-degree region is heated the least, since the boundary layer is the thickest there. Note the similarity in trends during the first 0.2 ms between the pressure data expressed in Fig. 42b and the surface temperature data expressed in Fig. 44.

Subfigures 44 A, B, C represent three separate tests. Note the symmetry in the results (-30, 30, -60, 60 degrees). Note also the reproducibility of the heat flux trends. The magnitude and trend of the heat flux during the settling period, expressed in Fig. 44, are almost identical for the entire range of nominal test conditions (Table 1) since they depend mostly on  $M_s$  and the geometry of the test section. The area size of the variable area-choked nozzle downstream affects the strength of STTR to some extent. STTR is weaker for a larger area.

The importance of the initial flow transients on the convective ignition performance was discussed in Section III-H and will be discussed further in Section V. It should be emphasized again that the abnormally high heat fluxes associated with the initial flow transients could not have been deduced from any pressure data and only the direct heat flux measurements revealed the extent of their trends and magnitudes.

(iii) Remarks Concerning the Calculation of Steady State Flow Conditions (Appendix III)

The temperature, pressure and flow velocity in the test section were calculated assuming equilibrium flow condition, i.e., variable  $C_p$ . The calculations assume that the flow velocity, temperature, and pressure in the test section become stable immediately after the shock wave is reflected and the nozzle downstream is choked with a certain mass flow. Actually, this immediate stability assumption is invalid during the settling time of the flow (0.8 - 1.0 ms). The theoretically calculated conditions should, however, be

valid after that period until the arrival of the rarefaction wave or cold flow.

The calculations of Ref. 19 show that if frozen conditions are assumed ( $C_p$  constant), the frozen temperature is about 25% higher than the equilibrium temperature, and the equilibrium pressure is about 12% higher than the frozen pressure.

The characteristic time of the vibrational relaxation process of the temperature from its frozen value to equilibrium value is given by the formula [109]:

$$\tau = C \cdot \frac{\exp(K_2/T)^{1/3}}{P}$$

Substituting the proper constants  $C$  and  $K_2$  for  $N_2$ , the value for  $\tau$  obtained for  $T = 1850$  K,  $P = 1.73$  MPa is  $\tau = 10.3 \mu s$ . That time is an order of magnitude smaller than the shortest ignition delay time measured in this work. Therefore, the equilibrium conditions were considered to be the experimental conditions in this work. Actually, the experimentally measured test section pressures (Figure 40, 42) were about 10% higher than the equilibrium values which are calculated based on the experimentally measured shock wave speed  $M_s$  at the entrance to the test section. This may be caused by the interaction of the attenuated flow behind the incident shock wave  $S$  with the reflected shock wave  $SR$  (Fig. 28). Therefore, the values calculated are corrected assuming adiabatic relations to account for that 10% deviation of the experimental test section pressures from their theoretical values. Details are given in Appendix III.

Note that the calculations are based only on the incident shock wave speed and the test section pressure data. No attempt was made in this work to measure directly the temperature and velocity in the test section (because it was highly impractical). However the errors expected in the calculated temperatures are quite small compared to the errors in pressures which are already corrected (since the pressures are measured). The error in velocity values is even smaller. Since the purpose of this work is to find the phenomenological differences of experimental trends rather than any exact values, it is quite reasonable to accept equilibrium conditions and a constant average test section pressure for the calculations of the flow conditions during the test time.

## SECTION V

### EXPERIMENTAL RESULTS

#### V-A. Introduction

The range of test conditions is summarized in Table 2. In each of the three test types specified in Table 2, only one flow property (i.e., pressure, temperature, velocity) was systematically varied while keeping the others unchanged. A better interpretation of the results is obtained in this manner. Since the ignition process investigated is of the convective type, the flow velocity was the main parameter which was changed in a large number of tests (thereby changing the Reynolds and Damkohler numbers of the flow). The vast majority of the tests fall into the category of "Nominal Conditions" (Table 2), to which all the test specimens were exposed and for which the "tailored conditions" were satisfied. A few tests (with M30 propellant only) were conducted under higher ambient temperatures. For that purpose the tailored conditions were relaxed somewhat (higher incident Mach number - Fig. 39). In both cases the gas velocity was controlled by means of the variable area choked nozzle downstream of the test section (Fig. 29).

The importance of the ambient pressure level for the convective ignition process is discussed in Section III-H. Since practical convective ignition situations occur under a wide range of ambient pressure conditions (as well as velocities), a series of tests were conducted in which the pressures were varied while the temperature and velocity were kept constant. This was done by varying the driven (1) and driver (4) initial pressures keeping the pressure ratio  $P_4/P_1$  constant (thus operating under tailored conditions). Since the shock wave magnitudes are dependent only on  $P_4/P_1$  (for the same gas composition), the temperature and the velocity are unaltered.

Flame spreading trends (and blow off phenomena) are of direct relevance to the convective ignition performance. Therefore, the flame spreading trends are presented and discussed here as major supplements to the main ignition results which deal with the delay time and location of the first ignition event.

Post ignition burning of a granular propellant in a flow field is important to understanding convective ignition in tandem configurations. A photographic display of major burning phenomena is given (Figs. 71 through 74) and discussed.

Graphite was added to some of the propellants in order to render them opaque to radiation and to determine whether graphite creates hot spots on the surface that promote ignition. The effect of graphite and carbon as additives to the propellants on the ignition performance was investigated in a series of tests.

Information regarding convective ignition in tandem configuration is relevant to the practical case of packed bed ignition. A series of tests was carried out with two propellants in various tandem configurations.

A general interpretation of the experimental results is given in light of the theoretical analysis of Section III. In particular, heat flux data

obtained from the series of tests with instrumented cylinders are used for the interpretation of the ignition and flame spreading. Additional information is obtained from scanning electron microscope studies of extinguished propellants surfaces.

V-B. Discussion of the Heat Transfer Data Obtained from the Instrumented Cylinder

The heat flux data obtained during the settling period of the flow ( $\sim 1$  ms) were previously discussed in connection with the starting process of the flow (IV-G). The reproducibility of the results was good and consistent trends were found. The abnormally steep temperature rise during that period is attributed to the existence of a high level of turbulence associated with the initial wave motion and boundary layer development. Typical surface temperature and heat flux data for the entire test time, at the points 0, 90, 180 deg. to the flow, are given in Figs. 45 and 46, respectively. The following features are typical to all of the heat flux data obtained:

- a) The steep surface temperature rise during the period of the initial flow transients and the high heat flux values associated with them are almost identical in all tests conducted under the same ambient pressure and temperature. Similar levels of surface temperature are reached at the points 0 and 180 deg. by the end of that period, but a much lower temperature is obtained at the 90 deg. point.
- b) The surface temperature rise (and the heating rate) during the steady period varies from test to test as the velocity is changed. In all cases, the highest heat flux levels are obtained at the 0 deg. point. The heat flux values increase gradually from both the 0 deg. point and the 180 deg. point toward the 90 deg. point. Similar values are obtained for the entire region of -30 to 30 deg. to the flow.
- c) After the end of the settling period (judged from the pressure data), the heat flux is still unsteady for the remainder of the test period but fluctuates around certain steady levels. In that respect the following features are noticeable:
  - 1) Though the average heat flux levels vary markedly around the cylinder perimeter, the amplitudes of the unsteady components of the heat flux are almost the same.
  - 2) The fluctuations in the heat flux levels at 0 and 180 deg. correlate well, however they correlate poorly with the 90 deg. point fluctuations.

A further discussion of the above items follows.

Unlike the pressure data (Fig. 42), the reproducibility of heat flux data (taken in identical tests) is good only for the first 3 ms of the test time. During that period a good correlation is obtained between the pressure fluctuations and the heat flux fluctuations. After that period, the reproducibility of the heat flux fluctuations pattern is poor but the average level of the heat flux is still fairly reproducible.

As expected (Section III-H), the heat flux levels are very sensitive to the ambient pressure levels since convective heat transfer is strongly dependent on the density of the fluid. That sensitivity is very pronounced during the initial flow transients. Figure 47 is a demonstration of that effect. Note that despite the complex patterns of the surface temperature traces, there is a consistent similarity of shape among the temperature

traces which correspond to the same angle of measurement.

The large surface temperature rise during the initial flow transients results in much shorter times to reach some prescribed surface temperature, as compared to the pure steady flow case. The time to reach a surface temperature of 200 C at  $\theta = 0, 90,$  and  $180$  deg. is shown in Fig. 48 as a function of Reynolds number. The rise rate behavior is very steep and the role of the initial rapid rise of the temperature is evident (Fig. 45) particularly for the higher pressure case (Fig. 47).

The experimentally measured surface temperatures of the pyrex cylinder (the backing substance of the thin film gauge) are converted to the approximate values of surface temperatures which are expected on the propellant specimen by the following relation:

$$T_{W, \text{propellant}} = \beta T_{W, \text{pyrex}}$$

where:

$$\beta = \frac{\sqrt{(K \cdot \rho \cdot C)_p \text{ pyrex}}}{\sqrt{(K \cdot \rho \cdot C)_p \text{ propellant}}}$$

The above relation is obtained from Eq. (IV-4) (App. IV) assuming that for the same flow conditions, the heat flux versus time at the propellant surface is identical to that at the pyrex surface. Clearly that assumption is incorrect when the propellant surface reaches temperatures above the gasification temperature (200 C), since a high heating rate is required for the gasification and heat transfer is reduced because of the blowing effect of the propellant vapors. Even under inert heating conditions, the heat transfer to the propellant is reduced as the temperature difference between the ambient temperature and the surface temperature decreases. Therefore, the expected propellant surface temperature cannot be calculated above approximately 200 C (the gasification temperature). Typically for the propellant specimens used in this work,  $\beta \sim 3$ . Referring to Fig. 45 (or Fig. 44), it is evident that a temperature rise in excess of 120 C is obtained after the first 1 ms of test time at the 0 and 180 deg. regions. That translates into a 360 C temperature rise for a propellant specimen if it had been inert. Since this is not the case, the actual surface temperature rise during the initial flow transient will be much lower; nevertheless, it is expected to be above the gasification point. Owing to the complexity of the heat flux trends during that period, it is very difficult to predict the exact levels of propellant surface temperature during that period and thereafter. A simplified simulation of the effects of a large initial propellant surface temperature jump at the initiation of the flow (to values above the gasification temperature) is given in Section III-H. Based on the results of the numerical solution shown in Fig. 25, it is very probable that the propellant surface cools down appreciably after the high heat flux rates, associated with the initial flow transients, subside. The surface temperature rise is resumed gradually due to the continued near steady state convective heat transfer and the exothermic chemical reactions which lead to ignition. This subject will be discussed further in connection with the interpretation of the ignition trends found experimentally.

The heat flux distribution trends during the steady period are as expected for a subcritical regime of flow around cylinders (see Section III-C). The heat flux results indicated correctly the extent of the front stagnation zone (i.e., it constitutes a large portion of the front surface). See the discussion of Eq. (31) for more details.

The post flow-settling-period unsteadiness of the heat flux (discussed in item (c)) could not have been inferred from the pressure data (which is rather steady then). Thus, low frequency free stream turbulence or velocity unsteadiness may exist. Since the flow velocity was not measured directly in this work, the existence of turbulence is a matter of conjecture based on the heat flux data of this work as compared to related turbulent heat transfer data published elsewhere. The high speed motion pictures taken at a rate of 5000 frames/sec did not reveal turbulence upstream of the specimens. In contrast, the wake turbulence was clearly in evidence.

The fundamental frequency of the heat flux fluctuations was found to be in the range of the expected frequency of vortex shedding from the wake (i.e., 500 to 1000 Hz). As suggested by Hinze [110], the free stream turbulence is expected to affect the heat transfer rate to the rear surface when the "frequency" of the energy-containing eddies (which is proportional to the free stream velocity divided by the integral length scale of the turbulence) is equal to the shedding frequency of vortices from the wake (a resonance effect). Thus, seemingly the heat flux fluctuations at the rear surface may be related to the existence of free stream turbulence. However, that does not explain the similar fluctuations encountered at the front surface. Also, the experimental evidence available from the literature [61] for the influence of free stream turbulence on the local heat transfer rate to cylinders is that the augmentation in heat transfer due to turbulence is the highest at the front stagnation zone and the lowest at the separation zone. This is definitely not the case in the present work (item (c - 1)). From the foregoing discussion it is concluded that though the existence of some degree of free stream turbulence cannot be ruled out, the fluctuations in the heat flux data are probably the result of velocity and temperature non-uniformities in the flow field (since the measured pressure is quite uniform). It may imply prolonged effects of the initial flow transients on the volume of gas in the driven section which flows through the test section during the test period.

Vortex shedding from the wake was observed photographically to have a distinct regularity only in the later stage of the test time. It is expected that the vortex shedding phenomena will result in rear surface heat flux fluctuations at the shedding frequency. However, as already mentioned, the fundamental frequency of the heat flux fluctuations was in the range of the vortex shedding frequency and it was quite difficult to filter the latter from the former. Spectral analysis of the heat flux data revealed in most cases prominent frequencies which might be associated with the vortex shedding only for the 180 deg. point. Indeed in Fig. 46 when comparing the heat flux data for the 0 deg. with the 180 deg. point, there is some indication of a unique frequency, which is superimposed on the fundamental one for the 180 deg. point. That frequency ( $\sim 1000$  Hz) may be associated with the vortex shedding.

The seemingly bad correlation between the heat flux measured at the 90 deg. point (separation zone) and the 0 and 180 deg. points may be due to fluctuations, in the location of the separation point, which are not in

phase with the velocity fluctuations. Since the period of the velocity fluctuations is a few times the residence time of flow around the cylinder, the heating conditions can be regarded as quasi-steady (see Section III-H). The long time heating trends are dependent solely on the steady average values of heat flux. Plots of the average values of heat flux for the steady portion of the test period, versus the Reynolds number of the flow, are shown in Fig. 49. The established trends are as expected, i.e., the heat flux increases with the Reynolds number ( $h' \sim Re^{0.45 \pm 0.05}$ ). The scattering of the data fairly represents the reproducibility of the heat flux data. The ignition data are therefore expected to have similar scatter.

#### V-C. Ignition Detection

The basic methods for ignition detection in this work (see Section IV-D) are: photo-detectors (photomultipliers and fiber optics), line scan Reticon camera (64 silicon elements), and high speed motion color photography. All ignition data given in this section are based on the photo-detectors' output. The Reticon camera was used for feasibility studies of its use in ignition detection applications. The high-speed motion photography was used mainly to obtain the extent of flame spreading and flow structure, but ignition data could also be deduced from it, though not nearly as accurately as those from the photo-detectors. The features of the ignition data obtained by the above mentioned techniques are discussed next.

##### (i) Ignition Data from the Photo-detectors

Typical ignition data from the photo-detectors are shown in Fig. 50. As described in Section IV-F, the data are originally recorded on the tape-recorder and then digitized and sent to a computer. Fig. 50 shows the data as they are recorded on a Biomation 1015 and presented on a monitor display.

Figure 50-A is a typical display of ignition data obtained for conditions of low oxygen concentration flow (10%  $O_2$ ) for M30 propellant. The light emission signals associated with the onset of ignition are rather weak and had to be greatly amplified in order to be distinguishable on the display (to optimize the digitation range). The noise level which is inherent to the tape recording can be judged from the signals prior to the shock wave arrival. The induced luminosity of the shock wave arrival marks clearly the initiation of the flow. Note that ignition starts first at the rear surface then at the front surface and finally at the separation zone. The low level of the light emission and the relatively slow onset of ignition are typical to all of the ignition data obtained for low oxygen concentration flow conditions.

Figure 50-B is a display of ignition data obtained for conditions of high oxygen content in the free stream (50%  $O_2$ , 50%  $N_2$ ) for M26 propellant. The light emission signals associated with the onset of ignition are very intense as compared to those obtained for the lower oxygen content flow. Note the vertical scales on sub-Figs. 50-A,B. The ratio of signal to noise is sufficiently high so that the tape noise is not apparent. Also, the shock-induced luminosity is very weak as compared to the flame luminosity. The data were distinguished the shock wave arrival (starting of the flow), the data were used without the ultra-violet filtering (which is used

on the other detectors). Therefore its output is the integration of the light emission over the entire visible spectrum. The ignition signal of detector 5 (for the case of Fig. 50-B) reached the saturation level of its photomultiplier. Note that ignition starts almost simultaneously on the entire cylinder surface and that the ignition signals are rather steep (compared to the lower oxygen content case). Ignition delay is an order of magnitude shorter than that of Fig. 50-A. Figure 50-B is quite typical of ignition data obtained for M26, PNC, and Plexiglas under conditions of 50% oxygen in the free stream. In general, for a given propellant, the ignition signals were more intense as the level of free stream oxygen was increased.

Though not shown in Fig. 50, all six detectors were used in each test (detector number 5 without filtering). Ignition times were counted from the time of shock wave arrival. In some cases, a phenomenon of a short sequence of ignition-extinction was observed (with period smaller than the residence time of flow  $t_f$ ). It was attributed to evanescent flow unsteadiness at frequency greater than  $1/t_f$  that stimulates premature ignition by momentarily distorting the boundary layer profiles of velocity and temperature. Therefore somewhat arbitrarily, ignition was considered to occur when the flame established lasted for more than  $3t_f$ . The points of ignition on the photo-detectors traces shown in Fig. 50 were considered arbitrarily to be those with amplitudes equal to three times the average noise level.

The effects of the large rise in propellant surface temperature, associated with the initial flow transients, on the ignition events were expected to be most pronounced for the case of a large amount of free stream oxidizer (section III-H). In particular, the possibility of transient ignition during the flow transient period was predicted. This phenomenon was indeed observed experimentally. Figure 51 shows the ignition data obtained from the six photo-detectors for M30 propellant under 50%  $O_2$ , 50%  $N_2$  flow. As expected, that phenomenon is most pronounced at the front stagnation point (detector #1) where the surface temperature rise is the largest, and less pronounced at the separation point (detector #4). The fluctuations of the photo-detectors' signals are most likely related to the fluctuations of the heat flux, discussed in the previous paragraph. Indeed, fluctuations of the detectors signals were observed for all the tests conducted. Note that the shock wave luminosity in the visible spectra (detector #5) interferes with the detection of the transient ignition. The transient ignition is detectable by the other detectors only after filtering.

#### (ii) Ignition Data from the Line Scan Reticon Camera

The principle of operation of the Reticon camera is discussed in Section IV-D. The calibration of the camera output is shown in Fig. 52-A. The same arrangement shown in Fig. 32 was used. Most of the 64 photo-diodes of the camera are focused on the 180 degrees of the exposed cylinder circumference. The light source which subtends less than 10 degrees is detected by only 4 photo-diodes (indication of the sharp focusing and spatial resolution obtainable with the camera lens system). In order to achieve maximum time resolution of the data, (each photo-diode is scanned every 0.2 ms for duration of 0.2 / 69 ms), the camera output was recorded on the tape. Display of the camera output for M30 propellant igniting under flow containing 10%  $O_2$  is given in Fig. 52-B. Ignition occurs after about 31 scanning periods. That corresponds to 6.2 ms. Horizontal amplification

of the signal is given in Fig. 52a -A,B,C. The signal is distorted to some degree due to frequency response limitations of the tape-recorder and due to signal saturation (as intense flame is established). The onset of ignition is easily detectable in sub-figure B. Based on the calibration (Fig. 52-A), the first ignition location is around the 90 deg. point. As seen from sub-figure C ignition occurs next at the front stagnation point and shortly after at the rear stagnation point. That kind of signal display, in addition to indicating the first ignition delay time and location, also depicts the time-wise and space-wise extent of flame spread. A much better and undistorted signal may be obtained using more advanced instrumentation. The future use of line scan cameras for ignition and flame spreading detection seems to be very promising.

### (iii) Ignition Data from High Speed Motion Photography

Ignition delays based on high speed photography (color films) were generally longer than the ones measured using the photo-detectors. The reasons for it: a) low time resolution - greater than 0.2 ms at 5000 frames/s, and b) the exposure time at the high framing rate was not sufficient to record the earliest stage of flame development. As already discussed, the onset of ignition was rapid and flame radiation was most intense in the high free-stream oxidizer ignition cases. For these cases, the ignition delays measured from the high-speed film (which records in the visible spectra) were in good agreement with the ones measured from the photo-detectors (which record the radiation in the near ultra-violet).

The pictures taken through the side windows of the test section recorded the flame distance from the surface at ignition time and its thickness. In all cases photographed, the first detectable flame was anchored to the surface. Fig. 53 is an example of a high-speed motion picture sequence of propellant igniting. Within 0.25 ms of the onset of convective heating, vapors originating at the front surface have been ignited and are burning. During the transients to full flame development, the vapors burned out and then re-established permanently within the next 0.5 ms. After another 1 ms, the combined effects of convective heating and heat feedback from the propellant decomposition produced sustained combustion over the entire surface of the cylinder

### V-D. Ignition Trends for the Various Propellants

Because of their ignitability over a wide range of free stream conditions, the vast majority of tests were conducted systematically with M30 and M26 (containing graphite) propellants.

Ignition data are given here for M30 triple-based propellants for constant pressure and temperature (solid lines of Fig. 54), for constant velocity and temperature (dashed lines on Fig. 54), and for constant pressure and constant higher temperature (Fig. 55). The choice of Reynolds number as the coordinate in Figs. 9 and 10, though somewhat arbitrary, is logical since only one parameter varies along each curve, either the velocity (or  $t_p$ ) or the pressure (density). Indeed the Reynolds number could have been replaced by any of the Damkohler numbers. The inert heating of the propellant during the steady state period prior to gasification is also a function of Reynolds number only. As shown in Fig. 56 a similar series of experiments were conducted for the double-based propellant M26 which contains graphite. The trends of the results are discussed next.

The solid lines (velocity variation only) in Figs. 10 and 11 are the best fits to the results of scores of tests. As is evident, the trends are most dependent on the level of  $O_2$  in the free stream. As expected, shorter ignition delay times are obtained for the higher free stream  $O_2$  cases; however, the dependence of the ignition delay on the Reynolds number is much more complex and one must consider the location of the first ignition. For that purpose, a statistical histogram was constructed (Fig. 57) which presents the locations of first ignitions and the consequent flame spreading tendencies, as they depend on the Reynolds number and  $O_2$  content of the flow (M30 propellant). As can be seen from Fig. 57, in the range of Reynolds numbers 1000-7000 ignition tends to occur first at the front stagnation region, regardless of the free stream  $O_2$  content. The transition to rear stagnation region ignition occurs at higher Reynolds numbers preceded by separation region ignition. In all cases ignition was detected distinctly first at any of the aforementioned regions and not elsewhere on the cylinder circumference. This is in accordance with the theoretical predictions of Section III. In essence, Figs. 9-11 are compilations of the ignition delay times of the three main regions of ignition, and the complexity of the ignition curves reflect the transitions of ignition preference from one region to the other. Note the ignition delay values on the solid line of 100%  $N_2$  in Fig. 54. For the low Reynolds numbers they drop steeply to a minimum, rise slightly, and then start dropping steeply again to a point of no ignition. This behavior reflects the transition from front stagnation region to rear stagnation region ignition. Indeed, the theoretical prediction expressed in Fig. 23 indicates the attainment of a minimum value for ignition delay time for front stagnation ignition under inert flow. The role of the Damkohler number of the flow (which decreases as the Reynolds number increases) on the ignition delay and location was emphasized in Section III. If it becomes sufficiently small, ignition may not be realized at all, particularly the ignition under inert flow.

Effects of Damkohler number ( $D_G$ ) and hydrodynamic mixing on ignition times and trends are demonstrated by the results obtained from a series of tests with partially inert, partially M30 propellant cylinders under various flow conditions (Fig. 58). The contribution of the propellant vapor evolving from the front surface to ignition promotion at the rear surface, is demonstrated in cases A and B. Note that the effect is most pronounced in the inert flow case C. Note also that in the last case (C) the flame does not spread to the front surface at all but it does spread in case A though the Reynolds number of the latter is smaller than that of the former. That demonstrates the effect of the free stream  $O_2$  on ignition promotion and flame spreading. Note, in particular, that the observed ignition time in case B at  $\phi = 0$  deg. is greater than that for  $\phi = 180$  deg., even though the heat flux for  $\phi = 0$  is larger than that for  $\phi = 180$ . Referring to Fig. 7, the flow in region (3) around  $\phi = 180$  deg. resembles the flow around  $\phi = 0$  deg.; however, the residence time of the former may be much greater, thus possibly the local  $D_G$  is larger than at  $\phi = 0$  deg., and the ignition time is shorter (see Section III-I).

The wavy shape of the ignition delay curve for the inert flow in Fig. 54 is more pronounced in Fig. 55 which is for the corresponding higher ambient temperature case. It may be due to more prominent competition between the various rate processes. The rates of inert heating and chemical reactions increase while the residence time of flow is reduced (since for a given Reynolds number the decrease in density which is associated with the increase in temperature is compensated by an increase in velocity). While

comparing Fig. 55 to Fig. 54, note that the no ignition point of Fig. 55 has a lower ignition delay but ignition occurs for lower Reynolds number.

Compared to M30, M26 ignites much more rapidly (Fig. 56). Indeed, for the 10 and 50%  $O_2$  conditions, ignition occurs in sub-millisecond time which is within the transient settling period of the flow. As discussed in paragraph B of this section, the propellant surface temperatures at the front and rear stagnation points rise momentarily to levels above the gasification temperature and if sufficient free stream oxidizer is present, a situation of transient or sustained sub-millisecond ignition may be obtained (Fig. 25). For the case of 50%  $O_2$ , 50%  $N_2$  (Fig. 26), ignition occurs at a very early stage of the flow development; hence there is no dependence on the Reynolds numbers (which are associated with the steady flow). Indeed for this case ignition occurred almost simultaneously at the front and rear stagnation points. The reduction of ignition delays for the M30 propellant (Fig. 54) in the 50%  $O_2$ , 50%  $N_2$  case, as the Reynolds number zero is approached, is probably also a consequence of the initial flow transients. The residence time is sufficiently long for the accumulating reactants to ignite while the surface temperature is still much above the gasification point.

Though seemingly the effect of the initial flow transients on the ignition trends is a drawback of the experimental facility (one might have preferred steady conditions from time zero), nevertheless the data obtained are valuable since initial flow transients occur in practice and they accompany all shock-induced flow.

The trend of the delay time curve for M26 under inert flow (Fig. 56) is different from that of M30. It is discussed in paragraph F in connection with the flame spreading trends of M26.

As seen from Figs. 54 and 56 (dashed curves), the ignition delays are very sensitive to the ambient pressure,  $P_E$ , (i.e., to the density). The trend is for a given Reynolds number or velocity, the ignition delay decreases or increases as the  $P_E$  increases or decreases. This trend is explained from the effects of  $P_E$  on the ignition delay times,  $t_{thermal}$  and  $t_{chemical}$ .

Increasing  $P_E$  results in the shortening of  $t_{thermal}$  due to the following reasons: a) if the velocity,  $U_E$ , is kept constant, the Re number increases with  $P_E$  (dashed curves on Figs. 54 and 56) and so do the inert heating rates, and b) the large initial temperature rise associated with the initial flow transients is much steeper for a higher  $P_E$  (this effect is expressed in Figs. 18 and 48 and discussed in paragraph B). Even if  $P_E$  is raised while the Re is kept constant (i.e.,  $U_E$  is decreased), the effect expressed in item b) is very pronounced.

The effect of  $P_E$  on  $t_{chemical}$  is complex. The  $t_{chemical}$  is adversely dependent on the magnitude of the instantaneous reaction rate, RR, which may be expressed as  $RR \propto D_G \cdot Y_{OX} \cdot Y_F \cdot f(T)$ . The concentrations  $Y_{OX}$  and  $Y_F$  depend directly on the values of the Damkohler numbers  $D_G$  and  $D_S$  (see Section III). For the dashed curves of Figs. 54 and 56,  $D_G \propto P_E$  and  $D_S \propto 1/P_E$ ; hence it is difficult to assess the effect of raising  $P_E$  on  $t_{chemical}$ . Note that in the case where there is significant amount of free stream oxidizer,  $Y_{OXE}$ , the  $t_{chemical}$  is rather sensitive to the partial pressure of the oxidizer,  $P_{OXE}$ , since  $RR \propto P_{OXE} \cdot Y_F$ . The similarity in ignition trends for pressure

variations in the cases  $Y_{O_2}=0$  and  $Y_{O_2}=0.1$  in Figs. 54 and 56 implies that the main pressure effect is through  $t_{thermal}$ .

General ignitability diagrams of the various propellants (and Plexiglas) tested are given in Figs. 59 and 60. The main results and trends are:

A. Compared to triple-based, single-based and double-based propellants ignite more rapidly in oxygen-containing flows.

B. The higher the oxygen content of the free stream, the shorter is the ignition delay time and the ignition site tends toward the front stagnation point (Fig. 57).

C. Flame blow-off phenomena occurred for low free stream oxygen concentration, low Damkohler number flows (i.e., high Reynolds number flows).

D. In the cases of single and double based propellants, as well with Plexiglas, ignition under 50%  $O_2$  flow conditions occurred many times within the initial flow transient time characterized by an almost simultaneous ignition at both front and rear stagnation points.

E. The high heating rates associated with higher velocities (i.e., higher Reynolds numbers) do not necessarily result in shorter ignition delay times (Figs. 54, 55), since the Damkohler numbers are lower.

The ignition trends expressed in items B, D and E have already been discussed. The following paragraph deals with possible mechanisms relating to the effects of free stream oxidizer ( $O_2$ ) on the ignition trends expressed in item A.

#### E. The Sensitivity to Free Stream Oxidizer ( $O_2$ )

##### (i) Propellant Ignition

As already mentioned, no ignition was obtained under pure inert conditions for the single and double based propellants. In fact, even increasing the free stream temperature and pressure to values up to 2400 K and 2.1 MPa did not result in ignition in those cases. On the other hand, as seen from Fig. 60, M26 without graphite ignited with as little as 2%  $O_2$  in the free stream under the nominal condition of free stream temperature and pressure of 1875 K and 1.7 MPa, respectively. M30, the triple-based propellant, ignited under inert gas conditions and was much less sensitive to the amount of free stream oxygen.

The effects of possible impurities of  $O_2$  in the inert gas ( $N_2$ ) were deemed insignificant. Typically, in order to dilute residual impurities (air) in the shock tunnel, the test gases (being 99.99% pure) were pumped in and out of the driven section several times prior to each test. By this process, the  $O_2$  impurity in the inert tests was limited to a range of less than 0.01% (in the nominal tests) up to 0.5% (in selected tests). In that range, the effect of the impurities on ignition was negligible, i.e., no ignition in the case of single- and double-based propellants (which did ignite for 2%  $O_2$ ) and identical ignition delays for the triple-based

propellant.

The inert heat transfer rate to the propellant is not affected appreciably by the ratio of  $O_2/N_2$  of the free stream during most of the ignition delay time. Thus, the contributions of the chemical reactions and flame structures of the propellants are the sources of the observed effects of  $O_2$  and the differences in propellant type. In addition, the propellants do not differ significantly in their thermal properties. Gasification temperatures of the propellants were always achieved during the test time as was evident from the high speed films and from the post-test diameter measurements and surface structure examination.

The compositions of the practical propellants M1, M26, and M30 are given in Table 1. The main component of M1 is nitrocellulose (NC), 83%. The main components of M26 are NC, 67% and nitroglycerin (NG), 25%. The main components of M30 are NC, (28%), NG, (22%) and nitroguanidine (NGU), 48%. Thus, NC is the major component in M1 and M26, and NGU is the major component in M30. Both M26 and M30 contain about the same amount of NG.

Table 1 also specifies the main atomic compositions of the homogeneous propellants tested and their oxygen balance (for complete combustion of their hydrogen and carbon contents). The M30 propellant contains slightly less oxygen than the other propellants but its oxygen balance is not as negative since it also contains less carbon. Thus, the atomic composition of M30 does not directly explain the differences in the ignition trends between M30 and the other propellants, particularly with respect to ignition under inert flow.

Though M1 is less energetic than either M26 or M30, it demonstrates approximately the same trends as M26 (ignition delay times being only slightly longer than the latter). Ignition trends similar to M1 were found for the NC/TMETN propellant which is the least energetic of all propellants (contains only 54% NC, the other component is less energetic than NG or NGU). Thus, it is concluded that the major difference is in the decomposition products and the flame structure of NGU versus NC.

Basically NC is a nitro compound including nitrate esters ( $C - O - NO_2$ ), and NGU is a nitro compound including nitramine ( $C - N - NO_2$ ). The mechanism of double-based (nitrate esters) propellant combustion have been widely studied (see Ref. 111 for a recent study).

The major features are:

- a) Decomposition products are:  $NO_2 + CH_2O +$  higher hydrocarbons.
- b) Flame zone temperature profile is subdivided to fizz zone, dark zone, and luminous flame zone.

The temperature gradient is the steepest in the fizz and luminous flame zones, and relatively flat in the dark zone (Fig. 1). It should be remembered, however, that this kind of profile is superimposed on the boundary layer profile and will be strongly affected by it. With respect to ignition, it is assumed (though there is no definite proof to it) that the fizz and dark zones already exist during the early stage of the ignition process. Indeed, the fizz zone (being close to the surface) is most important for ignition, since ignition occurs through the bootstrapping

process of gaseous phase/solid phase interactions. The dark zone temperature gradient being relatively low inhibits the transfer of energy from the luminous flame zone. After the boundary layer exists, the stage of luminous reaction zone may not be realized, since the reactants are diluted by the convective flow away from the surface.

$\text{NO}_2$ , a very strong oxidizer, is reduced in the fizz zone to NO and the principal fuels emerging from this zone are  $\text{H}_2$  and CO [112]. Thus, the combustion is incomplete and only about half the energy stored in the double-based propellant is liberated there. The reasons for it are: a) NO has a large activation energy for oxidation reactions, and the temperature at the end of the fizz zone (or in the boundary layer close to the surface) is not sufficiently high, and b) the radicals which are necessary to take part in the highly exothermic oxidation reactions of  $\text{H}_2$  and CO are either depleted (H, OH), or initially nonexistent (O). (The reaction  $\text{NO}_2 + \text{M} \rightarrow \text{NO} + \text{O} + \text{M}$  has too large an activation energy to be significant in the fizz zone). Thus, any addition of H, OH and O radicals to the fizz zone may eliminate the dark zone and cause the luminous zone to collapse to the surface, resulting in one stage intense heat release zone close to the surface to provide the impetus for ignition.

The addition of even small amounts of  $\text{O}_2$  to the free stream replenishes the boundary layer with the above radicals. A possible mechanism is:  $\text{O}_2$  diffuses toward the surface where chain branching reactions of  $\text{O}_2$  with HCO and H (radicals which exist in the fizz zone) would supply OH radicals to the oxidation of CO, via  $\text{OH} + \text{CO} \rightarrow \text{H} + \text{CO}_2$ , thus liberating heat to accelerate the other reactions. Description of the above types of reactions may be found in Ref. 113.

In conclusion, the presence of  $\text{O}_2$  in the free stream shifts the major exothermic reactions toward the surface (by accelerating them) where the residence time of the flow is larger and heat transfer to solid phase is enhanced, and thus results in ignition. Higher rates of heat transfer to the surface in inert free stream conditions would merely increase gasification.

In the case of M30 most of the NC is replaced by NGU which is less energetic and its decomposition routes are different from NC. Proposed decomposition products of NGU are:  $\text{H}_2\text{NCN} + \text{N}_2\text{O} + \text{H}_2\text{O}$  or  $\text{NH}_3 + \text{N}_2\text{O} + \text{HNCO}$  [114]. From Ref. 111, the decomposition of  $\text{N}_2\text{O}$  is an initial stage in the overall kinetic mechanism. The decomposition is characterized by:



Thus the reactions may not form large amounts of NO, and CO is probably oxidized to  $\text{CO}_2$  in earlier stages. It is conceivable that the energy release is more concentrated and the flame does not exhibit multi-zone structure. Since there are also NC and NG decomposition products available in the gaseous phase, they supply the H radicals which facilitate faster decomposition of  $\text{N}_2\text{O}$  at the lower temperature close to the solid surface. It is also known [115] that  $\text{NO}_2$  reacts exothermically with NGU (heterogeneous surface reaction); however, the chemical kinetic data are not available.

There is also the possibility of carbonaceous residues being formed on the surface during NGU decomposition (as was found from microscopic scanning of extinguished M30 propellants during the test series -(Fig. 69)) and acting as flame holders since they may reach much higher temperature. However, based on the results of this study, it is believed that the main effects are due to gas phase chemistry rather than solid phase residues which may form only after ignition is already obtained.

In conclusion, unlike M26 and M1 (and NC/TMETN), M30 ignites even under inert condition due to an intense one-stage reaction zone. The sensitivity to  $O_2$  in the free stream is less, because the concentration of H and CHO, which start the reaction mechanism with  $O_2$ , should be lower in NGU flame than in NC flame.

#### (ii) Polymer Ignition

Ignition of Plexiglas was obtained only under 50%  $O_2$ , 50%  $N_2$  flow. This is attributed to the tendency of the flame, which in this case is a pure diffusion flame in a boundary layer flow, to come closer to the surface for the higher free stream oxygen content. (Note for example the location of the diffusion flame zone in Figs. 9-A and 12-B). A low oxygen content flame will tend to burn closer to the outer edge of the boundary layer, away from the surface, thus affecting only slightly heat transfer to the solid phase. The ignition delays obtained were within the initial flow transients period. It is known [116] that the pyrolysis rate activation energy of Plexiglas depends strongly on the regression rate; it is much larger for the lower regression rates. Therefore, if a flame is not established during the initial transient period when the regression rate is momentarily high, the flame may not be established at all.

#### V-F. Flame Spreading and Blow-off Phenomena

A general statistical diagram of the first ignition site and the direction of the consequent flame spreading for M30 propellant is given in Fig. 57. More detailed trends of ignition and flame spreading for M30 and M26 (+ graphite) propellants are depicted in Figs. 61 through 64. The time-wise and space-wise appearance of flame are given for various free stream velocities and oxygen contents as well as for various ambient pressures. Information concerning the rapidity of flame spreading is thus obtained. That information is very important for practical applications since flame spreading may occur only on a portion of the propellant surface, hence, resulting in uneven burning. Also, the duration of flame spreading may be on the order of the first ignition delay time. In this latter case it would be more appropriate to talk about an average ignition delay in connection with practical granular propellant ignition.

In general, it is difficult to distinguish between flame spreading and ignition, since the photo-detectors used detect the appearance of the flame only. In many cases though, ignition is clearly distinguishable from flame spread particularly at the main regions of ignition, i.e., front and rear stagnation regions and flow separation region. One or two of these regions may be ignited independently without any flame spreading between them prior to ignition. Independent ignition at some site as opposed to flame spreading related ignition is considered to occur when no flame exists at the adjacent sites prior to its occurrence. Flame spreading occurs through any or all of the following mechanisms:

A. Heat is conducted away from a local burning site along the surface thus raising local surface temperatures to values capable of sustaining flame above the surface. The flame may propagate either upstream or downstream of its source.

B. Heat is conducted away from the flame front in the gaseous phase and the flame propagates through the combustible mixture. In the case where free stream oxidizer is present, the flame propagates in two paths; through the inner pre-mixed reaction zone (closer to the surface) and through the outer diffusion zone (see Section III-H). In turn, each of these zones may trigger the other so that the flame propagation is accelerated. Propagation down-stream is favored since propagation upstream may be slower than the convective flow velocity.

C. The flame is convected away down-stream, thus heating rapidly the surface ahead of it and raising its temperature to a level capable of sustaining the flame.

Flame spreading trends for M30 propellant are depicted in Figs. 61-63. The five points, in the range 0-180 deg. on each trace, correspond to the intensity peaks in the outputs of detectors 1,2,3,4 and 6 in accordance with Fig. 33. In the absence of more data, the points were connected by straight lines. Figure 61 demonstrates the effect of free-stream velocity in the case of 10% oxygen in the free stream. In general, the tendency is for shorter ignition delays (first occurrence) for higher velocities. The trends for subsequent ignition and flame spreading are more complex; in that respect the following items are observed:

- a) In all cases, the appearance of flame at the front stagnation point is due to independent ignition and not flame spreading from upstream ignition sites (the curves slopes are positive at the 0 deg. points).
- b) Ignition occurs distinctly at one of the three regions of ignition (0, 90, 180 deg.).
- c) Flame propagation is faster down-stream than upstream. Propagation upstream is faster on the rear surface than on the front surface.
- d) Flame propagation upstream on the front surface is faster for lower velocities.
- e) As velocity is raised, flame tends to be established on the rear surface only. Ignition, if it occurs on the front surface, occurs only at the front stagnation region and flame does not propagate upstream.
- f) A phenomenon of flame blow-off is observed for the front surface. That phenomenon is more pronounced for the higher velocities.

In view of the flow patterns around the cylinder (Fig. 7) and bearing in mind the mechanisms for flame propagation, the trends expressed in items (a)-(d) are understood. The flow circulation at the wake promotes flame spreading on the rear surface. The high forward velocity of flow in the front surface boundary layer impedes flame spreading upstream there. The blow-off phenomenon is not obvious. It will be discussed separately later.

A comparison of the 10%  $O_2$  flow cases shown in Fig. 61 with the corresponding 100%  $N_2$  flow cases is depicted in Fig. 62. The latter have longer ignition delays than the former. Compared with the 10% cases, the flame in the inert flow spreads slower and is established at the rear surface only for lower Reynolds number of flow. These trends are predictable, considering the general role of the free stream oxygen in promoting ignition and flame spreading.

The dependence of the flame spreading trend on the ambient pressure is

shown in Fig. 63. The role of the ambient pressure in shortening the ignition delays was discussed in paragraph D. As may be seen from Fig. 63, the flame spreading is accelerated as the pressure is raised (while keeping the velocity constant) regardless of the oxygen content in the outer flow. This is in accordance with the general increase with pressure of all rate processes governing ignition attainment.

As already mentioned, M26 without graphite did not ignite under inert flow. M26 with graphite did ignite and its flame spreading trend (depicted in Fig. 64) might reveal the role of graphite in attaining ignition. Typically, M26 (+ graphite) ignited only at either the front or the rear stagnation point. Flame appearance was very faint and flame spreading was very slow. Referring to Fig. 56, the ignition delays for the inert flow case decrease with the Reynolds number similar to the M30 case and reach some minimum at a relatively low Reynolds number, but, unlike the M30 case, the ignition delays keep rising indefinitely thereafter with the Reynolds number until the point of no-ignition is reached (despite the transition to rear stagnation region ignition). Unlike the M30 case (Fig. 62) where the flame is eventually always established over the entire rear surface, the flame in the case of M26 was found sometimes to be established at the rear stagnation region only (Fig. 64 for  $Re_D = 9300$ ). Though flame blow-off was observed to occur, the flame lasted for a much longer period than for the M30 case.

Bearing all the above information in mind, it is believed that the effects of the graphite additive on the ignition are physical in nature. It is possible that the graphite particles (which undergo very little ablation at the typical burning surface temperatures) accumulate to some extent on the propellant surface to form local hot spots. Thus, heat conduction to the condensed phase is enhanced through the graphite particles (which also have very high heat conductivity), a factor which may locally enhance subsurface exothermic reactions. That explains why the flame appearance was quite faint and why it was anchored to the regions of the highest heat transfer and the lowest free stream velocities, i.e., the stagnation points. As the velocity is raised, the erosive effect of the flow removes the graphite layer before it accumulates and the ignition characteristics approach those of the M26 without the graphite.

It should be mentioned that the role of carbonaceous matter in double-based propellants was addressed in conjunction with the phenomena of super-rate and platonization of double-based propellant burning rates [48]. One explanation is [117] that the carbon catalyzes the exothermic reactions involving the reduction of NO. The experimental results of the ignition and flame spreading trends are in support of a physical effect of graphite rather than a chemical one. M26 propellants coated with graphite (as opposed to containing it) were successfully ignited under inert flow, but the ignition delays were longer than for the M26 containing graphite. M26 containing graphite under reactive flow behaves exactly like the M26 without the graphite. Ignition delay times were very short (Fig. 56) and flame spreading was very rapid (as compared to M30). NC/TMETN propellant containing graphite or carbon did not ignite under inert flow. This may be attributed to either lower activity of subsurface reactions or simply to the lower energy content of this propellant as compared to the M26 propellant.

As already mentioned, a phenomenon of flame blow-off was observed for the higher velocities-low oxygen content flows. The terminology of blow-off

does not include the situation of transient ignition depicted in Fig. 51. It is used in connection with the premature extinction of quasi-steady flame. When the flame is blown away from the rear surface, it results in total extinction of the propellant burning. These cases are shown in Fig. 57. In other cases, the flame blow-off occurs at the front surface while the rear surface continues its burning (see Fig. 61). The flame on the rear surface was sustained for relatively prolonged periods prior to extinction (up to 8 ms), unlike the flame on the front surface (up to 4 ms). In any case, the flame was sustained for longer periods than the typical heat flux fluctuation period (less than 2 ms). Thus, these phenomena are not directly associated with flow instabilities. Such phenomena were observed also in the Kashiwagi et al. [19] experiments using the present shock tunnel facility. Their test specimen was a polymer (pure fuel) having a flat plate geometry. Thus, in his case the flame was a pure diffusion flame burning in a flat plate boundary layer. The flame blow-off phenomena observed in the Kashiwagi et al. experiments started from an upstream location and exhibited similar trends to the present ones with respect to their sensitivity to the free stream velocity and oxygen content. Kashiwagi et al. dismissed the possibility of flow instability effects on the basis of the much longer time scale of the observed flame instability as compared to that of the flow. They suggested that the reason for the flame blow-off phenomenon was the mismatch between the fuel supply rate and the fuel consumption rate which is more pronounced for lower oxygen content flow cases when the reaction zone is further from the surface. They also found (numerically) that the gas phase reaction zone moves toward the surface with time-wise increasing reaction rate in the high free stream oxygen level case, but it moves away from the surface in the low oxygen level case. In the latter case it moves toward the faster, lateral-flow velocity and is blown away downstream. Though they did not elaborate on it, the reason for the movement of the reaction zone (in the low oxygen level case) toward the boundary layer edge may be due to the time-wise increase in local fuel concentration which is accumulated from the heated fuel surface pyrolyzed upstream of the flame front. Thus, the oxygen is fully consumed further away from the surface. It should be remembered that the burning situation in the test facility is a quasi-steady state (not steady state), since the thermal boundary layer in the condensed phase is not fully developed even by the end of the test time (18 ms) and the surface temperature (and its pyrolysis rate) is constantly increasing.

The present experimental case is different from that of Kashiwagi et al. in two important aspects: (a) the geometry of the specimen is that of a cylinder and (b) the specimen is an active propellant. The flame under inert flow is a pre-mixed flame and the flame under oxygen-containing flow exhibits dual structure; the inner reaction zone is of the pre-mixed type and the outer is of the diffusive type. Clearly, the mechanism leading to the blow-away of the reaction zone (discussed before) applies only to the diffusive zone and most likely to sites upstream of the front stagnation zone (e.g., Fig. 61,  $Re_D = 19200$ ). It may explain some of the blow-off phenomena at the rear surface when the burning occurs under the presence of free stream oxygen. It should be noted that sustained burning under high free-stream velocities in marginal cases is possible only with the assistance of the free stream oxygen. In that case, the dual structure of the flame is much less pronounced (e.g., Fig. 17) and sustaining the flame is sensitive to the diffusive zone distant from the surface, since it acts like a constant pilot to the flame.

Since flame blow-off phenomenon occurred also for burning under inert flow where the flame is of the pure pre-mixed type, another mechanism should be sought to explain that phenomenon. Flame extinction of double-based propellants, after the attainment of sustained flame, was observed in radiation ignition experiments [13] but it occurred only in a situation of rapid deradiation preceded by overdriven burning (i.e., the self-sustained burning was accelerated by intense radiation for some duration). In that case the extinction was due to mismatching in relaxation times of gas phase and condensed phase processes (they are much longer for the latter). The present experimental case is different from the go-no-go radiation ignition case in that the external heat supply source, i.e., the convective flow, is not removed after the attainment of flame but lasts for the entire test period. Therefore, even if some overdriven ignition situation occurs which results in flame extinction, it should be temporary and the propellant should be re-ignited later after a period of much shorter duration than the original ignition delay.

Realizing that the thermal wave in the condensed phase is still developing when the extinction occurs, a plausible explanation for the blow-off phenomena is as follows: as the thermal wave develops (and surface temperature increases) subsurface reactions become more prominent and general reaction paths may change to yield a somewhat different composition of propellant products. In turn, the reaction paths of those products may be shifted toward slightly higher activation energies. The effect of gas phase reaction activation energies on the attainment of ignition and self-sustained flame is very prominent (e.g., Fig. 13). Thus, in marginal cases (i.e., high, free-stream velocity inert flows) even slight variations in activation energy values may result in extinction. Since for burning under high velocity flow conditions, most of the surface heat flux is due to the convective flow (e.g., Fig. 15) rather than the flame, the thermal wave continues to develop even after extinction and re-ignition do not occur. It should be emphasized, however, that the chemical kinetics of NC-based propellants are poorly understood and the suggested explanation is only a hypothesis.

#### G. Ignition and Flame Spreading in Tandem Configurations

Three tandem configurations of M30 propellant specimens were tested under both inert- and oxygen-containing flows. Flame spreading tendencies are demonstrated in Fig. 65 for the three configurations. High speed shadowgraph photographs of the post-ignition flow around the cylinders are shown in Fig. 66.

The main results are as follows:

- A. For the shorter separation distance, the second cylinder ignites first under both inert and reactive flows and flame spreads rapidly from the rear surface of the second cylinder to the rear surface of the first cylinder through the combustible gas trapped between the two cylinders.
- B. As the separation distance between the cylinders is increased to more than three cylinder diameters, the first cylinder ignites first under inert flow but the second cylinder ignites first under reactive flow.
- C. For the reactive flow case, the flame spreads appreciably both downstream and upstream to occupy most of the space between the cylinders.

The trends obtained are best understood by looking at Fig. 5 which

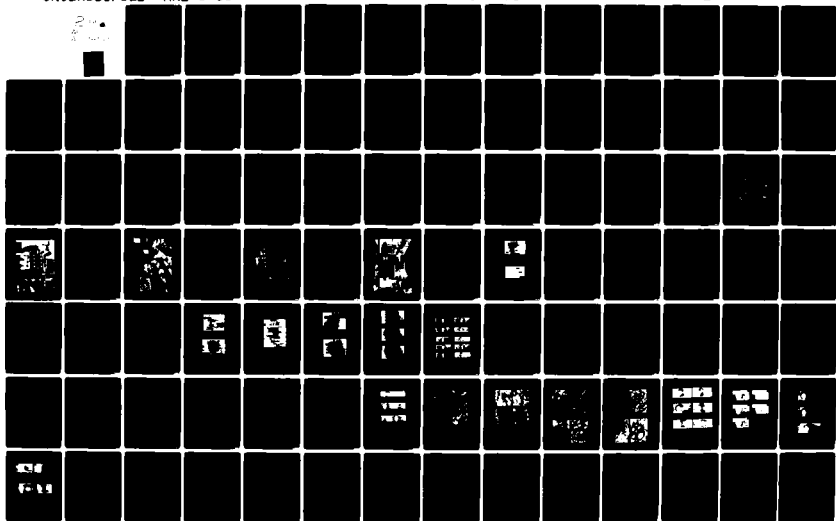
illustrates the flow patterns around cylinders in tandem configurations (see also Section III-C) as deduced by Kostic and Oka [62] from their convective heat transfer tests with cylinders. In the shortest separation distance case, the fluid is trapped in the space between the cylinders. The reactant products originating from the rear surface of the first cylinder and from the front surface of the second cylinder partly accumulate in the space between the cylinders and partly flow underneath the free shear layer of the first cylinder to accumulate in the wake of the second cylinder. In the absence of a flow renewal mechanism (i.e., vortex shedding) in the wake of the first cylinder, its surface temperature rises slower than that of the second cylinder. Thus ignition is favored at the rear surface of the second cylinder. Once ignited, the flame spreads rapidly to the first cylinder by means of diffusion through the combustible mixture and flow recirculation.

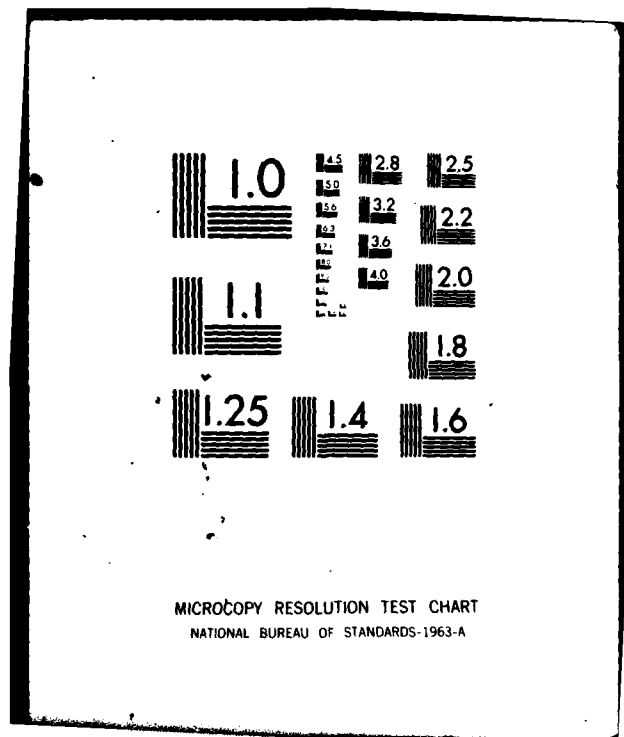
The case of the intermediate separation distance is close to the limiting case when the free shear layers which separate from the first cylinder impinge on the front surface of the second cylinder (see Fig. 6). In that limiting case, there is relatively little reactant flow (which originates from the space between the cylinders) to the wake of the second cylinder. Thus, in the case of inert flow, ignition may be favored at the separation zone of the first cylinder where reactant concentration is high and flow residence time is long. (The surface temperature is not much lower than that of the rear stagnation point because of the absence of the flow renewal mechanism). In the case of reactive flow, ignition may be favored at the rear surface of the second cylinder since the free stream oxygen has more access to it than to the rear surface of the first cylinder. As seen from Fig. 5 and from Fig. 66, the boundary layer of the second cylinder separates at around 120 deg. which indicates transition to turbulent boundary layer separation. The heat transfer rates at the rear surface of the second cylinder are then compatible with critical flow situation (Section III-C) and have a peak at the separation point.

As the distance between the cylinders is increased further, there is a regular vortex formation behind the first cylinder and the second cylinder is immersed in the far wake turbulent flow of the first cylinder. Thus, heat transfer rates are increased over the entire second cylinder surface. The highest heating rates are around the 120 deg. points of the second cylinder; thus first ignition is favored at these points in the reactive flow case. However, at that site under inert flow, there is probably too much dilution of the propellant reactive vapors with the free stream inert gas due to turbulent mixing, so that ignition is favored at the rear surface of the first cylinder.

In all cases when ignition occurred first on the second cylinder, the tendency was toward shorter ignition delay times than for the corresponding one-cylinder configuration case. In all cases when ignition occurred first on the first cylinder, the ignition delays were about the same as for the corresponding one-cylinder configuration case. It should be mentioned, however, that relative to the one-cylinder configuration, only a small number of tests were conducted with the tandem configurations. More tests are required to confirm the above trends.

AD-A091 852 PRINCETON UNIV NJ DEPT OF MECHANICAL AND AEROSPACE --ETC F/G 19/1  
CONVECTIVE IGNITION OF PROPELLANT CYLINDERS IN A DEVELOPING CRO--ETC(U)  
SEP 80 A BIRK, L H CAVENTY DAAG29-79-C-0140  
UNCLASSIFIED MAE-1486 ARO-13108.1-E NL





MICROCOPY RESOLUTION TEST CHART  
NATIONAL BUREAU OF STANDARDS-1963-A

#### H. Microscopic Study of the Specimen Surface

Several post-test specimen surfaces were scanned using a scanning electron microscope. Typical surface pictures of the major propellants, tested under 10% O<sub>2</sub>, 90% N<sub>2</sub> flow, are shown in Figs. 67 through 80. The propellants were extinguished by the cold flow and pressure drop at the end of the test period. Although there is no assurance to this effect, it is assumed that only a slight erosion and surface regression took place during the long post-test period of flow subsidence. The pictures were taken under two magnifications in order to obtain both general and detailed views of the surface.

Pre-test machined surfaces of M30 and M26 (+ graphite) propellants are shown in Figs. 67 and 68. The roughness scale is less than 2  $\mu\text{m}$ ; thus it is expected to have little effect on the boundary layer flow which is thicker than 200  $\mu\text{m}$  at the time of ignition (e.g., Fig. 10). The terminology "gasified" in Figs. 67 and 68 refers to the front surfaces on which flame appearance was not detected (but surface regression was evident). Both M30 and M26 gasified surfaces have a wrinkled appearance. The wrinkles are orderly and oriented in one direction. The M30 gasified surface is slightly rougher than the M26 surface and unlike the latter it is porous. The burnt surfaces of M26 and M30 are different in appearance. Small submerged pores are observed on the M26 surface which otherwise is still wrinkly (though the wrinkles dimensions are much larger). The M30 surface indicates "volcanic" type activity. The surface is riddled with craters (up to 10  $\mu\text{m}$  in diameter), and porous agglomerate formations protrude from it (up to 50  $\mu\text{m}$  size). Elongated NGU crystals are clearly distinguishable around the craters. Those features of the M30 burnt surface are much more pronounced at the front stagnation point area (Fig. 69) where the lateral flow velocity is lower. The separation point area is covered with loose NGU crystals, probably convected there from the entire front surface.

The indication is that in the case of the triple-based M30 propellant, propellant decomposition and gasification are more likely for the NC and NG components than for the NGU component. The craters and pores may be an indication of either strong subsurface gasification or chemical reactions. In the case of the M30 propellant, the mechanism of heat transfer in the condensed phase after the attainment of flame is probably three-dimensional, since the scale of surface roughness is comparable to that of the thermal wave and the upper surface layer is clearly non isotropic. It is difficult though to draw any conclusions from those pictures concerning the effects on ignition process and flame spreading (and blow-off) phenomena.

The burnt surface of the NC/TMETN propellant (Fig. 70) is quite smooth in comparison to the other propellants; however, it is riddled with large diameter pores (up to 20  $\mu\text{m}$ ). Of the propellants tested, this is the only propellant not subjected to a high pressure extrusion process which would tend to decrease the size of entrained gas pockets. The NC/TMETN propellant is softer than the other propellants and therefore its relative surface smoothness may be due to mechanical erosion. The molten appearance of the HMX burnt surface indicates the existence of a liquid phase on the burning surface.

### I. Photographic Study of Specimen Burning Under Various Flow Conditions

A kaleidoscope of burning phenomena of cylindrical propellants under cross flow conditions is shown in Figs. 71 through 74. The pictures (in color) were taken at a rate of about 5000 frames/s through the shadowgraph system shown in Fig. 30. The pictures which show the post ignition quasi-steady burning are very valuable in explaining some of the ignition and flame spreading trends. The extent of flame convection downstream of the wake is important for the tandem ignition situation.

An interesting observation is that the vortex shedding from the wake persisted even after the ignition when combustion in the wake was clearly visible. Vortex shedding was evident in the inert flow cases (pure pre-mixed flame) as well as in the oxidizer ones for the entire range of velocities. Past studies with the stabilization of a pure pre-mixed flame in the wake of a cylinder (e.g., Ref. 118) found that the vortex shedding phenomenon disappeared in intense flame situations. However, unlike those studies, the present situation is different in two important aspects: a) the approaching flow is very hot and therefore the density gradients along the boundaries of the flame and the free stream are not that severe, and b) the outer flow is not of the pre-mixed type (it is inert or oxidizer); thus, the flame has no tendency to propagate into the free stream and interferes less with the fluid dynamics.

The main structures of flame are exhibited in Fig. 71 in which a series of pictures show the burning of Plexiglas under 50%  $O_2$ , 50%  $N_2$  low velocity flow. Under such conditions the specimen was not extinguished at the end of the test time and kept burning well into the cold flow period. Its final extinguishment was preceded by a series of sequential events of reignition-extinction in correlation with the wave motion in the shock tunnel. During that period the flow velocity and temperature vary widely and the oxygen is diluted by the driver gas (helium). The pictures shown in Fig. 71 were taken during that aforementioned period. Thus in a way, they are a compilation of burning phenomena observed during the test periods of many tests conducted under a wide variety of flow conditions. Of all the materials tested, the Plexiglas flame was the brightest and thickest. In particular, note (pictures B and F) that despite the existence of an intense flame the vortex shedding from the wake continues (in fact it is more conspicuous) and the burning in the shedded vortices continues for a considerable period (the flow velocity is low, thus the turbulence level at the wake is low and the flame pockets keep their identity for a few cylinder diameters downstream). Thus, the chemical kinetics is not fast compared to the residence time of flow around the cylinder. Picture C shows the burning as the flow is momentarily brought to a halt (due to wave motion). Picture F shows distinct burning at three regions; at the thin front stagnation boundary layer, on the rear surface, and along the inside of the fuel rich free shear layer extending from the separation point. The last item implies flow circulation in the wake, since the pure fuel vapor (Plexiglas) requires oxygen for burning.

A sequence of pictures of M30 propellant burning under 10%  $O_2$  low velocity (5.6 m/s) flow is shown in Fig. 72. The flames of the M30 and NC/TMETN propellants were very faint and difficult to detect photographically. The M30 flame in the pictures of Fig. 72 which is

visually distinguishable at the front surface boundary layer was found by the photo-detectors to exist also on the rear surface. The boundary layer fluctuations indicate free stream velocity fluctuations (also deduced from the heat flux data). The large thickness of the boundary layer is due to: low velocity, high degree of surface gasification, and decreased gas density in the flame zones. Note that two flame zones are clearly visible. The dark zone between the flames is the zone where the second derivative of the temperature profile assumes the largest values (shadowgraph pictures). The existence of such a zone was predicted numerically (Section III-H) for burning under low velocity oxidizer containing flow (e.g., Fig. 9).

The flame thickness and the distance it is convected downstream are reduced as the flow velocity is increased. Figure 73 is a demonstration of that effect. Note that despite the very intense flame in the wake, a formation of vortices is still noticeable in situation B. A dark zone around the separation point is noticeable in the lower velocities cases (A, B). The same zone appears very bright in the higher velocity case (C). Possibly, in the lower velocity cases most of the gases originating from the front surface burn while they are still there (large Damkohler number) and little burning occurs around the cooler separation area. However, in the higher velocity cases, most of the gases originating from the front surface burn at the long residence time separation region. As the velocity is increased, the wake turbulence level increases and its integral length scale decreases, so that the wake reactants are diluted more rapidly and the flame extends to shorter distances downstream of the rear surface.

The transition to flame extinction for the cases A and B of Fig. 73 is shown respectively in cases B and A of Fig. 74. As might be expected, the flame is extinguished last at the rear stagnation zone. A comparison between the flame luminosity of M30 propellant (C) and the flame luminosity of M26 propellant (D) is also given in Fig. 74. The flame in case D is much more luminous than that of case C though the flow in case C is much lower in free stream oxygen content and the velocity is higher.

As may be seen from the series of pictures in Figs. 71 through 74, the onset of the flame has little effect on the fluid dynamics of the flow around the cylinder. The separation point location and the vortex shedding frequency do not change appreciably.

## SECTION VI

### CONCLUSIONS

The major conclusions of this research are:

- (1) The shock tunnel was successfully used to obtain ignition of cylindrical nitrocellulose-based propellants under cross flow conditions. The reproducibility of the test conditions was very good and as such the shock tunnel serves as a valuable tool in comparison studies of propellant ignitability under high convective heat fluxes (simulating practical situations). Given the brevity of the convective heating period, one should, however, exercise caution in interpreting the ignition results, particularly in cases of very short ignition delays (sub-millisecond). The transient flow conditions associated with the boundary layer development and the starting process of the flow result in extremely high heat transfer rates for a considerable portion of the ignition delay time. Indeed, in the shortest ignition delay cases, most of the ignition stimulus is provided during that transient flow period. In that respect it is necessary to know the time-wise heat transfer rates in the shock tunnel. One should not rely on empirical data of convective heat transfer under steady state conditions.
- (2) Depending on the test conditions, ignition was found to occur first in three distinct sites; the front stagnation region, the flow separation region, and the rear stagnation region.
- (3) Free stream oxygen content of the flow had a very dominant effect on ignition delay times and sites, particularly for low and moderate Reynolds numbers (up to 122,000). A higher content of oxygen in the free stream would reduce the ignition delay time considerably and shift the site of ignition toward the front stagnation point. This is a very important result, since in actual situations the flow usually contains oxidizing gases, e.g.,  $\text{NO}_2$ ,  $\text{NO}$ .
- (4) Single- and double-based propellants containing nitroglycerin and/or nitrocellulose could not be ignited under inert gas conditions (only one propellant containing graphite ignited). They ignited, however, when even small amounts of oxygen were present in the free stream. Triple-based propellant containing nitroguanidine as a major component ignited under inert conditions and was less sensitive to the oxygen content of the flow compared to the other propellants.
- (5) Compared to triple-based propellant, single- and double-based propellant ignited more rapidly in oxygen-containing flow.
- (6) A numerical solution was obtained for front stagnation ignition under transient flow conditions. As ignition was obtained, the solution always successfully yielded the transition to quasi-steady burning. Notably, in cases when the transition from ignition to fully developed flame is rapid, the values of surface temperature and heat flux overshoot prior to stabilizing on their steady state levels. Also, as the flame is developed two distinct flame zones are found in the case of fuel rich propellant burning under oxygen-containing flow. The ignition likelihood at other sites rather than the front stagnation was analyzed phenomenologically considering the front stagnation solution and the structure of flow around

cylinders. The experimental trends conformed qualitatively with the theoretical predictions.

(7) The role of the finite Damkohler numbers in determining ignition delays and sites was identified both theoretically and experimentally. It is concluded that for the present experimental conditions (which are typical to practical cases) the ignition of nitrocellulose-based propellants is a gas phase phenomenon. In particular, it is found that for sufficiently low Damkohler numbers ignition is not realized at all despite very high heat transfer rates to the propellant.

(8) Phenomena of partial and full premature flame extinction (or blow off) were observed in high-velocity, low-oxygen-content flow cases. An explanation based on time-wise shifting of chemical reaction paths is suggested.

(9) In that respect (Item 8) and referring to items 3, 4 and 5, it is clear that basic experiments are required to identify the key chemical reactions and flame structure of double- and triple-based propellants burning in inert and reactive environments, particularly during the initial stage when the solid phase thermal wave is not fully developed. Subsidiary measurements are required to identify surface dynamics phenomena, e.g., infrared pyrometer and high-speed photomicrography of the burning surface.

(10) In tests conducted with tandem configurations, the flame was observed to spread and fill most of the space between the propellant specimens. It is possible that ignition and burning of a bank of propellant cylinders (packed bed situation) may proceed in an explosive manner as the partially reactive decomposition products, accumulated from the propellants, ignite at once in a bulk situation. It is proposed, therefore, to devise experiments to study that effect.

(11) The investigation of the effect of rapidly developing pressure fields on the dynamics of the transition period from ignition to full flame development (as such is the case encountered in practice) is suggested.

(12) To summarize, the present work has identified specific ignition and flame spreading phenomena pertaining to practical applications and has elucidated many of the important factors in high heat transfer, transient convective flow ignition situations.

LIST OF REFERENCES

1. Most, W. J. and Summerfield, M., "Starting Thrust Transients of Solid Rocket Engines", AMS Report No. 873, Princeton University, Princeton, N.J., July 1969.
2. Summerfield, M., Shinnar, R., Hermance, C. E. and Wenograd, J., "A Critical Review of Recent Research on the Mechanism of Ignition of Solid Rocket Propellants", Aeronautical Engineering Laboratory Report No. 661, Princeton University, Princeton, N.J., August 1963.
3. Price, E. W. , Bradley, H. H. , Dehority, G. L. and Ibiricu, M. J. , "Theory of Ignition of Solid Propellants", AIAA Journal, Vol. 4, No. 7, 1966, pp. 1153-1181.
4. Merzhanov, A. G. and Averson, A. E. , "The Present State of Thermal Ignition Theory: An invited Review", Combustion and Flame, Vol. 116, 1971 pp. 89-124.
5. Bhaskaran, A. and Ramaprabhu, R., "Review of Solid Propellant Ignition Theories with Particular Reference to Their Application to Shock Tube Data", National Conference on Internal Combustion Engines and Combustion, 3rd, Roorkee, India, Dec. 10-12, 1976, Proceedings. (A78-27826 10-25) Meerut, India, Sarita Prakashan, 1976, pp. 431-441.
6. Altman, D. and Grant, A. F. , "Thermal Theory of Solid Propellant Ignition by Hot Wires", Fourth Symposium (International) on Combustion, Williams and Williams Co., Baltimore, Maryland, 1950, pp. 158-161.
7. Zarko, V. E. and Khlevoni, S. S. , "Hot Wire Ignition of Ballistic Propellants", Fizika Goreniya i Vzryva, vol. 4, No. 2, 1968, pp. 158-170.
8. McAlevy, R. F. , Cowan, P. L. and Summerfield, M., "The Mechanism of Ignition of Composite Solid Propellants by Hot Gases", Progress in Astronautics and Rocketry: Solid Propellant Rocket Research, Vol. 1, edited by M. Summerfield, Academic Press, New York, 1960, pp. 623-652.
9. Shanon, L. J. , "Composite Solid Propellant Ignition Mechanism", United Technology Center, Sunnyvale, California, Technical Report No. UTC-2138-ASR1, May 1966.
10. Beyer, R. B. and Fishman, N., "Solid Propellant Ignition Studies with High Flux Radiant Energy as a Thermal Source", Progress in Astronautics and Rocketry: Solid Propellant Rocket Research, Vol. 1, edited by M. Summerfield, Academic Press, New York, 1960, pp. 673-692.
11. Derr, R. L. and Fleming, R. W., "A Correlation of Solid Propellant Arc Image Ignition Data", 10th JANAF Combustion Meeting, Newport, RI, CPIA Publication 243, August 1973.

12. Deluca, L., Caveny, L. H., Ohlemiller, T. J. and Summerfield, M., "Radiative Ignition of Double Base Propellants: I. Some Formulation Effects", AIAA Journal, Vol. 14, No. 7, 1976, pp. 940-946.
13. Deluca, L., Caveny, L. H., Ohlemiller, T. J. and Summerfield, M., "Radiative Ignition of Double Base Propellants: II. Pre-ignition Events and Source Effects", AIAA Journal, Vol. 14, No. 7, 1976, pp. 1111-1117.
14. Bastress, R. F. and Niessen, W. R., "Solid Propellant Ignition Studies", Arthur D. Little, Inc., Boston, Mass., Technical Report AFRPL-TR-66-32, February, 1966.
15. Peretz, A., Caveny, L. H., Kuo, K. K. and Summerfield, M., "The Starting Transient of Solid-Propellant Rocket Motors with High Internal Gas Velocities", AMS Report No. 1100, Princeton University, Princeton, N.J., April 1976.
16. Niioaka, T., Takahashi, M. and Izumikawa, W., "Ignition of Double Base Propellant in Hot Stagnation Point Flow", Combustion and Flame 1979, Vol. 35, pp. 81-97.
17. Baer, A. D., Ryan, N. W. and Salt, D. L., "Propellant Ignition by High Convective Heat Flux", Progress in Astronautics and Rocketry: Solid Propellant Rocket Research, edited by M. Summerfield, Vol. 1, Academic Press, New York, 1960, pp. 653-672.
18. Hermance, C. E., "Solid Propellant Ignition Studies: Ignition of the Reaction Field Adjacent to the Surface of a Solid Propellant", Princeton University, AMS report No. 674, December 1963.
19. Kashiwagi, T., MacDonald, B. W., Isoda, H. and Summerfield, M., "Ignition of Solid Polymeric Fuels by Hot Oxidizing Gases", AMS Report No. 947, Princeton University, Princeton, N.J., Oct. 1970.
20. Hicks, B. L., "Theory of Ignition Considered as a Thermal Reaction", The Journal of Chemical Physics, Vol. 22, No. 1, 1954, pp. 414-429.
21. Niioaka, T. and Williams, F. A., "Ignition of a Reactive Solid in a Hot Stagnation Flow", Combustion and Flame, Vol. 29, pp. 43-54, 1977.
22. Bradley, H. H., "Theory of Ignition of a Reactive Solid by Constant Heat Flux", Combustion Science and Technology, Vol. 2, 1970, pp. 11-20.
23. Linan, A. and Williams, F. A., "Theory of Ignition of a Reactive Solid by Constant Energy Flux", Combustion Science and Technology, Vol. 3, 1971, pp. 91-98.
24. Niioaka, T. and Williams, F. A., "Ignition of a Reactive Solid in a Hot Stagnation-Point Flow", Combustion and Flame, Vol. 29, 1977, pp. 43-54.
25. Hermance, C. E., Shinnar, R. and Summerfield, M., "Ignition of an Evaporating Fuel in a Hot Oxidizing Gas, Including the Effect of Heat Feedback", Astronautica Acta, Vol. 12, No. 2, 1969, pp. 95-112.

26. Hermance, C. E. and Kumar, R. K., "Gas Phase Ignition Theory for Homogeneous Propellants under Shock Tube Conditions", AIAA Journal, Vol. 8, No. 9, 1970, pp. 1551-1558.
27. Kumar, R. K. and Hermance, C. E., "Ignition of Homogeneous Solid Propellants Under Shock Tube Conditions: Further Theoretical Development", AIAA Journal, Vol. 9, No. 8, 1971, pp. 1615-1620.
28. Anderson, R., Brown, R. S. and Shannon, L. J., "Ignition Theory of Solid Propellants", AIAA preprint, No. 64-156, January 1964.
29. Williams, F. A., "Theory of Propellant Ignition by Heterogeneous Reaction", AIAA Journal, Vol. 4, No. 8, 1966, p. 1354.
30. Waldman, C. H. and Summerfield, M., "Theory of Propellant Ignition by Heterogeneous Reaction", AIAA Journal, Vol. 7, No. 7, 1969, pp. 1359-1361.
31. Ciepluch, C. C. and Allen, H., Jr., "Ignition of Solid Propellant Rocket Motors by Injection of Hypergolic Fluids", ARS Journal, Vol. 31, No. 4, 1961, pp. 514-518.
32. Bradley, H. H., "A Unified Theory of Solid Propellant Ignition", Naval Surface Weapons Center Report No. TP5618, China Lake, California, 1974.
33. Keller, J. A., Baer, A. D. and Ryan, N. W., "Ignition of Ammonium Perchlorate Composite Propellants by Convective Heating", AIAA Journal, Vol. 4, No. 8, 1966, pp. 1358-1365.
34. Bastress, E. K. and Niessen, W. R., "Solid Propellant Ignition by Convective Heating", Final Report, Arthur D. Little, Inc., Cambridge, Mass., Report AFOSR 67-0932, 1966.
35. Churchill, S. W., Kruggel, R. W. and Brier, J. C., "Ignition of Solid Propellants by Forced Convection", AIChE Journal, Vol. 2, No. 4, 1956, pp. 568-571.
36. Lisitskii, V. I. and Merzhanov, A. G., "Ignition of Condensed Substances by a Stream of Hot Gas", Fizika Goreniya i Vzryva, Vol. 1, No. 2, 1965, pp. 62-68.
37. Grigorev, Y. M., Lisitskii, V. I. and Merzhanov, "Ignition of Condensed Substance in Hot Gas", Fizika Goreniya i Vzryva, Vol. 3, No. 4, 1967, pp. 512-526.
38. Lisitskii, V. I., "Experimental Verification of the Thermal Theory of Ignition", Fizika Goreniya i Vzryva, Vol. 6, No. 2, 1970, pp. 230-233.
39. Kuo, K. K., Koo, J. H., Davis, T. R. and Coates, G. R., "Transient Combustion in Mobile Gas-Permeable Propellants", Acta Astronautica, Vol. 3, 1976, pp. 573-591.
40. Krier Herman, Rajan, S. and Van Tassell, W. F., "Flame Spreading and Combustion in Packed Beds of Propellant Grains", AIAA Journal, Vol. 14, No. 3, 1976, pp. 301-309.

41. Pantofliceck, J. and Lebr, F., "Ignition of Propellants ", Combustion and Flame, Vol. 11, No. 6, 1967, pp. 464-470.
42. Baer, A. D. and Ryan, N. W., "An Approximate but Complete Model for the Ignition Response of Solid Propellants", AIAA Journal, Vol. 6, No. 5, 1968, pp. 872-877.
43. Andersen, W. H., "Model of Transient Ignition to Self Sustaining Combustion", Combustion Science and Technology, Vol. 5, 1979, pp. 75-81.
44. Rozenband, V. I., Barzykin, V. V. and Merzhanov, A. G., "Ignition of Condensed Substances by Convective Heat Fluxes of Medium Intensity Under Dynamic Conditions", Fizika Goreniya i Vzryva, Vol. 4, No.2, 1968, pp. 171-175.
45. Rozenband, V. I., Averson, A. E., Barzykin, V. N. and Merzhanov, A. G., "Some Characteristics of Dynamic Ignition Regimes", Fizika Goreniya i Vzryva, Vol. 4, No. 4, 1968, pp. 494-500.
46. Nelson, C. W., Gough, P. S. and Robbins, F. W., "Ignition Transients in Flamespreading Calculations", 17th Aerospace Sciences Meeting, New Orleans, January 15-17, 1979, 79-0166.
47. Kubota, N., Ohlemiller, T. J., Caveny, L. H. and Summerfield, M., "The Mechanism of Super-Rate Burning of Catalyzed Double Base Propellants", AMS Report 1087, Princeton University, 1973.
48. Sing, H. and Rao, K. R. K., "Platonization in Double-Base Rocket Propellants", AIAA Journal, Vol. 15, No. 11, 1977, pp. 1545-1549.
49. Kubota, N., "Determination of Plateau Burning Effect of Catalyzed Double-Base Propellant", 17th International Symposium on Combustion, The Combustion Institute, 1978, pp. 1435-1442.
50. Lengelle, G., Duterque, J., Verdier, C., Bizot, A. and Trubert, J., "Combustion Mechanisms of Double Base Solid Propellants", 17th International Symposium on Combustion, The Combustion Institute, 1978, pp. 1443-1451.
51. Morkovin, M. V., "Flow Around Circular Cylinder - A Kaleidoscope of Challenging Fluid Phenomena", Proceedings ASME Symposium of Fully Separated Flows, 1964, pp. 102-118.
52. Achenbach, E., "Total and Local Heat Transfer from a Smooth Circular Cylinder in Cross-Flow at High Reynolds Number", International Journal of Heat and Mass Transfer, Vol. 18, 1975, pp. 1387-1396.
53. Achenbach, E., "The Effect of Surface Roughness on the Heat Transfer from a Circular Cylinder to the Cross Flow of Air", International Journal of Heat and Mass Transfer, Vol. 20, 1977, pp. 359-369.
54. Lee, C. K. and Richardson, P. D., "Forced Convection from a Cylinder at Moderate Reynolds Numbers", International Journal of Heat and Mass Transfer, Vol. 17, 1973, pp. 609-613.

55. Perkins Jr., H. C. and Leppert, G. "Local Heat Transfer Coefficients on a Uniformly Heated Cylinder", International Journal of Heat and Mass Transfer, Vol. 7, 1964, pp. 143-158.
56. Richardson, P. D., "Estimation of the Heat Transfer From the Rear of an Immersed Body to the Region of Separated Flow", WADD Tech. Note 59-1, 1960.
57. Sano, Y. and Nishikawa, S., Chemical Engineering (Japan), Vol. 28, 1964, p. 956.
58. Virk, P. S., "Heat Transfer from the Rear of a Cylinder in Traverse Flow", Journal of Heat Transfer, Trans. ASME, Vol. 91, No. 1, 1970, pp. 206-207.
59. Mitchell, J. W., "Base Heat Transfer in Two-Dimensional Subsonic Fully Separated Flows", Journal of Heat Transfer, Trans. ASME, Vol. 93, 1971, pp. 342-348.
60. Matsui, H., Nishiwaki, N., Hirata, M. and Torii, K., "Heat Transfer Phenomena in Wake Flow of Cylinder", Fourth International Heat Conference in Paris, 2, FC 5.9, 1970.
61. Boulos, M. I. and Pei, D. C. T., "Heat and Mass Transfer from Cylinders to a Turbulent Fluid Stream- A Critical Review", The Canadian Journal of Chemical Engineering, Vol. 51, 1973, pp. 673-679.
62. Kostic, Z. G. and Oka, S. N., "Fluid Flow and Heat Transfer with Two Cylinders in Cross Flow", International Journal of Heat and Mass Transfer, Vol. 15, 1972, pp. 279-299.
63. Williams, F. A., "Combustion Theory", Addison-Wesley Publication Co., 1965, Chapter 12.
64. Chung, P. M., "Chemically Reacting Nonequilibrium Boundary Layer", Advances in Heat Transfer, Vol. 2, edited by Harnett, J. P. and Irvine, T. F. Jr., Academic Press, 1955, pp. 110-271.
65. Marble, F. E. and Adamson, T. C., Jr., "Ignition and Combustion in a Laminar Mixing Zone", Jet Propulsion, Vol. 24, No. 2, 1954, pp. 85-94.
66. Dooley, D. A., "Ignition in the Laminar Boundary Layer of a Heated Plate", 1957 Heat Transfer and Fluid Mechanics Institute, Stanford University Press, Stanford, 1957, pp. 321-342.
67. Tsuji, H., "Ignition and Flame Stabilization in the Laminar Boundary Layer on a Porous Flat Plate with Hot Gas Injector", Aerospace Research Institute, University of Tokyo, Report No. 3.
68. Cheng, S. I. and Kovitz, A. A., "Ignition in the Laminar Wake of a Flat Plate", Reinhold Publishing Corp., New York, 1957, pp. 418-427.
69. Sharma, O. P. and Sirignano, W. A., "Ignition of Stagnation Point Flow by a Hot Body", Combustion Science and Technology, Vol. 1, 1969, pp. 95-104.

70. Sharma, O. P. and Sirignano, W. A., "On the Ignition of Pre-mixed Fuel by a Hot Projectile", Combustion Science and Technology, Vol. 1, 1970, pp. 481-494.
71. Burke, S. P. and Schumann, T. E. W., "Diffusion Flames", Industrial Engineering Chemistry, Vol. 20, 1928, pp. 998-1004.
72. Emmons, H. W., "The Film Combustion of Liquid Fuel", Zeitschrift Fur Angewandte Mathematik and Mechanik, Bd. 36, Nr 1/2, 1956, pp. 60-71.
73. Zeldovich, Y. B., "On the Theory of Combustion of Initially Unmixed Gases", NACA TM 1296, 1951.
74. Waldman, C. H., "Theoretical Studies of Diffusion Flame Structure", Ph.D. Thesis, Department of Aerospace and Mechanical Sciences, Princeton University, Princeton, N.J., 1969.
75. Krishnamurthy, L., Williams, F. A. and Seshadri, K., "Asymptotic Theory of Diffusion-Flame Extinction in the Stagnation-Point Boundary Layer", Combustion and Flame, Vol. 26, 1976, pp. 363-377.
76. Tsuji, H. and Matsui, K., "An Aerothermochemical Analysis of Combustion of Carbon in the Stagnation Flow", Combustion and Flame, Vol. 26, 1976, pp. 283-297.
77. Kashiwagi, T., Kotia, G. G. and Summerfield, M., "Experimental Study of Ignition and Subsequent Flame Spread of a Solid Fuel in a Hot Oxidizing Gas Stream", Combustion and Flame, Vol. 24, 1975, pp. 357-364.
78. Kashiwagi, T. and Summerfield, M., "Ignition and Flame Spreading Over a Solid Fuel: Non-Similar Theory for a Hot Oxidizing Boundary Layer", Fourteenth International Symposium on Combustion, The Combustion Institute, 1973, pp. 1235-1247.
79. Levy, S., "Effect of Large Temperature Changes (Including Viscous Heating) upon Laminar Boundary Layers with Variable Freestream Velocity", Journal of Aerospace Sciences, Vol. 21, No. 7, 1954, pp. 459-474.
80. Howarth, L., "On the Solution of the Laminar Boundary Layer Equations", Royal Society of London, Proceedings, A164, No. 919, 1938, pp. 547-579.
81. Tokuda, N. and Yang, W. J., "Unsteady Stagnation Point Heat Transfer Due to Arbitrary Timewise-Variant Free Stream Velocity", Proceedings of Third International Heat Transfer Conference, Vol. II, 1966, pp. 223-232.
82. Carslaw, H. S., Jaeger, J. C., "Conduction of Heat in Solids", Oxford (Clarendon) Press, 1959, p. 88.
83. Summerfield, M., Caveny, L. H., Battista, R. A., Kubota, N., Gostintsev, Yu. A. and Isoda, H., "Theory of Dynamic Extinguishment of Solid Propellants with Special Reference to Nonsteady Heat Feedback Law", Journal of Spacecraft and Rockets, Vol. 8, No. 3, 1971, pp. 251-258.

84. Yang, W-J and Huang, H-S, "Unsteady Compressible Laminar Boundary Layer Flow Over a Flat-Plate", AIAA Journal, Vol. 7, No. 1, 1968, pp. 100-105.
85. Nikanjam, M. and Greif, R., "Heat Transfer During Piston Compression", Journal of Heat Transfer, Trans. ASME, Vol. 100, 1978, pp. 527-530.
86. Goluba, R. W. and Borman, G. L., "The Effect of Periodic Shock-Fronted Pressure Waves on Instantaneous Heat Flux Rates", International Journal of Heat and Mass Transfer, Vol. 12, 1969, pp. 181-1293.
87. Bingham, H. H., Weimer, D. K. and Griffith, W., "The Cylinder and Semicylinder in Subsonic Flow", Technical Report II-13, Department of Physics, Princeton University, Princeton, N.J., 1952.
88. Wittlieff, C. E., Wilson, M. R. and Hertzberg, A., "The Tailored-Interface Hypersonic Shock Tunnel", Journal of Aerospace Sciences, Vol. 26, No. 4, 1959, pp. 219-228.
89. Palmer, H. R. and Knox, B. E., "Contact Surface Tailoring in a Chemical Shock Tube", ARS Journal, Vol. 31, No. 6, 1961, pp. 826-828.
90. Trass, O. and Mackay, D., "Contact Surface Tailoring in a Chemical Shock Tube", AIAA Journal, Vol. 1, No. 9, 1963, pp. 2161-2163.
91. Duff, R. E., "Shock Tube Performance at Low Initial Pressure", The Physics of Fluids, Vol. 2, No. 2, 1959, pp. 207-216.
92. Hartunian, R. A., Russo, A. L. and Marrone, P. V., "Boundary Layer Transition and Heat Transfer in Shock Tubes", Journal of Aerospace Sciences, Vol. 27, No. 8, 1960, pp. 587-594.
93. Mirels, H., "Flow Nonuniformity in Shock Tube Operating at Maximum Test Times", The Physics of Fluids, Vol. 9, No. 10, 1966, pp. 1907-1921.
94. Mirels, H., "Laminar Boundary Layer Behind Shock Advancing into Stationary Fluid", NACA TN 3401, 1955.
95. Mirels, H., "Attenuation in a Shock Tube Due to Unsteady Boundary Layer Action", NACA TN 3278, 1956.
96. Mark, H., "The Interaction of a Reflected Shock Wave with the Boundary Layer in a Shock Tube", Cornell University, Graduate School of Aeronautical Engineering, Ithaca, New York, June 1957.
97. Davies, L., "The Interaction of the Reflected Shock with the Boundary Layer in a Shock Tube and its Influence on the Duration of Hot Flow in the Reflected Shock Tunnel", Part I - No. 880, Part II - No. 881, Aeronautical Research Council, London, C. P., 1965.
98. Davies, L. and Wilson, J. L., "Influence of Reflected Shock and Boundary Layer Interaction on Shock Tube Flows", The Physics of Fluids, Supplement I, 1969, pp. 37-43.

99. Taylor, G. I., "The Instability of Liquid Surfaces When Accelerating in a Direction Perpendicular to Their Planes", Royal Society of London, Proceedings, Vol. A201, No. 1065, 1950, pp. 192-196.
100. Markstein, G. H., "Flow Disturbances Induced Near a Slightly Wavy Contact Surface, or Flame Front Traversed by a Shock Wave", Journal of Aerospace Sciences, Vol. 24, No. 3, 1957, pp. 238-239.
101. Ostrowski, P. P. and Dabora, E. K., "Shock Tube Measurement of Nitric Oxide and Atomic Oxygen by Chemiluminescent Radiation", AIAA Journal, Vol. 17, No. 8, 1979, pp. 898-904.
102. Atallah, D. S., Allan, D. S., Comstock Jr. and Bakerjian, B. H., "The Ignition of Solid Propellants by Radiative, Convective and Chemical Heating", Arthur D. Little, Inc., Cambridge, Mass., Final Report AFOSR 69-3091TR, November 1969.
103. Maltsev, V. M. and Summerfield, M., "Investigation of the Spectral Radiation Characteristics of the Flame-Jet of Nitrate-Ester Propellants Containing Platonizing Catalysts", Unpublished Work, Guggenheim Lab, Princeton University, 1971.
104. Shapiro, A. H., "Compressible Fluid Flow", Vol. 1, Ronald Press Co., New York, 1953, Chapters 1, 2, 4.
105. Amann, H. O., "Experimental Study of the Starting Process in a Reflection Nozzle", The Physics of Fluids, Supplement I, 1969, pp. 150-153.
106. Smeets, G., "Streak Interferometric Studies of Head Wave Standoff in a Shock Tunnel", The Physics of Fluids, Supplement I, 1969, pp. 157-160.
107. Heilig, W. H., "Diffraction of a Shock Wave by a Cylinder", The Physics of Fluids, Supplement I, 1969, pp. 154-157.
108. Bryson, A. E. and Gross, R. W. F., "Diffraction of Strong Shocks by Cones, Cylinders and Spheres", Journal of Fluid Mechanics, Vol. 10, Part 1, 1961, pp. 1-6.
109. Vincenti, W. G. and Kruger, Jr. C. H., "Introduction to Physical Gas Dynamics", Robert E. Krieger Publishing Co., Huntington, New York, 1975, pp. 204-205.
110. Hinze, J. O., "Turbulence", Second Edition, McGraw-Hill Book Company, 1975, p. 761.
111. McCarty, K. P., "HMX Propellant Combustion Studies: Phase 1, Literature Search and Data Assessment", AFRPL-TR-76-59, December 1976, pp. 48-50.
112. Heller, C. A. and Gordon, A. S., "Structure of the Gas Phase Combustion Region of a Solid Double Base Propellant", Journal of Physical Chemistry, Vol. 59, 1955, pp. 773-779.

113. Westbrook, C. K., Creighton, J., Lund, C. and Dryer, F. L., "A Numerical Model of Chemical Kinetics of Combustion in a Turbulent Reactor", Journal of Physical Chemistry, Vol. 81, No. 25, 1977, pp. 2542-2554.
114. Stals, J. and Pitt, M. G., "Electronic Ground State Structure and Chemistry of Nitroguanidine", Australian Journal of Chemistry, Vol. 28, 1975, pp. 2629-2640.
115. "The Exothermal Reaction Between Nitroguanidine and Nitrogen Dioxide", RVO-TNO Technology Laboratory, TOCK-60180, 1970.
116. Chaiken, R. F., Anderson, W. H. et al., "Kinetics of Surface Degradation of Polymethylmethacrylate", Journal of Chemical Physics, Vol. 32, 1960, pp. 141-146.
117. Hewkin, D. J., Hicks, J. A. and Watts, H., "Combustion of Nitric Ester-Based Propellants - Ballistic Modification by Lead Compounds", Combustion Science and Technology, Vol. 2, 1971, pp. 307-327.
118. Zukoski, E. E. and Marble, F. E., "Experiments Concerning the Mechanism of Flame Blowoff from Bluff Bodies", Proceedings of the Gas Dynamics Symposium on Aerothermochemistry, Northwestern University, 1956, pp. 205-210.
119. BenReuven M. and Caveny L. H., "Nitramine Monopropellant Deflagration and General Nonsteady Reacting Rocket Chamber Flows", MAE Report No. 1455, Princeton University, Princeton, N.J., January 1980, pp. 67-74.
120. Hawrusik, F. and Vichnevetsky, R., "Block Tridiagonal Subroutine TRIBLC", Numerical Applications Memorandum No. 146, Rutgers University, N.J., September 1974.
121. Isaacson E. and Keller H. B., "Analysis of Numerical Methods", John Willey and Sons, Inc., 1966, pp. 101-102.
122. Strahle, W. C., "A Transient Problem on the Evaporation of a Reactive Fuel", Combustion Science and Technology, Vol. 1, No. 1, 1969, pp. 25-33.
123. Carnahan, B., Luther, H. A. and Wilkes, J. O., "Applied Numerical Methods", John Willey and Sons, Inc., 1969, p. 451.
124. Hilsenrath, J., Beckett, C. W., Benedict, W. S., Fano, L., Hoge, H. J., Masi, J. F., Nuttall, R. L., Touloukian, Y. S. and Woolley, H. W., "Tables of Thermodynamic and Transport Properties of Air, Argon, Carbon Dioxide, Carbon Monoxide, Hydrogen, Nitrogen, Oxygen and Steam", Pergamon Press, 1960.
125. Vidal, R. J., "Model Instrumentation Techniques for Heat Transfer and Force Measurements in a Hypersonic Shock Tunnel", WADC Technical Note 56-315, Cornell Aeronautical Laboratory, Inc., Buffalo, New York, February 1956.

126. Vidal, R. J., "Transient Surface Temperature Measurements", CAL Report No. 114, Cornell Aeronautical Laboratory, Inc., Buffalo, New York, March 1962.
127. Bogdan, L. and Garberoglio, J. E., "Transient Heat Transfer Measurement with Thin Film Resistance Thermometers Fabrication and Application Technology", Air Force Aero Propulsion Lab., Wright-Patterson Air Force Base, Ohio, AFAPL-TR-67-72, June 1967.
128. Smith, I. E. and Siddiqui, K. M., "The Measurement of Igniter Heat Flux in Solid Propellant Rocket Motors", AIAA/SAE 13th Propulsion Conference, Paper 77-901, Orlando, Florida, July 11-13, 1977.
129. Skinner, G. T., "Calibration of Thin Film Gage Backing Materials", ARS Journal, Vol. 31, No. 5, 1961, pp. 671-672.
130. Cook, W. J. and Felderman, E. J., "Reduction of Data from Thin Film Heat Transfer Gages: A Concise Numerical Technique", AIAA Journal, Vol. 4, No. 3, 1966, pp. 561-562.
131. Morse, P. P., "Vibration and Sound", McGraw-Hill Book Company Inc., 1948, pp. 235-237.

Table 1  
Propellant Formulations (a)

	Nominal M26 and M30 propellants:				
	M26E1	M30		M26E1	M30
Nitrocellulose	67.3%	28.4	C	24.9%	15.9
(13.15% nitration)			H	2.6	3.0
Nitroglycerin	25.0	22.2	N	14.8	33.8
Nitroguanidine		47.7	O	56.1	45.6
Barium nitrate	0.8				
Potassium nitrate	0.7		O.B. (d):	-30.9%	-20.8
Ethyl centralite	6.0				
Graphite	0.2(b)				
Cryolite		0.3			

Specific Lot of M1 Propellant:

Nitrocellulose	82.6	C	28.6
(13.15% nitration)		H	2.7
Dinitrotoluene	9.3	N	13.2
Dibutylphthalate	4.9	O	53.3
Diphenylamine	1.1		
K <sub>2</sub> SO <sub>4</sub>	2.1	O.B.:	-44.8%

NC/TMETN Propellant (c):

Nitrocellulose	53.9	C	25.1
(12.6% nitration)		H	3.0
Trimethylolethane	39.1	N	14.9
trinitrate		O	55.9
Triethylene glycol	7.0		
dinitrate		O.B.:	-35%

HMX/PU Composite Propellant:

Cyclotetramethylene	
tetranitramine	85.0
Polyurethane binder	15.0

- (a) Percentages are by weight  
 (b) One lot of M26 did not have graphite  
 (c) Total ethyl centralite in propellant is 1.7%  
 (d) Oxygen balance for complete combustion of C to CO<sub>2</sub>

Table 2  
Main Test Conditions

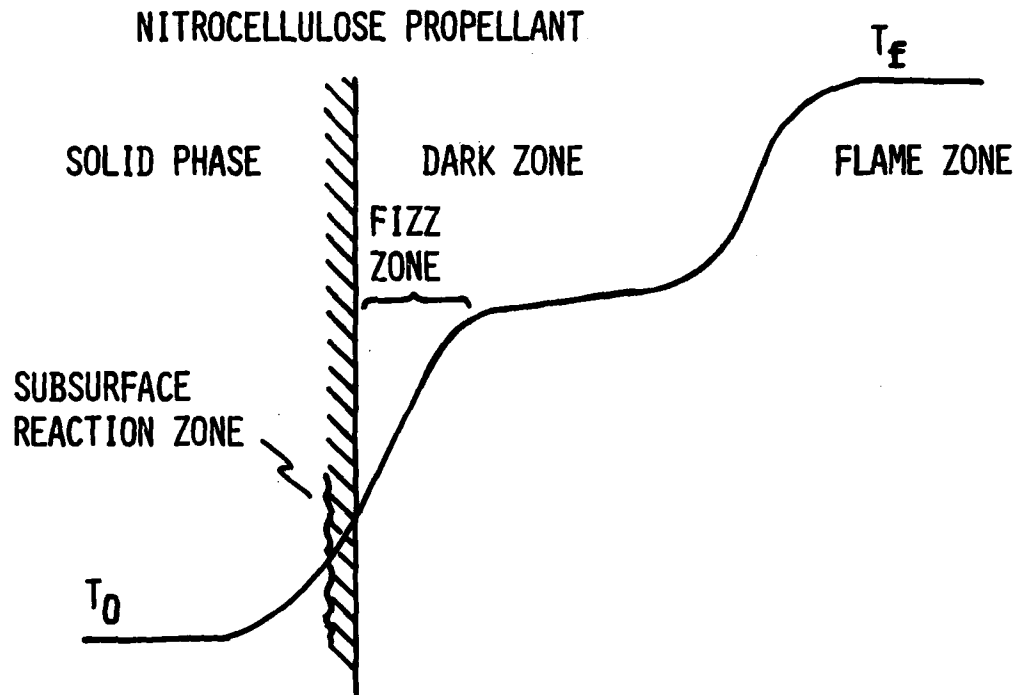
TEST TYPE	PRESSURE MPa	TEMPERATURE K	VELOCITY m/s	GAS COMPOSITION
NOMINAL CONDITIONS	1.7	1880	0 - 100	50% O <sub>2</sub> , 50% N <sub>2</sub>
				10% O <sub>2</sub> , 90% N <sub>2</sub>
				100% N <sub>2</sub>
HIGH TEMPERATURE	1.7	2250	5 - 70	100% N <sub>2</sub>
VARIABLE PRESSURE	1.03-2.34	1880	24.5	10% O <sub>2</sub> , 90% N <sub>2</sub> 100% N <sub>2</sub>

Table 3

Values of Physical Properties Used in Calculations

NOMINAL VALUES

$K_e$ (cal/cm-s-K)	0.000257
$\rho_e$ (g/cm <sup>3</sup> )	0.00314
$c_{pe}$ (cal/g-K)	0.285
$\mu_e$ (g/cm-s)	0.000901
$K_s$ (cal/cm-s-K)	0.00015
$\rho_s$ (g/cm <sup>3</sup> )	1.54
$c_{ps}$ (cal/g-K)	0.35
$\alpha$	0.5
$\eta$	2
$A_R$ (cm <sup>3</sup> /g-s)	$10^{10}$
$A_S$ (1/s)	$10^{17}$
$A_P$ (cm/g)	$10^5$
$E_R$ (kcal/mole)	14
$E_S$ (kcal/mole)	40
$E_P$ (kcal/mole)	16
$Q_R$ (cal/g)	2000
$Q_S$ (cal/g)	300
$L_V$ (cal/g)	120
$U_E$ (m/s)	10
$T_E$ (K)	1850
$P_E$ (MPa)	1.72
$t_f$ (s)	0.000175



### COMBUSTION ZONES AND PROCESSES OF DOUBLE BASE PROPELLANT

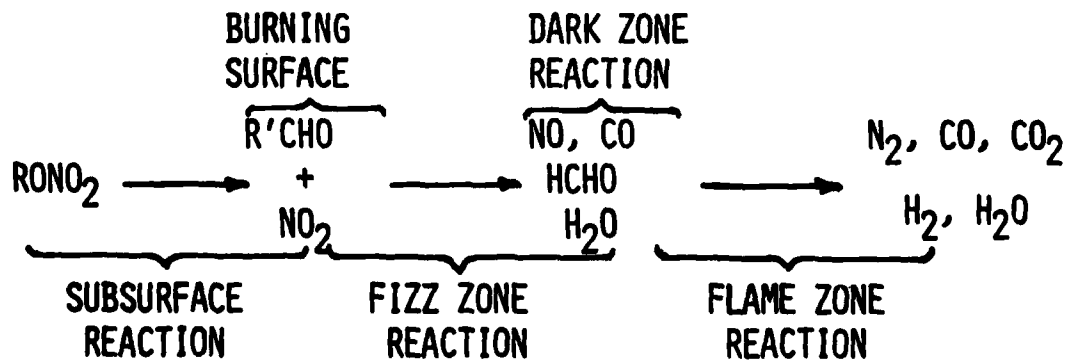


Fig. 1 Reaction scheme of combustion processes of double based propellants.

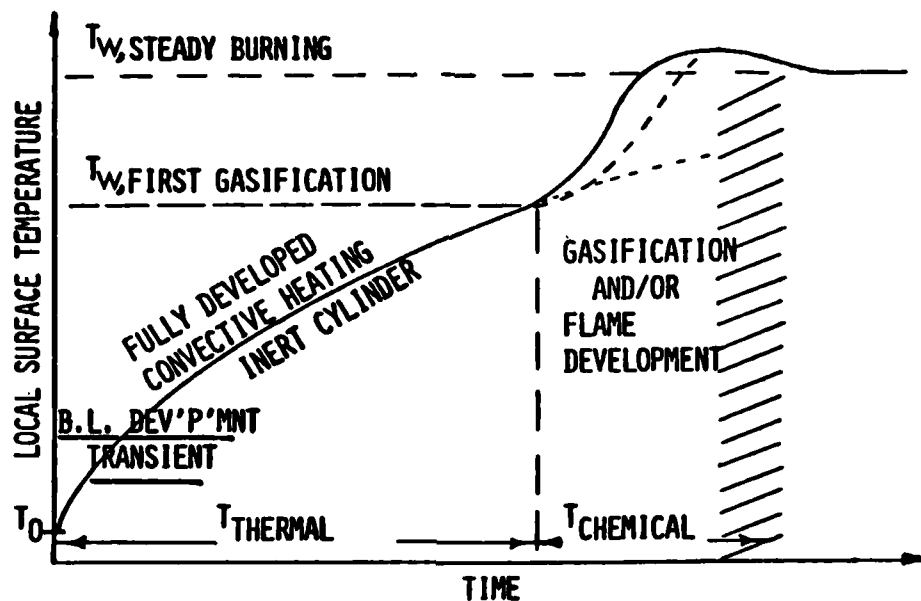


Fig. 2 Evolution of the local surface temperature of a convectively heated propellant cylinder.

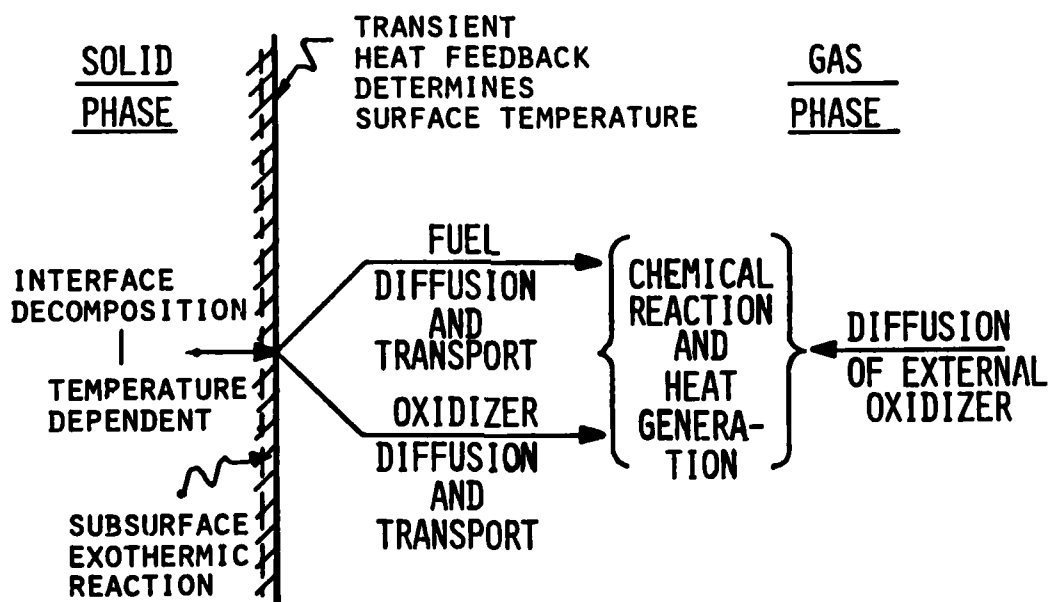
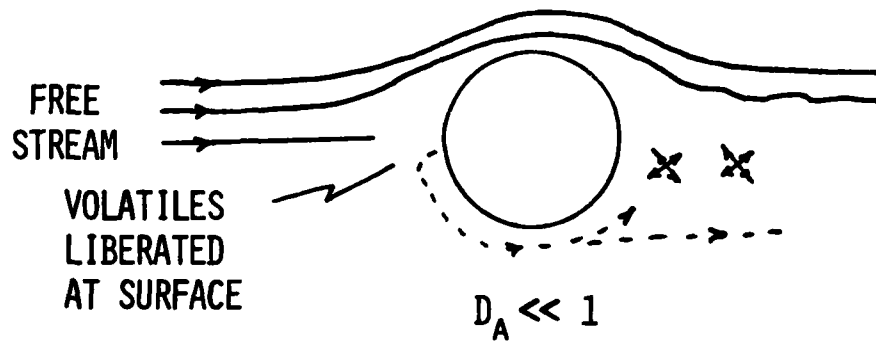


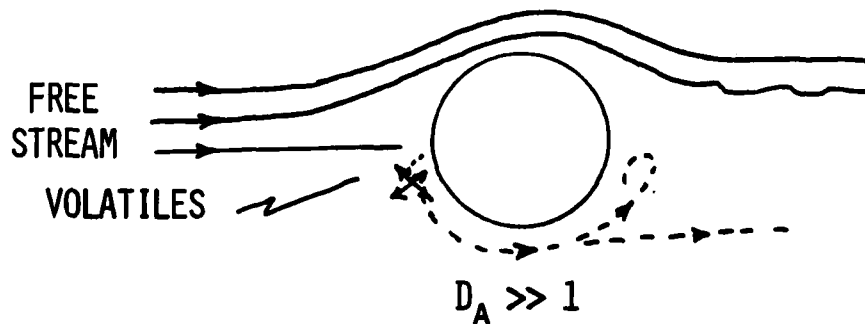
Fig. 3 Physical model of the interaction of solid phase-gas phase processes, leading to gas phase ignition.

### TWO IGNITION CONDITIONS

DAMKOHLE NUMBER:  $D_A = \frac{T_{\text{FLOW}}}{T_{\text{REACTION}}}$



(B) GASIFICATION OCCURS AT LEADING EDGE BUT  
IMPORTANT HEAT RELEASE OCCURS IN WAKE



(A) FIRST IGNITION OCCURS AT LEADING EDGE AND  
HOT COMBUSTION GASES ARE SWEEPED OVER SURFACE

Fig. 4 Examples of flow and reaction processes that occur when a propellant cylinder is ignited by convection.

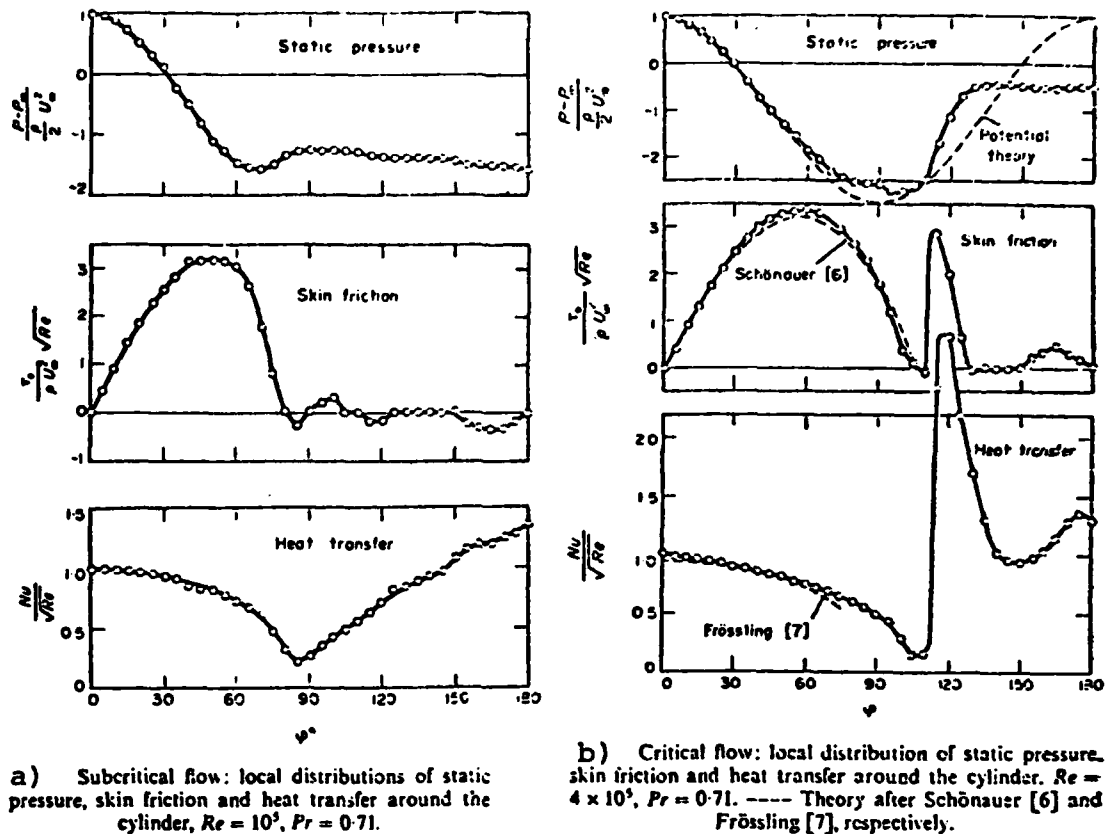


Fig. 5 Flow conditions around a cylinder for subcritical and critical Reynolds numbers. (from Ref. 52)

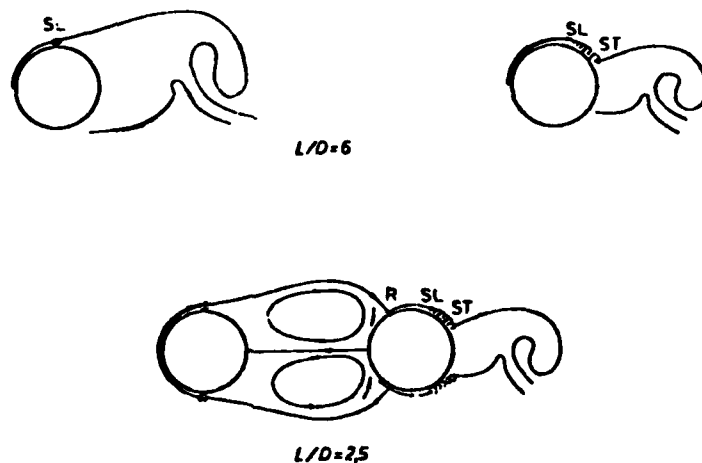


Fig. 6 Illustration of flow patterns around two cylinders showing effect of separation condition. (from Ref. 62)

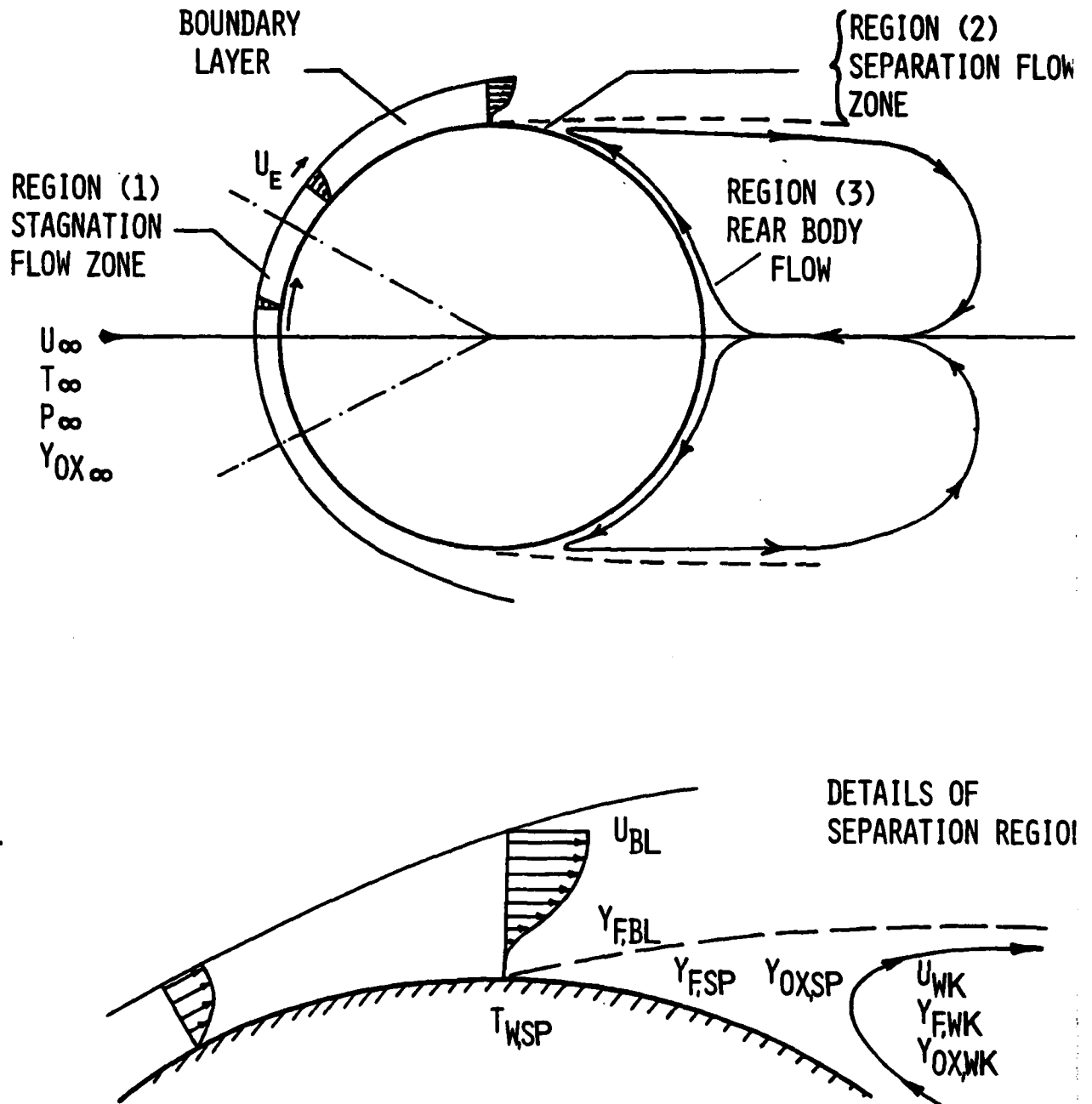


Fig. 7 Flow field around a cylinder in cross flow showing three zones where ignition criterion are being examined.

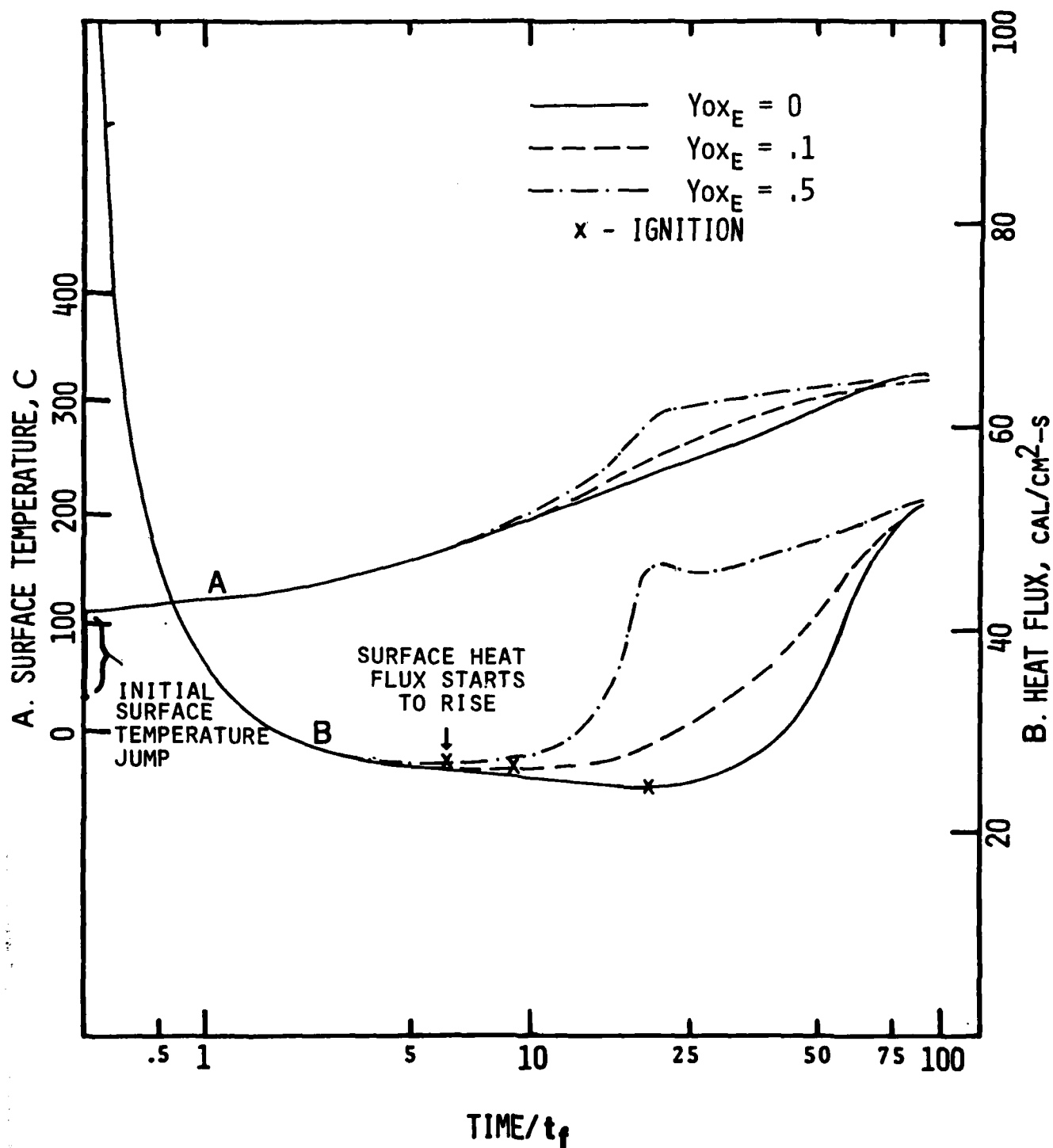


Fig. 8 The predicted evolution of the ignition process at the stagnation zone exhibits dramatic dependence of free stream oxidizer content.

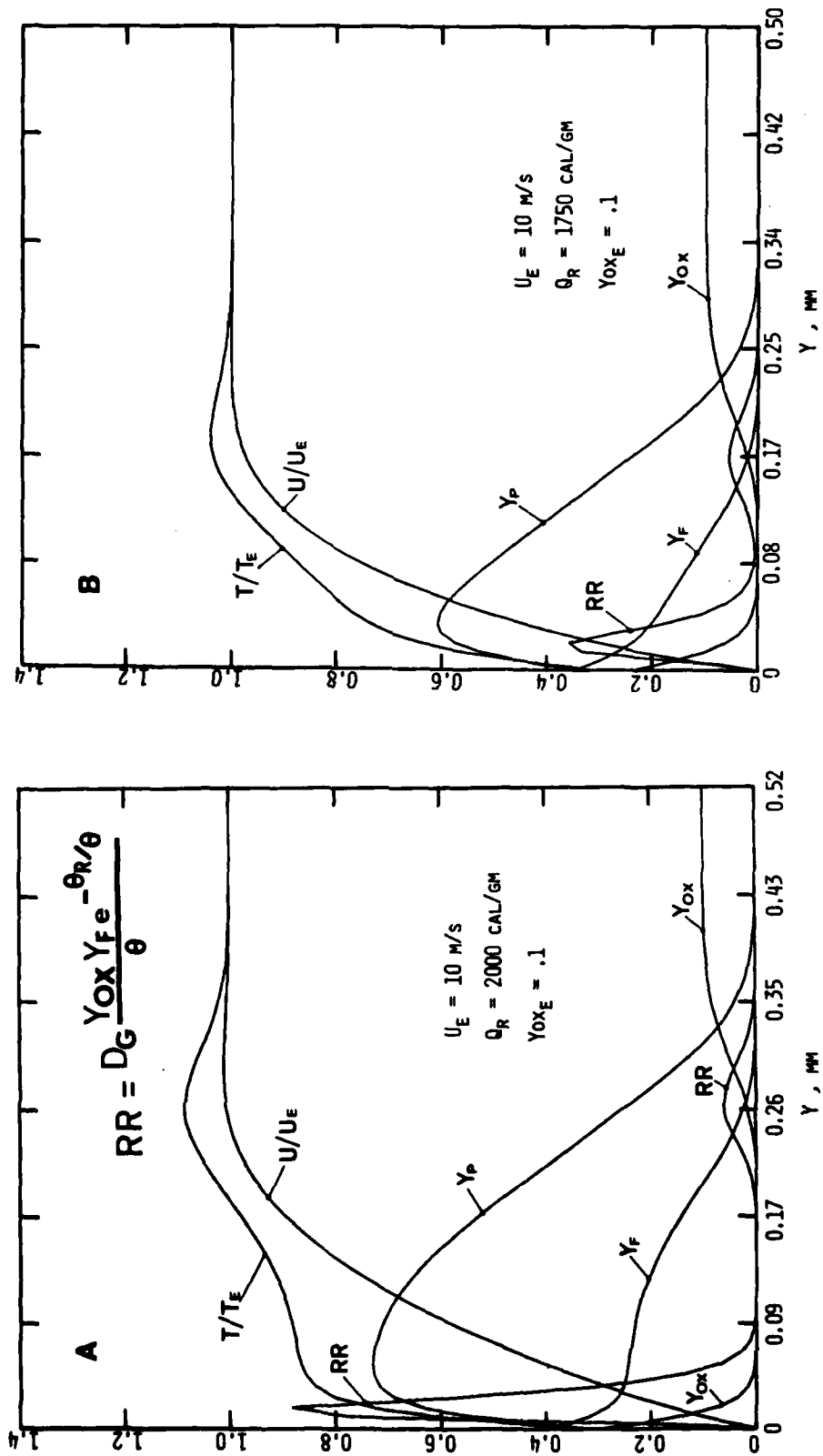


Fig. 9 Predicted boundary layer profiles of fully developed flame for two magnitudes of gas phase heat release.

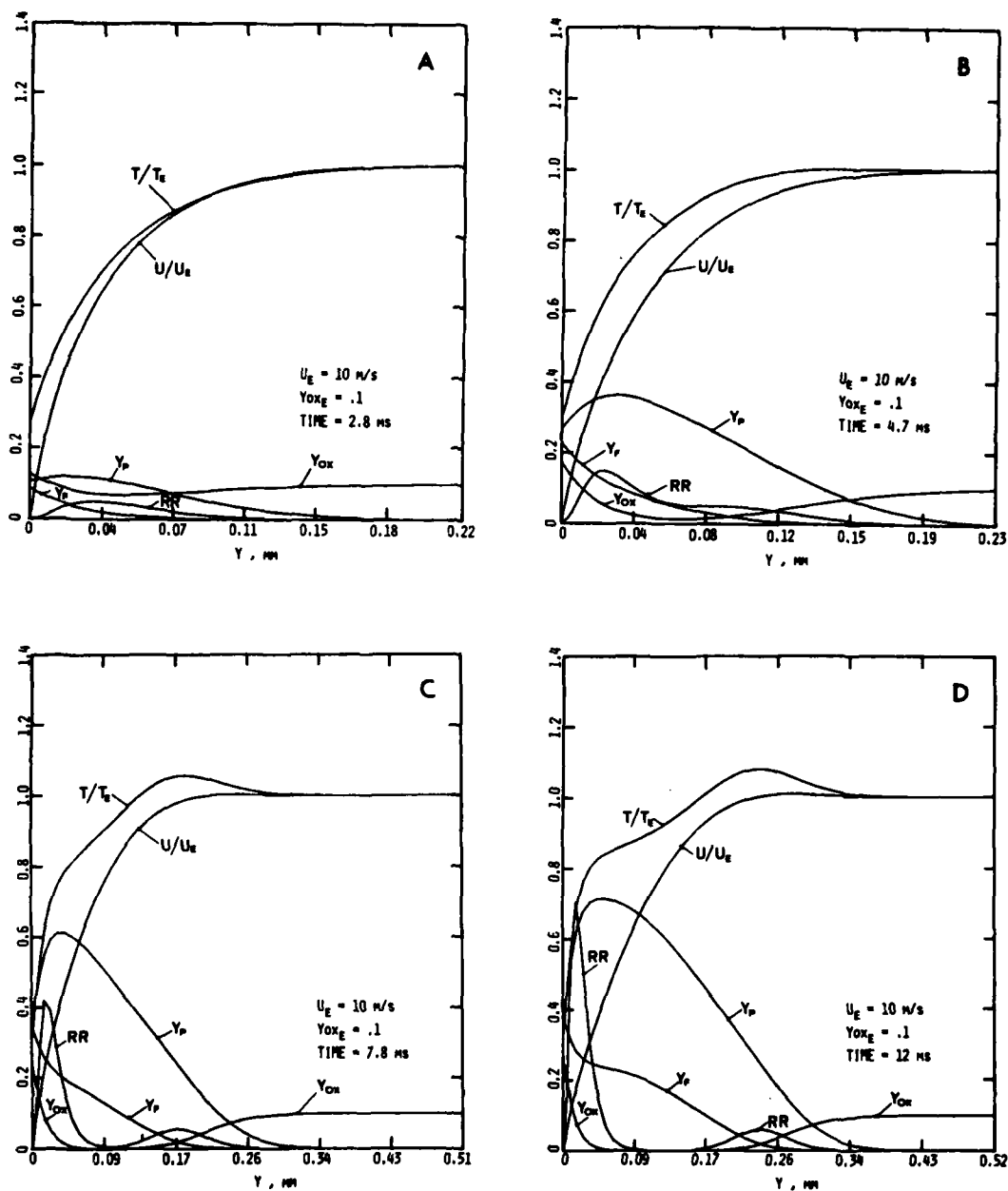
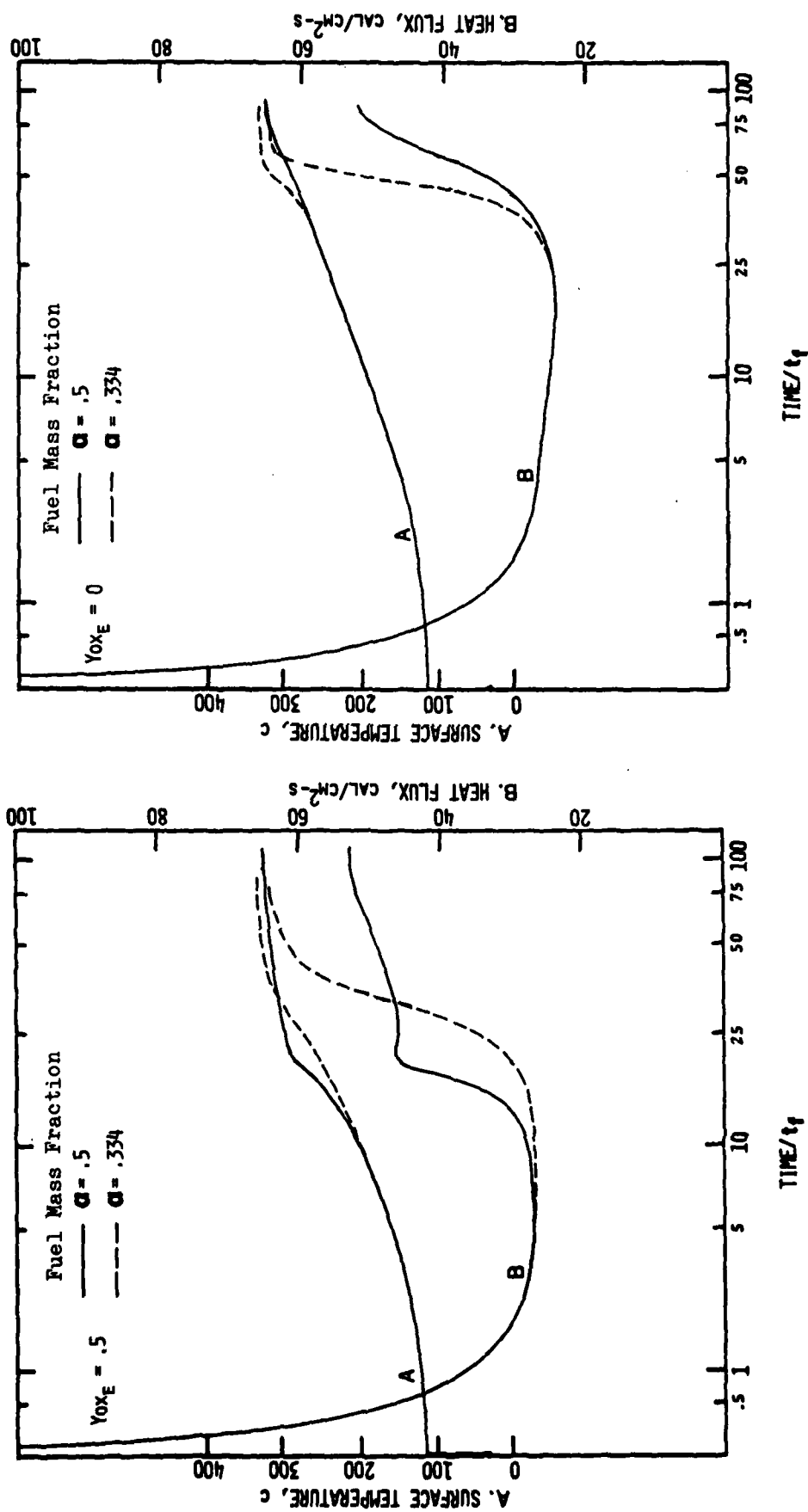


Fig. 10 The evolution of the boundary layer profiles from ignition (A) to fully developed flame (D).



- a)  $Y_{OX} = 0.5$  - Fuel rich propellant ignites faster.
- b)  $Y_{OX} = 0$  - Both propellants ignite in about the same time.

Fig. 11 Demonstration of the role of free stream oxidizer as ignition promoter for two cases of fuel rich and fuel balanced propellants.

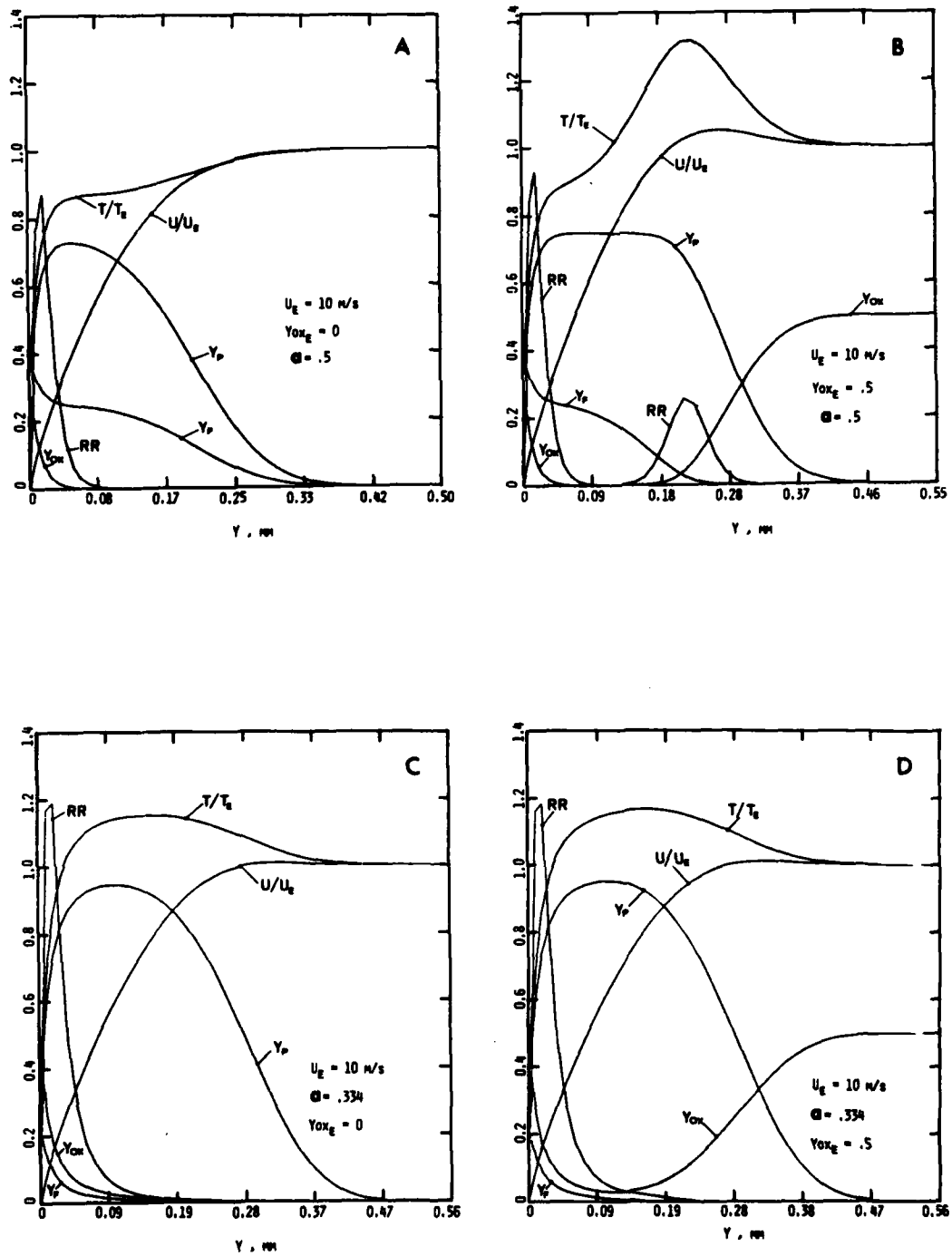


Fig. 12 Boundary layer profiles corresponding to Fig. 11 cases.

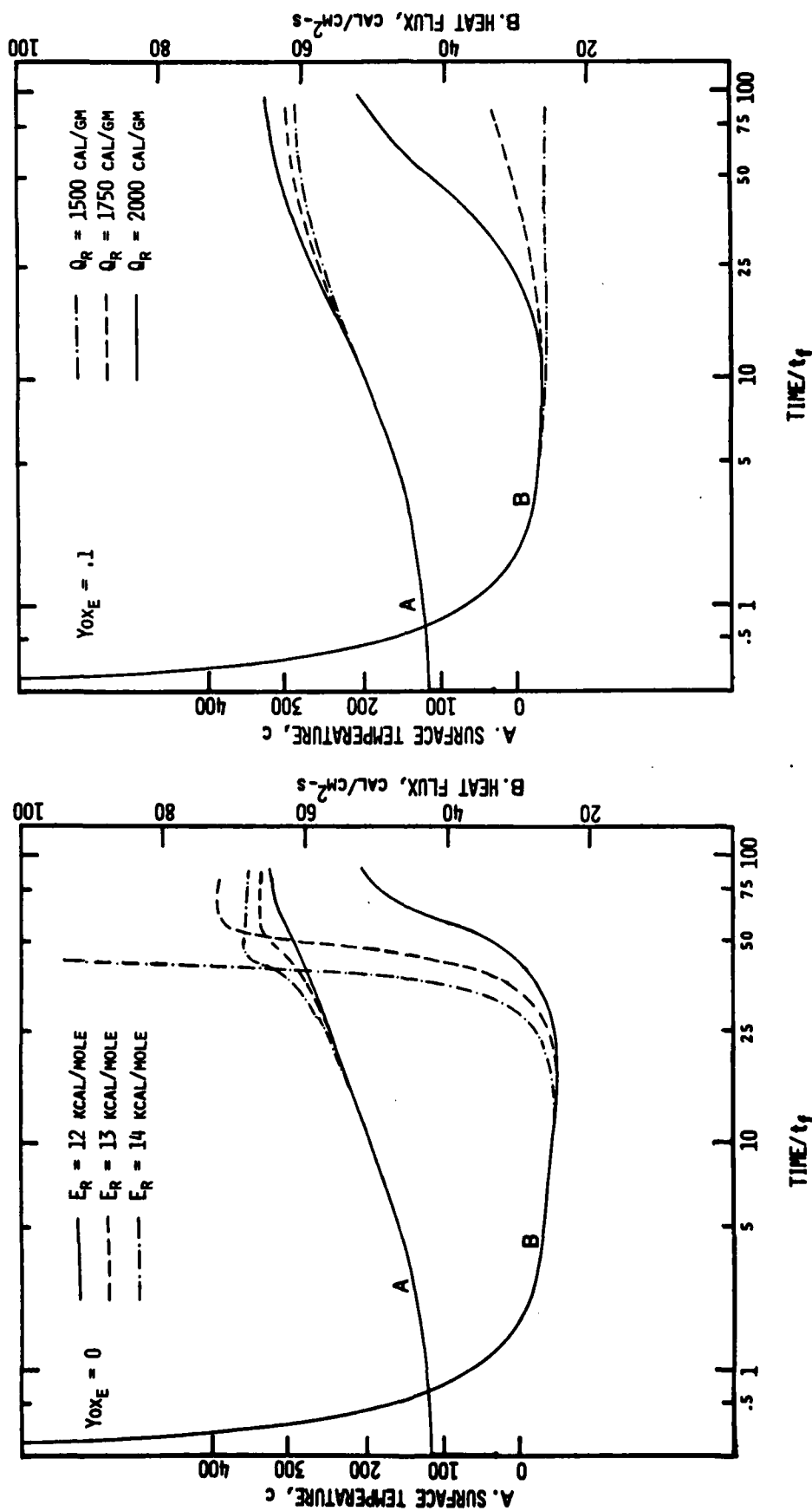


Fig. 13 The effects of gas phase activation energy on the ignition process.

Fig. 14 The effects of gas phase heat release on the ignition process.

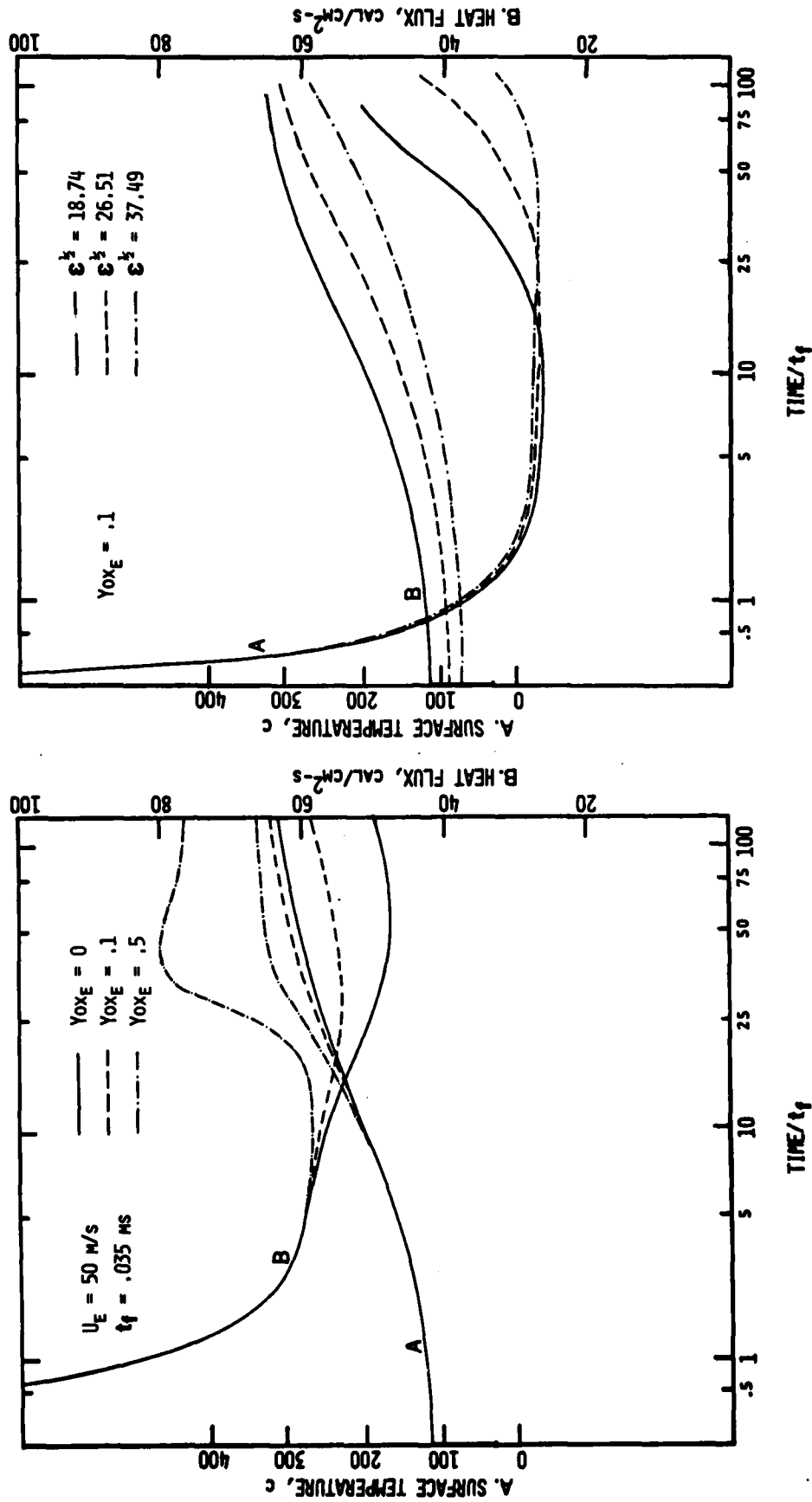


Fig. 15 The effects of free stream oxidizer for a case of higher convective flow velocity.

Fig. 16 The role of the thermal properties ratio  $\epsilon$  is very prominent in convective ignition process.

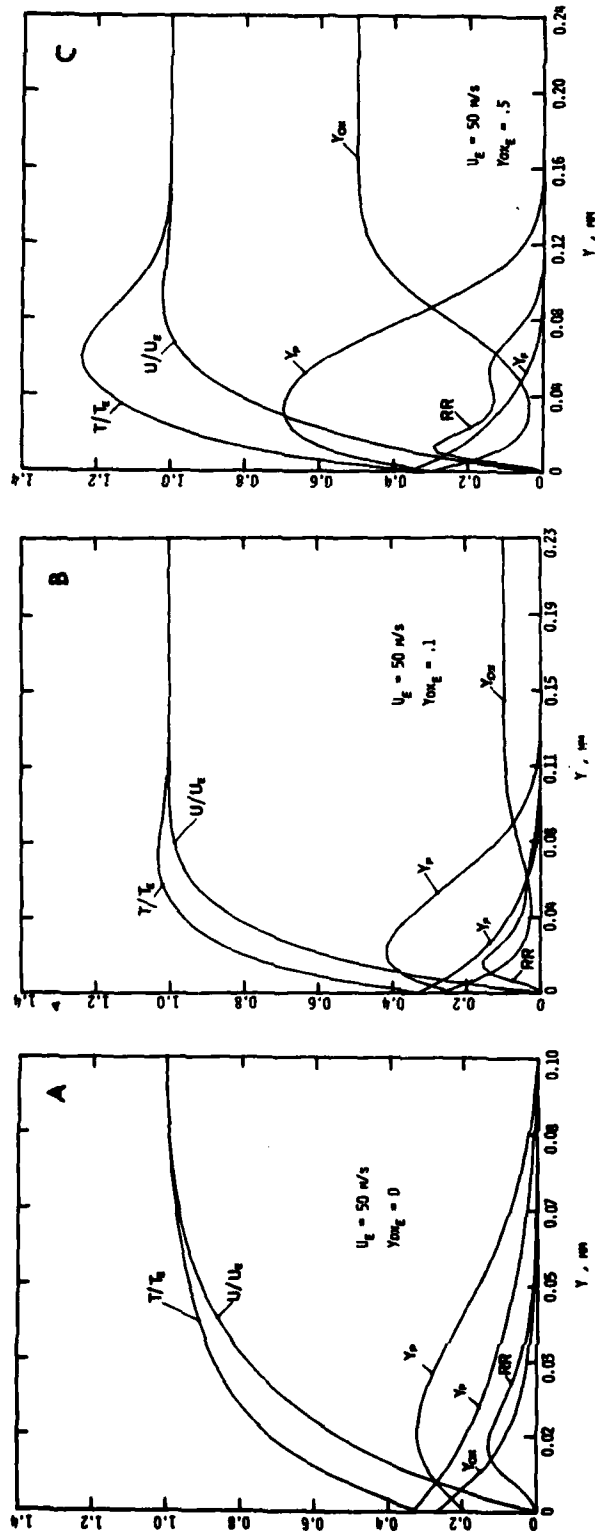


Fig. 17 Boundary layer profiles corresponding to Fig. 15.

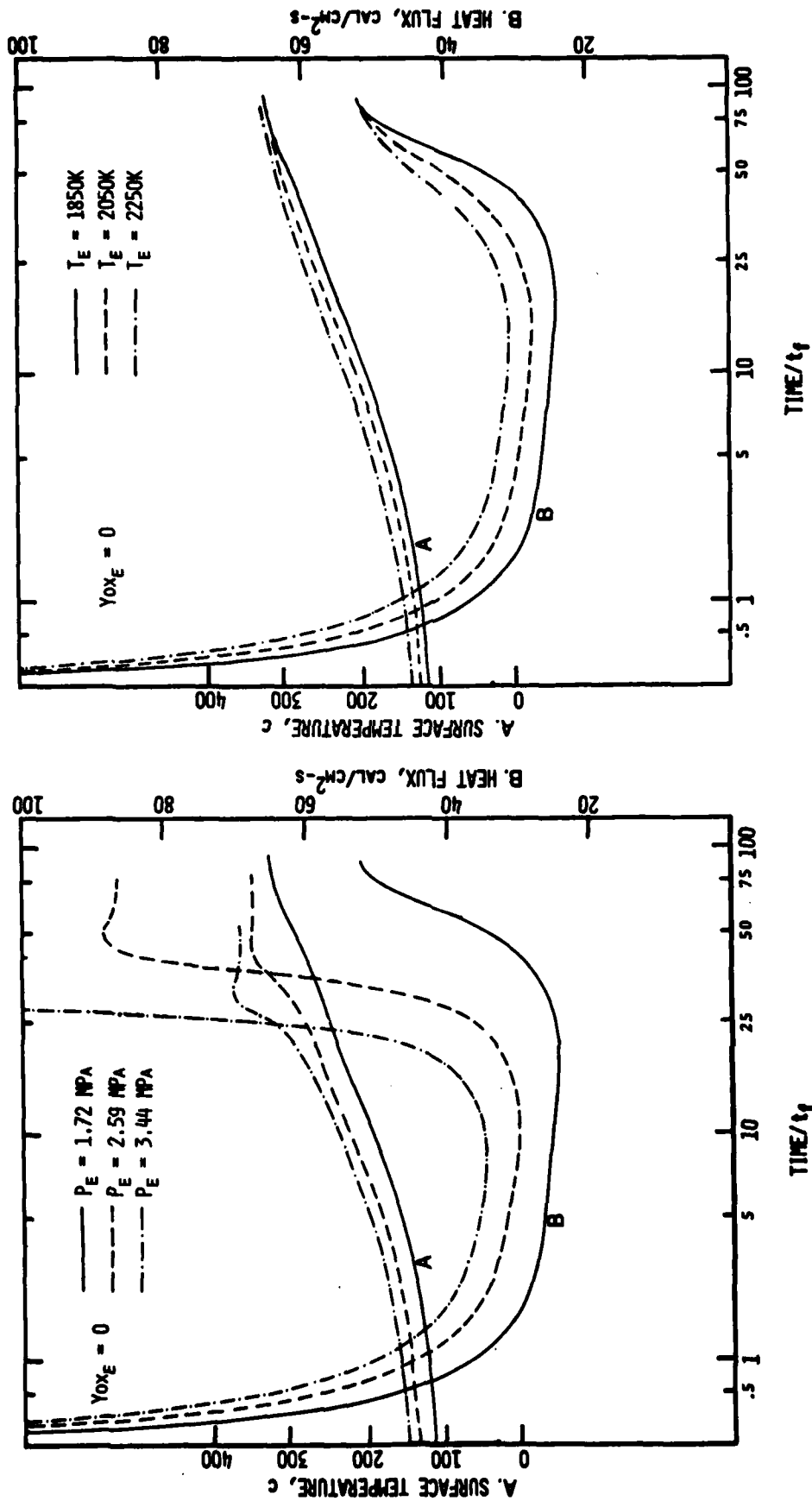


Fig. 18 The magnitude of the pressure has a tremendous effect on the ignition process.

Fig. 19 The effects of varying free stream temperature on the ignition process.

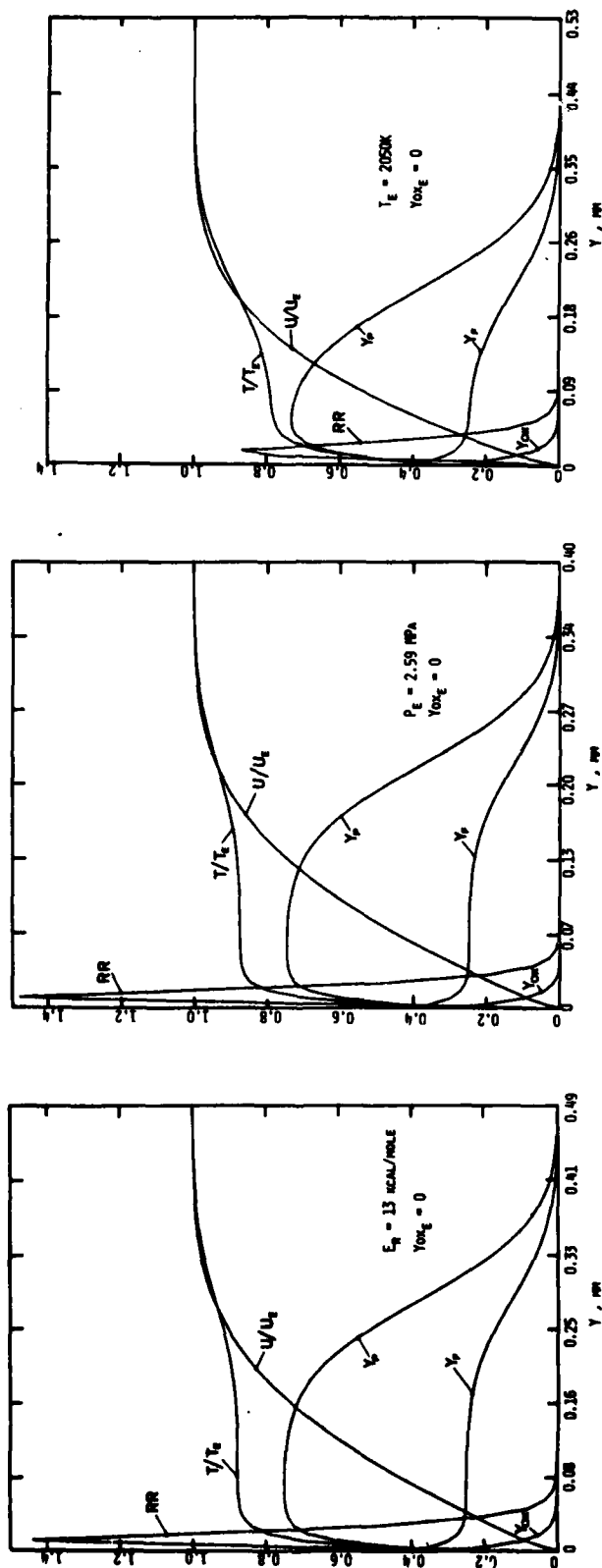


Fig. 20 Boundary layer profiles for lower gas phase activation energy.  
 Fig. 21 Boundary layer profiles for higher pressure.  
 Fig. 22 Boundary layer profiles for higher free stream temperature.

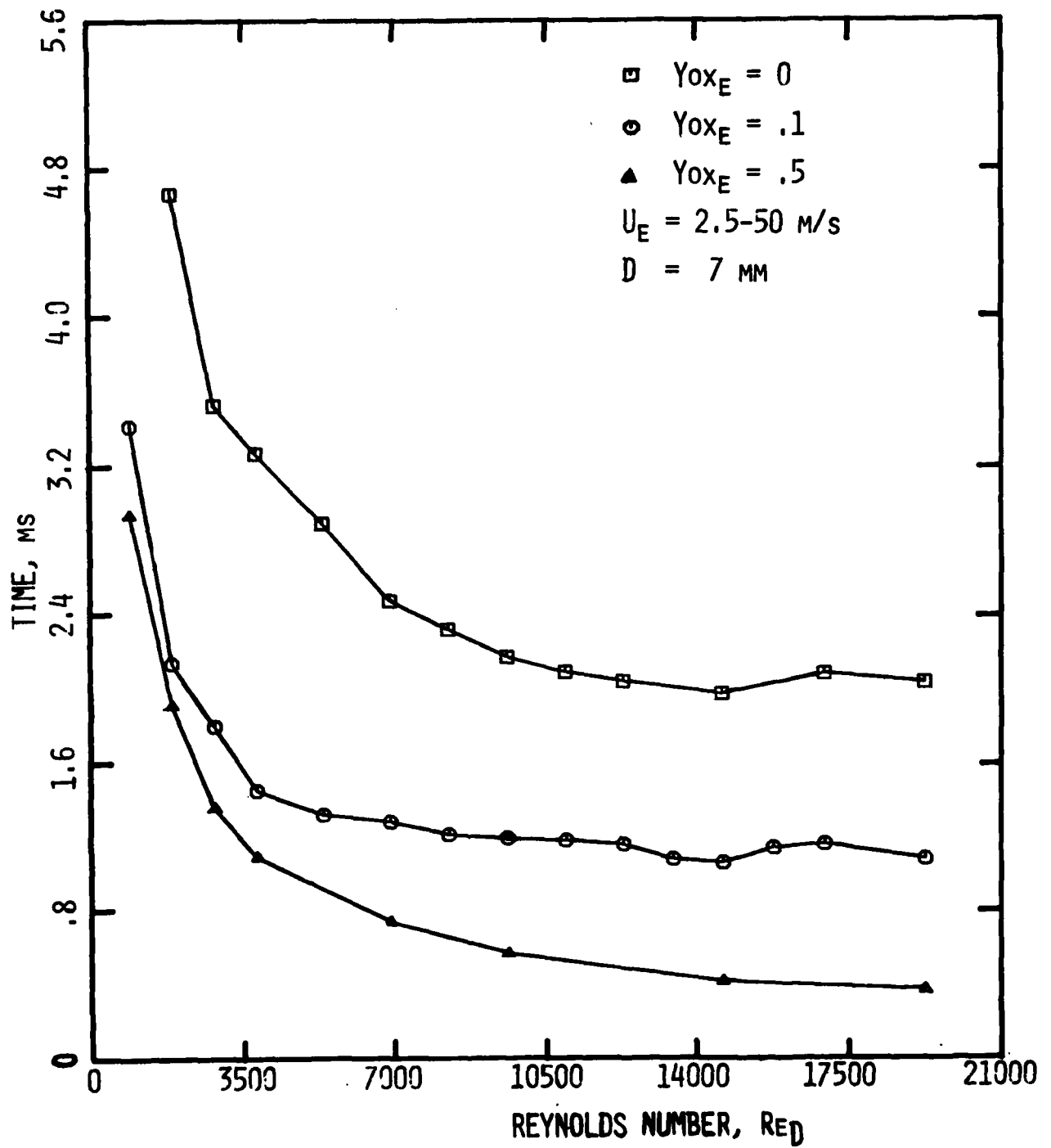


Fig. 23 The variation of predicted ignition delay time versus Reynolds number exhibits strong dependence on the amount of free stream oxidizer.

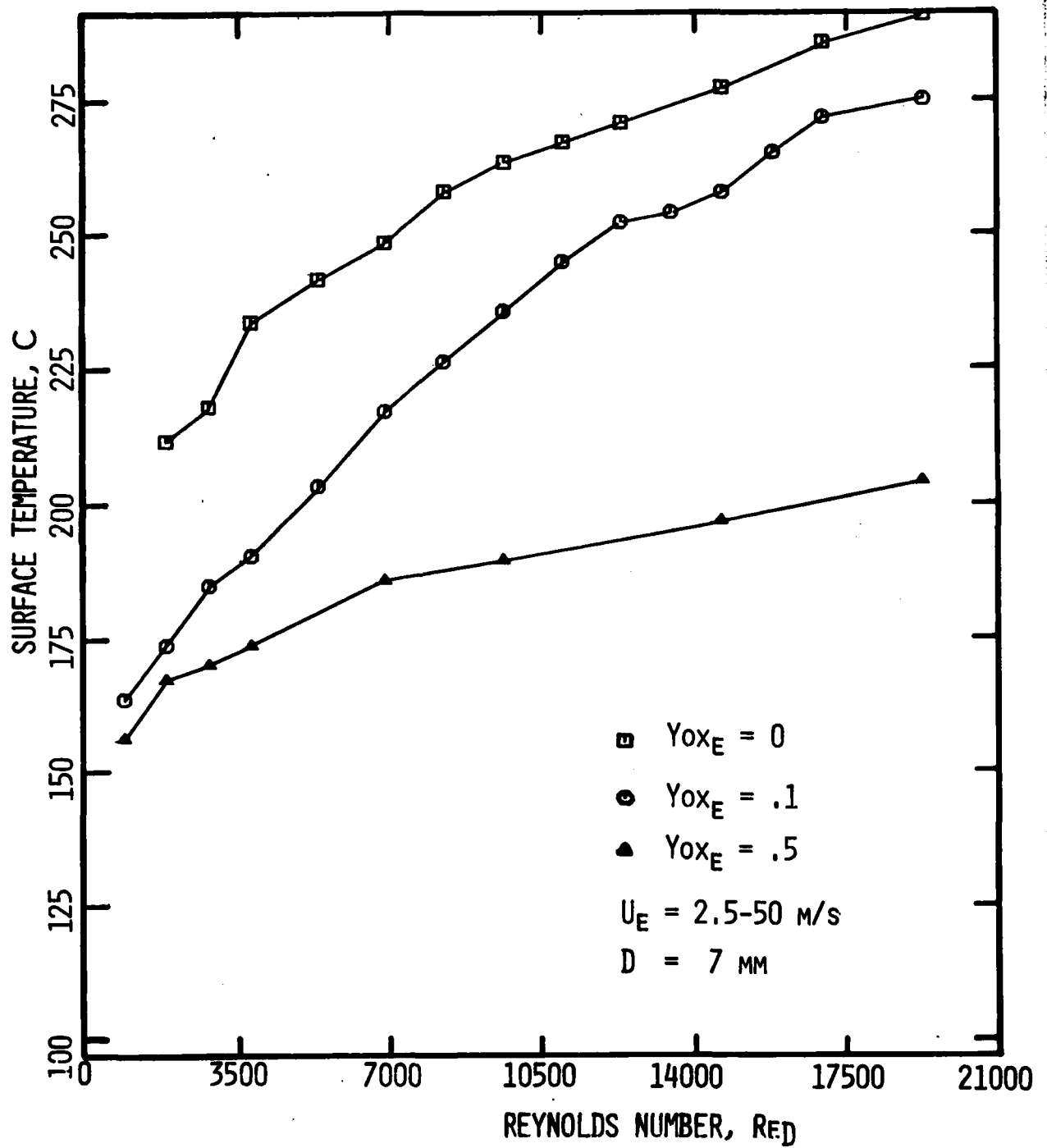


Fig. 24 Surface temperatures at the ignition time of Fig. 23 are very dependent on both the Reynolds number and the free stream oxidizer.

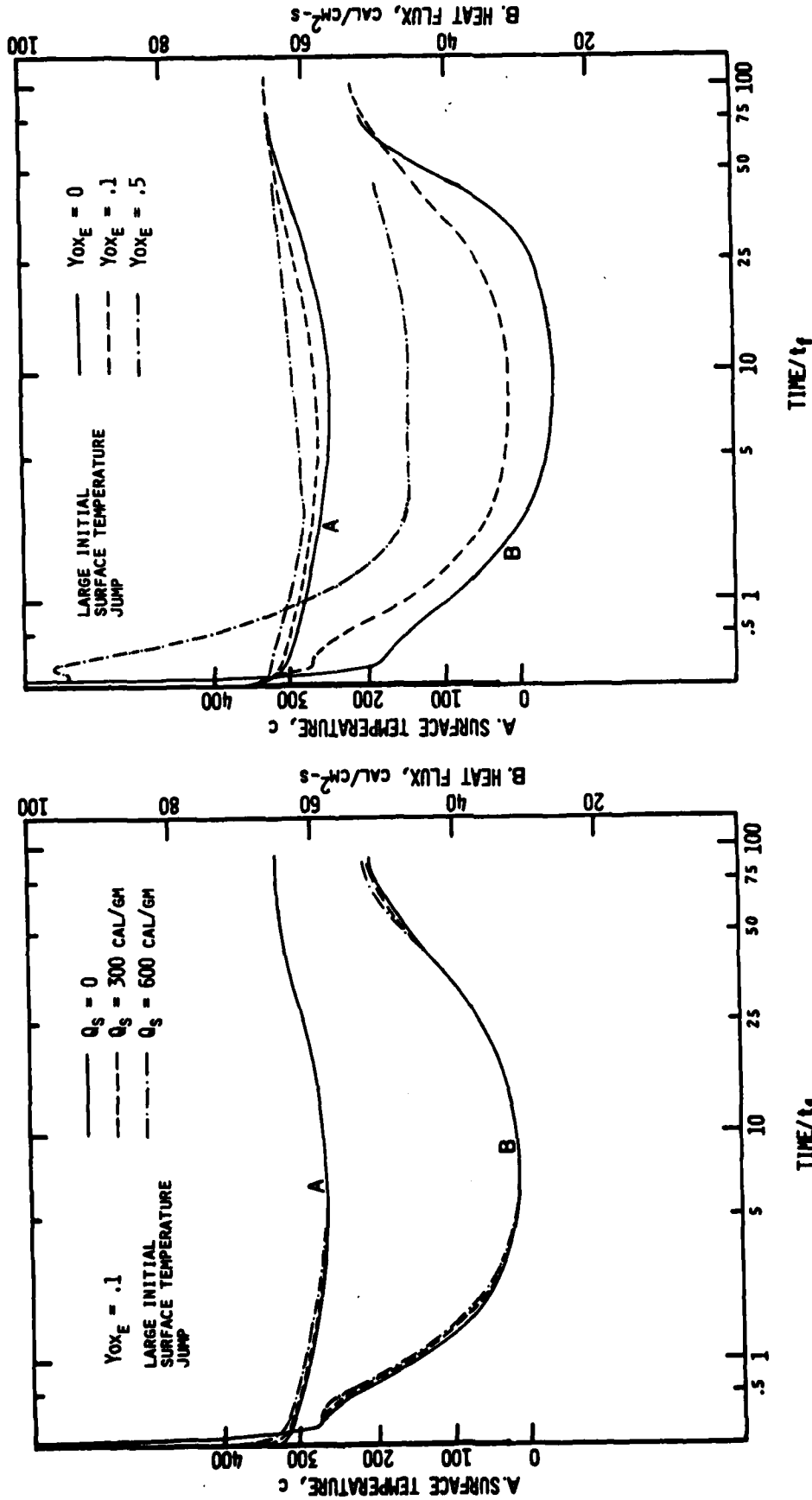


Fig. 25 The dependence of the ignition process on the amount of subsurface heat release is very weak.

Fig. 26 The ignition process for a case of a large initial surface temperature jump is very sensitive to free stream oxidizer.

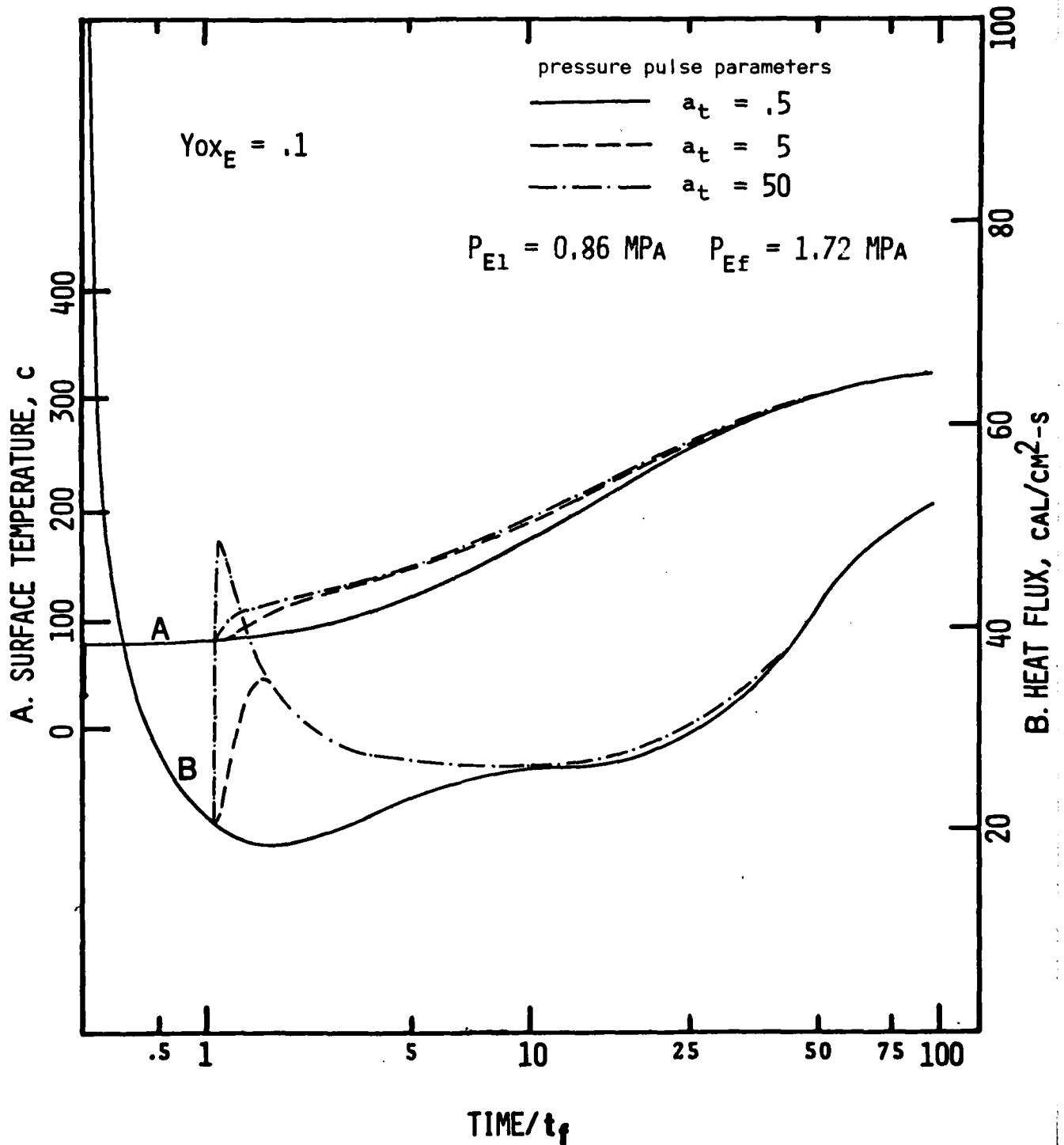


Fig. 27 The very large instantaneous heat fluxes associated with strong pressure pulse decrease ignition delay time appreciably.

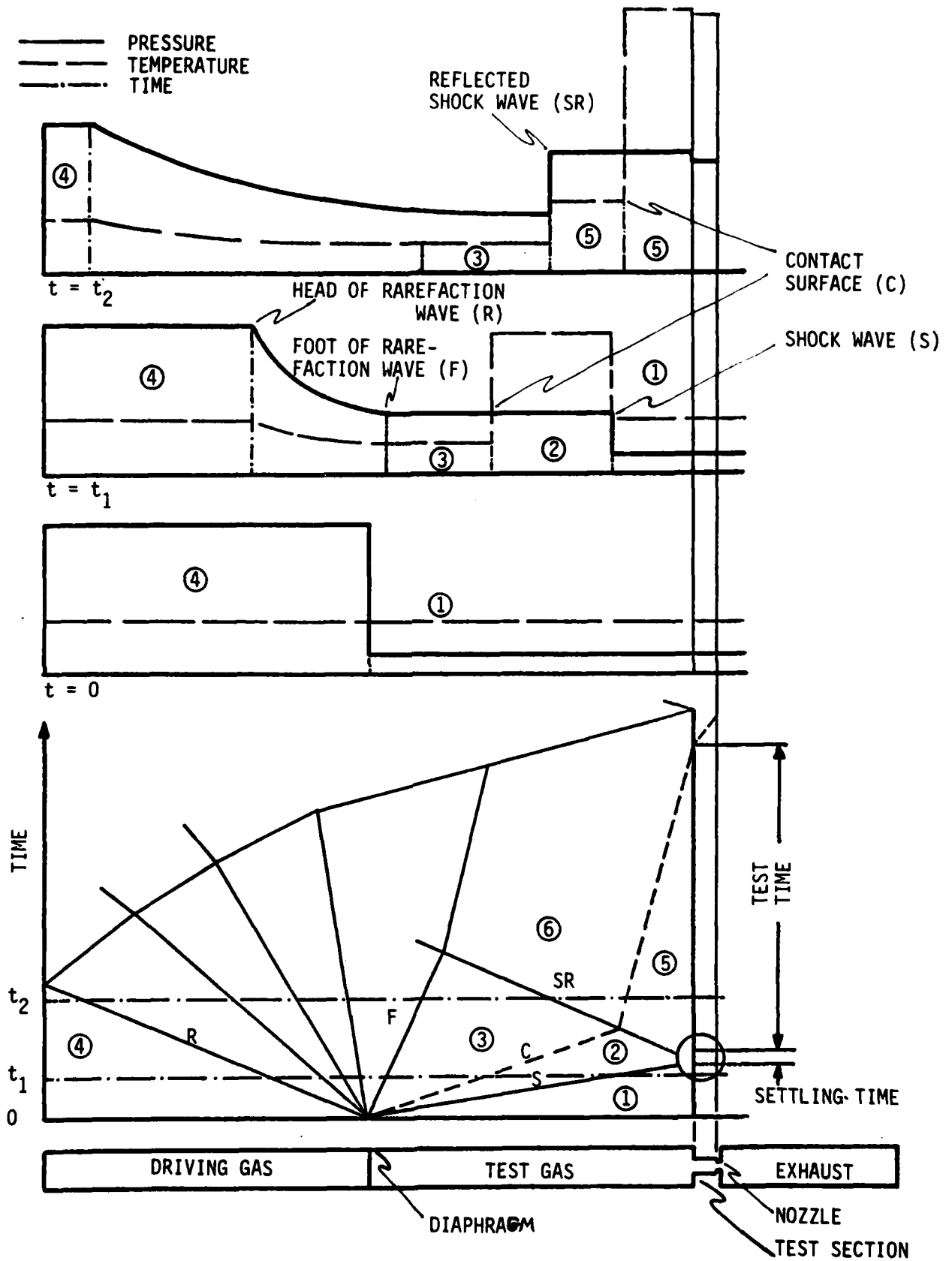


Fig. 28 Wave diagram showing pressure and temperature profiles for shock tunnel operation.

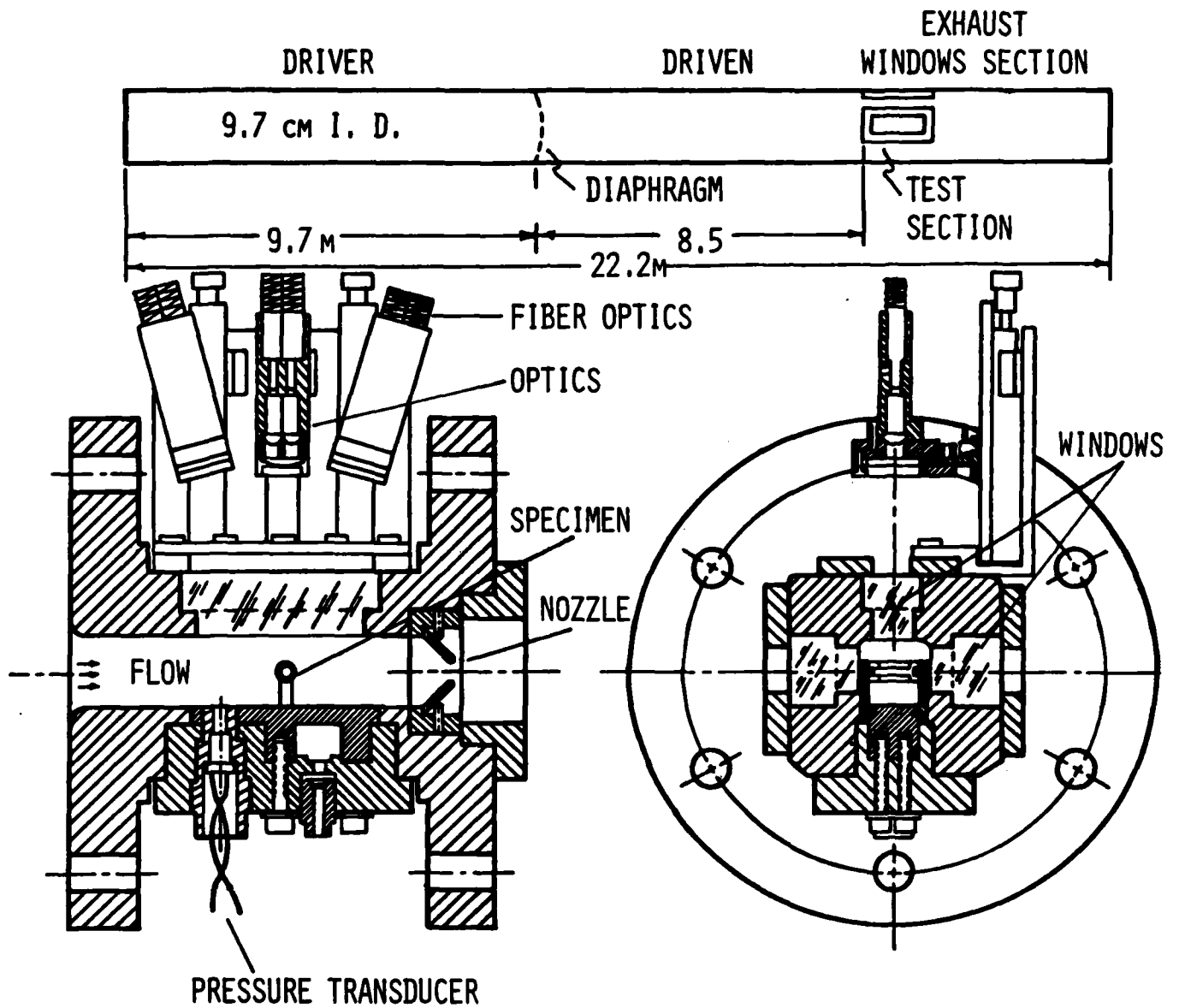


Fig. 29 Schematic diagram of the shock tunnel and detail of the test section.

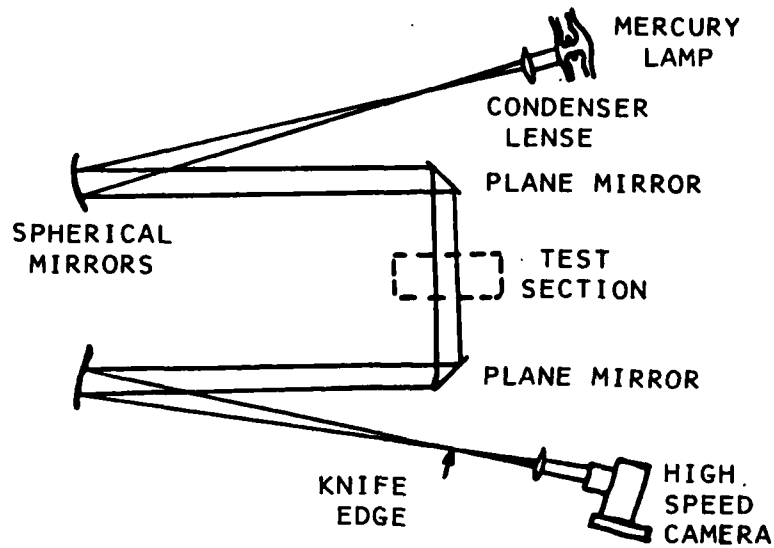


Fig. 30 Schlieren and shadowgraph optical systems (from Ref. 19)

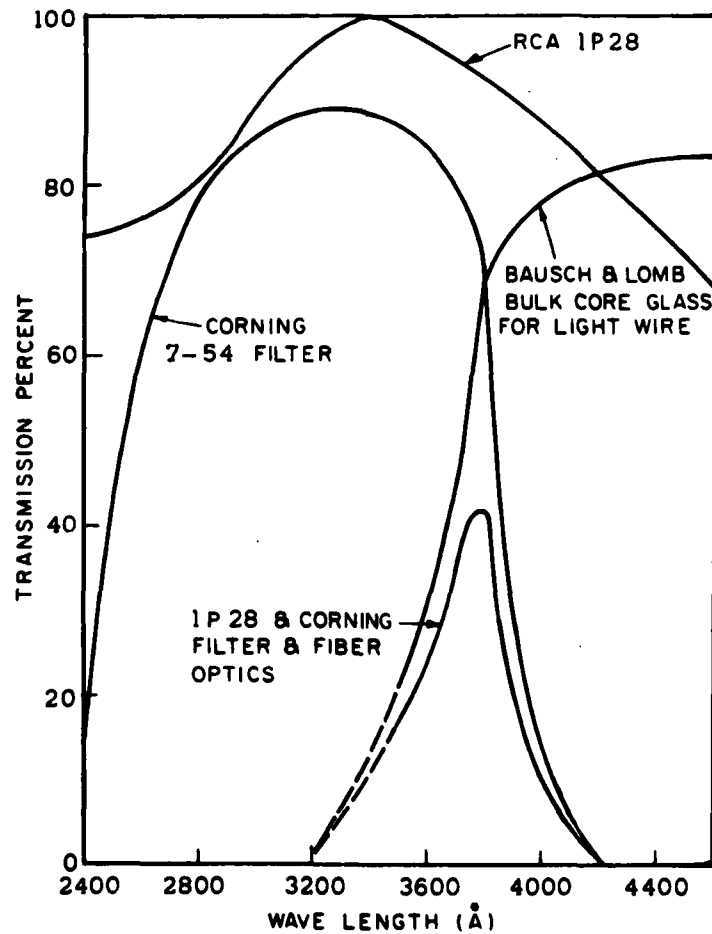


Fig. 31 Spectral response of detection system and its individual elements. (from Ref. 19)

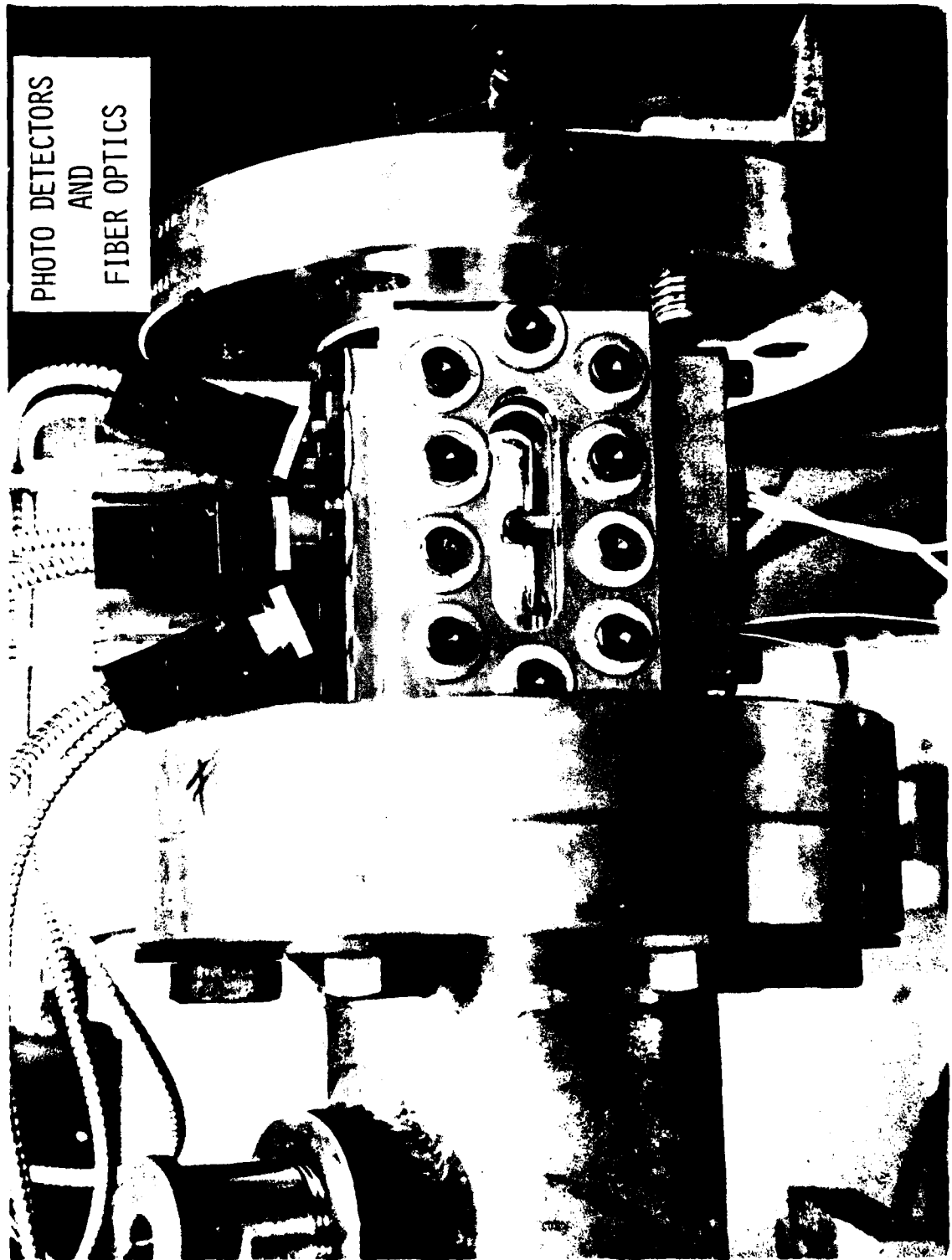


Fig. 32 Calibration of photo-detectors by means of a rotating miniature light bulb.

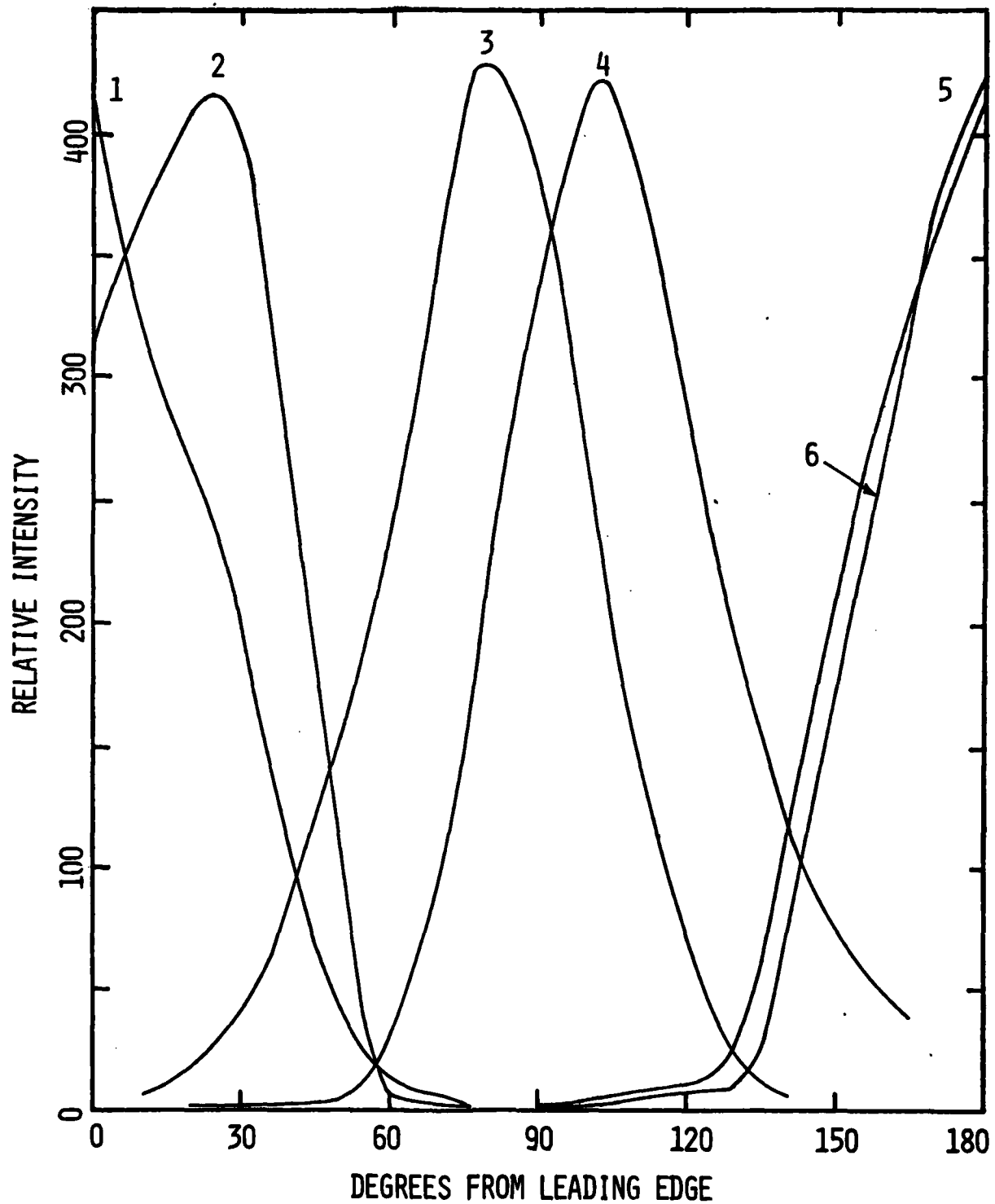


Fig. 33 Calibration of output from photo-detectors.

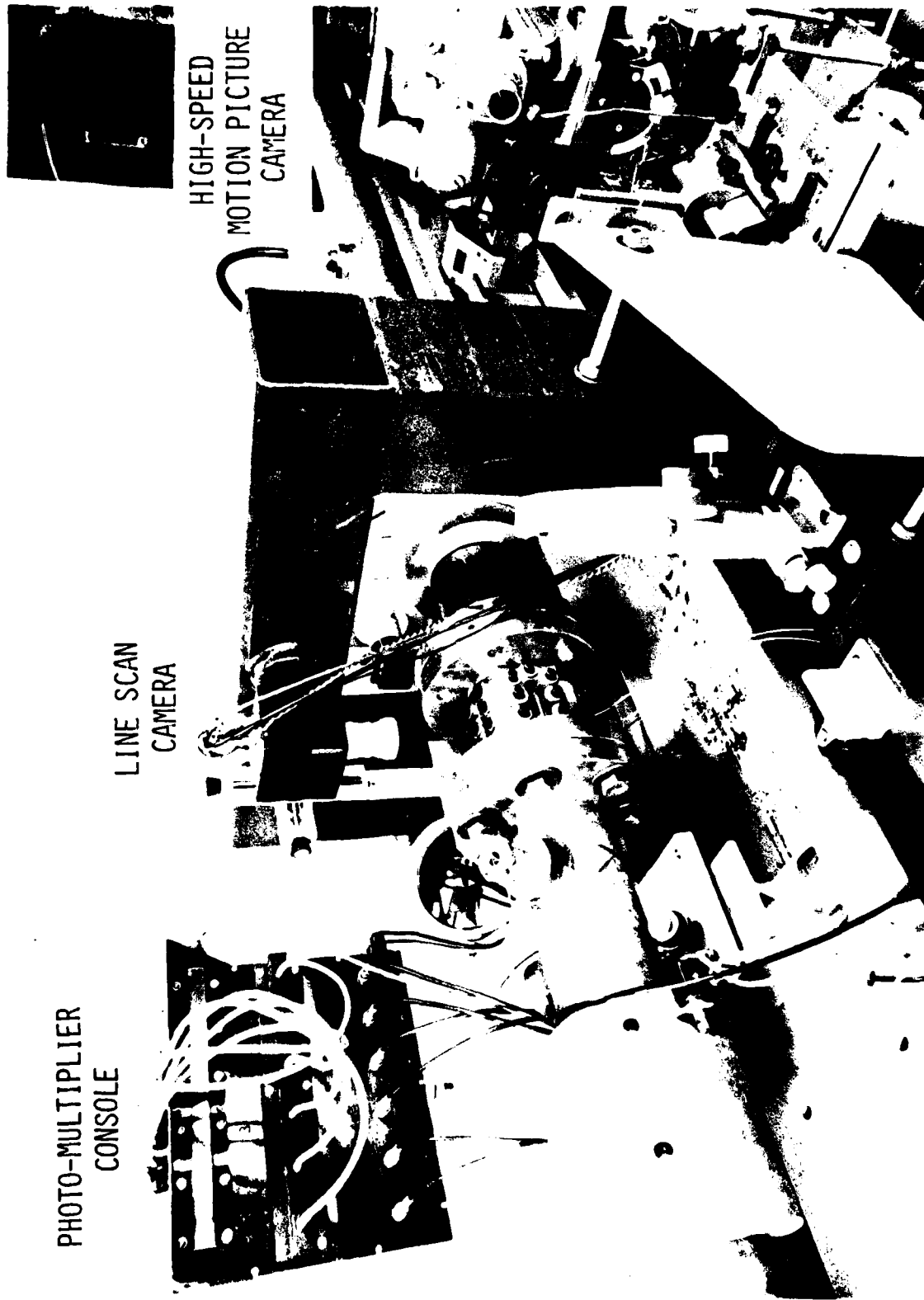


Fig. 34 Overall view of the test section and paraphernalia.

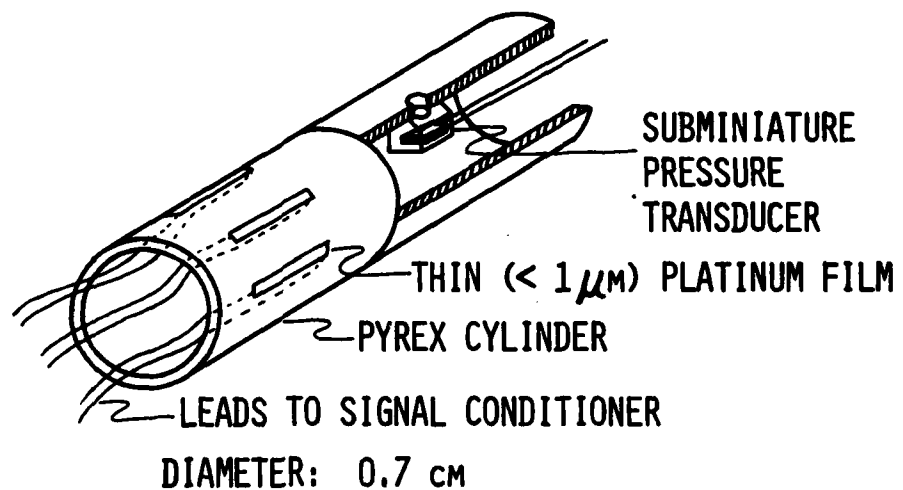


Fig. 35 Inert cylinder instrumented for heat flux and pressure measurements.

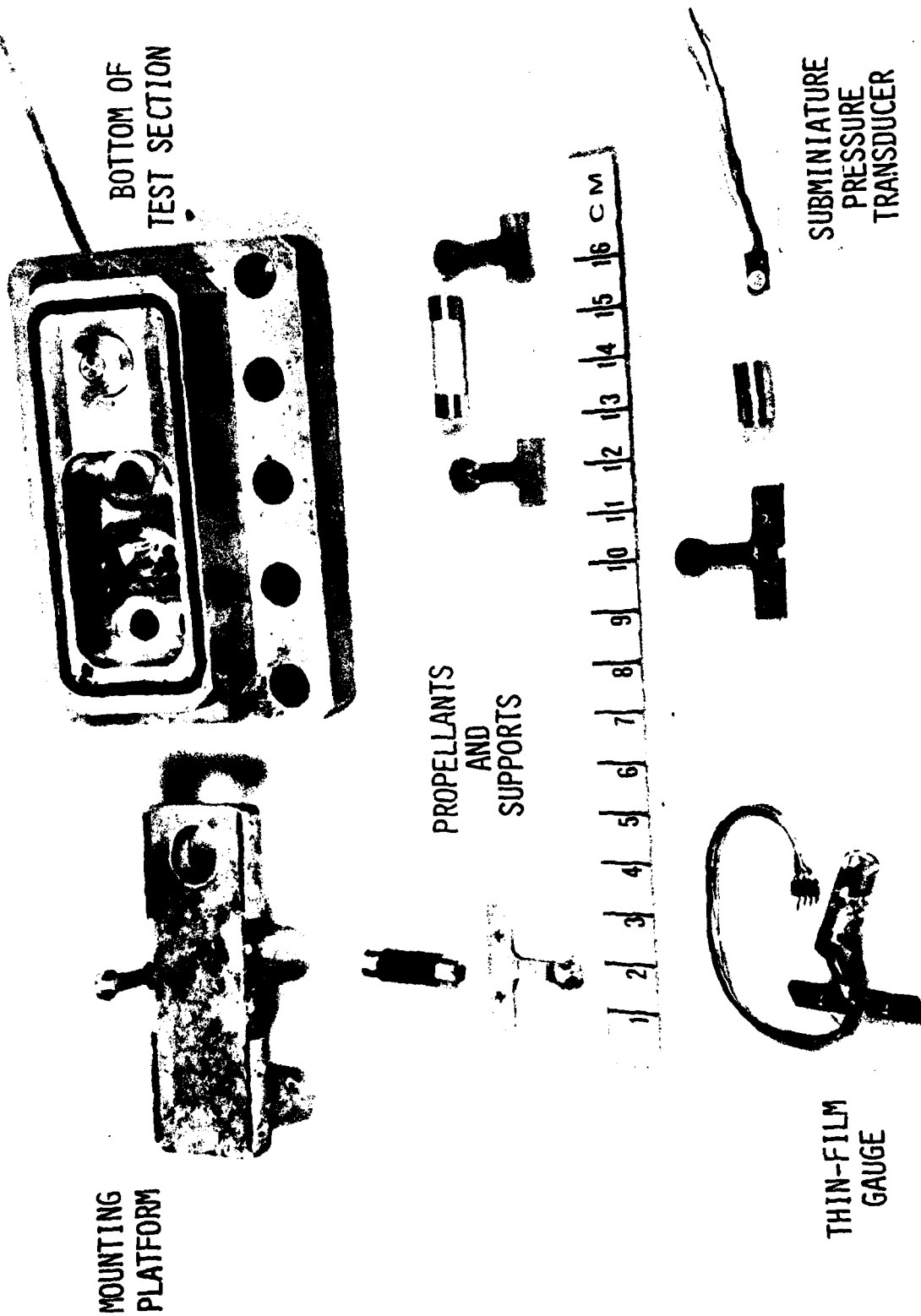


Fig. 36 Mounting platform, specimens and accessories.

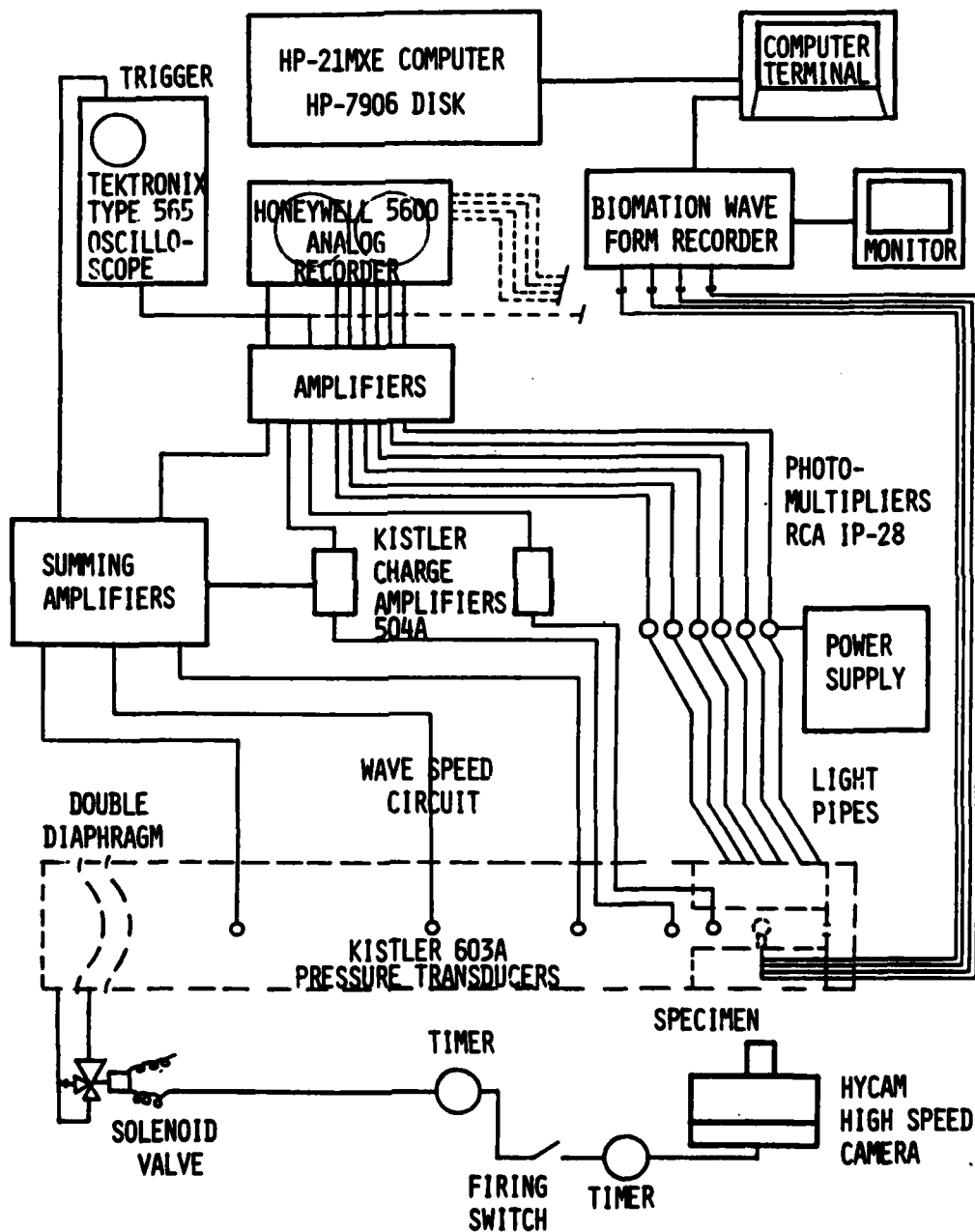


Fig. 37 Instrumentation for the convective ignition experiment.

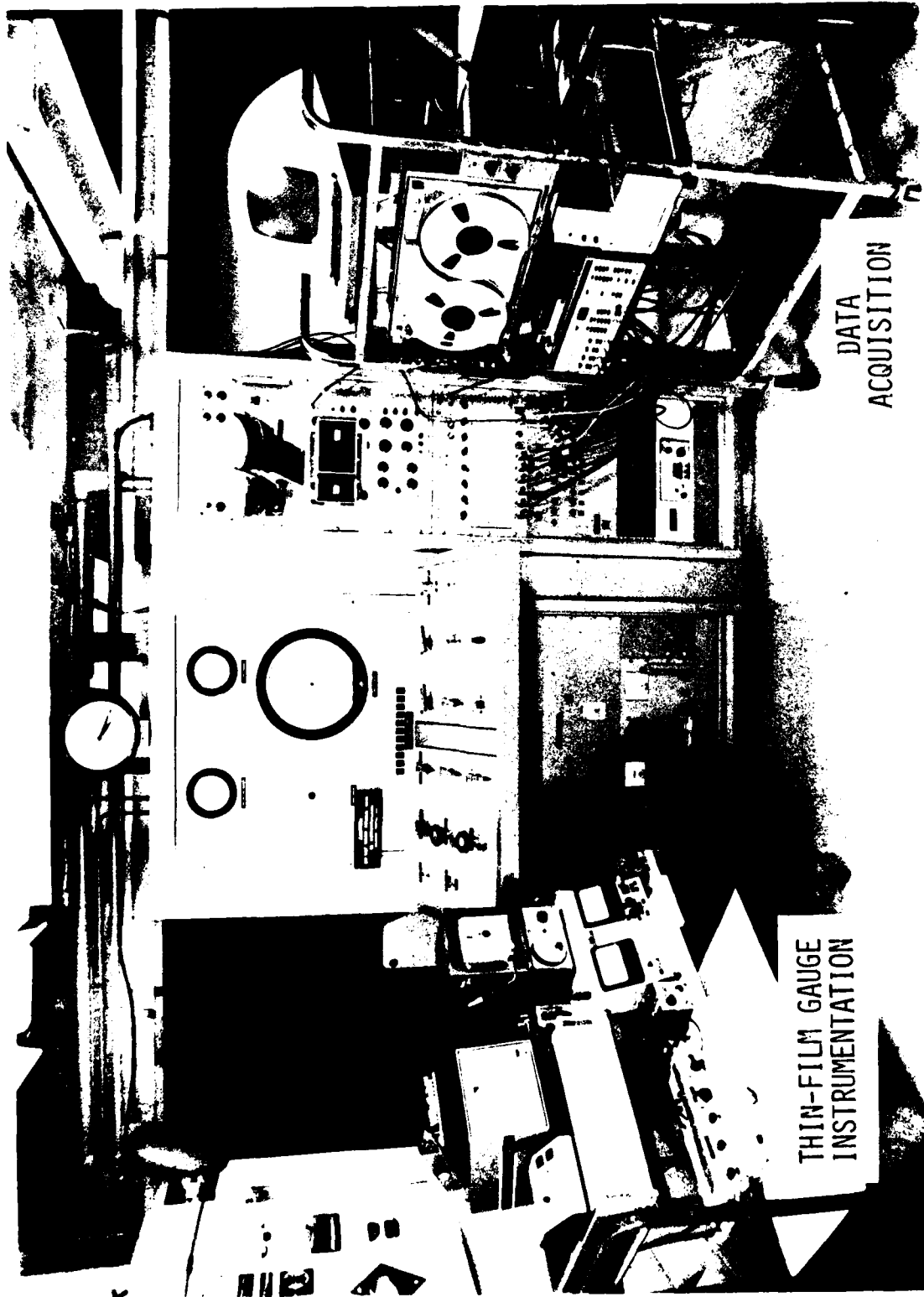


Fig. 38 Overall view of the control consoles of gas and electronic systems for the convective ignition experiment.

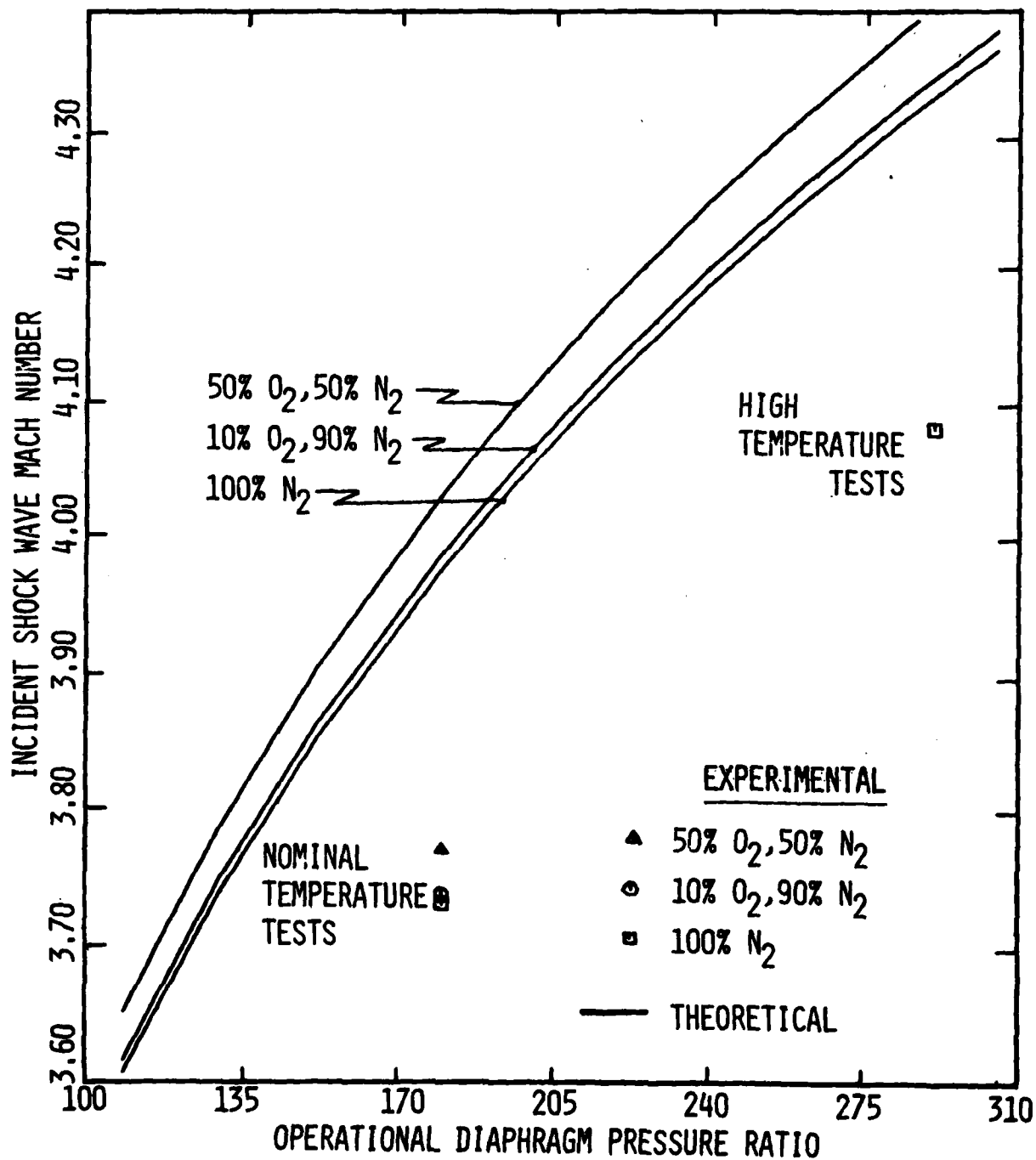


Fig. 39 Experimentally determined Mach number values of the incident shock wave at the entrance to the test section are lower than the theoretical values.

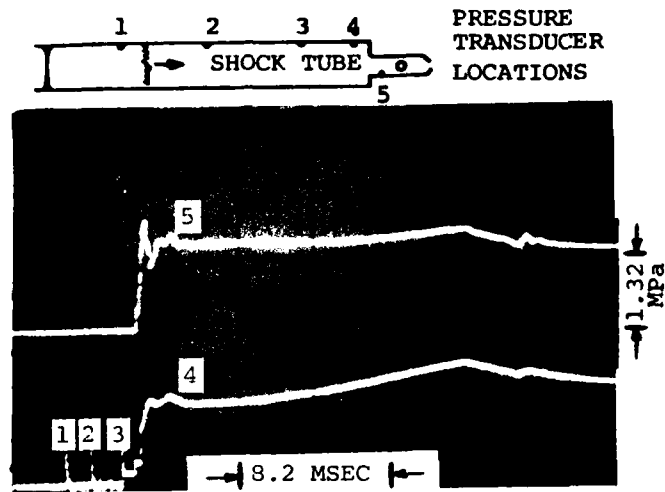


Fig. 40 Typical pressure data

- a) test section static pressure - top
- b) pressure indication for incident shock wave speed - bottom.

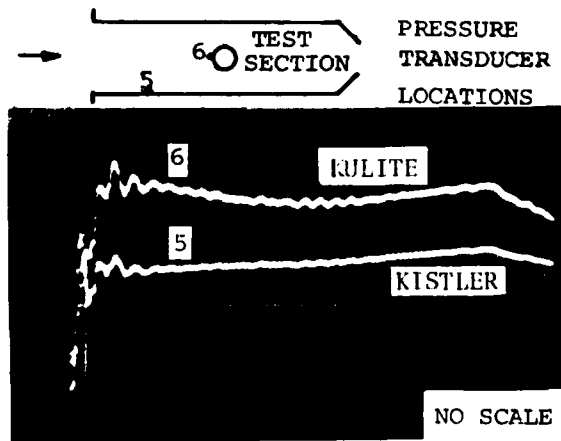
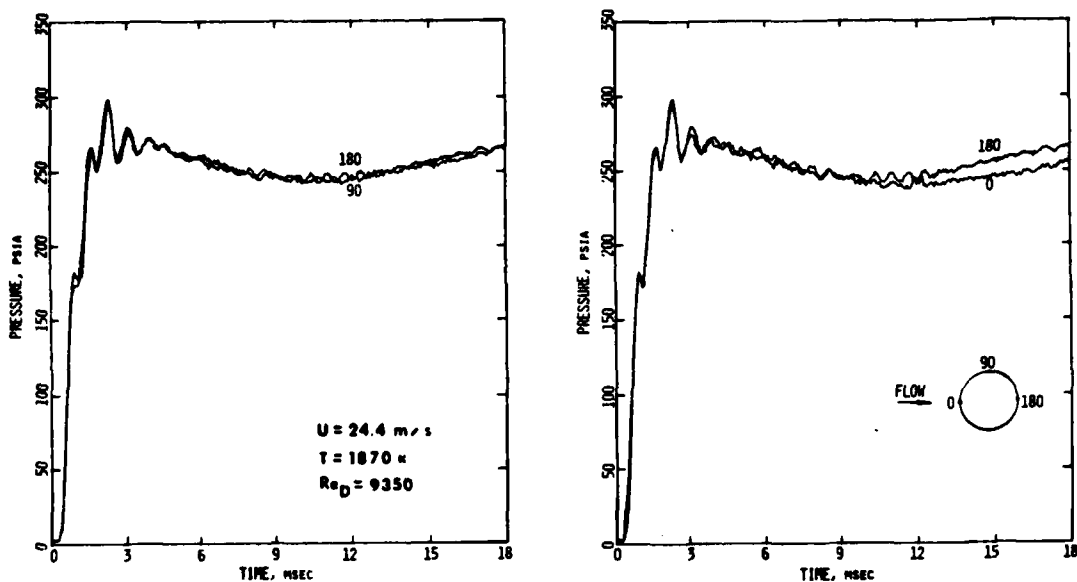
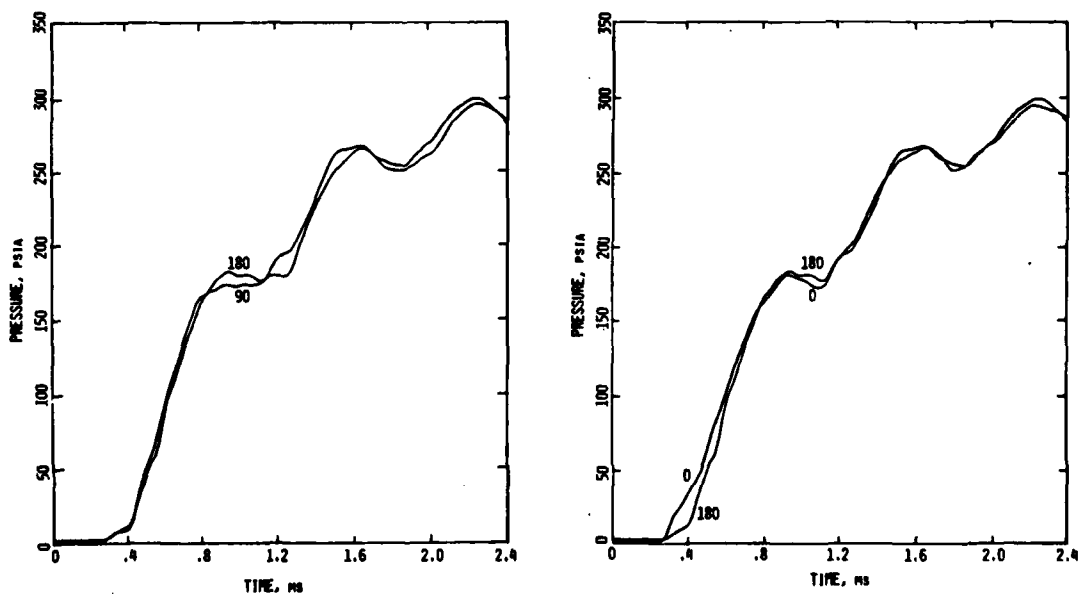


Fig. 41 Comparison of test section pressure data taken at two locations:

- a) instrumented cylinder - (6).
- b) bottom wall - (5).



a) Test time pressure distribution is very uniform.



b) The pressure distribution during the flow settling period.

Fig. 42 Pressure distribution measured around the cylinder perimeter (compilation of three tests) indicates high reproducibility of test conditions.

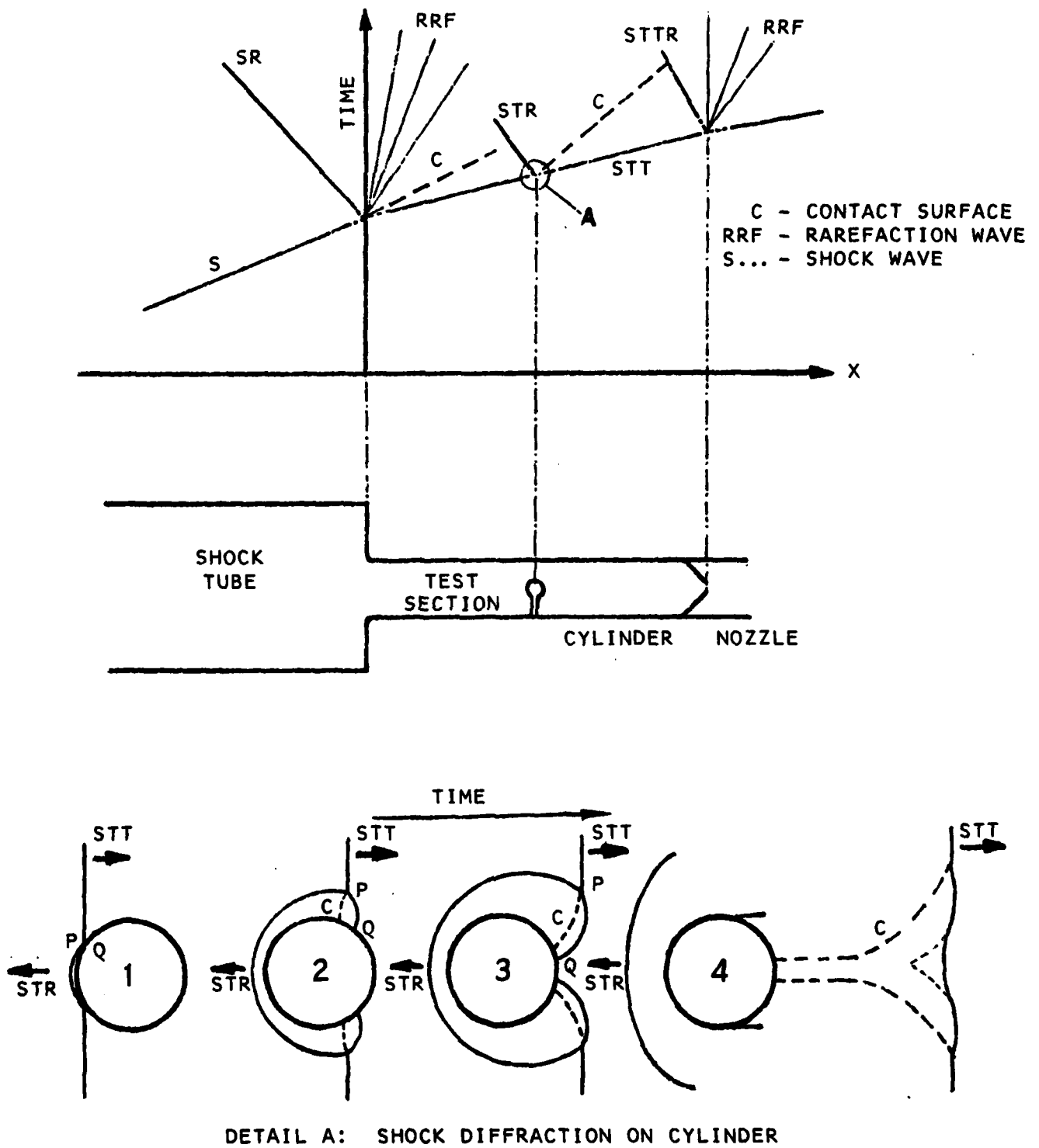


Fig. 43 Wave structure of the starting process of the flow.

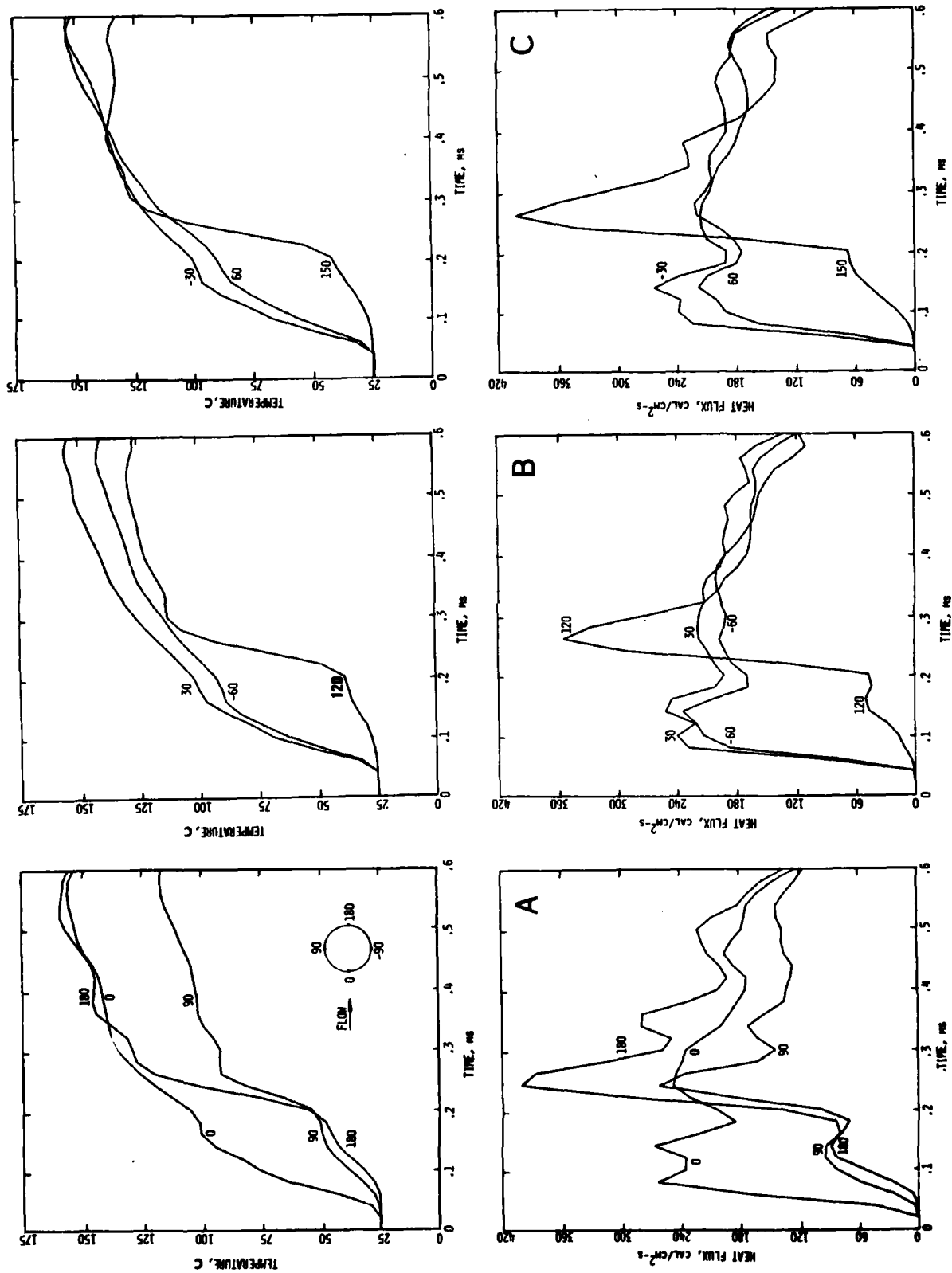


Fig. 44 The structure and magnitude of the surface temperature and heat flux distribution around the cylinder perimeter during the settling period of the flow indicate very strong initial flow transients.

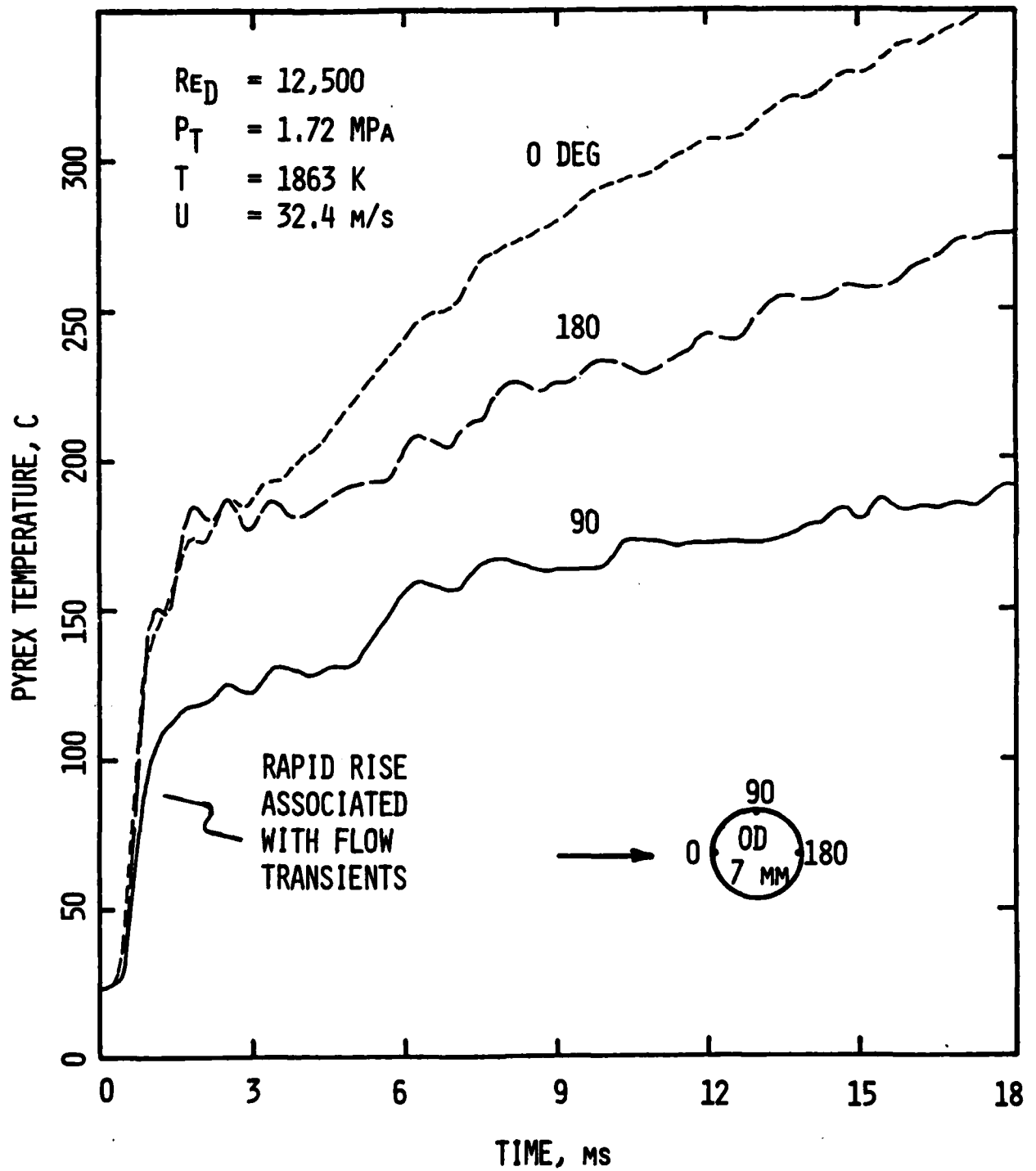


Fig. 45 Temperature transients on pyrex cylinders.

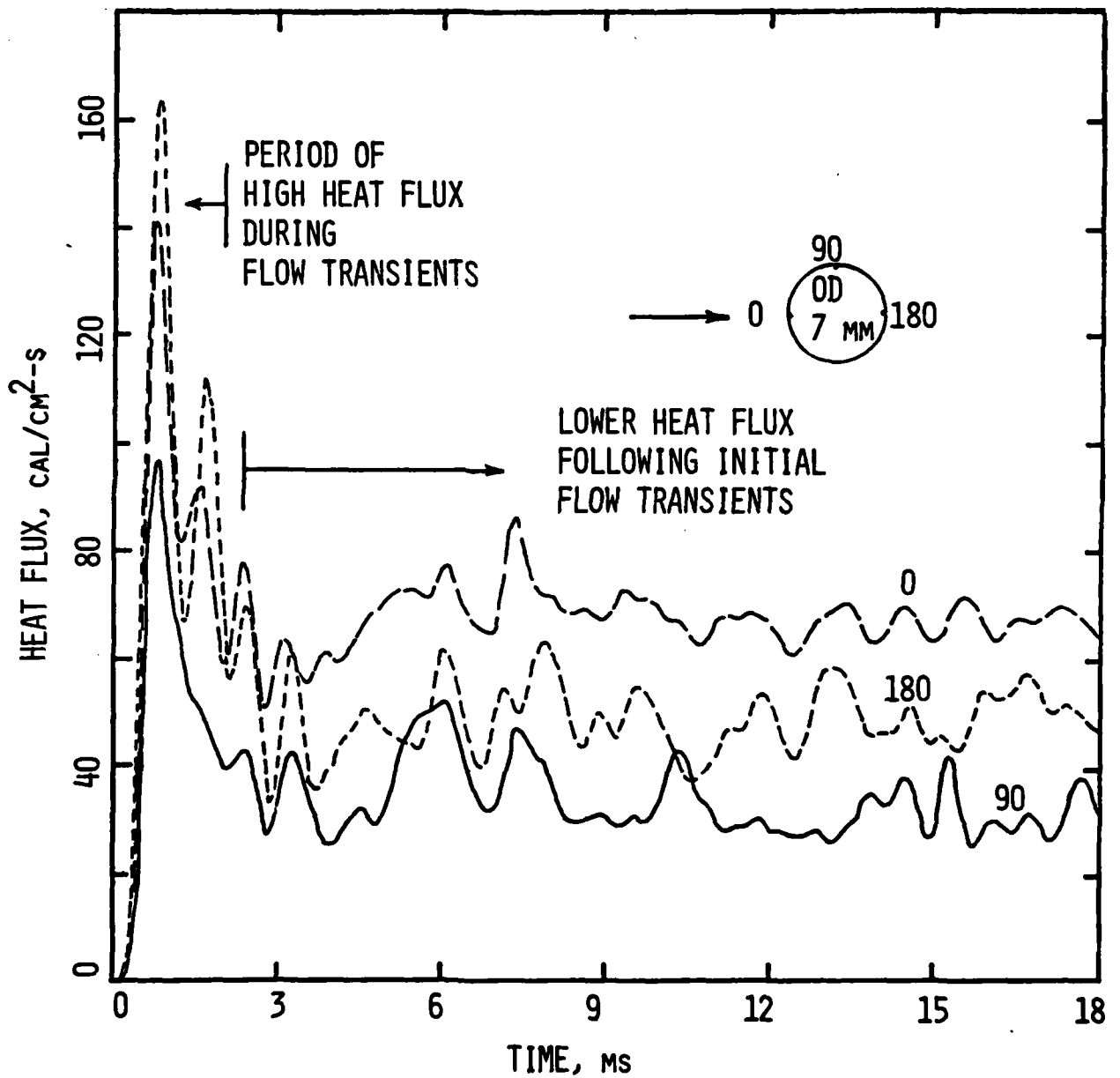


Fig. 46 Heat fluxes corresponding to Fig. 45 conditions.

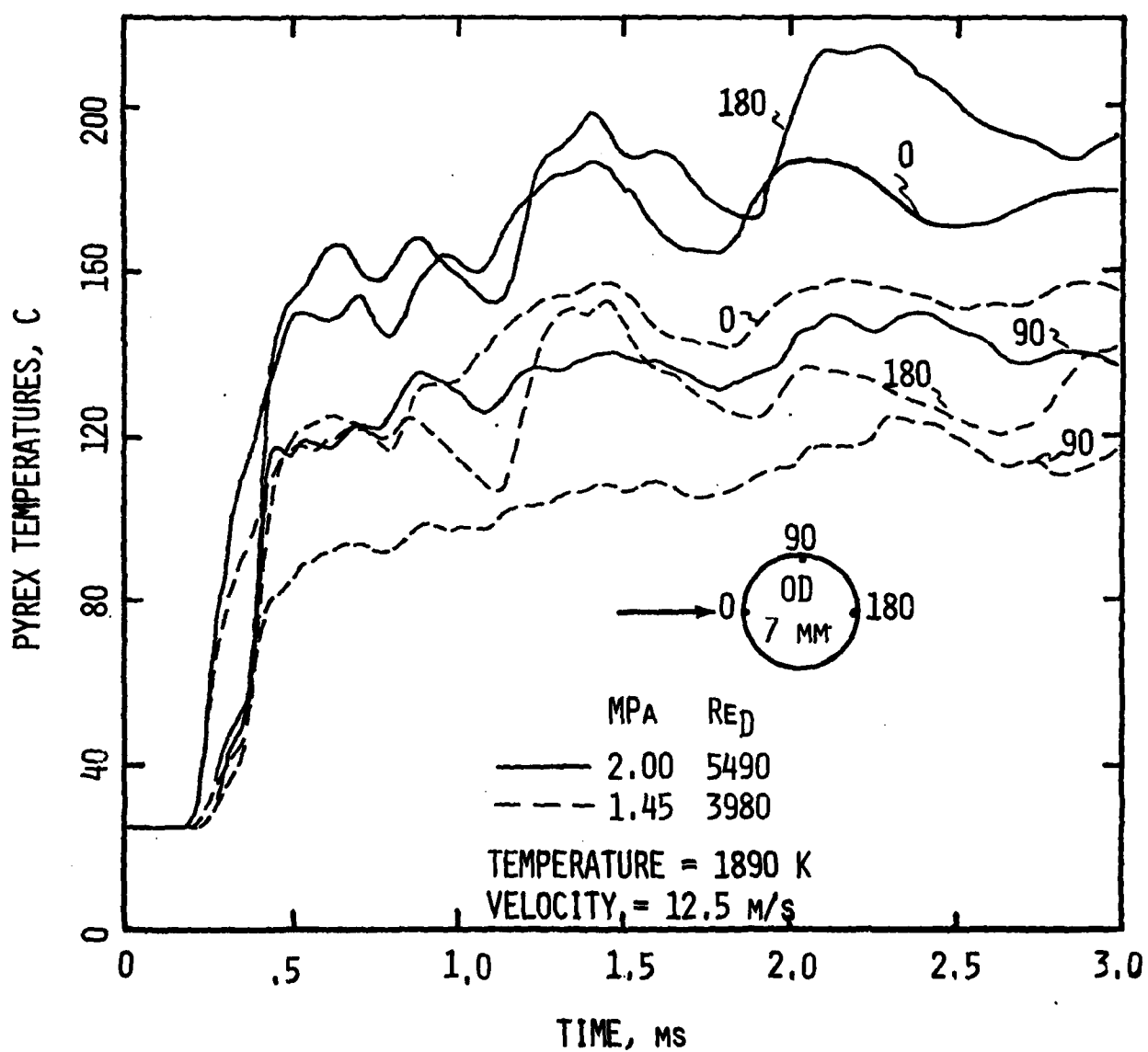


Fig. 47 Increasing the ambient pressure results in increased heating rates and more rapid surface temperature rise.

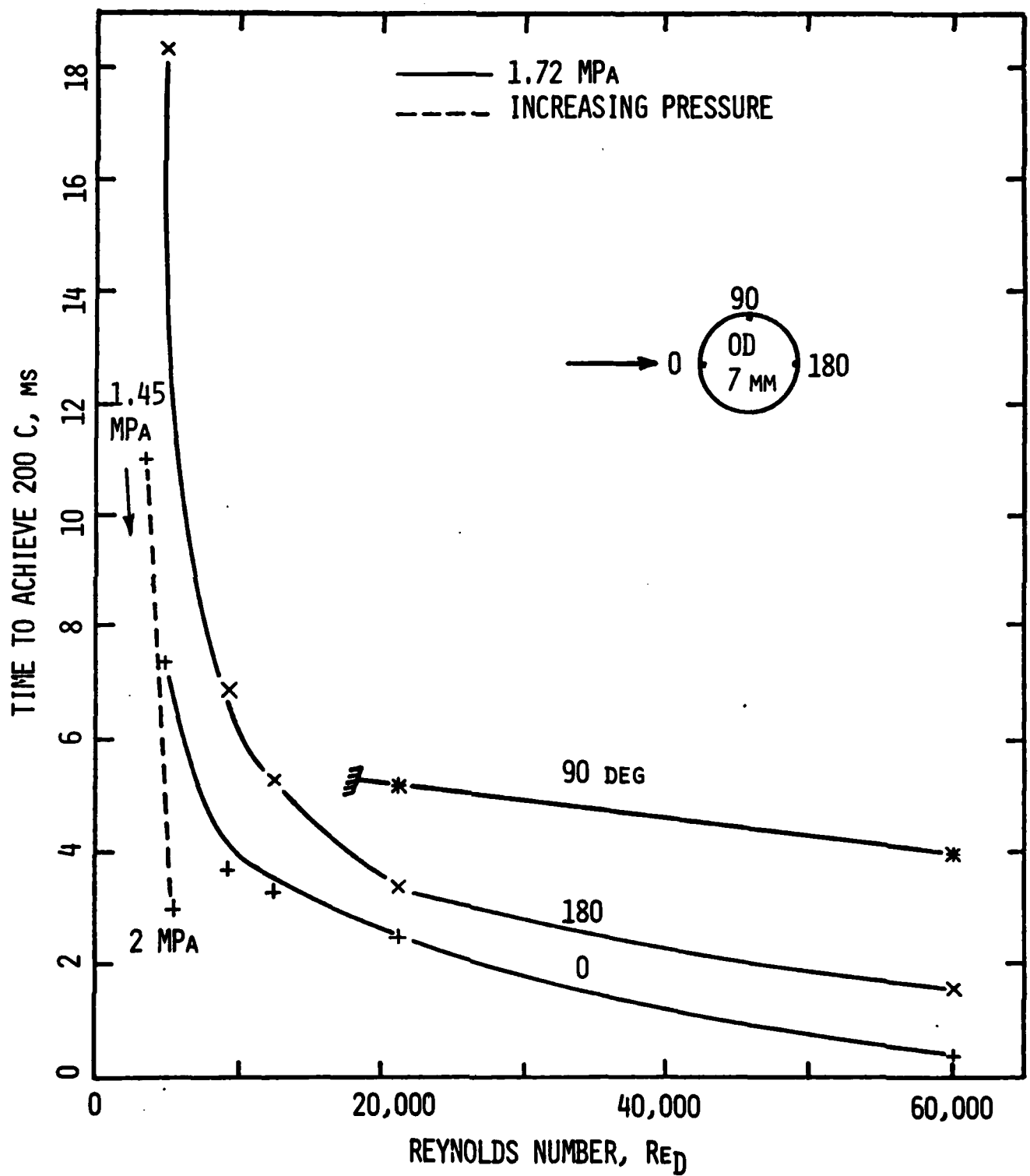


Fig. 48 Time to achieve a prescribed temperature rise is very dependent upon  $Re_D$  and pressure.

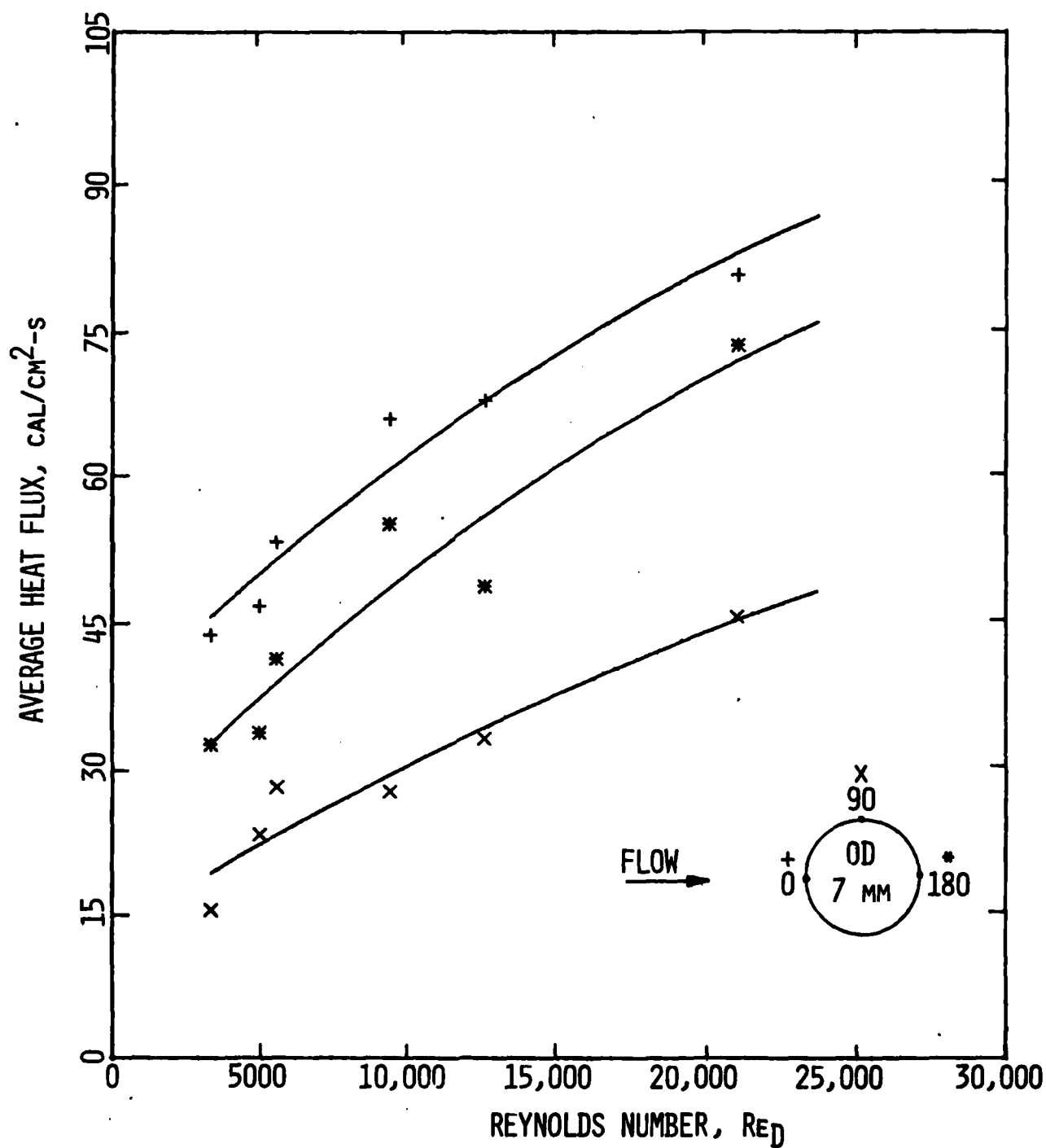
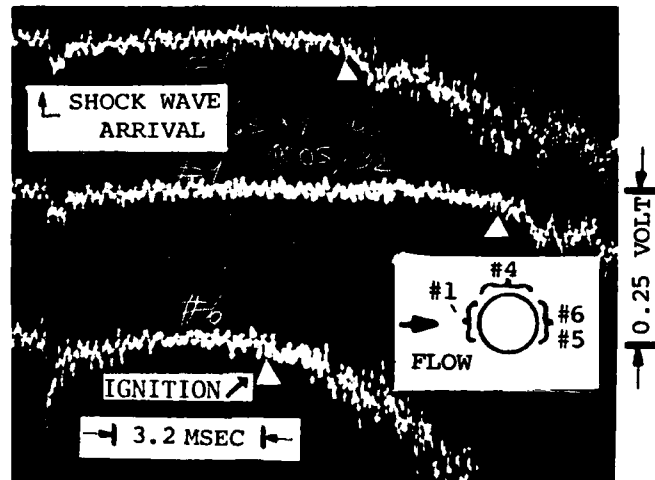


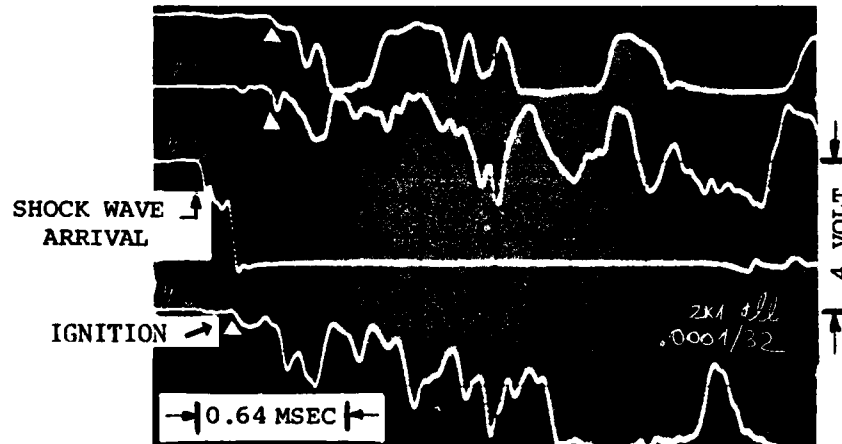
Fig. 49 Average heat flux during the steady period of the flow is the highest at the front stagnation point for the entire Re<sub>D</sub> range of tests.

A



M30 propellant under low oxygen content flow  
(90%N<sub>2</sub>&10%O<sub>2</sub>, U = 6.3 m/s) .

B



M26 propellant under high oxygen content flow  
(50%N<sub>2</sub>&50%O<sub>2</sub>, U = 23.4 m/s) .

Fig. 50 Typical photo-detector output signals.

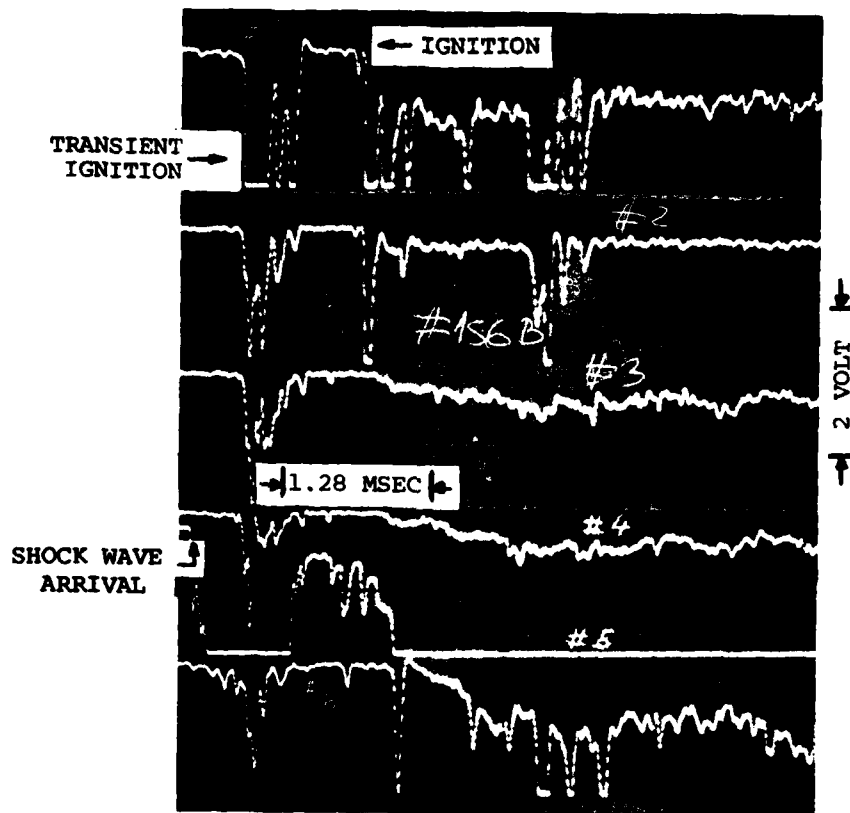
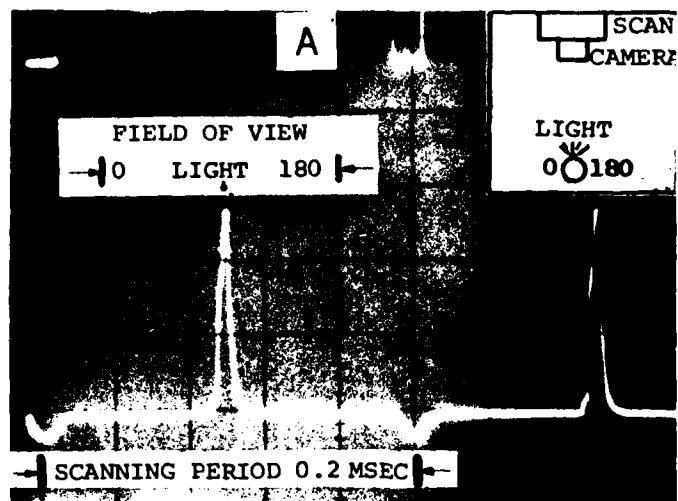
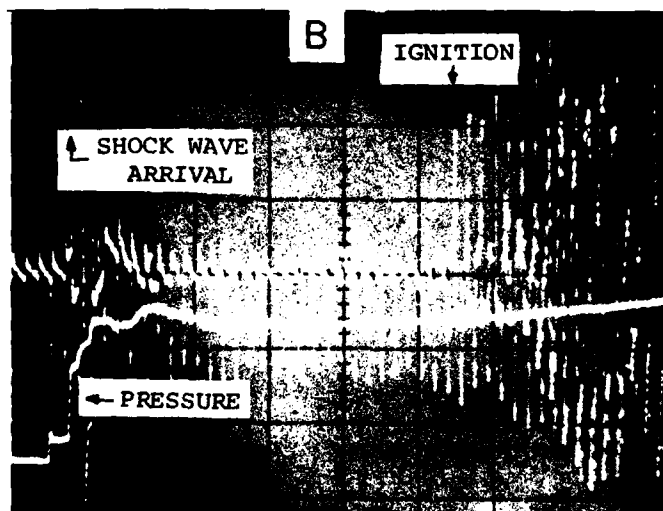


Fig. 51 Transient ignition phenomena are distinguished in the case of M30 propellant under high velocity and oxygen content flow ( $U = 60.8 \text{ m/s}$ ,  $50\%N_2$  &  $50\%O_2$ ).

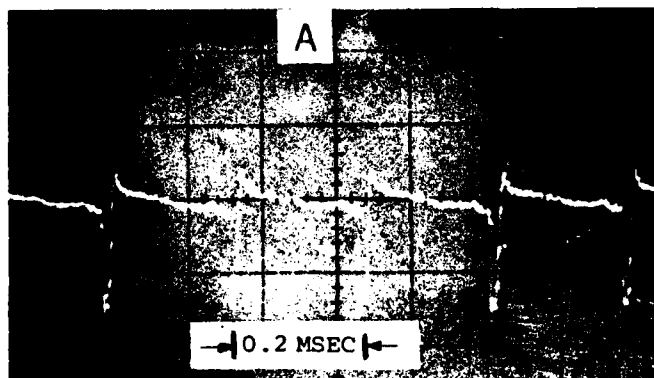


a) Calibration of the output signal from the scan camera.

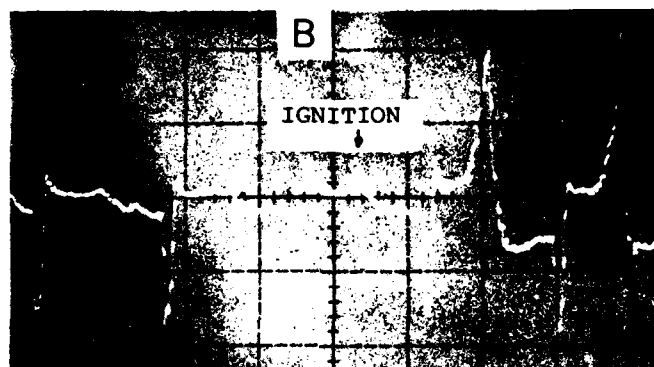


b) Test time output signal from the scan camera marks distinctly the arrival of the shock wave and the onset of ignition.

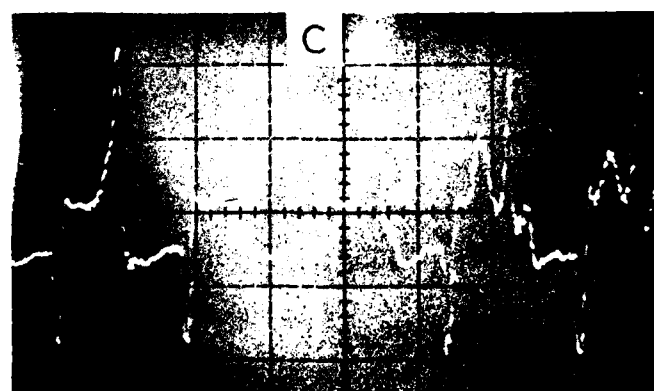
Fig. 52 Ignition and flame spreading detection by means of the Reticon line scan camera.



The periodic output signal prior to ignition.



Ignition occurs at the flow separation region.



Flame spreads on the entire specimen surface.

Fig. 52a Detailed look at the scan camera output during the onset of ignition and subsequent flame spreading.

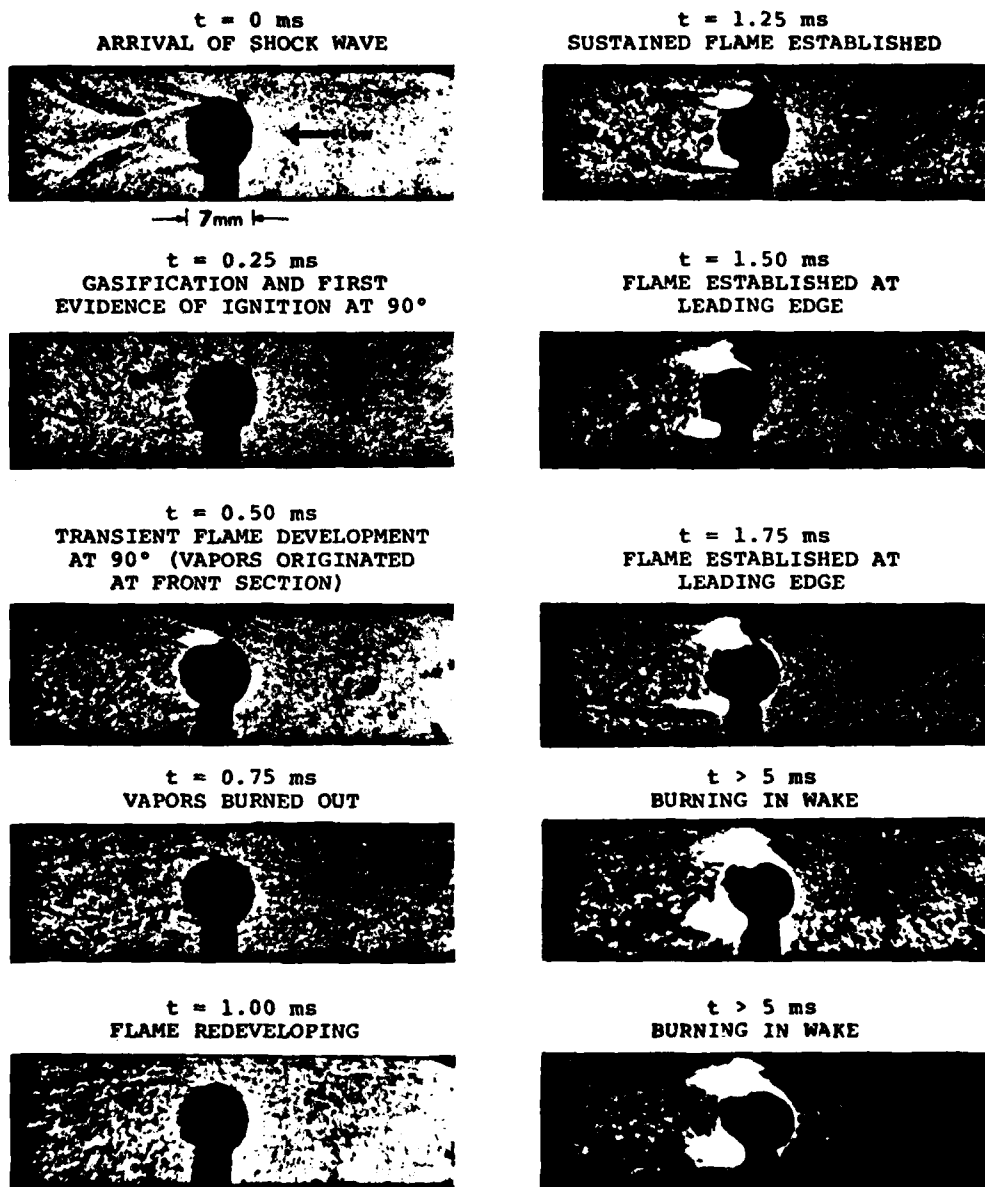


Fig. 53 Photographs showing convective ignition events (M26 propellant, 1.63 MPa, 1740 K, 140 m/s, 50%N<sub>2</sub>&50%O<sub>2</sub>,  $Re_D = 55000$ ).

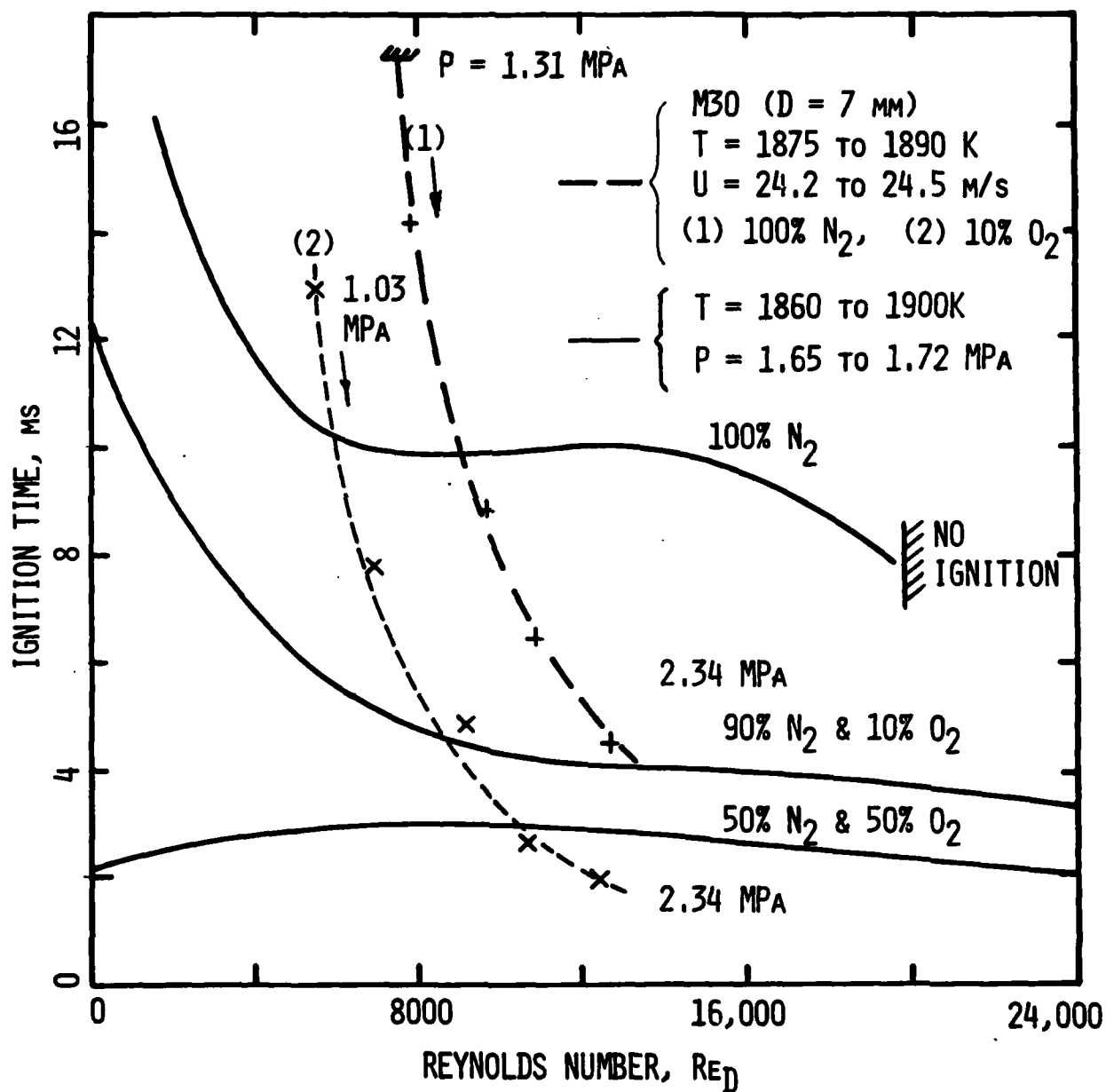


Fig. 54 Ignition data showing decreasing ignition times with increasing velocity, oxygen and pressure (for triple-based M30 propellant) .

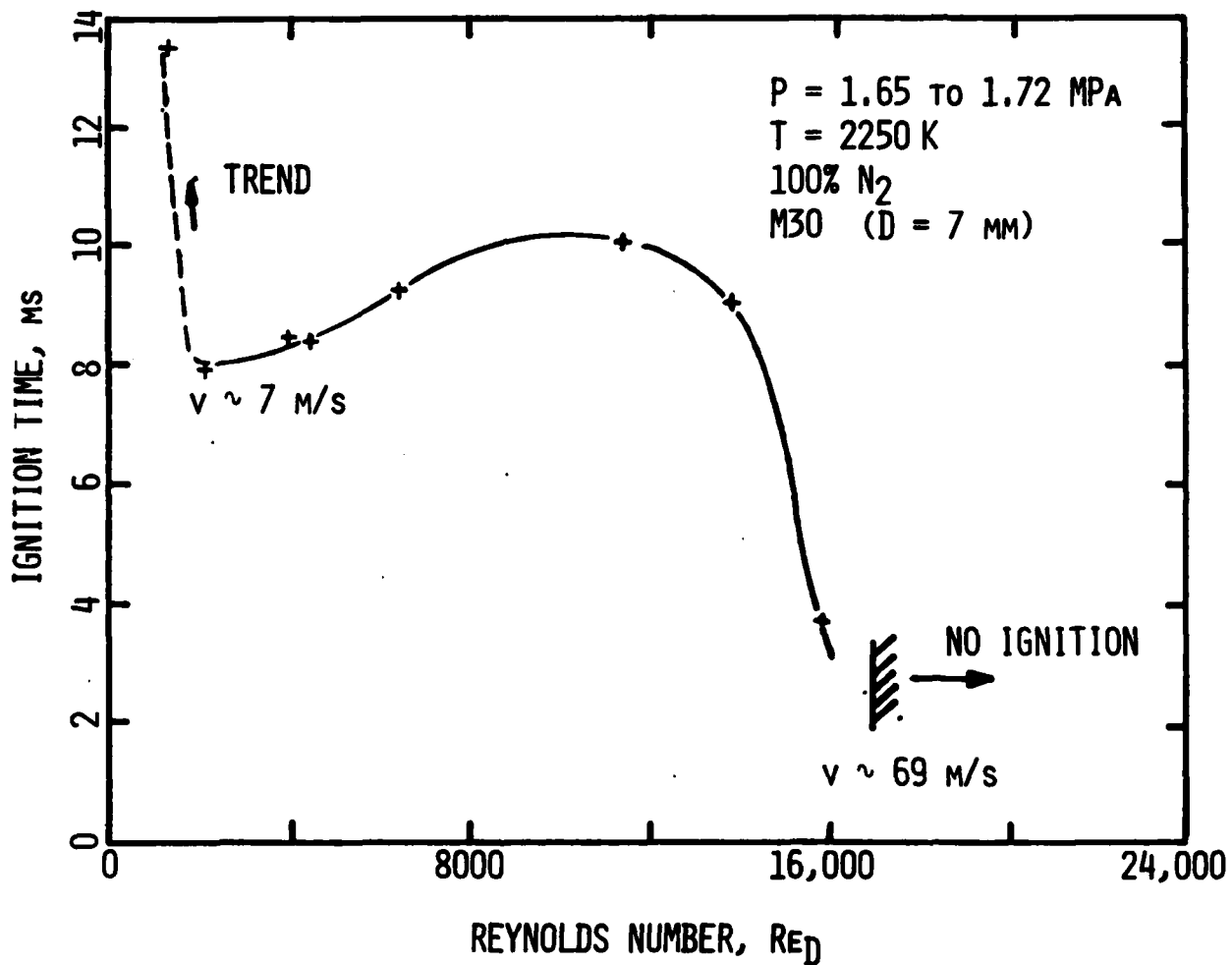


Fig. 55 Ignition data obtained under high temperature and constant pressure conditions (M30 propellant) .

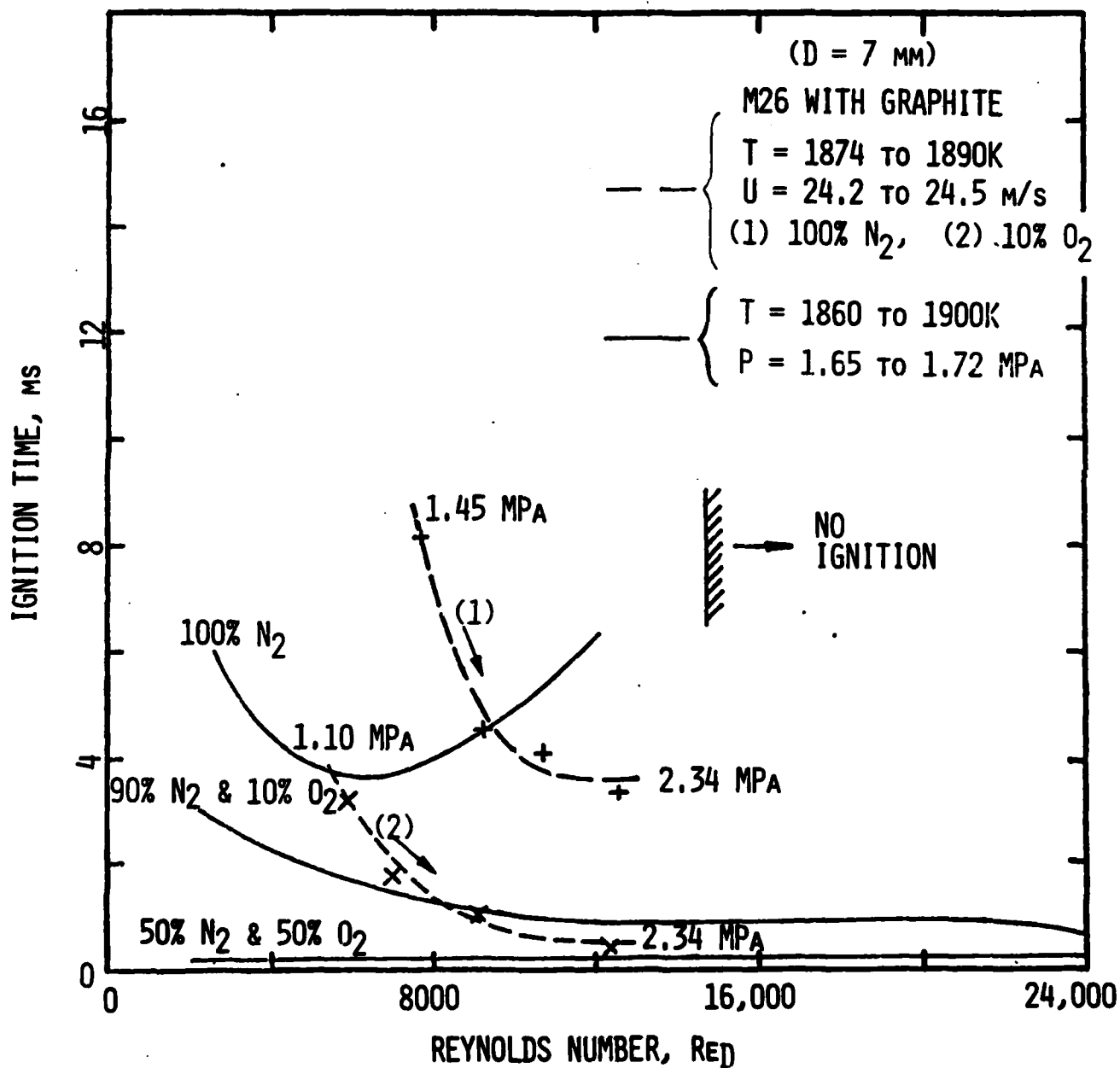


Fig. 56 Ignition data showing decreasing ignition times with increasing velocity, oxygen and pressure (for double-based M26 propellant) .

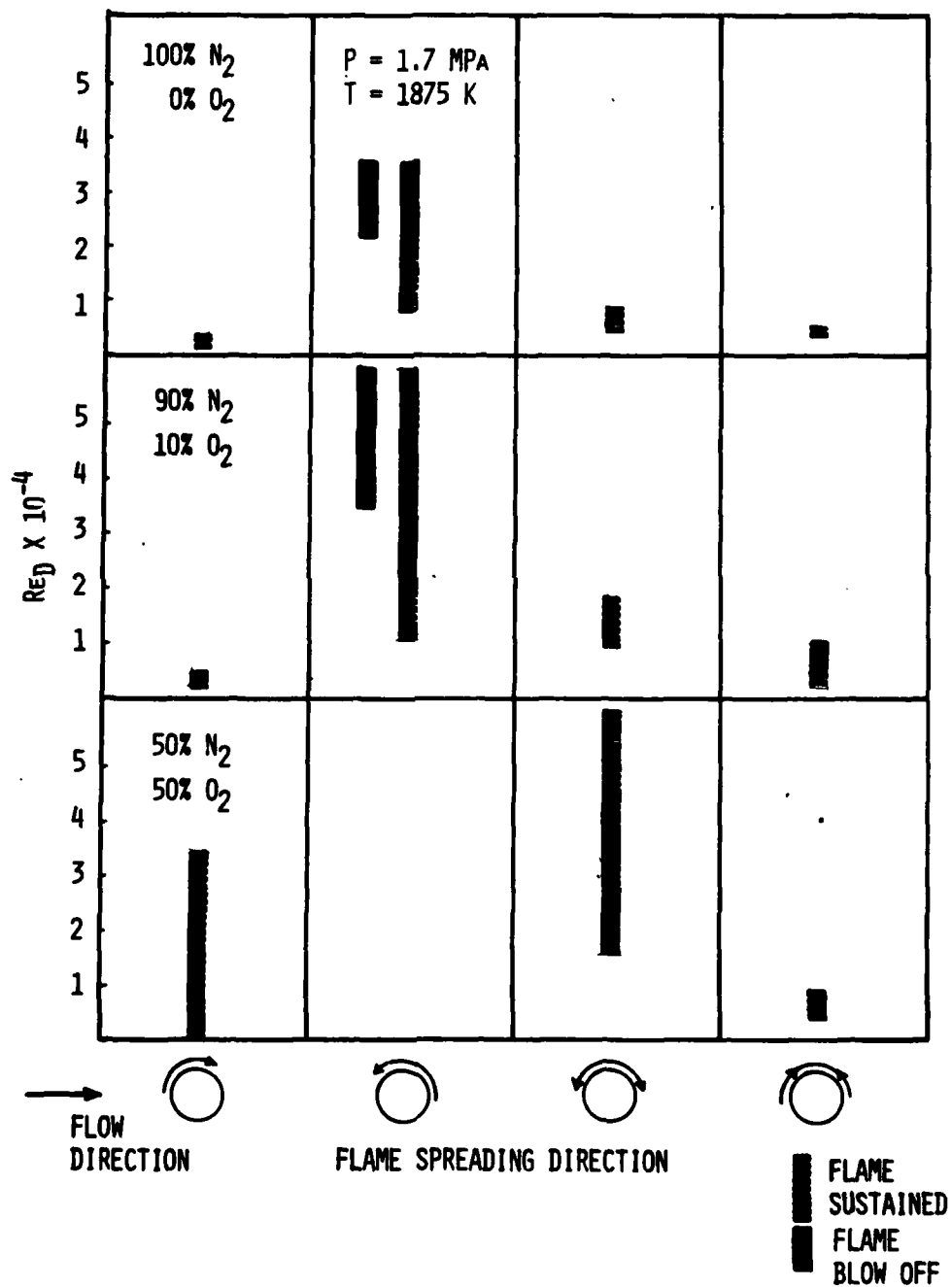


Fig. 57 Statistical diagram of flame spreading tendencies as a function of oxygen concentration and Reynolds number (M30 propellant).

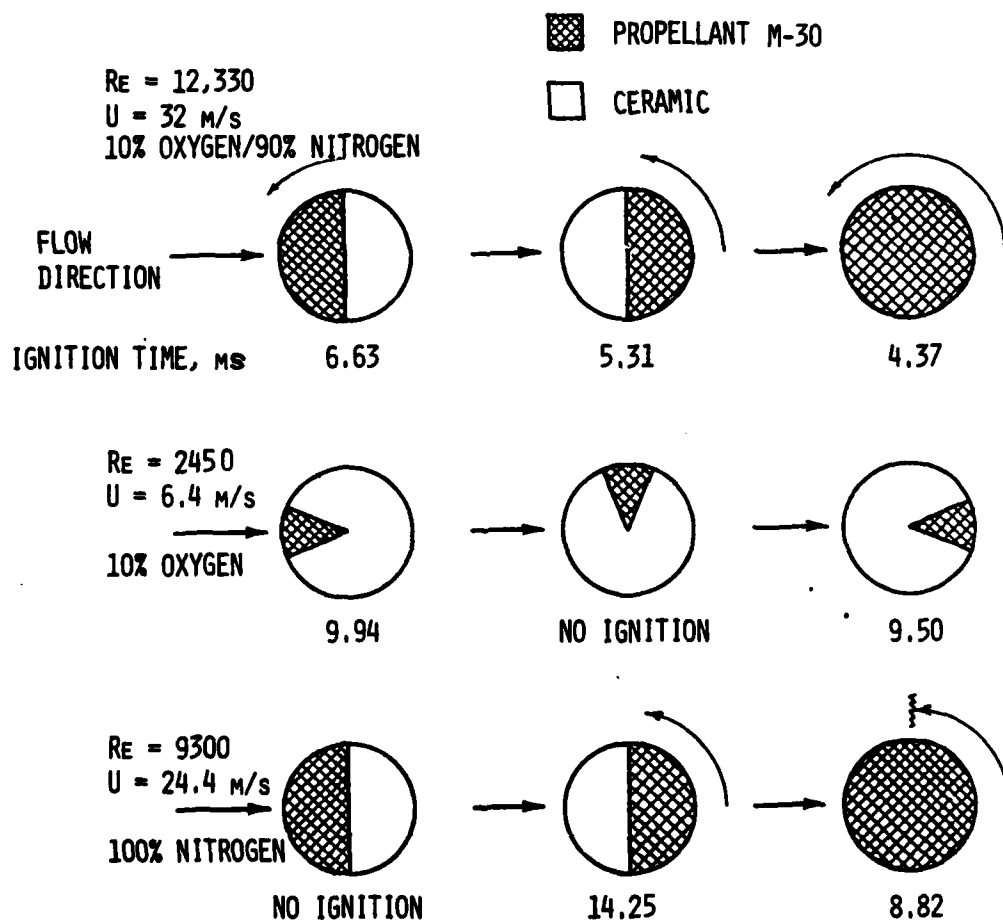


Fig. 58 Ignition trends as demonstrated by a series of partially inert cylindrical specimens.

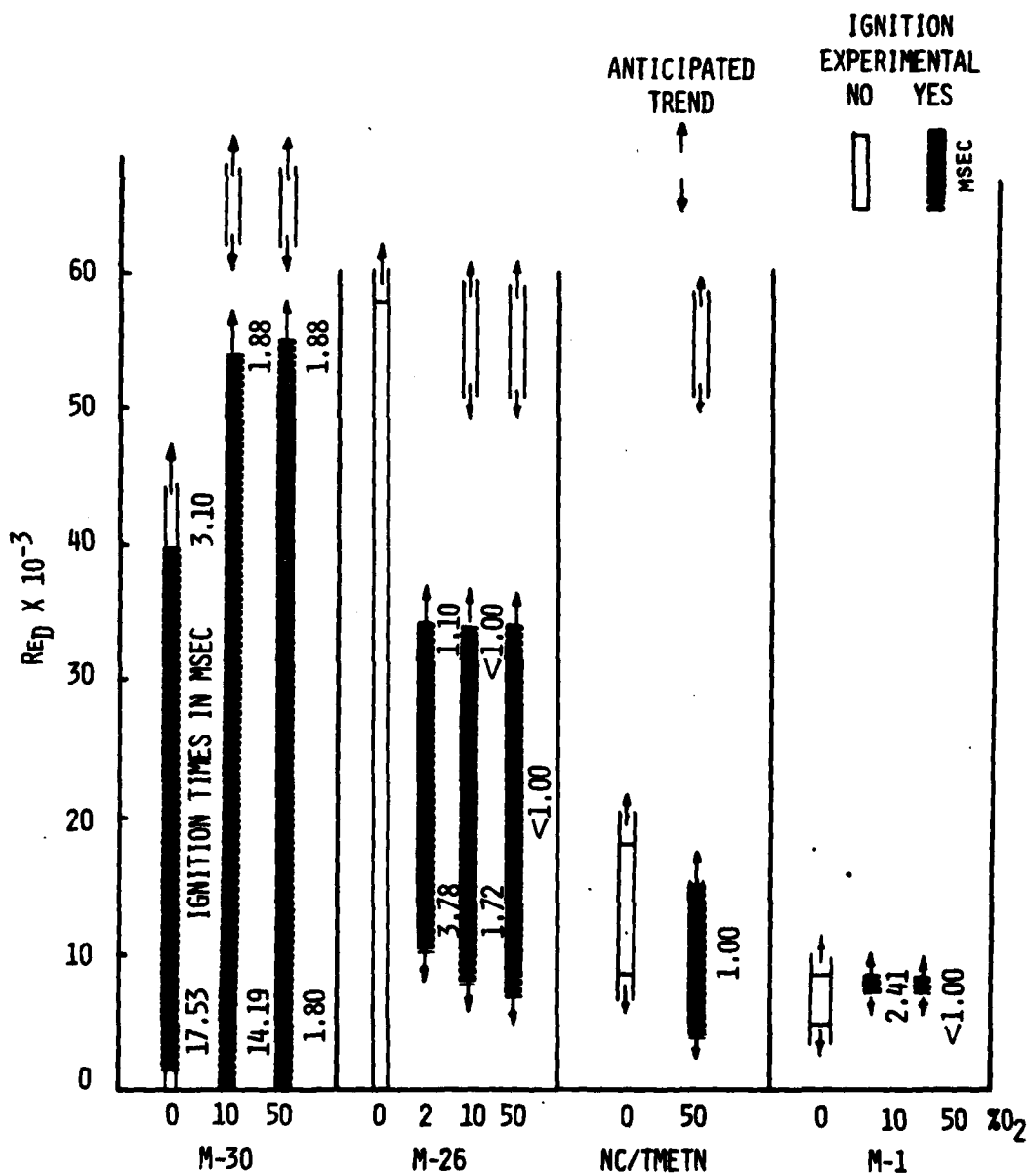


Fig. 59 Propellant ignition trends as a function of oxygen content and Reynolds number.

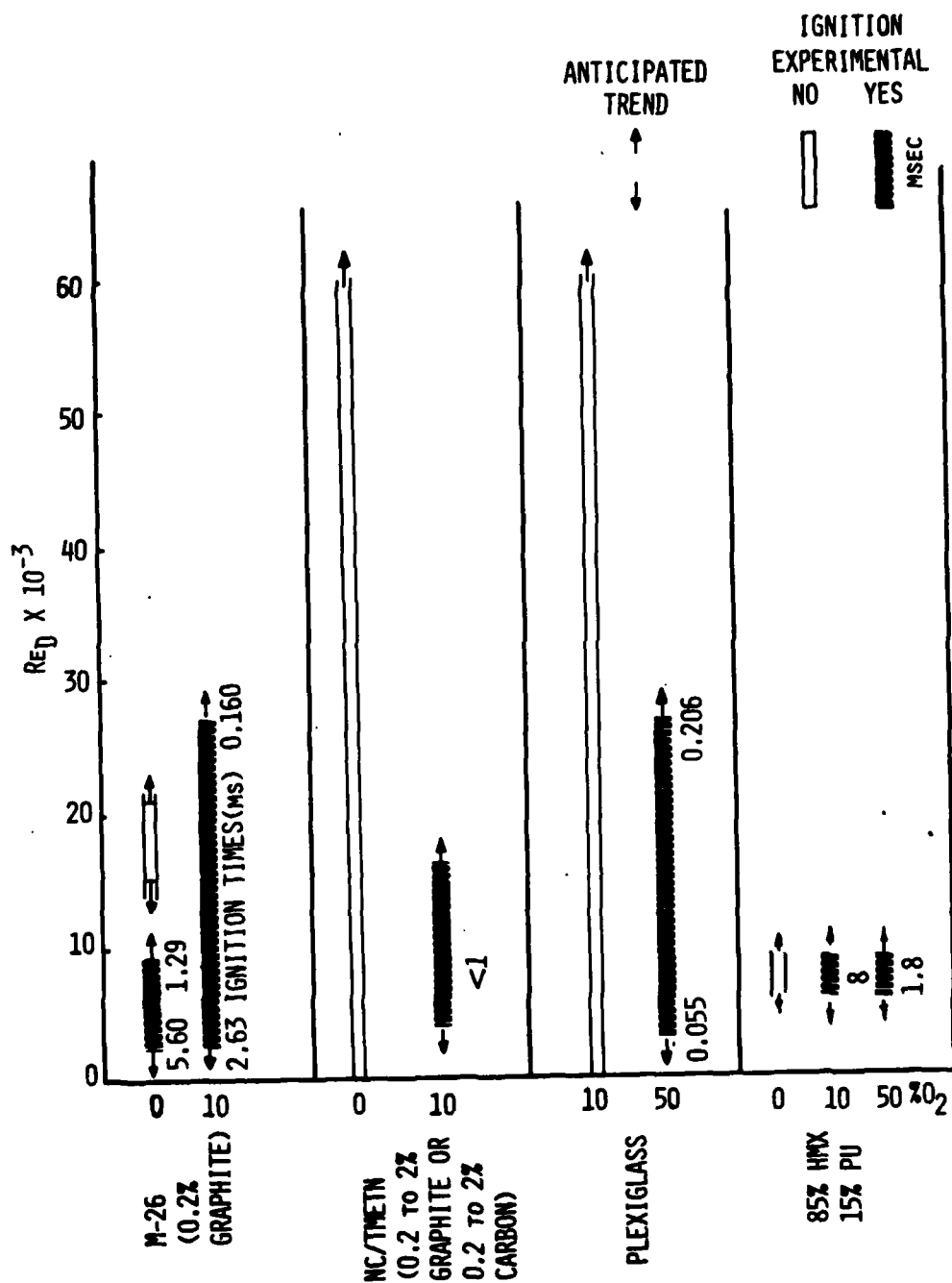


Fig. 60 Ignition trends for several special situations.

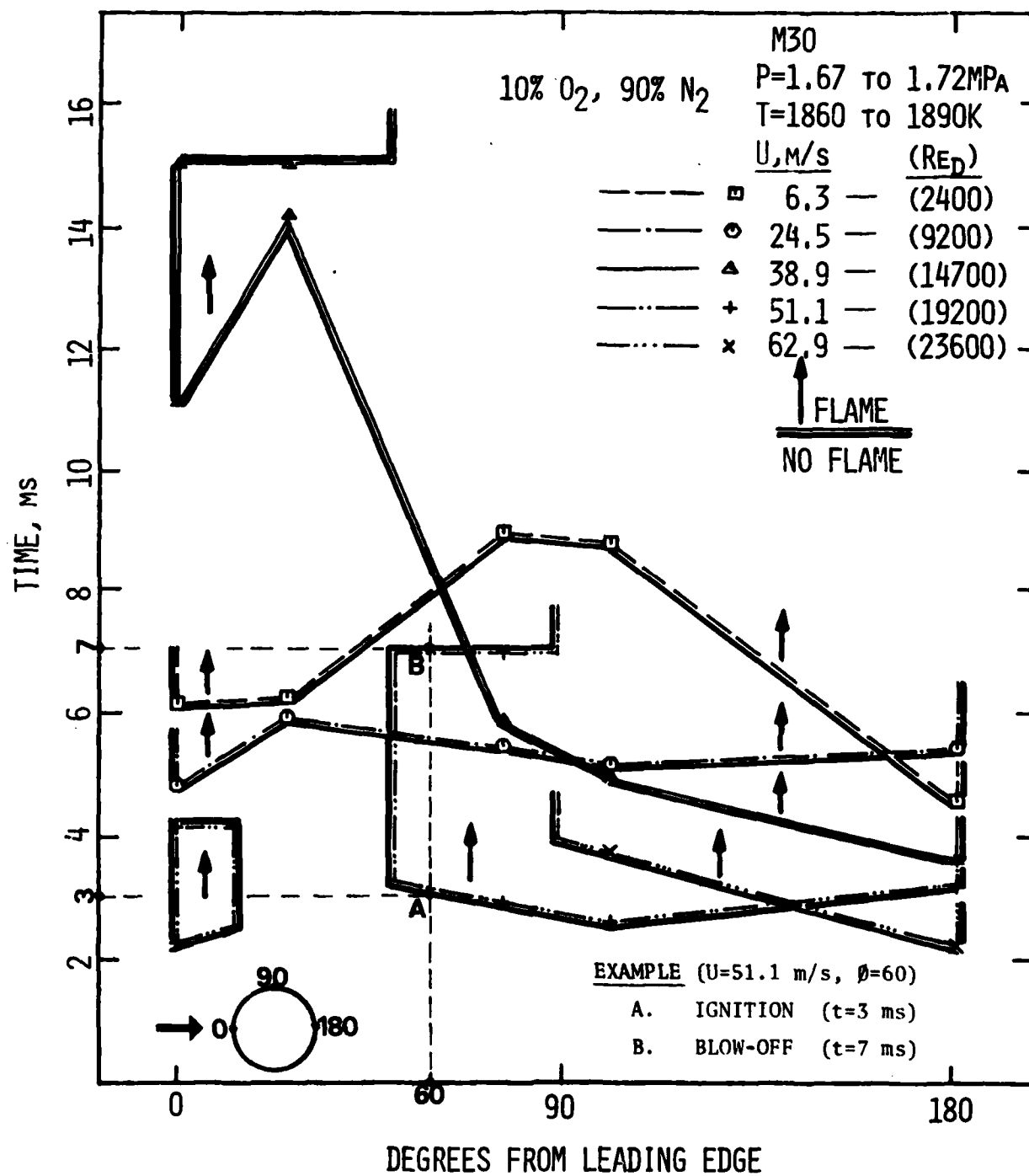


Fig. 61 Time-wise and space-wise flame spreading as a function of flow velocity (M30 propellant, 90%N<sub>2</sub>&10%O<sub>2</sub>) .

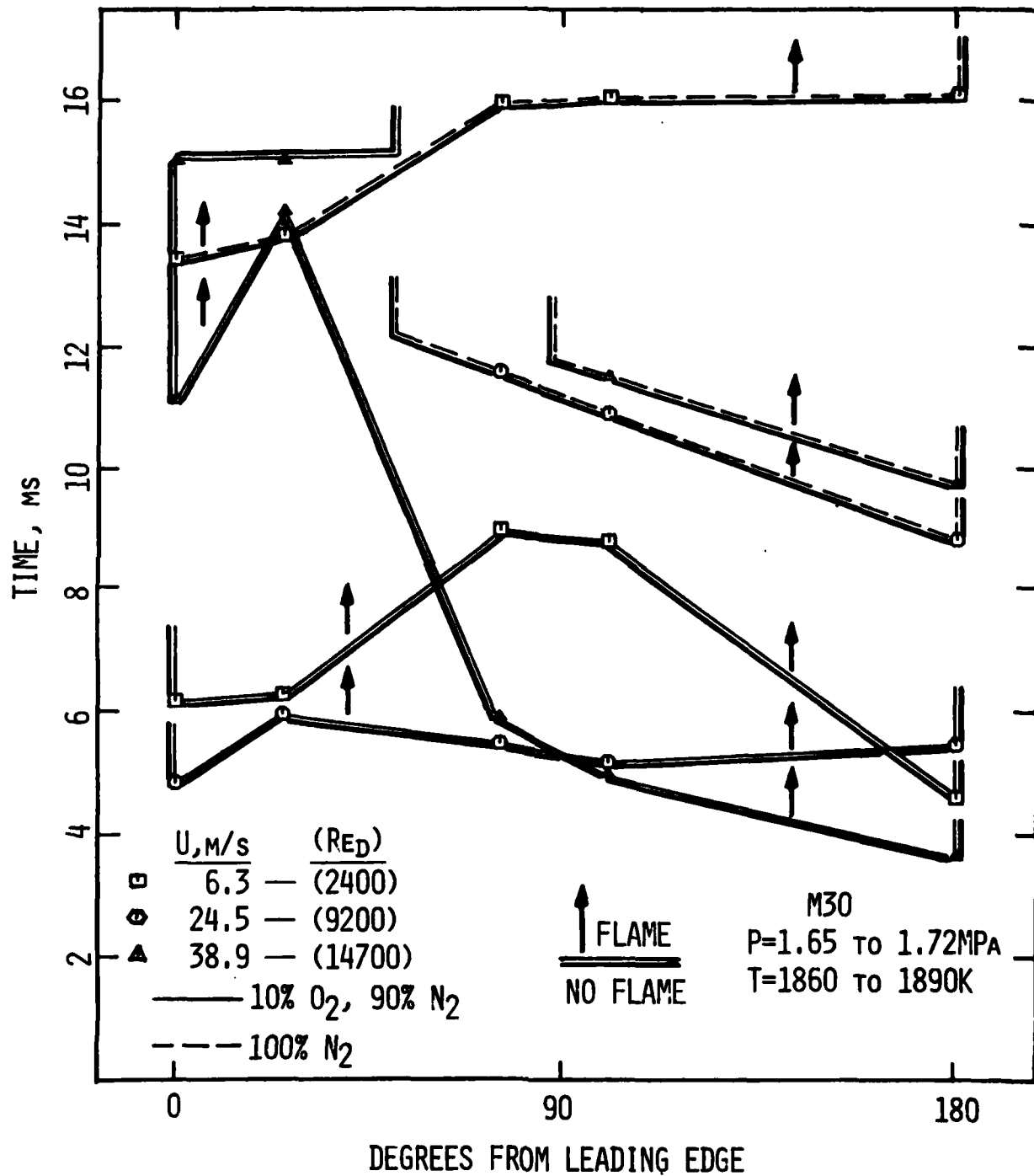


Fig. 62 Comparison between flame spreading as a function of velocity in inert and reactive flows (100%N<sub>2</sub>, 90%N<sub>2</sub>&10%O<sub>2</sub>, M30 propellant) .

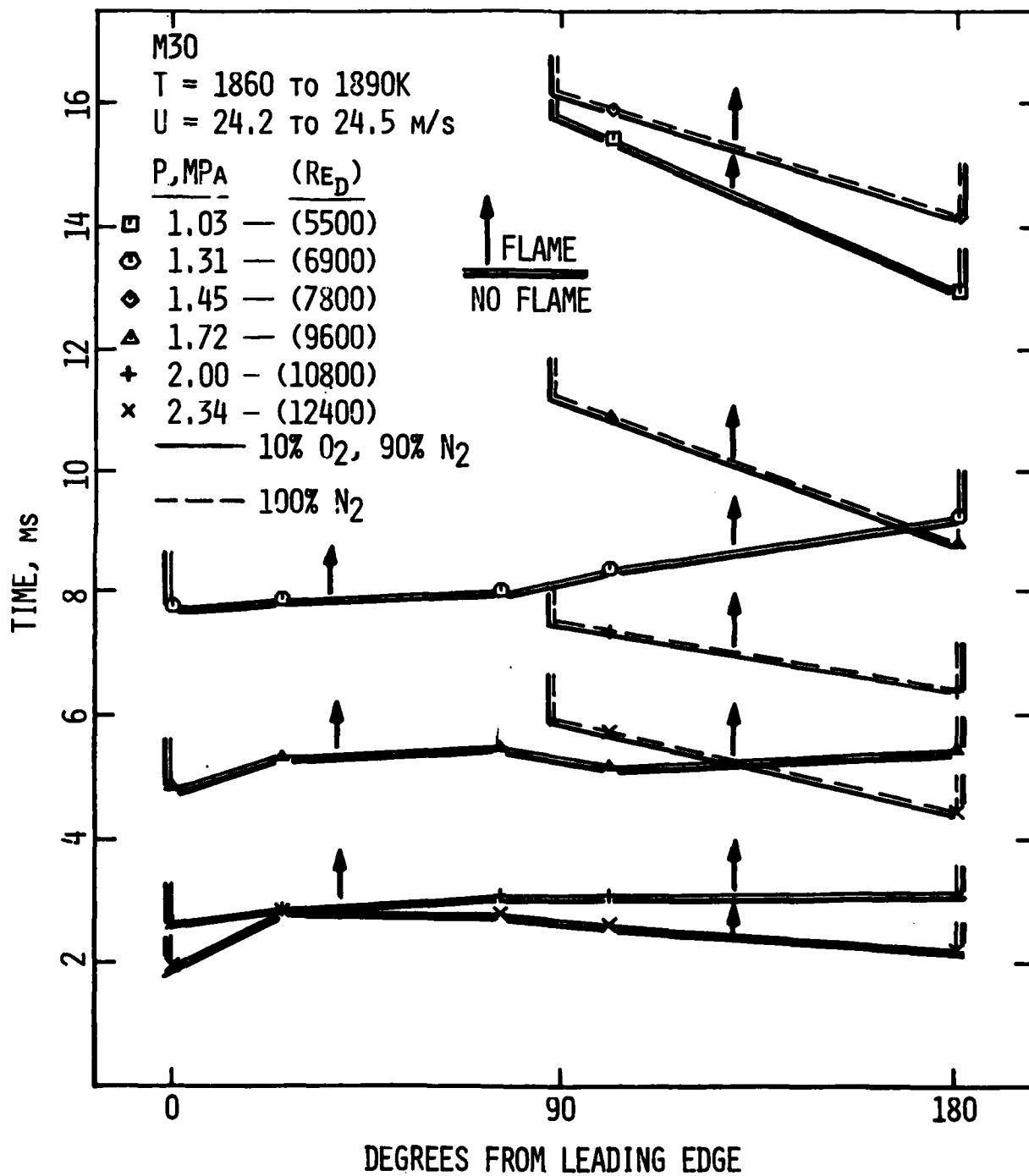


Fig. 63 Flame spreading as a function of pressure in inert and reactive flows (100% $N_2$ , 90% $N_2$ &10% $O_2$ , M30 propellant) .

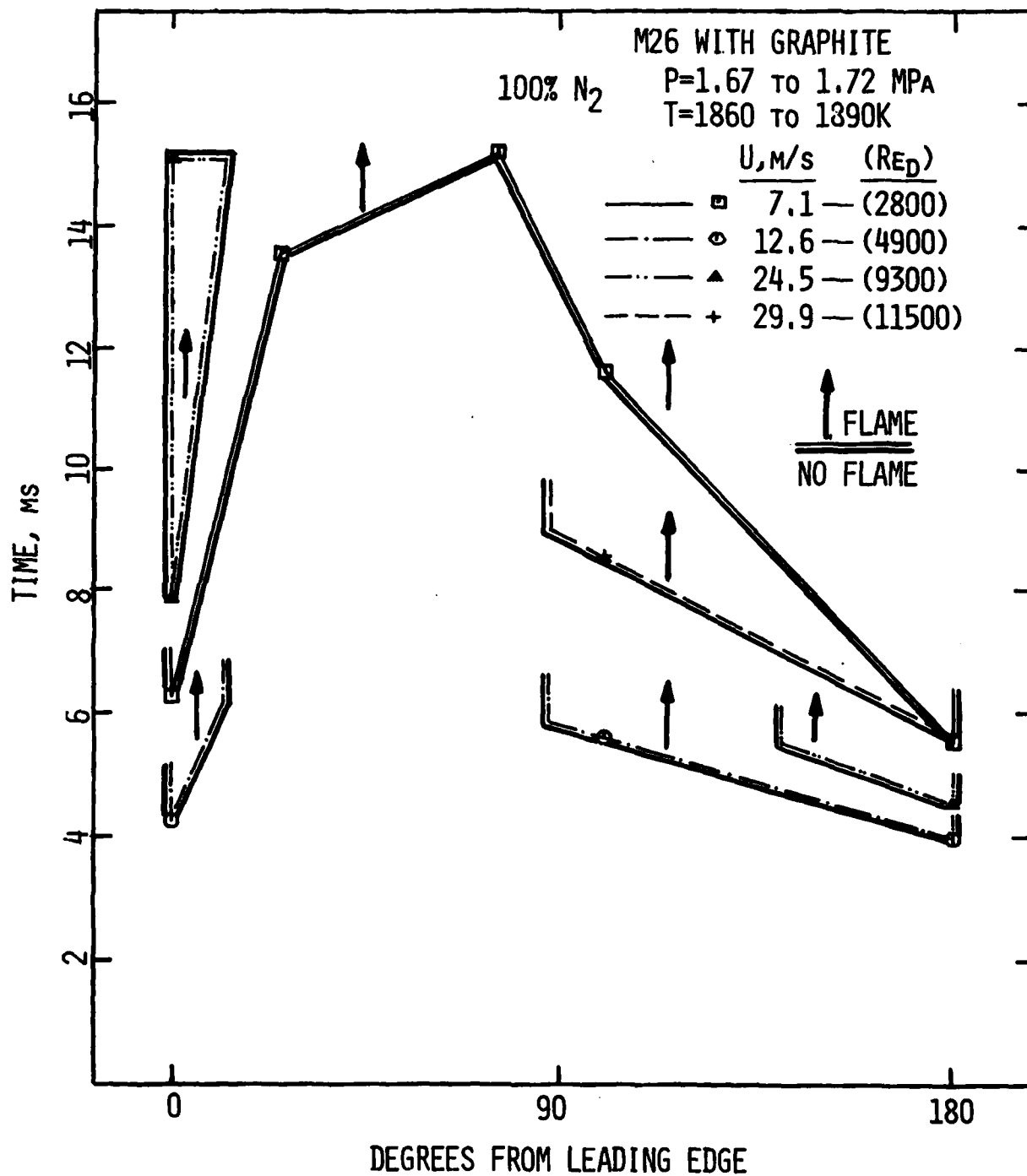


Fig. 64 Flame spreading as a function of velocity for M26 propellant containing graphite (100%N<sub>2</sub>) .

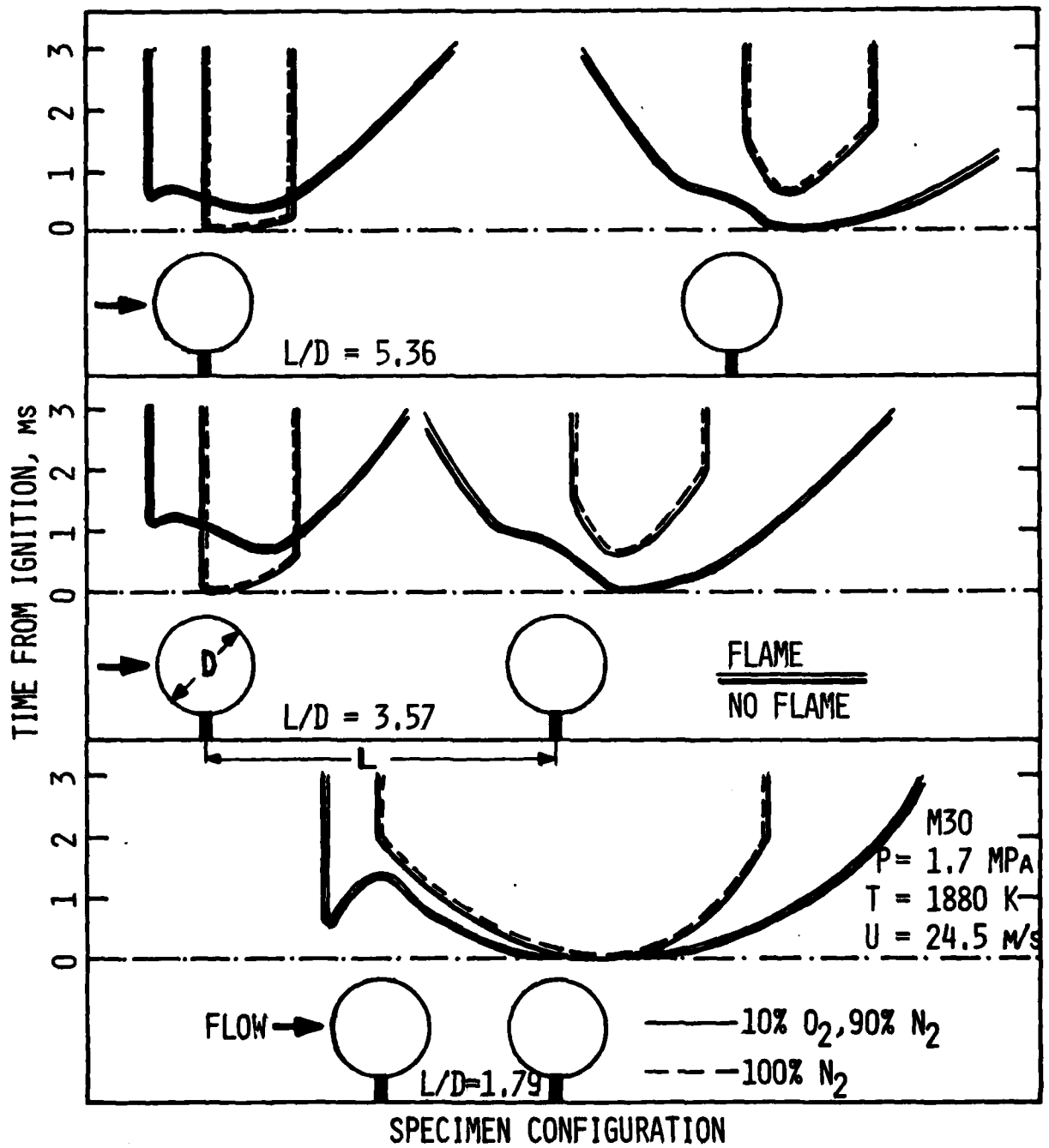


Fig. 65 Flame spreading for various tandem configurations in inert and reactive flows (100%N<sub>2</sub>, 90%N<sub>2</sub>&10%O<sub>2</sub>, M30 propellant) .

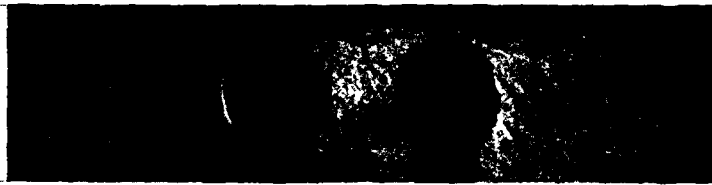


Fig. 66 Photographs showing flame spreading for the specimen configurations of Fig. 65 .

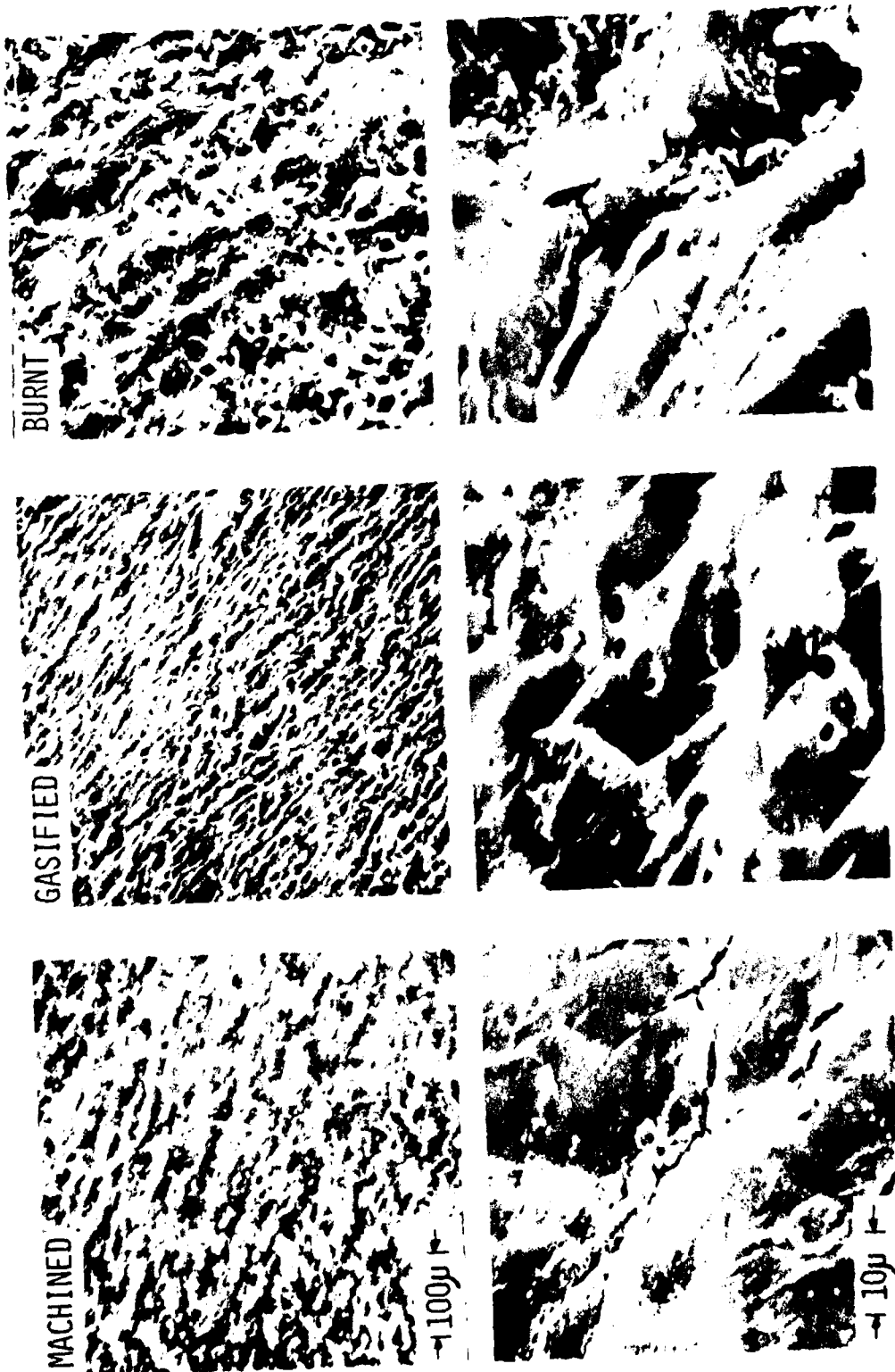


Fig. 67 Photomicrographs of M30 specimen surface before and after exposure to test conditions.

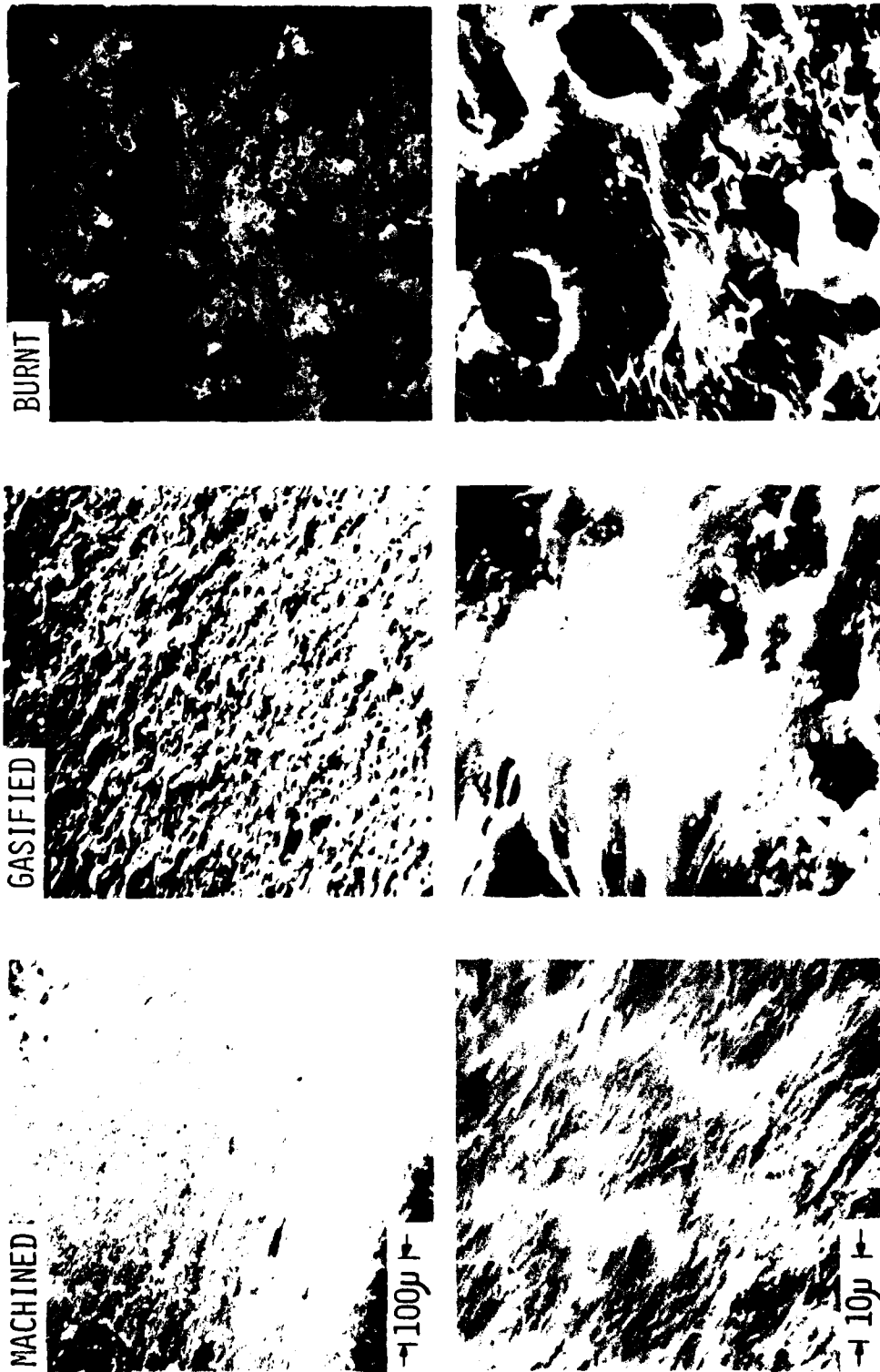


Fig. 68 Photomicrographs of M26 specimen surface before and after exposure to test conditions.

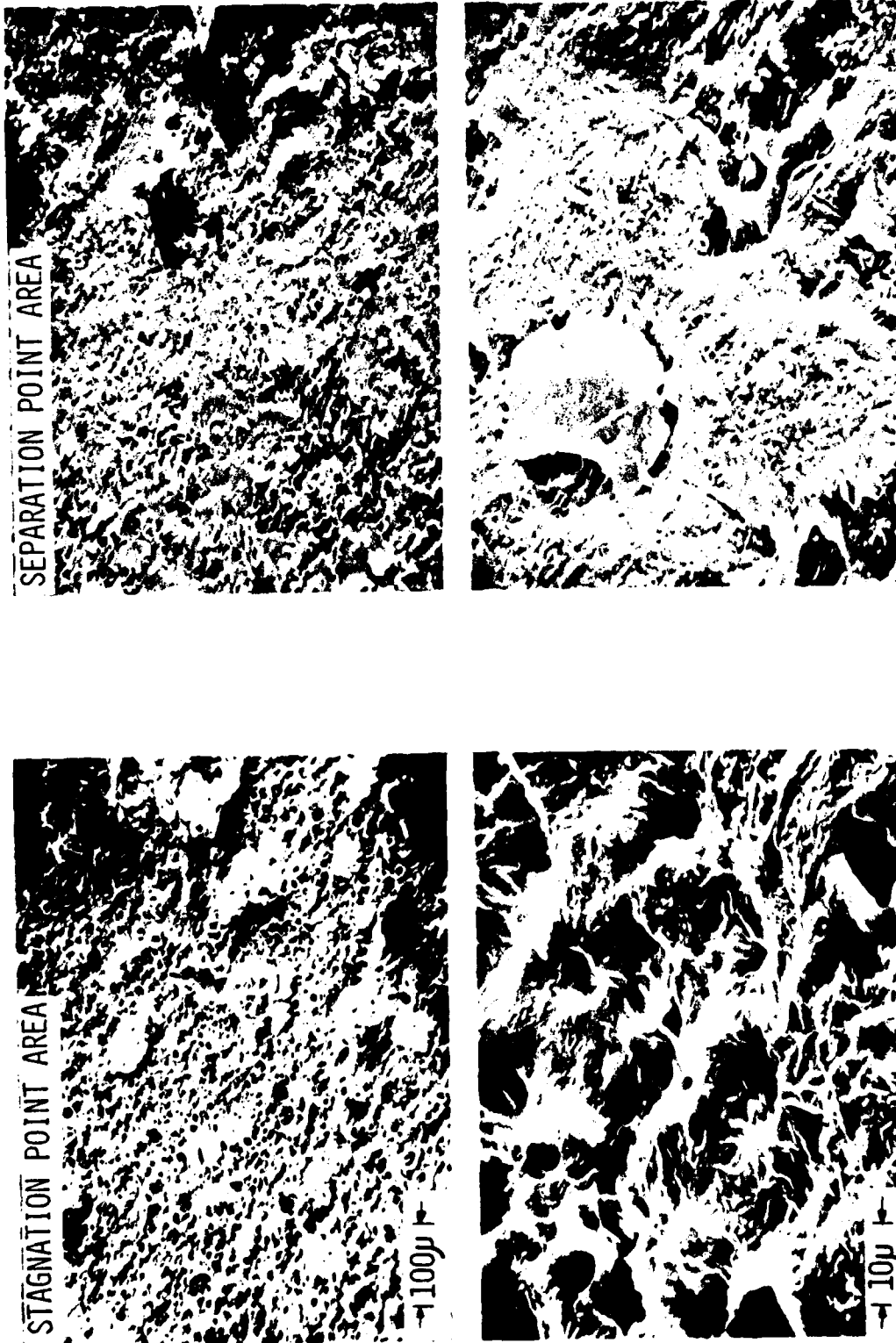


Fig. 69 Photomicrographs of burnt surfaces of M30 specimen taken from the front stagnation flow region and from the flow separation region.

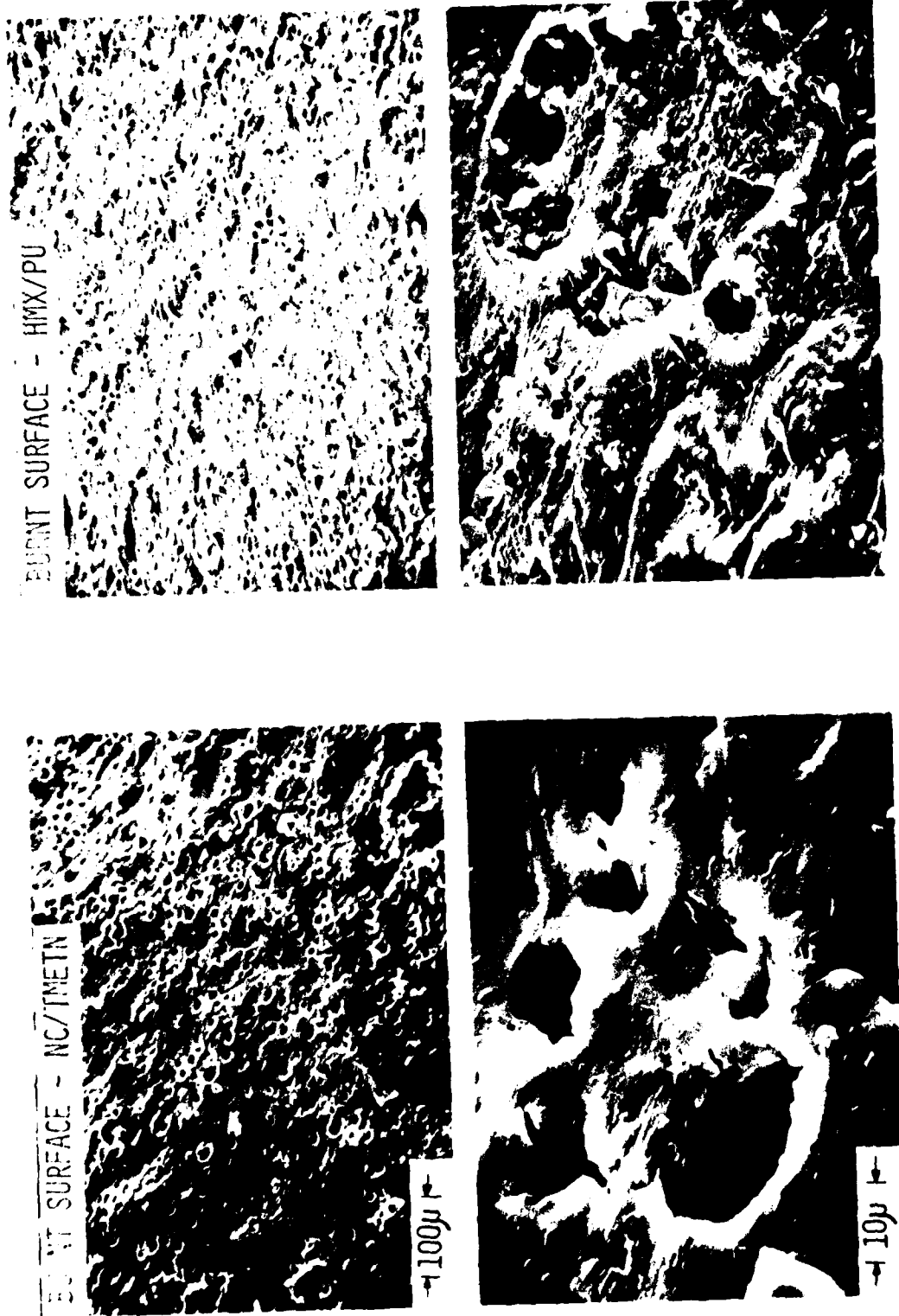


Fig. 70 Photomicrographs of burnt surfaces of NC/TMETN and HMX/PU specimens.

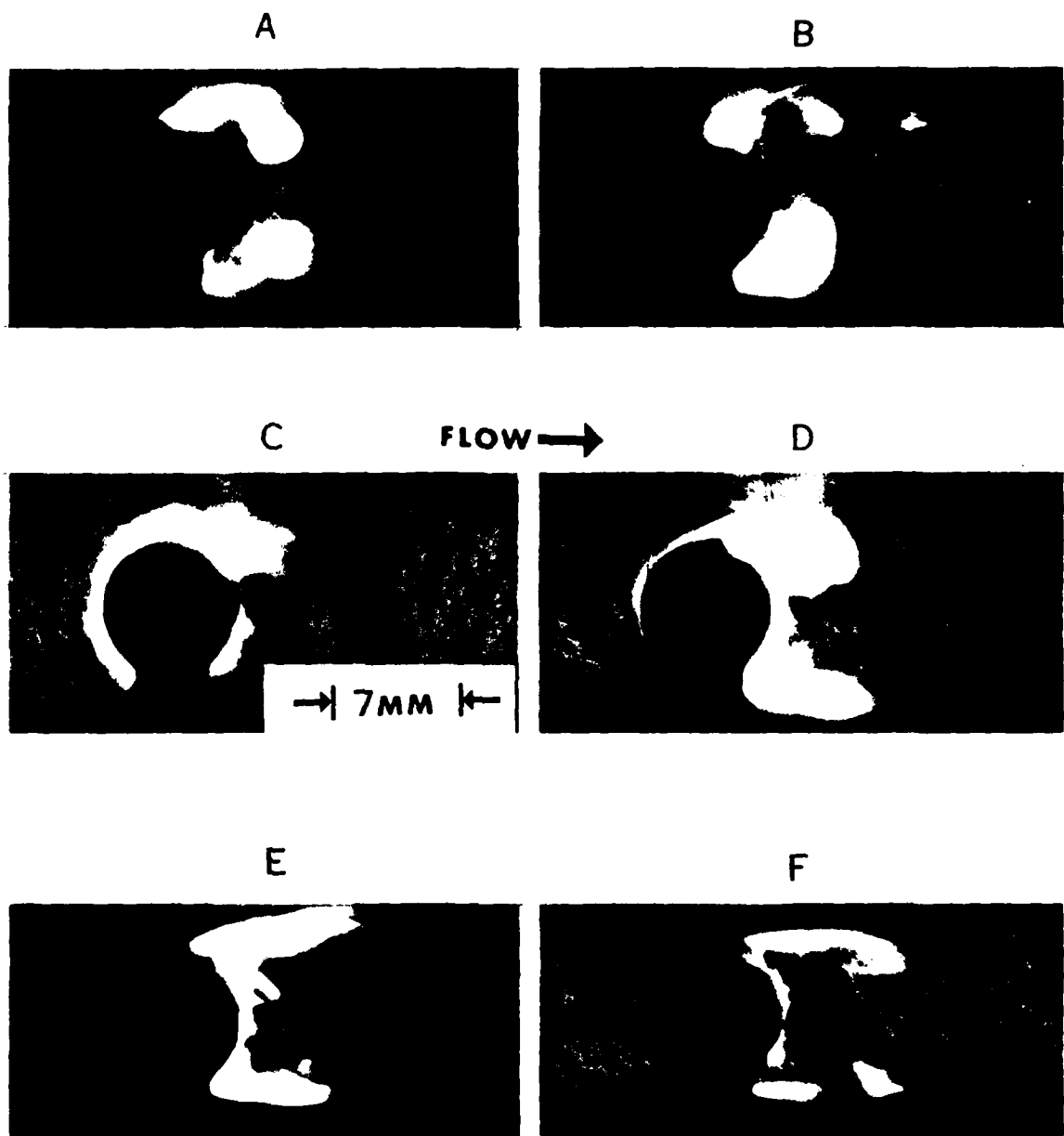


Fig. 71 Photographs showing kaleidoscope of burning phenomena under cross flow conditions (Plexiglas specimen, 50%N<sub>2</sub>&50%O<sub>2</sub>, U<15 m/s).

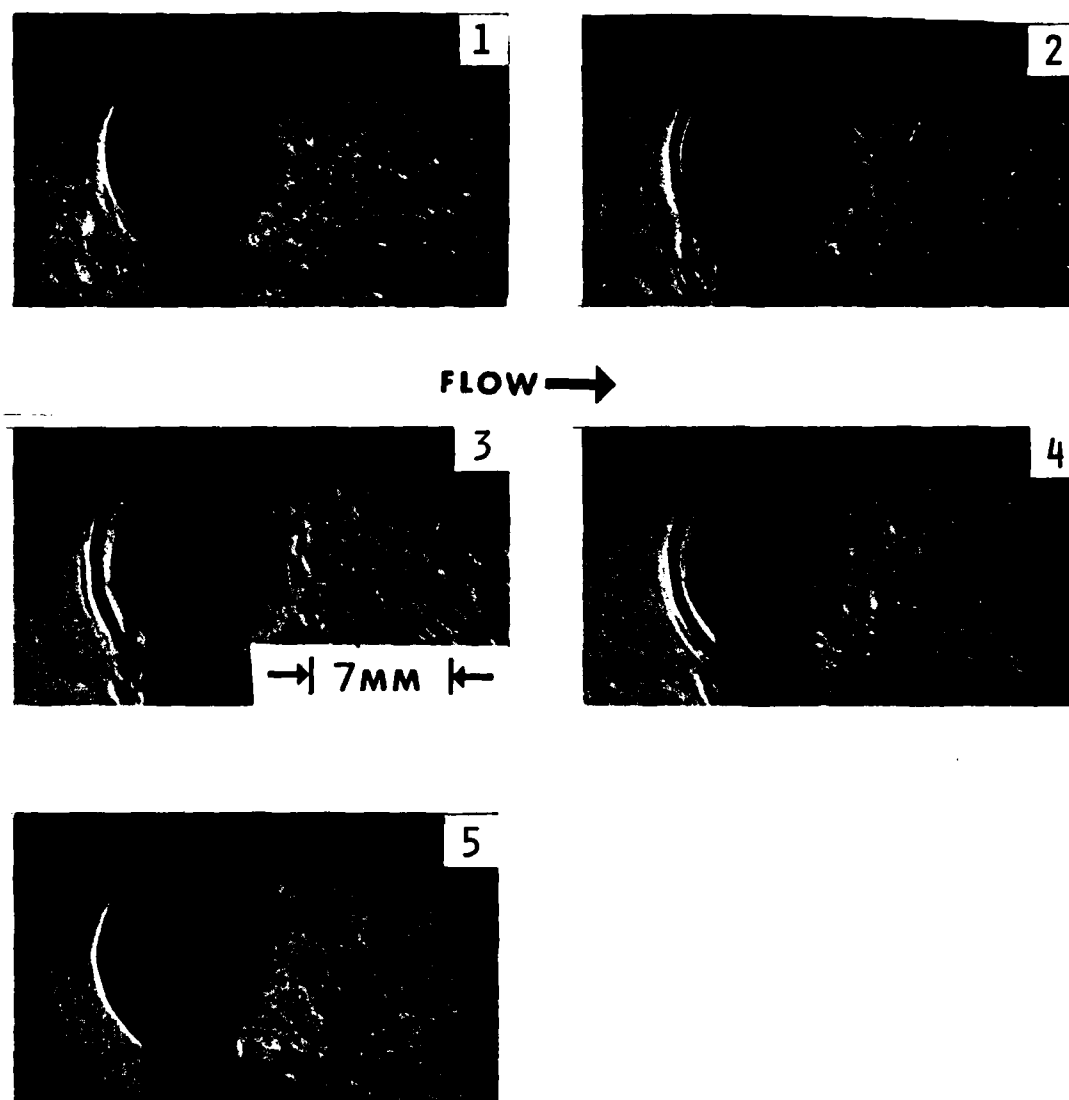


Fig. 72 Sequence of photographs showing front surface boundary layer fluctuations (M30 propellant, 90%N<sub>2</sub>&10%O<sub>2</sub>, U = 5.6 m/s, 5000 frames/s).

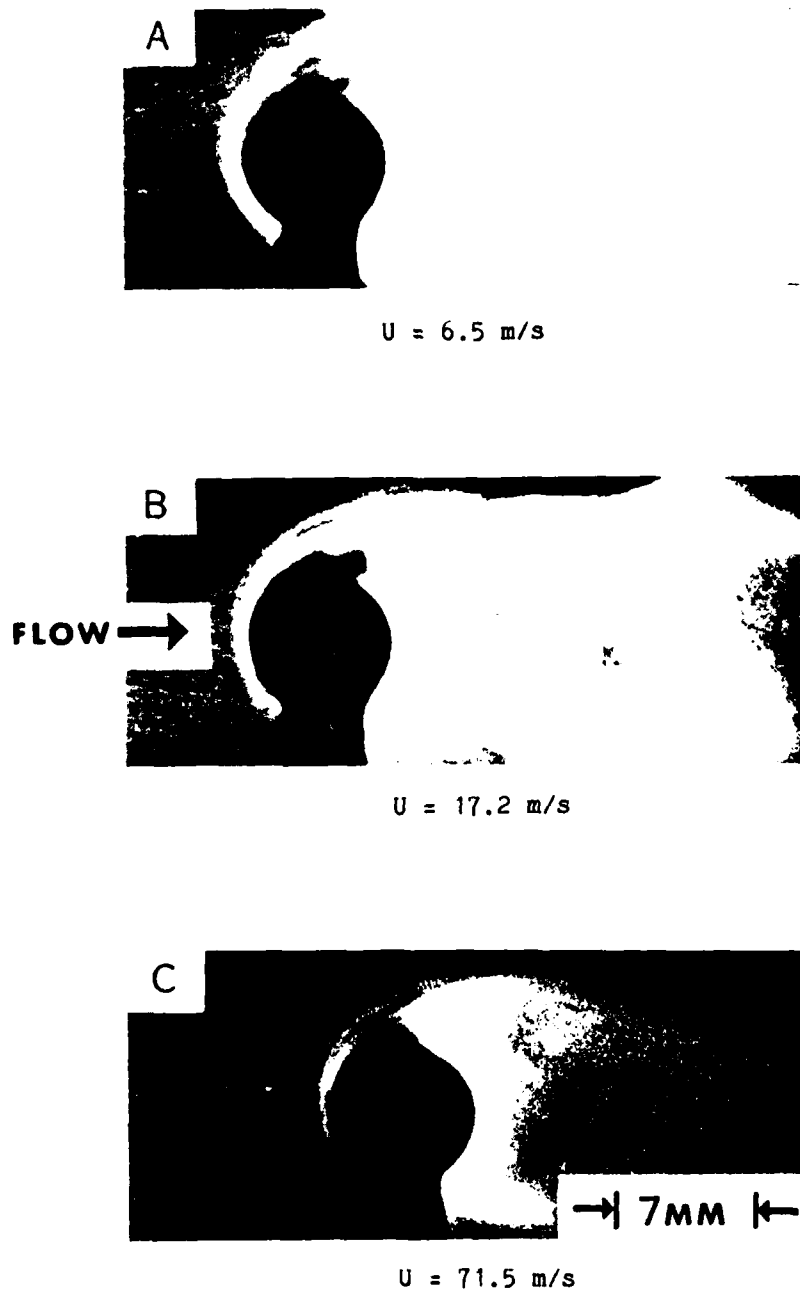
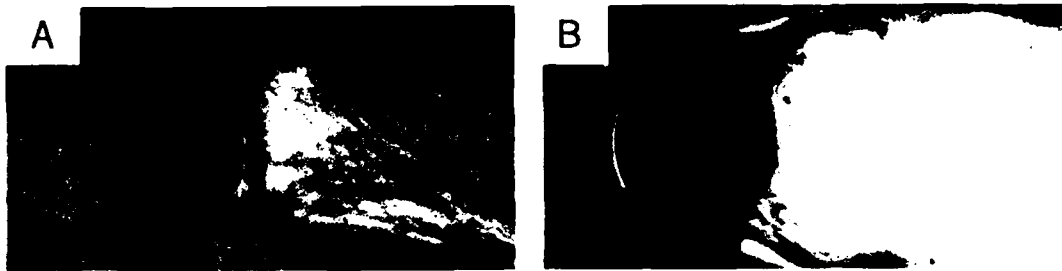
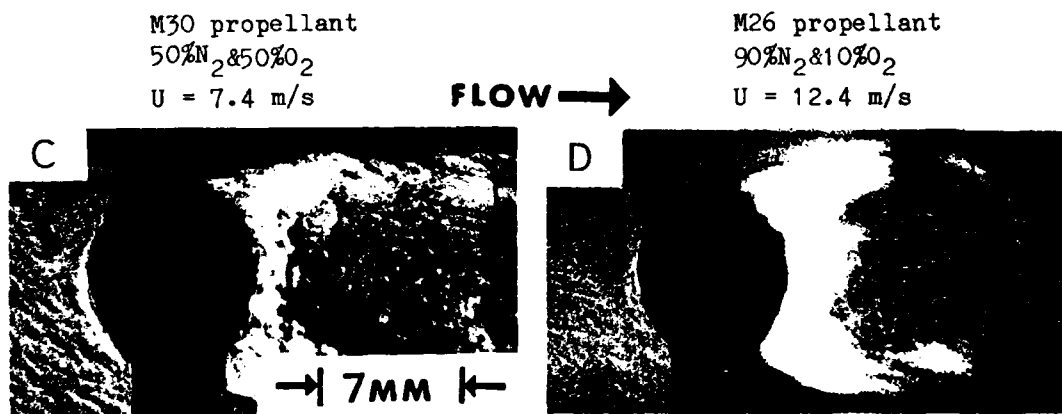


Fig. 73 Photographs showing flame appearance for a range of flow velocities (M26 propellant, 50%N<sub>2</sub>&50%O<sub>2</sub>) .



a) Flame extinction for cases A&B of Fig. 73 .  
(pictures A,B respectively)



b) The flame of M26 propellant is much more luminous than the  
flame of M30 propellant.

Fig. 74 Photographs depicting flame luminosity in special  
situations.

# APPENDIX I

## DERIVATION OF NON-STEADY REACTIVE BOUNDARY LAYER EQUATIONS FOR UNSTEADY FLOW CONDITIONS

The basic boundary layer equations (1) through (4) and transformations (6) through (8) are given in section III-E. The x, y, derivatives are expressed as:

$$\begin{aligned}\frac{\partial}{\partial x} &= f_e \mu_e u_e \cdot \frac{\partial}{\partial s} + \frac{\partial \eta}{\partial x} \frac{\partial}{\partial \eta} + \frac{\partial \tau}{\partial x} \cdot \frac{\partial}{\partial \tau} \\ \frac{\partial}{\partial y} &= \frac{f u_e}{(2s)^{1/2}} \cdot \frac{\partial}{\partial \eta} \\ \frac{\partial}{\partial t} &= \frac{\partial s}{\partial t} \cdot \frac{\partial}{\partial s} + \frac{\partial \tau}{\partial t} \cdot \frac{\partial}{\partial \tau} + \frac{\partial \tau}{\partial t} \cdot \frac{\partial}{\partial \tau}\end{aligned}\tag{I-1}$$

Integrating the continuity equation (1) we get:

$$\begin{aligned}f u &= f u_e \frac{\partial F}{\partial \eta} \\ f v &= -\frac{(2s)^{1/2}}{u_e} \frac{\partial \eta}{\partial t} - \eta \frac{\partial}{\partial t} \left[ \frac{(2s)^{1/2}}{u_e} \right] - F \cdot \frac{\partial \mu_e u_e}{(2s)^{1/2}} - \\ &\quad - (2s)^{1/2} f_e \mu_e u_e - (2s)^{1/2} \frac{\partial F}{\partial \eta} \frac{\partial \eta}{\partial x} - (2s)^{1/2} \frac{\partial F}{\partial \tau} \cdot \frac{\partial \tau}{\partial x}\end{aligned}\tag{I-2}$$

The following operators which appear in equations (1)-(4) are expressed as follows:

$$\begin{aligned}f u \frac{\partial}{\partial x} + f v \frac{\partial}{\partial y} &= \frac{f f_e u_e^2 \mu_e}{2s} \left[ 2s \left( \frac{\partial F}{\partial \eta} \frac{\partial}{\partial s} - \frac{\partial F}{\partial s} \frac{\partial}{\partial \eta} \right) - F \cdot \frac{\partial}{\partial \eta} \right] + \\ &\quad + f u_e \frac{\partial F}{\partial \eta} \cdot \frac{\partial \tau}{\partial x} \cdot \frac{\partial}{\partial \tau} - f \frac{\partial \eta}{\partial t} \cdot \frac{\partial}{\partial \eta} - f u_e \frac{\partial F}{\partial \tau} \cdot \frac{\partial \tau}{\partial x} \cdot \frac{\partial}{\partial \tau} - \\ &\quad - \frac{f u_e}{(2s)^{1/2}} \cdot \frac{\partial}{\partial t} \left[ \frac{(2s)^{1/2}}{u_e} \right] \cdot \eta \cdot \frac{\partial}{\partial \eta} \\ f \frac{\partial}{\partial t} &= f \frac{\partial s}{\partial t} \cdot \frac{\partial}{\partial s} + f \frac{\partial \tau}{\partial t} \cdot \frac{\partial}{\partial \tau} + f \frac{\partial \tau}{\partial t} \cdot \frac{\partial}{\partial \tau} \\ \frac{\partial}{\partial y} (Q \frac{\partial}{\partial y}) &= \frac{f u_e^2}{2s} \cdot \frac{\partial}{\partial \eta} (f Q \frac{\partial}{\partial \eta})\end{aligned}\tag{I-3}$$

$Q = Q(s, \eta, \tau)$  , is any quantity.

The pressure x-derivative is taken from the boundary layer edge equation:

$$\frac{\partial p}{\partial x} = \frac{\partial p_e}{\partial x} = -f_e \frac{\partial u_e}{\partial t} - f_e u_e \frac{\partial u_e}{\partial x}$$

New functions,  $Z_1$  and  $g$ , are defined:

$$Y_i = Y_{ie}(S, \tau) \cdot Z_i(\eta, S, \tau)$$

(I-4)

$$I = I_e(S, \tau) \cdot g(\eta, S, \tau)$$

Where  $Y_{ie}$ , and  $I_e$  correspond to the boundary layer edge.

Defining also:  $C \triangleq \frac{\rho \mu}{\rho_e \mu_e}$ , and  $S_c \triangleq \frac{\mu_e}{\rho_e D_{12}}$  - Schmidt number.

The following set of equations is obtained:

$$\begin{aligned} -\frac{\partial^2 F}{\partial \eta^2 \partial \tau} + \frac{\partial}{\partial \eta} \left[ C \cdot \frac{\partial^2 F}{\partial \eta^2} \right] + F \cdot \frac{\partial^2 F}{\partial \eta^2} = \frac{2S}{u_e} \cdot \frac{\partial u_e}{\partial \tau} \cdot \left[ \left( \frac{\partial F}{\partial \eta} \right)^2 - \frac{F^2}{S} \right] + \\ + 2S \cdot \left( \frac{\partial F}{\partial \eta} \cdot \frac{\partial^2 F}{\partial \eta^2 \partial \tau} - \frac{\partial^2 F}{\partial \tau} \cdot \frac{\partial^2 F}{\partial \eta^2} \right) + u_e \cdot t_f \cdot \frac{\partial F}{\partial \tau} \cdot \left( \frac{\partial F}{\partial \eta} \cdot \frac{\partial^2 F}{\partial \eta^2 \partial \tau} - \frac{\partial^2 F}{\partial \tau} \cdot \frac{\partial^2 F}{\partial \eta^2} \right) + \\ + \frac{1}{u_e} \cdot \frac{\partial u_e}{\partial \tau} \cdot t_f \cdot \left( \frac{\partial F}{\partial \eta} - \frac{F}{S} \right) + \frac{\partial^2 F}{\partial \tau} \cdot t_f \cdot \frac{\partial^2 F}{\partial \eta^2} - \\ - \frac{\partial^2 F}{\partial \tau} \cdot t_f \cdot \frac{\partial u_e}{\partial \tau} \cdot \left[ \left( \frac{\partial F}{\partial \eta} \right)^2 - \frac{F^2}{S} \right] - \left( \frac{\partial^2 F}{\partial \tau} \cdot \frac{t_f}{2S} - \frac{t_f}{u_e} \cdot \frac{\partial u_e}{\partial \tau} \right) \cdot \eta \cdot \frac{\partial^2 F}{\partial \eta^2} \end{aligned} \quad (I-5)$$

$$\begin{aligned} -\frac{\partial^2 Z_i}{\partial \tau^2} + \frac{\partial}{\partial \eta} \left[ \frac{C}{S_c} \cdot \frac{\partial^2 Z_i}{\partial \eta^2} \right] + F \cdot \frac{\partial^2 Z_i}{\partial \eta^2} = 2S \cdot \frac{\partial F}{\partial \eta} \cdot \frac{Z_i}{Y_{ie}} \cdot \frac{\partial Y_{ie}}{\partial S} + \frac{t_f}{S} \cdot \frac{W_i}{Y_{ie}} + \\ + 2S \cdot \left( \frac{\partial F}{\partial \eta} \cdot \frac{\partial^2 Z_i}{\partial \tau^2} - \frac{\partial^2 F}{\partial \tau} \cdot \frac{\partial^2 Z_i}{\partial \eta^2} \right) + u_e \cdot t_f \cdot \frac{\partial F}{\partial \tau} \cdot \left( \frac{\partial F}{\partial \eta} \cdot \frac{\partial^2 Z_i}{\partial \eta^2 \partial \tau} - \frac{\partial^2 F}{\partial \tau} \cdot \frac{\partial^2 Z_i}{\partial \eta^2} \right) + \\ + \frac{\partial^2 F}{\partial \tau} \cdot t_f \cdot \frac{\partial^2 Z_i}{\partial \tau^2} - \frac{\partial^2 F}{\partial \tau} \cdot t_f \cdot \frac{\partial Y_{ie}}{\partial \tau} \cdot \frac{Z_i}{Y_{ie}} \cdot \frac{\partial F}{\partial \eta} - \left( \frac{\partial^2 F}{\partial \tau} \cdot \frac{t_f}{2S} - \frac{t_f}{u_e} \cdot \frac{\partial u_e}{\partial \tau} \right) \cdot \eta \cdot \frac{\partial^2 Z_i}{\partial \eta^2} \end{aligned} \quad (I-6)$$

$$\begin{aligned} -\frac{\partial^2 I}{\partial \tau^2} + \frac{\partial}{\partial \eta} \left[ \frac{C}{I_e} \cdot \frac{\partial^2 I}{\partial \eta^2} \right] + F \cdot \frac{\partial^2 I}{\partial \eta^2} = 2S \cdot \frac{\partial F}{\partial \eta} \cdot \frac{I}{I_e} \cdot \frac{\partial I_e}{\partial S} + \\ + \frac{\partial}{\partial \eta} \left[ \frac{C}{I_e} \cdot \left( \frac{1}{I_e} - 1 \right) \cdot \frac{A_i Y_{ie}}{I_e} \cdot \frac{\partial I_i}{\partial \eta} \right] + \frac{u_e^2}{I_e} \cdot \frac{\partial}{\partial \eta} \left[ \left( \frac{1}{I_e} - 1 \right) \cdot C \cdot \frac{\partial F}{\partial \eta} \cdot \frac{\partial^2 I}{\partial \eta^2} \right] + \\ + 2S \cdot \left( \frac{\partial F}{\partial \eta} \cdot \frac{\partial^2 I}{\partial \tau^2} - \frac{\partial^2 F}{\partial \tau} \cdot \frac{\partial^2 I}{\partial \eta^2} \right) + u_e \cdot t_f \cdot \frac{\partial F}{\partial \tau} \cdot \left( \frac{\partial F}{\partial \eta} \cdot \frac{\partial^2 I}{\partial \eta^2 \partial \tau} - \frac{\partial^2 F}{\partial \tau} \cdot \frac{\partial^2 I}{\partial \eta^2} \right) + \\ + \frac{\partial^2 F}{\partial \tau} \cdot t_f \cdot \frac{\partial^2 I}{\partial \tau^2} - \frac{\partial^2 F}{\partial \tau} \cdot t_f \cdot \frac{\partial I_e}{\partial \tau} \cdot \frac{I}{I_e} \cdot \frac{\partial F}{\partial \eta} - \left( \frac{\partial^2 F}{\partial \tau} \cdot \frac{t_f}{2S} - \frac{t_f}{u_e} \cdot \frac{\partial u_e}{\partial \tau} \right) \cdot \eta \cdot \frac{\partial^2 I}{\partial \eta^2} + \\ + \frac{t_f}{S I_e} \cdot \frac{\partial^2 I}{\partial \tau^2} \end{aligned} \quad (I-7)$$

Equation (I-6) corresponds to the continuity and momentum equations. Equation (I-7) is the i-th species conservation equation, and Eq. (I-8) is the energy equation. The above equations are the most general reactive non-steady boundary layer equations.

# APPENDIX II

## THE NUMERICAL SCHEME FOR THE FRONT STAGNATION IGNITION EQUATIONS

The numerical scheme given here deals with the parabolic partial differential equations (p.d.e.), (24) through (28). Those equations are strongly coupled to each other by nonlinear terms. In addition, the time scales of the solution vary as various terms in the equations become dominant. Thus, at each time step all the equations are solved simultaneously and a provision for a variable time step is included.

Equations (24) through (28) are of the form:

$$-\frac{\partial u_i}{\partial t} + \frac{\partial^2 u_i}{\partial x^2} + f \cdot \frac{\partial u_i}{\partial x} = F_i(\tilde{u}) \quad (\text{II-1})$$

$$\tilde{u} = (u_1, \dots, u_m)$$

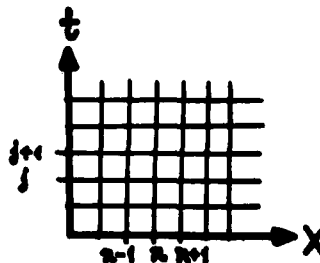
$u_i$  represents any of the dependent variables (G, H, Z,  $\theta$ ),  $f$  - represents  $F_m$  is the number of equations (4 in this case). Eq. (II-1) is now transformed into a general implicit finite difference form, as follows:

$$\begin{aligned} \frac{u_{i,n}^j - u_{i,n}^{j+1}}{\Delta t^j} + \theta \cdot \left[ \frac{u_{i,n+1}^{j+1} - 2u_{i,n}^{j+1} + u_{i,n-1}^{j+1}}{(\Delta x)^2} + \frac{u_{i,n+1}^{j+1} - u_{i,n-1}^{j+1}}{2 \cdot \Delta x} \cdot f_n^{j+1,p} \right] + \\ + (1-\theta) \cdot \left[ \frac{u_{i,n+1}^j - 2u_{i,n}^j + u_{i,n-1}^j}{(\Delta x)^2} + \frac{u_{i,n+1}^j - u_{i,n-1}^j}{2 \cdot \Delta x} \cdot f_n^j \right] = \\ = \theta \cdot F_{i,n}^{j+1} + (1-\theta) \cdot F_{i,n}^j \end{aligned} \quad (\text{II-2})$$

$\hat{\theta} = 1$  corresponds to a fully implicit solution,  $\hat{\theta} = 0$  corresponds to a fully explicit solution.

The numerical solution of a general p.d.e. of the type of Eq. (II-1), using the form of Eq. (II-2), is discussed in great detail by BenReuven [119]. The truncation error of Eq. II-2 is  $-O(\Delta t, \Delta x^2)$ . The artificial diffusion (i.e., the coefficient of  $\partial^2 u_i / \partial x^2$  within the truncation error term) is  $-O(f^2 \Delta x^2 / 12)$ , which is well below 1% of the value of the real diffusion coefficient (1).

The mesh of the finite difference elements contains  $N$  interior points so that:  
 $n = 0 \dots N+1$ .  
 $\Delta t^j = t^{j+1} - t^j = C \cdot \Delta t^{j-1}$ .  
 $C$  is some determined factor to account for the variable time scales.



The nonlinear terms included in  $F$  are linearized around their predicted values as follows:

$$u_{i,n}^{j+1,p} = (C+1) \cdot u_{i,n}^j - C \cdot u_{i,n}^{j-1}$$

$$f_n^{j+1,p} = (C+1) \cdot f_n^j - C \cdot f_n^{j-1}$$

$$F_{i,n}^{j+1} = \sum_{k=1}^m \left[ \left( \frac{\partial F_i}{\partial u_k} \right)_n^{j+1,p} \cdot (u_{k,n}^{j+1,p} - u_{k,n}^j) \right] + F_{i,n}^{j+1,p}$$

Defining:  $\alpha \triangleq \frac{\Delta t}{2 \cdot \Delta x}$  and  $\beta \triangleq \frac{\Delta t}{(\Delta x)^2}$

For each time level  $j$ , the  $m$  equations (II-1) are transformed into  $m$  equation (II-2) to be solved for the time level  $j+1$ . Thus, the number of unknowns is  $m \times N$ . The system is written as:  $A \cdot U = R$  where  $A$  is a tridiagonal block matrix.

The coefficients of  $U$  -  $u_{i,n+1}^{j+1}, u_{i,n}^{j+1}, u_{i,n-1}^{j+1}$ , that form the upper diagonal, the main diagonal and the lower diagonal elements of  $A$  are respectively:  $c_{ik,n}^j, a_{ik,n}^j, b_{ik,n}^j$ . Each of them constitutes an array of  $m \times m \times N$ . The elements of  $R$  -  $d_{k,n}^j$  constitute arrays of  $m \times N$ .

The general expressions of the elements of  $A$ ,  $U$  and  $R$  are given below:

$$c_{ik,n}^j = [\theta \cdot \beta^j + \theta \cdot \alpha \cdot f_n^{j+1,p}] \cdot \delta_{ik} \quad n = 1 \dots N-1$$

$$a_{ik,n}^j = [1 - 2\theta\beta^j] \cdot \delta_{ik} - \theta \cdot \Delta t \cdot \left( \frac{\partial F_k}{\partial u_i} \right)_n^{j+1,p} \quad n = 1 \dots N$$

$$b_{ik,n}^j = [\theta \cdot \beta^j - \theta \cdot \alpha \cdot f_n^{j+1,p}] \cdot \delta_{ik} \quad n = 2 \dots N$$

$$d_{k,n}^j = -u_{k,n}^j - (1-\theta) \cdot \beta^j \cdot [u_{k,n+1}^j - 2u_{k,n}^j + u_{k,n-1}^j] - \\ - (1-\theta) \cdot \alpha \cdot [u_{k,n+1}^j - u_{k,n-1}^j] \cdot f_n^j + \Delta t \cdot (1-\theta) \cdot F_{k,n}^j + \\ + \theta \cdot \Delta t \cdot \left\{ F_{k,n}^{j+1,p} - \sum_{i=1}^m \left[ \left( \frac{\partial F_k}{\partial u_i} \right)_n^{j+1,p} \cdot u_{i,n}^{j+1,p} \right] \right\} \quad n = 1 \dots N$$

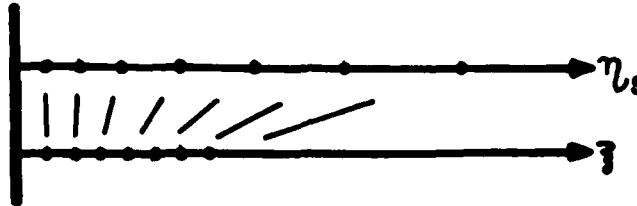
The tridiagonal matrix equation is solved using the computer Routine developed by Ref. 120.

The solid phase equation (28) is coupled to equations (24) through (27) through the heat transfer boundary condition. In order to get good accuracy for the heat transfer and the subsurface heat release calculations, a fine grid has to be used close to the wall. In order also to account for the

progression of the thermal wave deep into the solid phase, the mesh has to cover a wide range. Therefore the coordinate  $\eta_s$  of Eq. (28) was transformed as follows:

$$\xi \equiv \frac{1}{B} \cdot \ln \left( \frac{A + \eta_s}{A} \right)$$

The numerical scheme for the solid phase equation treats the transformed equation with the coordinate  $\xi$ . The values chosen for A and B are:  $A = 10^{-4}$ ,  $B = 10^4$ . A depiction of the relation between  $\eta_s$  and  $\xi$  is shown below:



The appearance of the solid phase equation is similar to Eq. (II-1) and it is solved accordingly.

For each time step, a value of surface temperature  $\theta_w$  is guessed and the gas phase and solid phase sets of equations are solved separately. From the established new profiles of temperature, the heat transfer boundary condition is checked for validity. It was considered to be satisfied when:

$$\left| - \left( \frac{\partial \theta}{\partial \eta} \right)_w - \epsilon'' \left( \frac{\partial \theta_{s,0}}{\partial \eta_s} \right)_w - F_b \cdot g \right| < 10^{-3} \cdot \left( \frac{\partial \theta}{\partial \eta} \right)_w$$

If not satisfied, the solution was reiterated around  $\theta_w$  using the method of Regula Falsi [121]. Each solution of the gas phase equations was reiterated until the following condition was satisfied:

$$\text{MAX} \left[ \sum_{i=1}^N |u_{i,n,x+1}^{j+1} - u_{i,n,x}^{j+1}| \right] < 10^{-9}$$

I - is the iteration number. For  $I > 1$ , the values  $u_i$  of iteration I were used as the predicted values for iteration  $I+1$ .

To account for the boundary layer growth and yet keep fine resolution of the mesh, (for the fixed number of elements used,  $N+1$ ) the distance grid size was multiplied by a factor of 2, as the edge of the boundary layer approached the edge of the grid. In particular:

$$\text{IF: } \frac{1}{4} \sum_{n=N-3}^N G_n > 0.995$$

$$\text{THEN: } \Delta \eta_{\text{new}} \equiv 2 \Delta \eta_{\text{old}}$$

$$u_{i,n_{\text{new}}} = u_{i,2n_{\text{old}}-1}$$

To avoid infinite steepness of the boundary layer profiles at time  $\tau = 0$ , proper starting conditions were devised, somewhat similar to those used by Strahle [122].

For a very small  $\tau$ , the profiles of  $Y_F$  and  $Y_{OX}$  are assumed to be unchanged from their values at  $\tau = 0$ , thus only the velocity and temperature profiles are dealt with. From equations (24) through (30), the equations of interest for the starting of the flow are:

$$\begin{aligned} -\frac{\partial G}{\partial \tau} + \frac{\partial^2 G}{\partial \eta^2} + F \cdot \frac{\partial G}{\partial \eta} &= G^2 - \theta \\ -\frac{\partial \theta}{\partial \tau} + \frac{\partial^2 \theta}{\partial \eta^2} + F \cdot \frac{\partial \theta}{\partial \eta} &\approx 0 \\ -\frac{\partial \theta_{s\tau}}{\partial \tau} + \frac{\partial^2 \theta_{s\tau}}{\partial \eta^2} - \frac{F}{\epsilon^{1/2}} \cdot F_w \cdot \frac{\partial \theta_{s\tau}}{\partial \eta} &= 0 \\ -\left(\frac{\partial \theta}{\partial \eta}\right)_w &= F_w \cdot g + \epsilon^{1/2} \cdot \left(\frac{\partial \theta_{s\tau}}{\partial \eta}\right)_w \end{aligned} \quad (II-3)$$

Similar to Ref. 122, the following initial profiles were chosen:

$$\begin{aligned} G_{s\tau} &= \left(\frac{a_1 \tau}{\tau^{1/2}} - 1\right) \cdot e^{-\frac{a_1 \tau}{\tau^{1/2}}} + 1 \\ \theta_{s\tau} &= \left(\frac{b_1 \tau}{\tau^{1/2}} - 1 + \theta_w\right) \cdot e^{-\frac{b_1 \tau}{\tau^{1/2}}} + 1 \\ \theta_{s\tau} &= \left(\frac{c_1 \tau}{\tau^{1/2}} + \theta_w - \theta_0\right) \cdot e^{-\frac{c_1 \tau}{\tau^{1/2}}} + \theta_0 \end{aligned} \quad (II-4)$$

The above profiles are physically reasonable since they satisfy accurately the boundary conditions at the surface and at the boundary layer edge. They are also an exact description of the initial conditions for  $t = 0^+$ , i.e.:

$$\begin{aligned} G_{s\tau}(\eta=0, \tau=0) &= 0 & G_{s\tau}(\eta>0, \tau=0) &= 1 \\ \theta_{s\tau}(\eta=0, \tau=0) &= \theta_w & \theta_{s\tau}(\eta>0, \tau=0) &= 1 \\ \theta_{s\tau}(\eta=0, \tau=0) &= \theta_w & \theta_{s\tau}(\eta>0, \tau=0) &= \theta_0 \end{aligned}$$

There are seven unknown parameters to be determined:  $a_1, a_2, b_1, b_2, C_1, C_2, \theta_w$ . Seven relations are required to find them. The relations are obtained as follows:

Three relations are obtained by substituting Eqs. (II-4) in the first three equations of (II-3). The relations are found for  $\eta=0, \tau \rightarrow 0$ .

Three additional relations are obtained by integrating the same equations (II-3) from  $\eta, \tau=0$  to  $\eta, \tau \rightarrow \infty$ , and then substituting Eqs. (II-4).

The last relation is obtained by substituting Eqs. (II-4) in the fourth equation of (II-3).

The values obtained are:

$$a_1 = -\frac{1}{2}\sqrt{\frac{2}{\epsilon}} \quad ; \quad a_2 = \sqrt{\frac{2}{\epsilon}}$$

$$b_1 = -(1-\theta_w) \cdot \frac{1}{2}\sqrt{\frac{2}{\epsilon}} \quad ; \quad b_2 = \sqrt{\frac{2}{\epsilon}}$$

$$c_1 = -(\theta_w - \theta_w) \cdot \frac{1}{2}\sqrt{\frac{2}{\epsilon}} \quad ; \quad c_2 = \sqrt{\frac{2}{\epsilon}}$$

$$\theta_w = \frac{1 + \theta_w \cdot \epsilon^{1/2}}{1 + \epsilon^{1/2}}$$

The value obtained for  $\theta_w$  is exactly the value corresponding to the jumping conditions expressed by Eq. (32).

As a by-product of the above process of determination, the proper starting time for the numerical solution,  $\tau_{st}$  is also obtained:

$$\tau_{st} \sim \left[ \frac{F_w \cdot (a_1 + a_2)}{\theta_w} \right]^2 \sim \left( \frac{F_w}{\theta_w} \right)^2$$

The following nominal values were used in the numerical solution:

$$\Delta \tau_{st} = 3 \cdot 10^{-4} \quad \Delta \tau = 3 \cdot 10^{-3} \quad \Delta \tau_{st} = 10^{-6}$$

$$\hat{\theta} = 0.8 \quad N = 51 \quad \tau_{st} = 10^{-6} \quad C_{st} = 1.5$$

As the boundary layer was established, the time step factor, C, was changed to 1. The maximum  $\Delta \tau$  used was 0.1. However, for the period of steady inert heating, the time scale of the equations was changed in stages to -  $\Delta \tau \sim \epsilon^{1/2} \cdot \Delta \tau$  (see Section III-E) and the numerical solution proceeded with  $\Delta \tau = 0.1$ . The time scale was changed again to much smaller values when chemical reaction rate terms, or free stream non-steadiness terms became prominent.

The solid phase equation (28) was solved with  $\hat{\theta} = 0.5$  (corresponding to Crank Nicolson method [123]). The accuracy and repeatability of the numerical solution was proven satisfactory for a range of time steps and C values around the nominal ones used. Provided that  $\tau_{st}$  was sufficiently small, the solution proved to be almost insensitive to the starting profiles used. It approached the values given by (II-4) in few time steps. The stability of the solution was not satisfactory for  $\theta = 0.5$  (when chemical rate terms became prominent), and therefore  $\theta = 0.8$  was used.

# APPENDIX III

## CALCULATIONS OF THE PHYSICAL CONDITIONS IN THE TEST SECTION

The notations in this section refer to Fig. 28. The physical conditions in the shock tunnel are calculated by assuming that the shocked gas is in thermodynamic equilibrium. Combining the relations between values across a rarefaction wave with the interface conditions  $P_3 = P_2$ ,  $U_3 = U_2$ , the following relation is obtained:

$$\frac{P_2}{P_1} = \frac{P_4}{P_1} \cdot \left[ 1 - \frac{\gamma_4 - 1}{2} \cdot \frac{U_2}{C_4} \right]^{\frac{2\gamma_4}{\gamma_4 - 1}} \quad (\text{III-1})$$

The conservation of mass, momentum and energy across the incident shock wave are, respectively:

$$\rho_1 w_1 = \rho_2 (w_1 - u_1) \quad (\text{III-2})$$

$$P_1 + \rho_1 w_1^2 = P_2 + \rho_2 (w_1 - u_1)^2 \quad (\text{III-3})$$

$$H_1 + \frac{1}{2} w_1^2 = H_2 + \frac{1}{2} (w_1 - u_1)^2 \quad (\text{III-4})$$

The equation of state for perfect gas:

$$P_2 = \rho_2 \tilde{R} T_2 \quad (\text{III-5})$$

If a mixture of two gases is considered in the driven section,  $X_1$  being the mole fraction of gas 1, then:

$$\tilde{R} = \frac{R}{M} = \frac{R}{X_1 M_1 + (1 - X_1) M_2}$$

$$H = \frac{X_1 M_1}{M} H_1 + \frac{X_2 M_2}{M} H_2 = H(T)$$

H is the enthalpy per-unit mass.

The relations across the reflected shock wave are:

$$\rho_2 (w_2 + u_2) = \rho_3 (w_2 + u_3) \quad (\text{III-6})$$

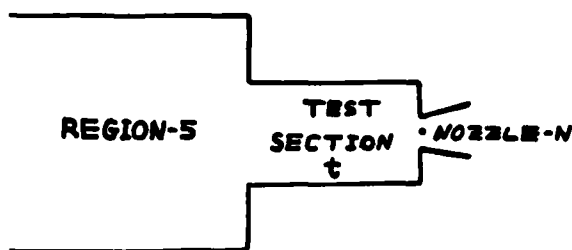
$$P_2 + \rho_2 (w_2 + u_2)^2 = P_3 + \rho_3 (w_2 + u_3)^2 \quad (\text{III-7})$$

$$H_2 + \frac{1}{2} (w_2 + u_2)^2 = H_3 + \frac{1}{2} (w_2 + u_3)^2 \quad (\text{III-8})$$

Equation of state:

$$P_3 = \rho_3 \tilde{R} T_3 \quad (\text{III-9})$$

The relations above are dependent on the rate of flow through the nozzle. The relations between region 5 and the test section are:



$$\rho_s A_s U_s = \rho_t A_t U_t \quad (\text{III-10})$$

$$P_s A_s + \rho_s A_s U_s^2 = P_t (A_s - A_t) + P_t A_t + \rho_t A_t U_t^2 \quad (\text{III-11})$$

$$H_s + \frac{1}{2} U_s^2 = H_t + \frac{1}{2} U_t^2 \quad (\text{III-12})$$

Equation of state:

$$P_t = \rho_t \tilde{R} T_t \quad (\text{III-13})$$

The relations between the test section and the nozzle throat plane are:

$$\rho_t A_t U_t = \rho_N A_N U_N \quad (\text{III-14})$$

$$P_t A_N + \rho_t U_t^2 A_t = P_N A_N + \rho_N U_N^2 A_N \quad (\text{III-15})$$

$$H_t + \frac{1}{2} U_t^2 = H_N + \frac{1}{2} U_N^2 \quad (\text{III-16})$$

Equation of state:

$$P_N = \rho_N \tilde{R} T_N \quad (\text{III-17})$$

The nozzle is choked, and therefore:

$$U_N = \sqrt{\gamma_N \tilde{R} T_N} \quad (\text{III-18})$$

For each of the regions- 2,5,t,N the pressure, temperature, density, and velocity are unknowns. Also  $W_1$  and  $W_2$  are unknowns. Thus, there are 18 unknowns and 18 nonlinear algebraic equations. The first five equations (III-1) through (III-5) constitute one set of coupled equations, and the balance of the equations (III-6) through (III-18) constitute a second set of coupled equations. By algebraic manipulations, the first set was reduced to 2 nonlinear algebraic equations with the unknowns:  $\frac{\rho_1}{\rho_2}$ ,  $W_1$

The second set was reduced to 4 nonlinear algebraic equations with the unknowns:  $W_2 + U_2$ ,  $\frac{\rho_2}{\rho_s}$ ,  $\frac{\rho_t}{\rho_s}$ ,  $\frac{\rho_t}{\rho_N}$

The equations were solved using a computer routine for the solution of nonlinear algebraic equations. The enthalpy tables given by Ref. 124 were approximated to Chebyshev polynomials, and so used in the equations. Once the above 6 unknowns were found, all the original 18 unknown physical values were obtained very easily from uncoupled simple relations.

To find the operating conditions required to obtain some prescribed test condition, e.g.,  $P_t$ ,  $T_t$  or  $U_t$ , the entire solution had to be iterated about a value of  $P_1$ ,  $P_4/P_1$  or  $A_N$ . A Regula Falsi method of iteration [121]

was used. Note for example that for a given  $P_4/P_1$  any combination of  $P_t$  and  $U_t$  is obtainable by varying  $P_1$  and  $A_N$ .

In practice,  $W_{exp}$  was measured as well as  $P_{texp}$ . Using the experimental value ( $W_{exp}$ ) the problem is reduced to a solution of only 5 nonlinear algebraic equations, 4 of which, simultaneously. The values obtained from  $W_{exp}$  for  $P_t$  were generally different from  $P_{texp}$  (due to non-ideal flow conditions). The values for  $T_{texp}$  were approximated from the measured  $P_{texp}$  and the calculated  $P_t$  and  $U_t$  by applying the isentropic relation:

$$\frac{T_{texp}}{T_t} = \left( \frac{P_{texp}}{P_t} \right)^{\frac{\gamma_t - 1}{\gamma_t}}$$

The value of  $U_{texp}$  is then found from the relations between the test section and the nozzle, based on  $P_{texp}$  and  $T_{texp}$ .

# APPENDIX IV

## CONSTRUCTION AND OPERATION OF THIN FILM GAUGES

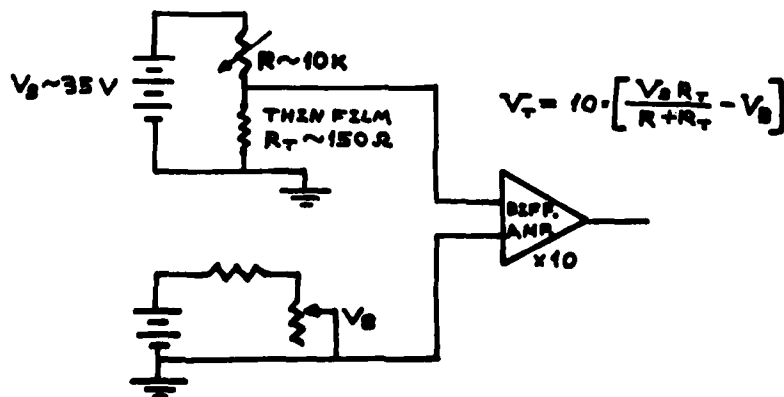
The thin-film resistance thermometer is used for surface temperature and heat transfer measurements when very rapid response times are desired. In essence, it is a device that measures the surface temperature history of a slab of material which is characterized as semi-infinite, homogeneous, and isotropic. Comprehensive studies of its construction, calibration and performance have been conducted over the years [125-127]. Thin-film resistance thermometry has found its applications in shock tunnel flows [19,125], measurements of igniter heat flux in solid propellant rocket motors [128], and in a wide range of test facilities characterized by unsteady heat transfer under pressure and velocity oscillations [85,86].

Basically, the thin film gauge is a thin film of electrically conducting material (e.g., platinum), coated or deposited on a substrate backing material (e.g., pyrex) which is a good electrical insulator. The backing material functions mechanically as a support for the thin film and thermally as a heat sink. The thickness of the thin film is made sufficiently small so that its presence on the substrate has a negligibly small effect on the substrate surface temperature. Thus, its instantaneous temperature is also the substrate surface temperature had it been exposed to the ambient temperature. To achieve better sensitivity in the measurements of very low heat transfer rates, the thermal conductivity of the substrate selected is kept low. By contrast the thermal conductivity of the film is kept high.

Due to its small thickness, the thin film has a considerable electrical resistance and as electrical current is passed through it, even a small temperature rise of the film results in a measurable voltage variation. To prevent electrical heating of the film, the electrical current is kept sufficiently low. If the temperature rise is not too large, the relation between the film temperature and its electrical resistance is linear and can be expressed as:

$$R_T = R_o \cdot [1 + a \cdot (T_T - T_o)] \quad (IV-1)$$

where "a" is the coefficient of resistivity, the subscript "o" refers to initial conditions and "T" refers to the instantaneous thin film conditions. The electrical circuit of the gauge used in the present work is shown below:



$V_B$  is a bias voltage adjusted to get  $V_T = 0$  when  $T_T = T_0$ . Thus:

$$V_B = V_S \cdot \frac{R_0}{R_0 + R}$$

Accordingly:

$$T_T - T_0 \approx \frac{V_T \cdot R}{10 \cdot V_S \cdot R_0 \cdot a} \quad (\text{IV-2})$$

The resistance  $R$  is large compared to  $R_T$  so that the current passing through the film remains almost constant (4 mA). If an upper limit is imposed on the electrical heating of the film, (i.e.,  $V_T^2/R_T$ ), then for a prescribed temperature rise and amplification factor, the following expression is obtained:  $V_T^2 = C \cdot R_0 \cdot a^2$  ( $C$  is a constant). Thus in order to get high sensitivity (i.e., large  $V_T$ ), a material with large "a" and large initial resistance is required. The most commonly used material combinations for thin film gauges are platinum film and pyrex substrate. The platinum is chosen mostly because of its inert nature, high melting point, and high resistance. That combination was also chosen for the present work.

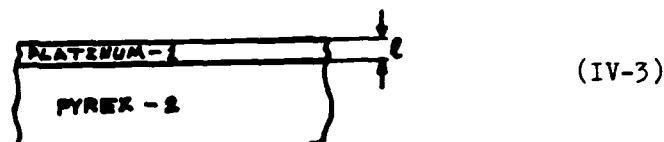
In the construction of the thin-film gauge, special attention was paid to avoid making disturbances in the boundary layer. The thin film gauge is shown in Figs. 35 and 36 and its construction process was as follows:

- (1) small holes (0.5 mm) are drilled through the pyrex tube for the electrical circuit electrodes.
- (2) The pyrex surface is acid cleaned and a thinned Hanovia Liquid Platinum is air brushed on the pyrex to form the film stripes. (The thinning is 50/50 by a mixture of 75% Trichlore and 25% Xylene).
- (3) The coated pyrex is heated up in the oven to 725 C. At that temperature the pyrex softens, the liquid platinum solvent vaporizes completely, and a very thin, 0.2  $\mu$ m, platinum film is formed. The film has a uniform thickness and it is fused onto the pyrex surface.
- (4) After cooling, the electrodes are potted in the holes with Silver Epoxy #3017 ACME E-Solder paste.
- (5) The electrical wires passing through the pyrex tube are potted with RTV #560 Aerospace Viscous Silicone Rubber.
- (6) The gauge is heated in the oven to 200 C and allowed to cool slowly. In this manner all pastes are hardened and structural stresses are relieved.
- (7) Surfaces around the holes are carefully smoothed.

The calibration of the gauge was done in the temperature range 25 to 200 C. The gauge was put in the oven and the entire electrical circuitry was connected to its leads. A radiation shield around the gauge and adjacent thermocouple prevented temperature discrepancies between the film and the thermocouple bead. Automatic registered readings of  $V_T$  versus the thermocouple output were taken as the gauge was cooling very slowly inside the oven (6 hours). The linearity between  $T_T$  and  $V_T$  expressed by Eq. (IV-2) was quite satisfactory. For better accuracy, the data ( $T_T$  vs.  $V_T$ ) was fitted using a polynomial expression of the order of 2. A value a 0.002/deg. C was obtained.

The incident heat transfer rate is calculated from the surface-temperature-time data. For that purpose, the thermal properties of the substrate (pyrex) must be known. One way of obtaining the heat transfer rate is by solving numerically the heat conduction equation. Another way is by using an integral expression developed from the classical heat conduction

theory to approximate the heat transfer into semi-infinite medium, i.e.:



$$q(t) = \sqrt{\frac{k_2 \rho_2 c_{p2}}{\pi}} \cdot \left\{ \frac{T(t)}{\sqrt{t}} + \frac{1}{2} \cdot \int_0^t \frac{T(t) - T(\tau)}{(t-\tau)^{3/2}} d\tau + \frac{1}{2} \cdot \frac{l}{k_1} \cdot \left( \frac{k_1 \rho_1 c_{p1}}{k_2 \rho_2 c_{p2}} - 1 \right) \cdot \frac{q(t)}{\sqrt{t}} \right\} \quad (IV-3)$$

The above expression is an alternate form of the expression given by Ref. 125.

Conversely, the surface temperature can be expressed as:

$$T(t) = \frac{1}{\sqrt{\pi \cdot k_2 \rho_2 c_{p2}}} \cdot \int_0^t \frac{q(\lambda)}{\sqrt{t-\lambda}} d\lambda - q(t) \cdot \frac{l}{k_1} \cdot \left( \frac{k_1 \rho_1 c_{p1}}{k_2 \rho_2 c_{p2}} - 1 \right) \quad (IV-4)$$

Expressions (IV-3) and (IV-4) were developed with the assumption of constant thermal properties. In reality, the thermal properties are functions of the temperature (their values are accurately known for platinum and pyrex). The main values of importance are those of the substrate (pyrex). Their temperature dependencies are either given in tables or expressed functionally [129]. For the purpose of the calculations based on Eq. (IV-3), values corresponding to the mean temperature are taken. If the partial differential equation of the heat conduction is solved numerically, the exact functional dependence of the thermal properties on temperature may be used.

Defining: 
$$\tau_R \triangleq \frac{\rho_1^2 c_{p1}^2 l^2}{k_2 \rho_2 c_{p2}}$$

The error in either the temperature or the inferred heat transfer rate due to thermally neglecting the sensor (the film) is:

$$\frac{\delta q}{q} = \frac{\delta T}{T} \sim \frac{\sqrt{\pi}}{2} \cdot \frac{\sqrt{\tau_R}}{\sqrt{t}}$$

The substrate surface temperature attains 91% of the ideal temperature change in a time  $\tau = 100 \cdot \tau_R$ . For the case of platinum and pyrex and  $l = 0.2 \mu m$  -  $\tau = 14 \mu s$ . Thus the response time is very fast. In the present work the highest data sampling rate was 50 KHz which corresponds to 20  $\mu s$  intervals. Therefore the heat flux data was calculated neglecting the sensor thickness ( $l = 0$ ). Both methods of solution were tried, i.e., direct numerical solution of the heat conduction equation and solution of Eq. (IV-3). Note that even Eq. (IV-3) has to be solved numerically. A numerical scheme developed by Ref. 130 was used for that purpose. Both solutions gave similar results. The first method (the direct solution) is more sensitive than the second (Eq. (IV-3)) to high frequencies and revealed too much of the artificial noise introduced to the data because of the finite sampling rate of the data acquisition system. The second solution filters that noise to some degree. The heat transfer data shown in this work is based on the solution of Eq. (IV-3) for  $l = 0$ .

AD-A091 852 PRINCETON UNIV NJ DEPT OF MECHANICAL AND AEROSPACE --ETC F/G 19/1  
CONVECTIVE IGNITION OF PROPELLANT CYLINDERS IN A DEVELOPING CRO--ETC(U)  
SEP 80 A BIRK, L H CAVENY DAAG29-79-C-0140

UNCLASSIFIED MAE-1486

ARO-13108.1-E

NL

3-3



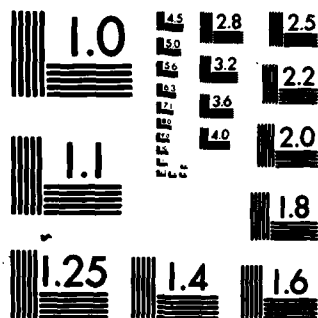
END

DATE

FILED

81-1

DTIC



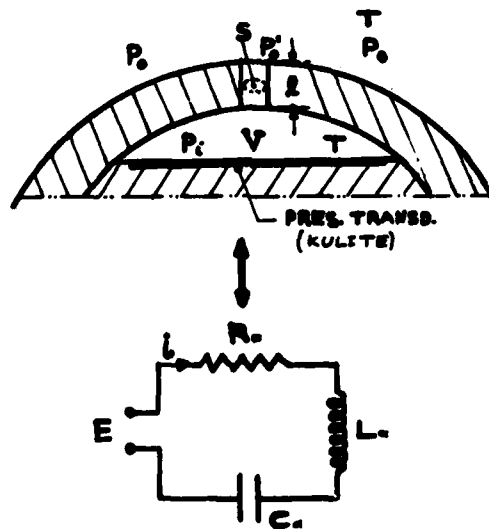
MICROCOPY RESOLUTION TEST CHART  
NATIONAL BUREAU OF STANDARDS-1963-A

# APPENDIX V

## MOUNTING CONFIGURATION AND PERFORMANCE OF THE MINIATURIZED PRESSURE TRANSDUCER IN THE INSTRUMENTED CYLINDER

The geometry and size of the instrumented cylinder precluded a flush mounting configuration for a pressure transducer. Considerations of available space dictated the choice of a thin line design-miniaturized pressure transducer. A custom modified Kulite LQL-125-200- integrated sensor strain gauge type pressure transducer was chosen and successfully used. The mounting of this pressure transducer was carefully designed to: a) ascertain rapid response time, b) avoid natural frequency pressure ringing phenomenon, and c) avoid damping of the pressure signals in the range of the characteristic frequency of the test pressure oscillations.

The mounting configuration, shown below, constitutes a Helmholtz resonator [131] which under low amplitude ambient pressure variations is analogous to LCR electrical circuit.



The momentum, mass and energy equations for the resonator are:

$$\rho \frac{du}{dt} = \frac{P_o' - P_i}{l_o} \quad l_o = l + 0.8\sqrt{V}$$

$$\rho u S = \frac{dP_i}{dt} \cdot V$$

$$\frac{dP_i}{dt} = \hat{c}^2 \cdot \frac{d\rho}{dt} = \gamma \cdot R \cdot T \cdot \frac{d\rho}{dt}$$

The above equations yield:

$$\frac{d^2 P_i}{dt^2} = \frac{\hat{c}^2 \cdot (P_o' - P_i) \cdot S}{l_o V} \quad (V-1)$$

The analogy between Eq. (V-1) and the LCR circuit is as follows:

$$\underbrace{L_1 \frac{di}{dt}}_{P_0 - P_1} + \underbrace{\frac{1}{C_1} \int i dt}_{P_1} + \underbrace{i R_1}_{P_0 - P_1} = \underbrace{E}_{P_0}$$

$$i \Rightarrow uS$$

(V-2)

$$\begin{aligned} \text{ORIFICE} & \rightarrow L_1 \Rightarrow \frac{\rho \ell}{S} \rightarrow Z_L = \frac{W \cdot \rho \cdot \ell}{S} \\ \text{CHAMBER} & \rightarrow C_1 \Rightarrow \frac{V}{\rho C^2} \rightarrow Z_C = \frac{\rho \cdot C^2}{W \cdot V} \\ \text{OPEN END} & \rightarrow R_1 \Rightarrow \frac{\rho W^2}{2\pi C} \rightarrow Z_R = \frac{\rho \cdot W^2}{2\pi C} \end{aligned}$$

The resistance  $R_1$  corresponds to open end acoustic radiation.  $Z_j$  are the impedances of the elements  $j$ .  $W$  is the frequency of  $P_0$ . The various dimensions of the resonator are:  $\ell = 0.5$  mm,  $S = 0.2$  mm<sup>2</sup>,  $V = 5$  mm<sup>3</sup>. For  $T = 1800$  K, the fundamental frequency of the orifice-chamber configuration is:  $C/2\ell = 38$  KHz. Thus, it can be treated as a resonator, up to  $W = 300$  KHz.

The natural frequency of the resonator is:

$$\nu_0 = \frac{1}{2\pi \sqrt{L_1 C_1}} \Rightarrow \frac{1}{2\pi} \cdot \sqrt{\frac{C^2 S}{V \cdot (\ell + 0.8 \ell)}} \quad \text{--- (V-3)}$$

For the above values -  $\nu_0 = 29$  KHz which is much smaller than the natural frequency of the pressure transducer itself - 200 KHz.

During the initial transient conditions of the flow, Eqs. (V-1) and (V-2) do not hold. The response time of  $P_1$  to the initial large pressure jump at the initiation of the flow can be approximated from the time it takes to charge the chamber to the ambient pressure  $P_0$  assuming that the orifice is choked. For  $T = 1000$  K and for  $P_0/P_1 = 20$  at  $t = 0$ , and assuming an adiabatic charging process, a value of 25  $\mu$ s is obtained for the time it takes  $P_1$  to reach  $P_0/2$ . As deduced from the experimental results, the initial rise time of  $P_1$  to the full value of  $P_0$  was about 80  $\mu$ s.

Typical test pressure fluctuations were significant for frequencies less than 10 KHz which are far below  $\nu_0$ . Evaluating the impedances defined in Eq. (V-2) for  $W = 10$  KHz and  $T = 1800$  K, the damping of the AC components of  $P_0$  is less than 10%. Indeed, excellent experimental agreement was obtained between the Kulite and the Kistler pressure transducers mounted flush at the bottom of the test section (see Fig. 41). Note that in order to improve the performance one would like to keep  $V$  and  $\ell$  as small as possible and  $S$  as large as possible.

From both the theoretical analysis and the experimental results, the frequency resolution of the pressure data obtained from instrumented cylinder is better than 10 KHz.